4-1-2019 10:00 AM

Optimal algorithms for deriving estimates of phytoplankton biomass in lakes from LANDSAT satellite imagery

Michael A. Dallosch
The University of Western Ontario

Supervisor
Creed, Irena F.
The University of Western Ontario Co-Supervisor
Trick, Charles G.
The University of Western Ontario

Graduate Program in Biology
A thesis submitted in partial fulfillment of the requirements for the degree in Master of Science

Recommended Citation

Dallosch, Michael A., "Optimal algorithms for deriving estimates of phytoplankton biomass in lakes from LANDSAT satellite imagery" (2019). *Electronic Thesis and Dissertation Repository*. 6087.
https://ir.lib.uwo.ca/etd/6087

Abstract

The frequency, intensity, and geographical distribution of harmful phytoplankton blooms are on the rise globally. There is a scientific need for estimates of historical and current phytoplankton data. This research develops mathematical algorithms for accurate assessment of surface chlorophyll-*a* (chl-*a*), a proxy for phytoplankton biomass, within freshwater lakes. Variations and levels of chl-*a* are then used as a basis for improved scientific understanding of phytoplankton blooms. Landsat satellite images (4-5 TM, 7 ETM and 8 OLI) were used to create a ±30-year predictive model (1984 to 2017) for seven ecoregions (ranging from the tropics to arctic). Correlation tests for 82 algorithms were conducted to establish the best fit models (linear, exponential, logarithmic, power) for chl-*a* and environmental parameters that interfere with the chl-*a* assessment (true colour, TSS, and turbidity). Three band algorithms involving absorbent and reflective bands multiplied by the near infrared band using power regression provided a generalisable predictive model across all regions (R^2 ranges from 0.40 – 0.81, $p < 0.05$). These best fit models provide accurate estimates for data collected over a wide range of geographic regions to develop a historical context of phytoplankton biomass as a basis for evaluating the effects of global scale changes on phytoplankton blooms.

Keywords

Remote sensing, lakes, phytoplankton, chlorophyll-*a*, blooms, water quality, Landsat

Co-Authorship Statement

This Master's thesis was funded by NSERC Create ABATE (Algal bloom assessment through technology and education), with data provided by the United States Geological Survey (USGS), National Water Monitoring Council databases (NWIS and STORET), Giblin & King, 1992, Government of British Columbia, Alberta Environment and Parks, Dorest Environmental Science Center (DESC, 2017), Sass *et al*., 2007, Sorichetti *et al*, 2014, Fallu & Pienitz, 1999; Mederios *et al*., 2012; Symons *et al*., 2012, Swedish University of Agricultural Sciences (Miljodata SLU) and the United Nations GemStat database. Michael A. Dallosch will be the first author for all manuscripts derived from this thesis, as he conducted the remote sensing techniques of atmospheric correction, data processing, and statistical analysis, with contribution to the definition of the research problem, design of the methods, interpretation of the results, and the writing of the manuscripts. Irena F. Creed will be the second author as she contributed to the definition of the research problem, design of the methods, interpretation of the results, and the writing of the manuscripts.

Acknowledgments

I would like to first send my sincere gratitude to my supervisor Dr. Irena F. Creed, for her guidance and support throughout my two-year venture into remote sensing of lakes. You have provided me with a great wealth of experiences that have, and will continue to shape me throughout my academic career. From the wetlands of Alberta to Lake Victoria of Uganda, I will be forever grateful for the magnitude of life experiences you provided. I would also like to thank Dr. Charles Trick, for acting as co-supervisor half-way through my thesis, for providing his insight and knowledge towards the completion of my thesis.

I would like to thank my advisory committee, Dr. Hugh Henry and Dr. Danielle Way for their continued support and encouragement, and Dr. Ben Rubin, for his knowledge of statistical analysis and acting as advisor for the last 8 months of my thesis.

Thank you very much to Dave Aldred for his wonderful help as a result of his deep knowledge and experience in remote sensing and scientific writing. This extends to Jacqueline Serran, Aleksey Paltsev, Dr. Ben DeVries, Dr. Mark Carrol, and Jennifer Rover for their great contribution to my thesis regarding remote sensing, GIS and scientific writing, as their contributions were invaluable.

To the members of Creed Lab and associates – Camille Chemalli, Haibin “Rick” Dong, Eric Enanga, Kevin Erratt, Erika Freeman, Reneé Howard, Mali Mehdizadeh, Saloni Salaria, Oscar Senar, Veerta Singh, and Jason Were – your insight, knowledge and friendship has been invaluable. Thank you very much to the members of Create ABATE, as being able to meet and interact with you all has greatly enriched my personal and professional development.

I would like to thank all my friends and family for their continued support in all that I do. To my mother, Debbie Dallosch who taught me so much about life and the world. To my younger brother Adam Dallosch, who taught me a magnitude of patience, and my older brother Ryan Dallosch, who set the example.

This thesis was provided financial support from an NSERC CREATE grant awarded to Dr. Irena Creed.

Table of Contents

List of Tables

List of Figures

List of Appendices

List of Abbreviations

6SV	Second Simulation of the Satellite Signal in the Solar Spectrum–Vector
BCF	Boreal coniferous forest
Chl-*a*	Chlorophyll-*a*
COST	Cosine of the solar zenith angle
DDV	Dark dense vegetation
DOC	Dissolved organic carbon
DOM	Dissolved organic matter
DOS	Dark object subtraction
ETM+	Enhanced thematic mapper plus
FNU	Formazin nephelometric turbidity unit
LaSRC	Landsat surface reflectance code
LEDAPS	Landsat ecosystem disturbance adaptive processing system
NIR	Landsat Near-infrared band (Band 4 for TM and ETM+, Band 5 for OLI)
NTU	Nephelometric turbidity unit
OLI	Operational land Imager
PTW	Polar and boreal tundra woodland ecoregion
SHF	Subtropical humid forest ecoregion

TCF	Temperate continental forest ecoregion
TM	Thematic Mapper
TMF	Tropical Moist deciduous forest ecoregion
TPD	Temperate desert ecoregion
TPS	Temperate steppe ecoregion
TSS	Total suspended solids

Chapter 1

1 Introduction

1.1 Problem statement

The frequency and magnitude of phytoplankton blooms in freshwater and marine ecosystems around the world appear to be increasing (Winter *et al.*, 2011; Anderson, 2014; Pick, 2016) (Figure 1.1). Phytoplankton are widely considered to be one of the most important groups of photosynthetic organisms in global biogeochemical cycling (Carr & Whitton, 1982; Paerl & Otten, 2013; Wehr *et al*., 2015), producing up to 40% of the atmospheric oxygen and serving as the carbon entry point for aquatic food webs (Falkowski and Raven, 2007). In addition, these autotrophs are key in the remineralization of N, with some able to fix atmospheric nitrogen (N_2), store and cycle phosphorus (P), and cycle iron from the photic zones (Carr & Whitton, 1982; Molot *et al.*, 2014; Wehr *et al*., 2015) – all processes that maintain the biogeochemical availability of these major nutrients (Schlesinger, 1997). In spite of the positive ecological attributes of phytoplankton, the formation of excessive levels of phytoplankton – termed blooms and usually measured using the biomass proxy, chlorophyll-*a* per volume – often indicate an imbalance of the ecosystems (phytoplankton grow, yet are not consumed into the food web). The unconsumed, lingering biomass has negative ecological and human health risks.

There is some debate regarding the drivers of bloom development, with increases in temperature, nutrients, and light availability considered the main requirements. Under these conditions, certain genera of phytoplankton will grow at rates greater than consumption or loss rates that result in the accumulation of cells. While many of these blooms are considered non-threatening, the accumulation of some cyanobacteria genera, such as *Anabaena* and *Microcystis,* are associated with the production toxins (such as microcystins). These toxins can cause neurological and endocrine damage in humans, and alterations in aquatic ecosystems including light deprivation, nutrient sedimentation, and deoxygenation (Wagner & Adrain, 2009; Paerl & Otten, 2013). With this potential sequence of events the bloom is often denoted as a harmful algal bloom (HAB) (Paerl & Otten, 2013).

Cyanobacteria are the largest contributor to freshwater bloom events (Lopez *et al.*, 2008; Taranu *et al.*, 2015; Huisman *et al.*, 2018). Anthropogenic climate change is theorized to be the main driver of increased bloom activity (Pearl & Huisman, 2008). Toxin-producing cyanobacteria are most often found in nutrient-rich lakes; however, there has been an increase in the number of reports from nutrient-poor lakes (Winter *et al.*, 2011; Callieri *et al.*, 2014; Cottingham *et al.*, 2015).

Despite the suggestion of increasing freshwater blooms from reports, much of the historical evidence is anecdotal, relying on locations and events where observers were interested enough to make reports, and at fine spatial scales. Spatially and temporally extensive surveys of freshwater lakes are needed to confirm the existence of a trend towards increased blooms and to evaluate the relationship of bloom frequency to external drivers including anthropogenic climate change. Archived and current satellite images provide the opportunity to make these surveys.

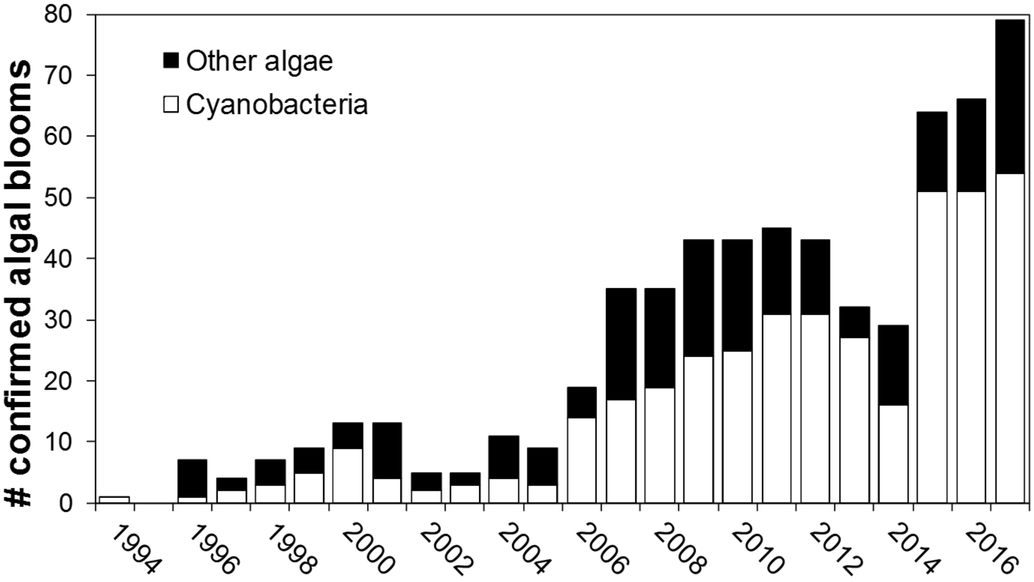

Figure 1.1 Increase in algal bloom reports in Ontario, Canada from 1994 to 2017 (adapted from Winter *et al.*, 2011).

1.2 Remote sensing of freshwater phytoplankton biomass

To assess the levels of accumulated phytoplankton biomass in large numbers of lakes, or lakes that are difficult to assess, remote sensing can be valuable. Space-borne satellite remote sensors use electromagnetic radiation to image the surface of the Earth. Electromagnetic radiation produced by the sun across a spectrum of wavelengths travels through space to be intercepted by the Earth and is reflected, absorbed, scattered, and/or reradiated back to space in different proportions at different wavelengths dependent on factors such as the angle of incidence, Earth-to-sun distance and the properties of the radiated surfaces of the Earth. The most important spectral region in optical remote sensing is the visual to infrared spectrum; wavelengths in this spectrum provide a great deal of insight into surface conditions as many important parameters (e.g., vegetation and water) interact with those wavelengths and modify them depending on their properties (Camps-Valls, 2012). The atomic properties of all surface materials affect the proportion of electromagnetic radiation that is absorbed or reflected at every wavelength differently, resulting in unique peaks of absorption or reflectance at particular wavelengths. Charted against wavelength, these proportions form a spectral curve that is unique for every surface material.

Remote sensors measure the radiant flux density (watts $(\mathrm{W})/\mathrm{m}^2$) at the top of the atmosphere of electromagnetic radiation reflected from the Earth within specific wavelength ranges (bands) and in discrete spatial units (pixels). Algorithms can be applied to this top-of-atmosphere (TOA) radiance $(\mathrm{W}/(\mathrm{m}^2 \times \mathrm{sr} \times \mu\mathrm{m}))$ to derive measures such as TOA reflectance (proportion of incoming radiation that is reflected by the Earth’s surface, atmosphere and clouds) or surface (bottom-of-atmosphere) reflectance (proportion of incoming radiation that is reflected by the Earth’s surface) to examine surface properties or characterize surface types. Specific surface materials can be identified when their peak absorption or reflectance coincides with band wavelength ranges (bandwidths) of the sensors; the majority or absence of radiance or reflectance in the bandwidth can be attributed to the presence of the surface material.

The Landsat satellite series has been imaging the Earth since 1972, making it the longest active running systems of optical space-borne remote sensors. There are many remote sensors available that are capable of modeling phytoplankton biomass (Table 1.1). However, Landsat images since the launch of the Landsat Thematic Mapper (TM) sensor in 1982 have the temporal (1982-present) and spatial resolution (30-meter pixels) that is adequate for monitoring freshwater lakes.

Studies as early as Carpenter & Carpenter (1983) have used Landsat images to estimate phytoplankton biomass (a summary of studies can be found in Appendix A). Chl-*a* concentration is most often used as a proxy for phytoplankton biomass in these studies as it is most often the main photosynthetic pigment present in phytoplankton. The spectral curve of chl-*a* exhibits two absorption peaks, at 440 nm (blue) and 670 nm (red) wavelengths.

The broad bandwidths of Landsat sensors can make it difficult to distinguish between chl-*a* and non-chl-*a* pigments as well as other constituents in water (Vincent *et al.*, 2004). For example, blue bandwidths in Landsat sensors do not capture the blue absorption peak of chl-*a*, and therefore these bands are considered as reflective bands (Table 1.2). Similarly, all carotenoids and chlorophyll pigments feature absorption peaks in the red bandwidths (650-700 nm), and community compositions can strongly influence reflectance in the green bandwidths (550-600 nm) (Schalles, 2006). Further, different algal taxa from different algal classes (e.g., *Navicula* (Bacillariophycea), *Anabaena* (Cyanobacteria), *Peridinium* (Pyrrophyceae), *Chlorella* (Chlorophyceae)) may contain additional accessory pigments such as chlorophyll-*b*, chlorophyll-*c* and phycocyanin that can shift the peak absorption or reflectance of phytoplankton to higher or lower wavelengths by increasing or decreasing the rate of absorption or reflectance (Schalles, 2006). Other constituents present in water that may also influence absorption or reflectance in a bandwidth are sediments and dissolved organic matter (DOM). These influences can make it difficult to determine if measured reflectance in a broad Landsat sensor bandwidth is the result of chl-*a* or of one or more other constituents.

Empirical modelling is often used to estimate chl-*a* concentration from Landsat images where *in situ* samples of chl-*a* concentration at the water surface (< 1 m depth) are regressed to measurements of radiance or reflectance from images taken at the same times and locations to develop predictive models. The models can then be applied to the temporal and spatial range of its inputs. Empirical models frequently use exponential curves as chl-*a* concentrations are often not normally distributed.

Table 1.1 Overview of satellite sensors available for phytoplankton biomass monitoring.

Agency	**Satellite**	**Sensor**	**Spectral Bands**	**Spatial/Temporal Resolution**	**Availability**
NASA[1]	Landsat 5	TM[6]	7 Bands	30 m/ 16 days	1984-2013
NASA	Landsat 7	ETM+[7]	8 Bands	30 m/ 16 days	1999-Present
NASA	Landsat 8	OLI/TIRS[8]	11 Bands	30 m/ 16 days	2013-Present
ESA[2]	ENVISAT[4]	MERIS[9]	15 Bands	1000 m (Ocean) 300 m (Terrestrial) / Daily	2002-2011
ESA	Sentinel 2-a	MSI[10]	13 Bands	10-20 m/ 5 days	2015-Present
ESA	Sentinel 3-a	OCLI[11]	21 Bands	300 m/ Daily	2016-Present
NASA	Terra and Aqua	MODIS[12]	36 Bands	250 m to 1000 m/ Daily	1999-Present
NOAA[3]	Suomi NPP[5]	VIIRS[13]	36 Bands	250 m/ Daily	2012-Present

[1] National Aeronautics and Space Administration, [2] European Space Agency, [3] National Oceanic and Atmosphere Association, [4] Environmental Satellite, [5] Suomi National Polar-Orbiting Partnership, [6] Thematic Mapper, [7] Enhanced Thematic Mapper Plus, [8] Operational Land Imager/Thermal Infrared Sensor, [9] Medium Resolution Spectrometer, [10] MultiSpectral Instrument, [11] Ocean and Land Colour Instrument, [12] Moderate Resolution Imaging Spectroradiometer, [13] Visible Infrared Imaging Radiometer Suite

Table 1.2 Summary of Landsat TM, ETM+ and OLI/TIRS bands and wavelength ranges (bandwidths).

Landsat 4-5 TM	**Wavelengths (nm)**
Band 1 - Blue	450-520
Band 2 - Green	520-600
Band 3 - Red	630-690
Band 4 - Near Infrared (NIR)	760-900
Band 5 - Shortwave Infrared (SWIR) 1	1,550-1,750
Band 6 - Thermal	10,400-12,500
Band 7 - Shortwave Infrared (SWIR) 2	2,080-2,350
Landsat 7 ETM+	**Wavelength (nm)**
Band 1 - Blue	450-520
Band 2 - Green	520-600
Band 3 - Red	630-690
Band 4 - Near Infrared (NIR)	770-900
Band 5 - Shortwave Infrared (SWIR) 1	1,550-1,750
Band 6 - Thermal	10,400-12,500
Band 7 - Shortwave Infrared (SWIR) 2	2,090-2,350
Band 8 - Panchromatic	520-900
Landsat 8 OLI/TIRS	**Wavelength (nm)**
Band 1 - Ultra Blue	435-451
Band 2 - Blue	452-512
Band 3 - Green	533-590
Band 4 - Red	636-637
Band 5 - Near Infrared (NIR)	851-879
Band 6 - Shortwave Infrared (SWIR) 1	1,566-1,651
Band 7 - Shortwave Infrared (SWIR) 2	2,107-2,294
Band 8 - Panchromatic	503-676
Band 9 - Cirrus	1,363-1,384
Band 10 - Thermal Infrared (TIRS) 1	10,600-11,190
Band 11 - Thermal Infrared (TIRS) 2	11,500-12,510

1.2.1 Interference of additional non-pigment water constituents

The estimation of chl-*a* concentration is inherently difficult due to the presence of sediments and DOM in freshwater lakes. These constituents have their own unique spectral signatures and when mixed in a medium of water with phytoplankton, can change the expected spectral curve of chl-*a* drastically (Schalles, 2006). The variability of concentrations of chl-*a* and these other constituents makes it additionally difficult to isolate correlations between radiance or reflectance as observed by satellites and chl-*a* concentrations when samples from multiple lakes or from the same lake over time are used (Lymburner *et al*., 2016; Lin *et al.*, 2018). Variabilities in spectral curves as a result of changes in water chemistry will increase with distance, as lakes closer together are more related than those further apart as a result of similarities in climate and geology, where temperature, precipitation, vegetation, and soil chemistry can alter the discharge of sediments and DOM, thereby increasing lake productivity. Modelling chl-*a* concentration in turbid waters is still more difficult with Landsat sensor data as the broad bandwidths can encompass the peak signals of these additional constituents.

Empirical models require *in situ* samples. Measures of sediments and DOM are not often available in most water quality databases. Where sediments and DOM data are not available, more commonly measured metrics such as true colour, dissolved organic carbon (DOC), total suspended solids (TSS), and turbidity may be used. DOC is highly correlated with true colour (MECP, 2017) which can be described as the yellowness or brownness of water, where higher true colour indicates darker waters. True colour is predominantly influenced by the presence of dissolved humic and fluvic acids (Watts *et al.,* 2001). TSS and turbidity consists of all suspended matter (including sediments and phytoplankton), with TSS measuring total mass per volume, where turbidity measures relative clarity (Gray *et al*, 2000; Anderson, 2005; Khalil *et al.,* 2013; Teixeira *et al*, 2016).

To overcome these issues, band radiances or reflectances are often multiplied (band combination), divided (band ratio) or combined into more complex equations (algorithms). Band combinations, ratios, or algorithms model relationships between reflective and absorptive bands. Chl-*a* concentration in non-turbid or oligotrophic waters are traditionally identified through Blue and Green bands (O'Reilly *et al.,* 1998; Carder *et al.,* 2004; Sudheer *et al.,* 2006; Salem *et al.,* 2017). Other commonly used models use Red-to-Blue ratios or combinations of Red and Blue band radiance or reflectance (Han & Jordan 2005; Sass *et al.,* 2007), or Green-to-Red ratios or combinations of Green and Red band radiance or reflectance (Brezonik *et al.,* 2005; Ha *et al.,* 2017).

However, DOM is predominantly measured at shorter wavelengths (Olmanson *et al.,* 2016), while the addition of sediments increases the total reflectance of water with the greatest increase in shorter wavelengths (Schalles, 2006). Therefore, models using Blue and Green band radiance or reflectance show poor results within inland waters (Moses *et al*., 2009). Both DOM and sediments are found to have less influence on absorption or reflectance in the Near-Infrared (NIR) band (Gitelson *et al.*, 2007), so that many studies have found the use of a Red-to-NIR ratio performed best in turbid waters (Han *et al.*, 1994; Dall'Olmo *et al.*, 2003; Signh *et al.*, 2014); however, the applicability of these models is less known over larger temporal and spatial scales (Lin *et al.*, 2018). Three-band algorithms have also been used for monitoring chl-*a* in turbid waters, as first described by Gitelson *et al* (2003; 2011), and later adapted by Keith *et al*. (2018). These models multiply a modelled difference between the peak reflectance in the Green band and peak absorption in the Red band by the NIR band; similarly, the applicability of these algorithms at large temporal and spatial scales is relatively unknown.

1.2.2 Atmospheric Correction

Atmospheric conditions can greatly affect the absorption and scattering of wavelengths from the top of the atmosphere to the Earth's surface and back. Atmospheric conditions vary over time and will introduce shifts in radiance measured by a sensor that are not indicative of changes on the surface. It is therefore important to remove the effects of the atmosphere from satellite radiance measurements when assessing surface characteristics across space and time.

Atmospheric correction methods are either image-based (dependent on information in the image only) or radiative transfer- (or physical-) based (requiring independent data for optical atmospheric properties at the time of image acquisition). Dark Object Subtraction (DOS; Chavez, 1988) and Cosine of the solar zenith angle (COST; Chavez, 1996) image-based atmospheric corrections rely on the presence of dark pixels and assume that their measured radiance is a result of the atmosphere; however, lakes will often be the darkest pixels present in an image so that the assumption would be invalid (Moses *et al*., 2015; Siegal *et al*., 2000). Radiative transfer-based corrections such as "Second Simulation of the Satellite Signal in the Solar Spectrum–Vector" (6SV) (Vermote *et al.,* 2006), Landsat ecosystem disturbance adaptive processing system (LEDAPS) (Masek *et al.,* 2013), and Landsat surface reflectance code (LaSRC) (Vermote *et al.,* 2016) rely on a magnitude of variables, most importantly aerosol scatter, that are highly variable over inland waters and can be difficult to acquire.

The 6SV method corrects for two key aspects of atmospheric light absorption and scatter: Rayleigh and Mie scattering. Rayleigh scatter is attributed to the molecular properties of the atmosphere (N_2, O_2, O_3, H_2O, CO_2, etc.), while Mie scatter is a result of aerosols (dust, water vapour, etc.) which range in size from 0.001 μm to about 20 μm (Vermote & El Saleous, 2007). The model makes use of the Dark, Dense Vegetation (DDV) method (Kaufman, 1997) to estimate aerosol optical thickness. DDV is a terrestrial model, however, and the application to inland waters may not be appropriate and can result in negative reflectance in water (Nazeer *et al.*, 2014).

Due to the intrinsic problems of using terrestrial aerosol calculations, only the effects of Rayleigh scattering (considered to be relatively stable and therefore correctable over inland waters (Wang *et al*., 2007) on path radiance are considered in this study. Atmospheric gas concentrations can be assumed to be constant; therefore, total Rayleigh scatter radiance can also be assumed to be constant depending on the solar elevation angle. While radiance may provide similar results, the influence of Rayleigh scatter within the blue portion of the electromagnetic spectrum is large (Young, 1981), making a correction for Rayleigh scattering especially important for Blue bands.

1.3 Research objective

The objective of this research is to identify the combinations, ratios, or algorithms of Landsat band reflectance and the regression types that can be used to create models for predicting chl-*a* concentrations in freshwater lakes across a range of geographic regions with limited confusion from the presence of other freshwater optical constituents. This objective is achieved by:

1) identifying strong and significant correlations between *in situ* sampled chl-*a* concentrations from freshwater lakes and combinations, ratios, or algorithms of Landsat band reflectance across a number of ecoregions;
2) identifying the regression type (linear, exponential, logarithmic, or power) that provides the most strong and significant correlations between *in situ* sampled chl-*a* concentrations and the tested combinations, ratios, or algorithms of Landsat band reflectance across the same ecoregions;

3) determining whether significant correlations exist between *in situ* sampled freshwater optical constituents (true colour, DOC, TSS and turbidity) within the same ecoregions for each tested combination, ratio or algorithm of Landsat band reflectance; and
4) assessing the predictive power of chl-*a* retrieval models developed using (a) the most strongly correlated combinations, ratios, or algorithms of Landsat band reflectances as predictor variables and (b) the regression type that provided the most strong and significant correlations between chl-*a* concentration and the tested combinations, ratios, or algorithms of Landsat band reflectance, and (c) for which there were no significant correlations with other freshwater optical constituents.

The results of this study will help researchers survey phytoplankton biomass in freshwater lakes across large spatial and temporal extents. These surveys can be used to quantify the existence of trends in lake trophic states and serve as a foundation for further analysis such as evaluating the potential drivers of increasing algal blooms.

1.4 Thesis structure

This thesis is to be structured in monograph format. Chapter 1 provides an introduction and overview of the problem surrounding phytoplankton blooms and the application of remote sensing to solving this problem. Chapter 2 describes the different study regions in which models relating Landsat surface reflectance to chl-*a* concentration (as a proxy of phytoplankton biomass) are developed. Chapter 3 describes the methods used for atmospheric correction of Landsat image data and for model development. Chapter 4 describes the results and Chapter 5 expounds upon the results and discuss their implications. Chapter 6 will conclude the research, summarize the findings, and identify their significance for future research.

Chapter 2

2 Study Region

Correlations between chl-*a* concentration and other freshwater optical constituent samples and Landsat image data were developed for seven ecoregions or groupings of ecoregions defined by the Food and Agriculture Organization of the United Nations (FAO, 2012): Polar/Boreal Tundra Woodland (PTW), Boreal Coniferous Forest (BCF), Temperate Continental Forest/Temperate Mountain System (TCF), Temperate Steppe (TPS), Temperate Desert (TPD), Subtropical Humid Forest (SHF) and Tropical Rainforest/Tropical Moist Deciduous Forest (TMF) (Figure 2.1). Ecoregions are identified by dominant vegetation and climatic conditions (evapotranspiration, precipitation, humidity and temperature; Table 2.1) that can heavily influence aquatic ecosystems. Ecoregions were chosen for modelling based on data availability. PTW and TMF regions included the Polar and Boreal Tundra Woodland ecoregions and the Tropical Rainforest and Tropical Moist Deciduous Forest ecoregions respectively; ecoregions were combined due to climactic and vegetative similarities and a relatively small data sample size for each individual ecoregion. Each ecoregion is as described by the UN FAO Global Ecological Zones (Simons *et al.* 2001).

The means of temperature and precipitation measurements are calculated from National Oceanic and Atmospheric Administration (NOAA) grid 30-year (1981-2010) climate normals (temperature: Fan & van den Dool (2008); precipitation: Schneider *et al.* (2011)). All information regarding climate, soils, topography and dominant vegetation can be found in table 2.1.

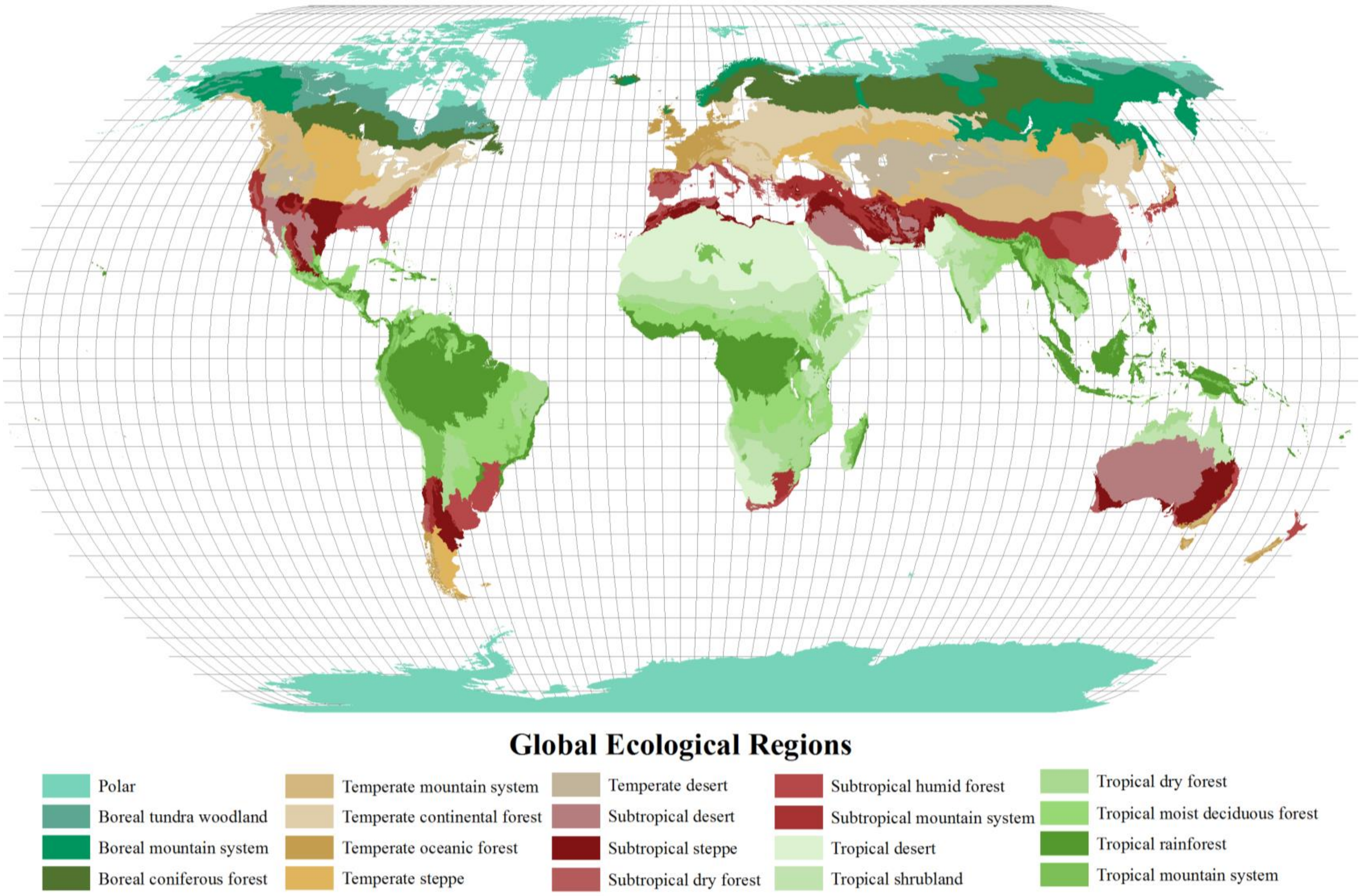

Figure 2.1 Global ecological regions as described by the United Nations Food and Agriculture (data provided by FAO Geonetwork)

Table 2.1 General descriptions of climate, topography, soil and vegetation characteristics, distributions of lake trophic status, and number of *in situ* sample measurements of freshwater chl-*a* concentration and optical constituents for each ecoregion or grouping of ecoregions used in this study.

	Polar/Boreal Tundra Woodland (North America) (PTW)	**Boreal Coniferous Forest (North America and Sweden) (BCF)**	**Temperate Continental Forest/Temperate Mountain System (North America) (TCF)**	**Temperate Steppe (North America) (TPS)**	**Temperate Desert (North America) (TPD)**	**Subtropical Humid Forest (North America) (SHF)**	**Tropical Moist Deciduous Forest (North and South America)/Tropical Rainforest (Caribbean) (TMF)**
Climate[1]	Polar: no warm (≥ 10°C) summer months Boreal Tundra Woodland: long, very cold winters and short cool or mild summers	Long, very cold winters and short cool or mild summers	Temperate Continental Forest: warm and frequently humid summers and cold winters Temperate Mountain System: drier and cooler summers and cold winters			Hot, humid summers and mild winters	
Mean annual temperature (°C yr^{-1}) (1981-2010)[2]	Polar: -11 (-20 - +5) Boreal Tundra Woodland: -4 (-11 - +4)	North America: 0 (-4 - +6) Sweden: +2 (-5 - +9)	Temperate Continental Forest: +8 (0 - +16) Temperate Mountain System: +5 (-7 - +17)	+8 (+1 - +17)	+8 (-1 - +20)	+18 (+13 - +24)	Tropical Moist Deciduous Forest (North America): +25 (+19 - +34) Tropical Moist Deciduous Forest (South America): +25 (+15 - +33) Tropical Rainforest: +25 (+17 - +30)

	Polar/Boreal Tundra Woodland (North America) (PTW)	Boreal Coniferous Forest (North America and Sweden) (BCF)	Temperate Continental Forest/Temperate Mountain System (North America) (TCF)	Temperate Steppe (North America) (TPS)	Temperate Desert (North America) (TPD)	Subtropical Humid Forest (North America) (SHF)	Tropical Moist Deciduous Forest (North and South America)/Tropical Rainforest (Caribbean) (TMF)
Mean annual total precipitation (mm yr^{-1}) (1981-2010)[3]	Polar: 230 (66 - 1500) Boreal Tundra Woodland: 500 (175 - 1200)	North America: 700 (300 - 1700) Sweden: 700 (400 - 1000)	Temperate Continental Forest: 1000 (500 - 1600) Temperate Mountain System: 1000 (140 - 4000)	500 (250 - 1200)	300 (100 - 700)	1300 (1000 - 1700)	Tropical Moist Deciduous Forest (North America): 1500 (700 - 4000) Tropical Moist Deciduous Forest (South America): 1500 (500 - 4600) Tropical Rainforest: 2100 (700 - 4500)
Topography[1]	Polar: rolling upland and lowlands Boreal Tundra Woodland: lowland plains, coastal marshes and wetlands	North America: mosaic of uplands, wetlands and lakes Sweden: undulating plains and rolling hills	Temperate Continental Forest: level plains and rolling hills Temperate Mountain System: mountains	Level to rolling plains	**b**asins, plateaus and plains	Plains and gentle slopes	Tropical Moist Deciduous Forest (North America): plains, rolling hills and everglades Tropical Moist Deciduous Forest (South America): flat Brazilian and Guiana Shields Tropical Rainforest: lowlands

		Polar/Boreal Tundra Woodland (North America) (PTW)	**Boreal Coniferous Forest (North America and Sweden) (BCF)**	**Temperate Continental Forest/Temperate Mountain System (North America) (TCF)**	**Temperate Steppe (North America) (TPS)**	**Temperate Desert (North America) (TPD)**	**Subtropical Humid Forest (North America) (SHF)**	**Tropical Moist Deciduous Forest (North and South America)/Tropical Rainforest (Caribbean) (TMF)**
Soils[1]		Polar: thin or absent morainal deposits Boreal Tundra Woodland: cryosolic and mesisolic	North America: luvisols, humo-ferric podzols and brunisols Sweden: acidic podzols, cambisols and histosols	Temperate Continental Forest: of luvisols, brunisols and gleysols Temperate Mountain System: luvisols, brunisols in interior plains, humo-ferric podzols in wet mountainous areas, and chernozems in drier valleys	Chernozems, solonetzic soils to south, and luvisols in elevated areas	Aridisols in basins and entisols in floodplains	Ultisols, with entisols and inceptisols dominating floodplains and alluvial bottomlands	Tropical Moist Deciduous Forest (North America): calcareous soils Tropical Moist Deciduous Forest (South America): ferrisols and utisols Tropical Rainforest: ultisols, inceptisols, and oxisols
Vegetation[1]		Polar: sparse at high latitudes (*Betula* spp. on coasts and further south terrestrially, *Picea* spp. along rivers) Boreal Tundra Woodland: extensive around wetlands and in transition to boreal forests (birch and pine species in drained locations)	North America: spruce species in wet soils, *Picea* spp. in drier soils in west Sweden: *Betula* spp, *Populus tremula* (L.), *Alnus* spp., *Salix* spp.	Temperate Continental Forest: mixed coniferous and deciduous species with forest loss attributed to agriculture and urbanization Temperate Mountain System: diverse (hemlock, pine, spruce and grass species)	Grasslands with *Populus tremuloides* (Michx.) and *Populus balsamifera* (L.) in northern transitional areas, *Populus* spp. *and Quercus macrocarpa* (Michx.) in eastern transitional areas, and *Quercus* spp. and *Carya* spp. in southern transitional areas	*Artemisia tridentata* (Nutt.) and short grasses with intermittent brush species	Diverse with *Quercus myrtifolia* (Willd.), *Quercus virginiana* (Mill.), *Quercus laurifolia* (Michx.), *Magnolia grandiflora* (L.), *Magnolia virginiana* (L.) in coastal plains and *Quercus* spp., *Carya* spp., *Liquidambar styraciflua* (L.), *Acer rubrum* (L. 1753), *Andropogon gerardi* (Vitman), *Panicum* spp. and *uniola* spp. and woody vines further inland	Tropical Moist Deciduous Forest (North America): tall deciduous trees (> 100 species) Tropical Moist Deciduous Forest (South America): dense three canopy level forests Tropical Rainforest: high canopy dense forests (> 5000 vascular plant species)
Lake trophic status	Oligotrophic (0.0 - 2.6 μg L^{-1})	50%	18%	23%	8%	20%	21%	35%
	Mesotrophic	47%	42%	48%	41%	56%	50%	32%

		Polar/Boreal Tundra Woodland (North America) (PTW)	**Boreal Coniferous Forest (North America and Sweden) (BCF)**	**Temperate Continental Forest/Temperate Mountain System (North America) (TCF)**	**Temperate Steppe (North America) (TPS)**	**Temperate Desert (North America) (TPD)**	**Subtropical Humid Forest (North America) (SHF)**	**Tropical Moist Deciduous Forest (North and South America)/Tropical Rainforest (Caribbean) (TMF)**
	(2.6 - 20.0 μg L^{-1})							
	Eutrophic (20.0 - 56.0 μg L^{-1})	2%	31%	16%	25%	17%	21%	27%
	Hypereutrophic (56.0 - 155 μg L^{-1})	1%	9%	10%	19%	6%	8%	7%
	> 155.0 μg L^{-1}	0%	1%	2%	6%	1%	1%	0%
Selected *in situ* samples	Chl-*a* (n)	18 (0.65-115.7 μg L^{-1} chl-*a*) 1991-199 10 oligotrophic 5 mesotrophic 1 eutrophic 2 hypereutrophic	30 (1.3-112.5 μg L^{-1} chl-*a*) 1984-2017 4 oligotrophic 17 mesotrophic 4 eutrophic 5 hypereutrophic	82 (0.5-136.4 μg L^{-1} chl-*a*) 1985-2016 13 oligotrophic 50 mesotrophic 14 eutrophic 5 hypereutrophic	24 (1.3-74.5 μg L^{-1} chl-*a*) 1985-2015 3 oligotrophic 11 mesotrophic 9 eutrophic 1 hypereutrophic	30 (0.95-96.9 μg L^{-1} chl-*a*) 1985-2008 6 oligotrophic 15 mesotrophic 5 eutrophic 4 hypereutrophic	36 (1.29-102 μg L^{-1} chl-*a*) 2010-2014 3 oligotrophic 16 mesotrophic 10 eutrophic 7 hypereutrophic	30 (0.02-97 μg L^{-1} chl-*a*) 1986-2010 5 oligotrophic 16 mesotrophic 8 eutrophic 1 hypereutrophic
	True colour (n)	18	28	44	n/a	14	34	14
	TSS (n)	n/a	n/a	18	27	17	28	16
	Turbidity (n)	n/a	16	21	37	21	35	16

[1] Simons et al. 2001

[2] National Oceanic and Atmospheric Administration (NOAA) grid 30-year (1981-2010) climate normals (Fan & van den Dool 2008)

[3] National Oceanic and Atmospheric Administration (NOAA) grid 30-year (1981-2010) climate normals (Schneider et al. 2011)

[4] Carlson & Simpson, 1996

Chapter 3

3 Methodology

3.1 Freshwater lake sample data

In situ sample measurements of chl-*a* concentration and optical constituents of water (true colour or DOC, TSS, and turbidity) in freshwater lakes were collected from the following sources (table 3.1):

Table 3.1 *In situ* sample measurements of chl-*a* concentration and optical constituents of water (true colour or DOC, TSS, and turbidity) in freshwater lakes by regional source

Region	**United States**	**Canada**	**Sweden**	**Paraguay**
Chl-a (n)	158	71	14	7
Years	1985-2015	1984-2016	1999-2017	2000-2004
True colour (n)	69	55	69	0
Years	1990-2014	1984-2016	1989-2016	N/A
TSS (n)	106	0	0	0
Years	2001-2016	N/A	N/A	N/A
Turbidity (n)	114	16	16	0
Years	1986-2014	1985-2010	2016	N/A
Sources	United States Geological Survey (USGS) National Water Monitoring Council databases (NWIS and STORET), Giblin & King, 1992	Government of British Columbia, Alberta Environment and Parks, Dorest Environmental Science Center (DESC, 2017), Sass *et al.*, 2007, Sorichetti *et al*, 2014, Fallu & Pienitz, 1999; Mederios *et al.*, 2012; Symons *et al.*, 2012	Swedish University of Agricultural Sciences (Miljodata SLU)	United Nations GemStat database

Only samples taken ≤ 1 m from the water surface and collected within the growing season (all months in TMF, July-October for all other ecoregions) were used. For a detailed list of each samples used in each region see table 3.2. Sample lakes ranged in size from 4.5 to 163,000 ha with a median area of 90 ha. An overview of the methods can be found in Figure 3.2.

Table 3.2 Total number of *in situ* sample measurements of chl-*a* concentration and optical constituents of water (true colour or DOC, TSS, and turbidity) in freshwater lakes by ecoregion

Ecoregion	**PTW**	**BCF**	**TCF**	**TPS**	**TPD**	**SHF**	**TMF**
Chl-a (n)	18	30	82	24	30	36	30
True colour (n)	18	28	44	N/A	14	34	14
TSS (n)	N/A	N/A	18	27	17	28	16
Turbidity (n)	N/A	16	21	37	21	35	16

3.1.1 Chlorophyll-*a*

Chl-*a* concentration (μg L^{-1}) is commonly measured by a spectrophotometry but fluorometry and high-performance liquid chromatography (HPLC) are also used (Hambrook-Berkman & Canova, 2007). A known volume of water sample is filtered through a 47 mm GF/F glass-fiber filter with a nominal porosity of 0.7 μm. The filters were then stored at -80°C until analysis. Filters were submerged in a 90% acetone solution for 24 hours at -4°C for chl-*a* extraction. Chl-*a* concentration was measured in a spectrophotometer and calculated using the Jeffery and Humphrey (1975) method.

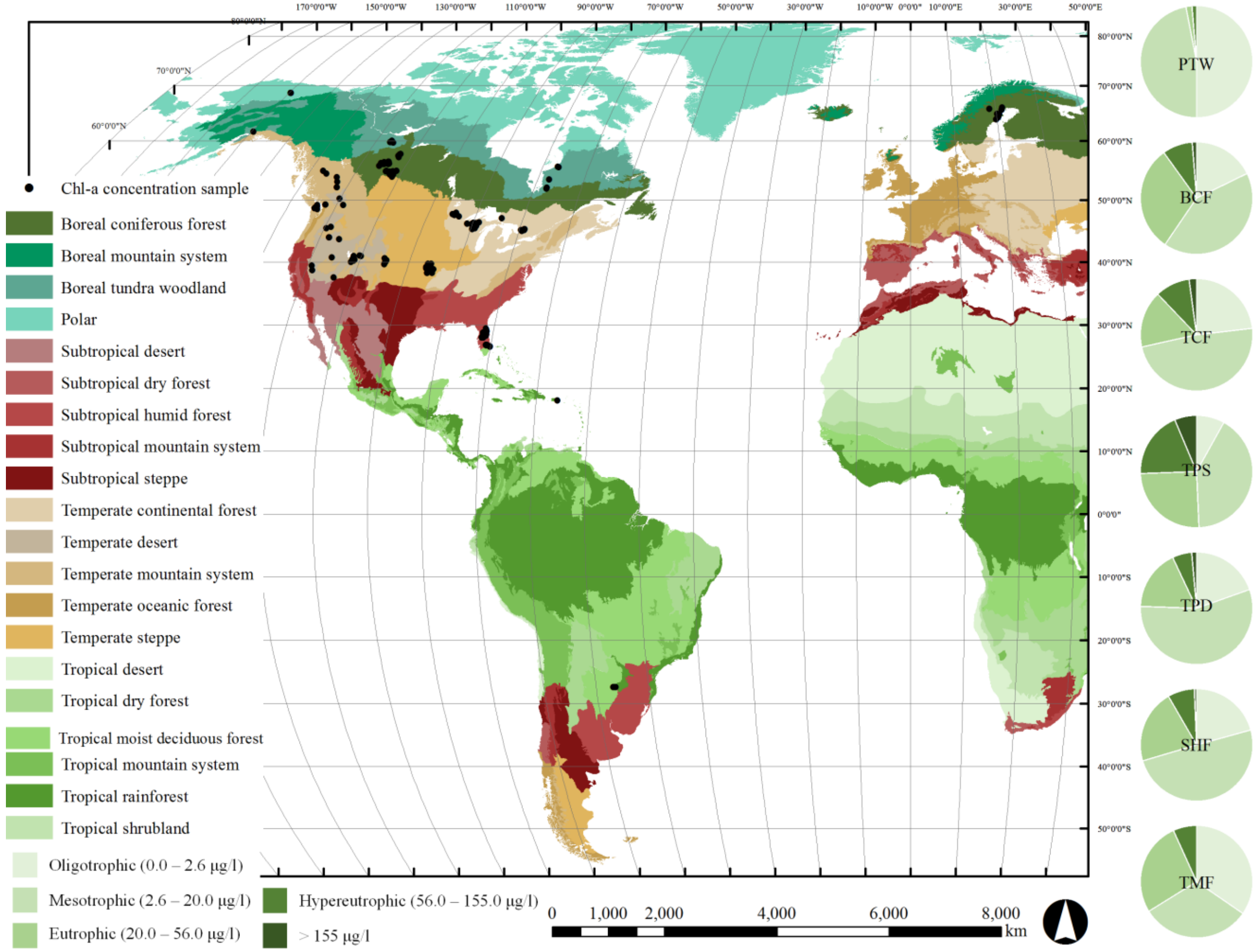

Figure 3.1 Surface water chl-*a* concentration sample distribution. Total chl-*a* samples taken at a depth of <1.0m. Pie charts indicate the distribution of lake trophic state as specified by Carlson & Simpson (1996) and determined by chl-*a* concentration.

3.1.2 True colour

True colour is the colour of water after particulate matter has been removed through filtration (usually through a 0.45 μm pore filter). In natural waters, colouration is mainly a result of DOM, dissolved sediments and tannins. The absorbance of filtered water was measured at 410 nm via spectrophotometer and the absorbance is converted to true colour units (TCU) using Hazen’s Cobalt-Platinate (also known as Platinum-Cobalt or Pt-Co) Standards calibration regression which compares the absorbance to the absorbance curve of a 1 mg Pt-Co solution, where 1 mg Pt-Co L^{-1} is equal to 1 TCU. There were no true colour samples in the PTW or TPS ecoregions.

3.1.3 Dissolved organic carbon (DOC)

Dissolved organic carbon (DOC measured in mg L^{-1} samples were used in lieu of true colour where true colour data were not available (PTW region only) as there has been found to be a significant correlation between the variables (MECP, 2017). Water samples are filtered through a 0.45 μm pore filter and oxidized to form carbon dioxide, the mass of which is then measured using a conductivity detector (Potter & Wimsatt, 2005).

3.1.4 Turbidity

Turbidity is an indicator of the relative clarity of water expressed as the intensity of light scattered in water by both suspended and dissolved materials in water, including phytoplankton and other microscopic organisms. Turbidity was commonly measured with either a single- or multiple-detector nephelometer. The instrument shines white light (400-680 nm) through water and measures the intensity of water reflected back at 90° from the incident angle to determine the level of scattering expressed in Nephlometric Turbidity Units (NTUs) (U.S. Environmental Protection Agency, 1993). Turbidity sample data from the Swedish University of Agricultural Sciences are derived from light shone at 780-900 nm and are expressed in Formazin Nephelometric Units (FNUs) (International Organization for Standardization, 1999; Anderson, 2005); these are the only turbidity samples available for the BCF ecoregion and were therefore comparable for the intra-ecoregion analysis. There were no turbidity samples in the PTW ecoregion.

3.1.5 Total suspended solids

TSS (mg L^{-1}) is the dry weight of all suspended and undissolved particles including sediments and phytoplankton within a unit volume of a water sample. Water samples were typically mixed and filtered through a pre-weighed glass-fiber filter which was then heated and weighed to determine mass per volume (Fisher Scientific, 2007). There were no TSS samples in the PTW or BCF ecoregions.

3.2 Landsat image acquisition and processing

3.2.1 Landsat data acquisition

Landsat Level-1 at-satellite radiance images are geo-registered and corrected for terrain relief displacement using digital elevation models (USGS, 2017). Landsat Level-2 images are provided as surface reflectance products corrected for atmospheric effects using LEDAPS (TM/ETM+) and LaSRC (OLI/TIRS) algorithms (USGS, 2018a; USGS, 2018b). Due to the failure of the Scan Line Corrector (SLC) aboard Landsat 7 on May 31, 2003, 22% of pixels in images after this date (SLC-off) are missing values.

Sample locations were mapped to the grid-based Worldwide Reference System (WRS-2) Landsat catalogue system to identify the (longitudinal) paths and (latitudinal) rows in which samples were found. Landsat 4-5 TM, 7 ETM+ (SLC-on) and 8 OLI/TIRS Level-1 and -2 images (1984-2017) with < 10% cloud coverage and within ±2 days of sample dates were downloaded from the USGS EarthExplorer data catalogue (https://earthexplorer.usgs.gov/) for:

- 157 scenes (specific dates and path/row combinations) (123 Landsat 4-5 TM, 24 Landsat 7 ETM+, 10 Landsat 8 OLI/TIRS) corresponding to chl-*a* samples;
- 65 scenes (49 Landsat 5 TM, 6 Landsat 7 ETM+, 10 Landsat 8 OLI/TIRS) corresponding to true colour and DOC samples;

- 41 scenes (30 Landsat 5 TM, 4 Landsat 7 ETM+, 7 Landsat 8 OLI/TIRS) corresponding to TSS samples; and
- 74 scenes (59 Landsat 5 TM, 11 Landsat 7 ETM+, 4 Landsat 8 OLI/TIRS) corresponding to turbidity samples.

A summary of Landsat images per WRS-2 path/row combination by ecoregion is found in Table A.1.

3.2.2 Top-of-atmosphere radiance calibration

TOA radiance ($\mathrm{W}/(\mathrm{m}^2 \times \mathrm{sr} \times \mu\mathrm{m})$) measured by Landsat sensors are scaled using multiplicative (gain) and additive (bias) scaling factors to 8-bit (0-255; Landsat TM and ETM+) and 16-bit (0-65,000; Landsat OLI/TIRS) integer value ranges (digital numbers or DNs) for transmission and storage in Level-1 products. Level-1 products include metadata pertaining to the image acquisition including date, time, solar elevation and the scaling factors. DNs are recalibrated to TOA radiance using the standard equation (Chandar & Markham, 2003):

$$L_\lambda = (DN_\lambda \times G_\lambda) + B_\lambda \tag{3.1}$$

where L is TOA radiance for wavelength range or band λ, G is the band multiplicative rescaling factor (gain), and B is the band additive rescaling factor (bias).

3.2.3 Top-of-atmosphere reflectance corrected for Rayleigh scattering

Correction of TOA radiance for Rayleigh scatter was applied using an inverse algorithm based on a simplified radiative transfer model presented by Gilabert (1994):

$$\begin{aligned} L_{r(\lambda)} = {} & \left(\frac{ESUN_\lambda \times \cos\theta_s \times P_r}{4\pi \times (\cos\theta_s + \cos\theta)}\right) \times \left(1 - \exp\left(-\tau_r(\lambda) \times \left(\left(\frac{1}{\cos\theta_s}\right) + \left(\frac{1}{\cos\theta}\right)\right)\right)\right) \\ & \times t_{oz} \uparrow (\lambda) \times t_{oz} \downarrow (\lambda) \end{aligned} \tag{3.2}$$

where L_r is the Rayleigh path radiance for wavelength range or band λ, $ESUN$ is the mean solar exo-atmospheric irradiance, P_r is the Rayleigh phase function, θ_s is the solar zenith angle in degrees, θ is the satellite viewing angle in degrees (equal to 0° for Landsat 4, 5 and 7 sensors and for nadir-looking Landsat 8 OLI/TIRS images), τ_r is the Rayleigh optical thickness, and $t_{oz}\uparrow$ and $t_{oz}\downarrow$ are upward ozone transmittance and downward ozone transmittance respectively. The Rayleigh phase function (P_r), explained by Chendrasekhar (1960) and later adapted by Vermote *et al*. (2006) for the 6SV radiative transfer algorithm, describes the angular distribution of scattered light via equation 3.3:

$$P_r = \frac{3}{4} \cdot \frac{1-\gamma}{1+2\gamma} \cdot (1 + cos^2\Theta) + \frac{3\gamma}{1+2\gamma} \qquad (3.3)$$

where Θ is the scattering angle (180° − θ_s), $\gamma = \delta/(2- \delta)$, and δ is the depolarization factor as described by Young (1980), which is a factor denoting the polarization of anisotropic particles at right angles and is dependent on the wavelength, atmospheric pressure (constant) and air mass (constant). Rayleigh optical thickness (τ_r) is calculated via equation (3.4) (Hansen & Travis, 1974; Bodhaine *et al*., 1994):

$$\tau_r = 0.008569\lambda^{-4} \cdot (1 + 0.0113\lambda^{-2} + 0.00013\lambda^{-4}) \qquad (3.4)$$

where λ is the band specific mid-wavelength value (measured in nm). Upward and downward ozone transmittance are calculated as described by Sturm (1984) via equations 3.5 and 3.6:

$$t_{oz} \uparrow = \exp(-\tau_{oz}) \qquad (3.5)$$

$$t_{oz} \downarrow = \exp\left(\frac{-\tau_{oz}}{cos\theta_s}\right) \qquad (3.6)$$

where τ_{oz} is the constant ozone optical thickness as calculated by Jorge *et al* (2017). Rayleigh path radiance is subtracted from TOA radiance to determine Rayleigh corrected TOA radiance ($\hat{L}_\lambda$) via equation 3.7:

$$\hat{L}_\lambda = L_\lambda - L_r \qquad (3.7)$$

$\hat{L}_\lambda$ is converted to TOA reflectance as described by the USGS via equation 3.8:

$$\rho_\lambda = \frac{\pi \cdot \hat{L}_\lambda \cdot d^2}{ESUN_\lambda \cdot cos\theta_s} \tag{3.8}$$

where ρ is TOA reflectance for wavelength range or band λ and d is the Earth-to-sun distance in astronomical units. This correction method converts to TOA reflectance to avoid issues regarding shifts in the solar zenith angle due to latitude and time of year. The goal of this method is to provide a robust correction that does not rely on terrestrial-based aerosol predictions. Errors due to shifts in aerosols can still provide error; however, these errors are limited by using images with lower total cloud coverage (less atmospheric hydrological activity and therefore more homogenous water vapour).

3.2.4 Landsat 7 ETM+ to Landsat 8 OLI reflectance comparison

The OLI sensor in Landsat 8 introduced differences in bandwidths from TM/ETM+ sensors, particularly in Red and NIR bands (bands 3 and 4 (TM/ETM+) and bands 4 and 5 (OLI) respectively; Table 1.3). In order to have confidence in models that combine reflectance from these sensors, it is important to ensure that reflectance measured in these bands are comparable between sensors.

Pairs of corresponding Landsat 7 ETM+ and Landsat 8 OLI images with cloud coverage < 5% within ±8 days (offset between acquisitions of Landsat 7 and Landsat 8) of each other were acquired (only Landsat ETM+ and OLI images were compared as the Landsat TM sensor was discontinued prior to the launch of Landsat 8). Seven pairs of images meeting these criteria were located in British Columbia, Alberta and Ontario, Canada, and in California and Kansas, U.S.

Random points (10,000 at a minimum 90-meter distance) were generated in the central 22-km strip of the Landsat ETM+ images where scan line failure did not create missing data. Clouds were masked using high confidence cloud pixels identified in the Pixel Quality Assessment band provided with Level-2 products, and reflectance values were sampled at each remaining point.

Differences in sampled reflectance for each band λ between the sensors were evaluated using: (1) the mean absolute error (MAE; unsigned mean of differences between Landsat 8 sampled reflectance (λ) and Landsat 7 sampled reflectance (λ)); (2)

bias (signed mean of Landsat 8 sampled reflectance (λ) minus Landsat 7 sampled reflectance (λ)); and (3) the coefficient of determination (R^2), slope and intercept of linear regressions developed using Landsat 8 sampled reflectance (λ) as a dependent variable and Landsat 7 sampled reflectance (λ) as an independent variable.

3.2.5 Lake boundary delineation

Surface water pixels were identified using the Dynamic Surface Water Extent (DSWE) model developed by Jones (2016) and adapted by DeVries *et al* (2017). The model is implemented using a python script with Landsat Level-2 surface reflectance data as inputs, specifically the Blue, Green, Red, NIR, SWIR1 and SWIR2 bands, and a CFmask band (a generated cloud cover band developed with LEDAPS for Landsat TM and ETM+ and with LaSRC for OLI). The model generates an output raster with pixel values denoting terrain, water, cloud, and cloud shadow. DSWE model results are preferred over water pixels identified in the current USGS Level-2 Pixel Quality Assessment band for determining lake boundaries as there is higher confidence in separating pixels influenced by emergent vegetation. Contiguous groups of water pixels were vectorized without polygon simplification (i.e., lake vector boundaries matched pixel boundaries). The polygons were subsequently buffered inwards by 15 m (1/2 pixel width) to minimize the effects of spatial differences in lake boundaries less than pixel width and the spectral effects of edge pixels where the reflectance of vegetation and shallow depths mix with the reflectance of water. After buffering, lake polygons smaller than 4.5 ha (50 pixels) were discarded, also for the purpose of reducing the potential of mixed pixels.

3.3 Lake selection for correlation testing

Sample coordinates were joined to lake polygons derived from corresponding Landsat images within ± 2 days of each other, consistent with the time window suggested by Sass *et al* (2007). When multiple samples were taken from the same lake within the two-day window surrounding image acquisition, sample values were averaged. Lake polygons were used to extract representative lake reflectance values instead of extracting reflectance values at the sample points because of the uncertainty of the sample coordinates (i.e., spatial precision and whether the coordinates represented sample or lake coordinates). Extracting reflectance values in a polygon assumes that chl-*a* concentration and other constituents are relatively homogeneous throughout a lake so that a sample taken in one location is representative of samples taken in any other location. To satisfy this assumption, lakes with a relatively high standard deviation of TOA radiance values in the Red band were discarded as light in this bad is more highly scattered by algal cell walls (Menken et al, 2006). The threshold of allowable standard deviation was determined separately for each ecoregion given the requirements for a minimum number of samples for each ecoregion and the apparent differences in TOA radiance variability in lakes between ecoregions. Lakes with a standard deviation of Red band TOA radiance greater than the median for the ecoregion were discarded.

While standardized criteria for sample-to-image time window matching, image cloud coverage and Red band TOA radiance standard deviation in lakes were established, exceptions were made to criteria in some ecoregions. Samples were matched within ±3 days instead of ±2 days in the PTW and TMF ecoregions due to limited samples. Images containing cloud coverage < 60% were acquired in the PTW and BCF ecoregions due to limited samples and < 25% in the TMF ecoregion due to the fact that few images were found at < 10% cloud coverage. Lakes in the TPS ecoregion were found to have relatively low standard deviations of Red band TOA radiance, and therefore only lakes with a standard deviation of Red band TOA radiance greater than the 75th percentile were removed. Conversely, lakes in the TPD region exhibited relatively high standard deviations of Red band TOA radiance, and therefore only lakes with a standard deviation of Red band TOA radiance greater than the 25th percentile were removed.

After removing lakes with a standard deviation of Red band TOA radiance greater than the median in the TCF ecoregion, there was a disproportionate number of oligotrophic (≤ 2.6 μg chl-a L^{-1}) and mesotrophic (> 2.6 and ≤ 20 μg chl-a L^{-1}) chl-*a* samples, resulting in a non-normal distribution of chl-*a* concentration (Figure 3.1). As the majority of mesotrophic lakes had chl-*a* concentrations ≤ 10 μg $L^{-1,}$ lakes with a standard deviation of Red band TOA radiance greater than the median of this subset were also discarded. The pixel depth (or bit-depth) in Landsat TM and ETM+ images are poor at discerning subtle changes in oligotrophic waters (8-bit compared to Landsat OLI’s 16-

bit) (Kutser, 2012; Baghdadi & Zribi, 2016). Therefore, in order to provide more eutrophic (> 20 and ≤ 56 µg chl-*a* L^{-1}) and hyper-eutrophic (> 56 and ≤ 155 µg chl-a L^{-1}) lakes in the sample distribution, chl-*a* concentration samples from the BCF in northern Alberta (Sass et al., 2007) were added to the samples in the TCF ecoregion.

The numbers of chl-*a* concentration samples by year and the distributions of sample trophic states for each ecoregion are given as in table 3.3:

Table 3.3 Chl-*a* concentration samples per ecoregion by year and the distributions of sample trophic states

Ecoregion	PTW	BCF	TCF	TPS	TPD	SHF	TMF
Chl-a (n)	18	30	82	24	30	36	30
Years	1991-1999	1984-2017	1985-2016	1985-2015	1985-2008	2010-2014	1986-2010
Concentration range (µg L^{-1})	0.65-115.7	1.3-112.5	0.5-136.4	1.3-74.5	0.95-96.9	1.29-102	0.02-97
Number of images	9	21	39	19	28	12	30
Oligotrophic (%)	56%	13%	16%	13%	20%	8%	17%
Mesotrophic (%)	27%	57%	61%	45%	50%	44%	53%
Eutrophic (%)	6%	13%	17%	38%	17%	28%	23%
Hyper-Eutrophic (%)	11%	17%	6%	4%	13%	20%	3%

3.4 Correlation testing and regression modelling

Sample chl-*a* concentration, true colour or DOC, TSS, and turbidity were related to mean corrected TOA reflectance within corresponding lake polygons after reflectance pixels identified as high confidence cloud or cloud shadow in the Pixel Quality Assessment band provided with Level-2 products were removed.

For each ecoregion, sample chl-*a* concentration, true colour or DOC, TSS, and turbidity (dependent variables) were related to four reflectance band means and 78 combinations of reflectance band means (independent variables, hereinafter referred to as algorithms; Appendix D) using four different regression equation types: (1) linear (no data transformations); (2) exponential (natural log transformation of dependent variable); (3) logarithmic (natural log transformation of independent variable); and (4) power (natural log transformations of both variables). For section 4.2, 71 algorithms are tested to compare regression methods, as 11 algorithms provided negative x-axis values (and therefore not log-transformable). Pearson correlation (R) was used to assess the strength of the relationship between each constituent and each algorithm. P-values were used to assess the significance ($P < 0.05$) of the relationships. Pearson correlation tests were performed prior to outlier removal to assess initial fit. Outliers were identified using Cook's distance > 4/n and removed in a maximum of three iterations from selected models. A total of 7,872 models were generated and only generalizations of the results and specific algorithms are given in this thesis. The resulting models may expect considerable variability, a summary of expected potential error can be found in table

Table 3.4 Summary of potential variables associated with this study design that may introduce variability into the developed models.

Error producing variable	Description
1. Temporal lag between image and sample	Landsat sensors have a 16 day temporal resolution, and so the likelihood of matching an image to a sample is low. Many genera of phytoplankton can move vertically in the water column and what may have been measured at the surface one day, may not be visible by the sensor the next day (or vice versa). This possibility would introduce the highest potential of variability in the models, creating a very high mismatch of potential reflectance measurements.
2. Lake bottom effect	Lake bathymetry mapping is a time intensive procedure requiring *in situ* sonar measurements. Light can penetrate into the water (deeper at shorter wavelengths) and reflect the bottom of the lake, increasing the total reflectance. Standard deviation thresholds can reduce the total variation introduced, but only for oligotrophic lakes with more complex bathometry.
3. Aerosol scatter	Aerosols present in the atmosphere (e.g., fine dust, water vapour), are not corrected for in this study. The presence of increased aerosols can increase total atmospheric scatter, particularly at shorter visible wavelengths. The presence of water vapour is minimize by percent cloud coverage thresholds, however increases in dust particles (from forest fires or volcanic eruptions) are not considered in this study and may introduce variability in the models.
4. Varying algal communities	The composition of phytoplankton communities is not often assessed or tested in water quality analysis, and are therefore not reported. It is unknown what the community compositions are within the given *in situ* data. Differing taxa may contain additional pigments (e.g., chlorophyll-*b*), which can add

	to/change the spectral absorbance and reflectance observed in the lake. These changes are more often subtle and in which the Landsat bandwidths may not be affected as extensively. While this can still affect the total reflectance measured, this would introduce limited variance in the models.
5. Varying constituent concentrations	It is well known that the presence of sediments and DOM can greatly affect the spectral absorption of the lakes, introducing vary high variation into the model. The application of band algorithms is designed to minimize this effect by assessing differences between bands measurements related to the presence of chl-*a*. Measurements of true colour, TSS and turbidity are tested with the same algorithms to determine a difference in correlation. Therefore the potential variability within the finalized models should be minimized.

3.5 Spatial cross-validation of regression models

To provide confidence that selected models provide predictive capabilities across large geographic extents, a spatial cross-validation technique was implemented using the MLR package in R (Bernd *et al*, 2016). This function randomly removes spatial clusters in a specified number of iterations of a size specified by the user as a testing dataset; the remaining samples are used as a training dataset. This package requires the creation of what are called tasks, learners and resampling descriptions to create a resampling function. Tasks specify the input data (chl-*a* samples) to be targeted for prediction, and the spatial context (sample coordinates). A learner is a prediction model which for this study is set to the linear regression type and for which the standard error of the model is measured. A resampling description defines the resampling method (“SpRepCV” or Spatial Resampling Cross-Validation), the number of folds or testing samples (30%), and the desired number of iterations (100).

The resulting resampled data is used to create a 1:1 scatterplot in which the slope, intercept and bias of the model are calculated. The resample function calculates the Root Mean Square Error (RMSE) and MAE of the model predictions. RMSE is used to measure predictive power and is calculated as:

$$RMSE = \sqrt{\frac{\sum_{i=1}^{n}(y_i - x_i)^2}{n}} \tag{3.2}$$

where *y* is the observed reflectance value and *x* is the predicted value at point i. MAE is used to determine the average predictive error and is calculated as:

$$MAE = \frac{1}{n}\sum_{i=1}^{n}|y_i - x_i| \tag{3.3}$$

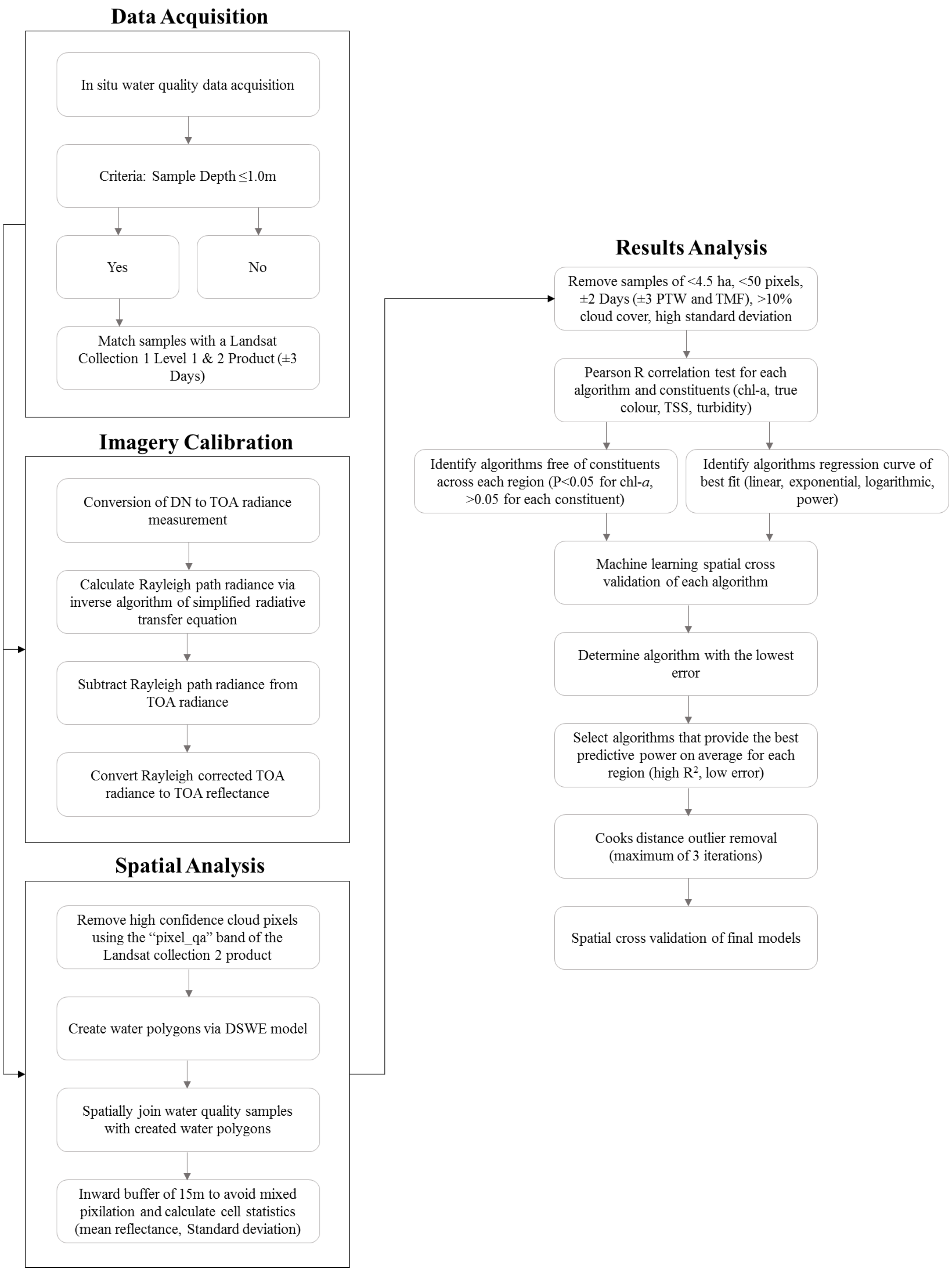

Figure 3.2 Flowchart overview of methodology from data acquisition to validation of the final models.

Chapter 4

4 Results

4.1 Landsat 7 ETM+ to Landsat 8 OLI reflectance comparison

Blue, Green and Red bands showed the smallest differences in reflectance between Landsat 7 ETM+ and Landsat 8 OLI sensors as illustrated by MAE and bias (Table 4.1). While NIR band reflectance showed the largest differences as illustrated by MAE, bias was small and NIR band reflectance showed the greatest correlations with each other in the sample pairs as illustrated by the coefficient of determination when the reflectance were regressed to each other R^2). All regression comparisons were significant ($p < 0.05$) with slopes close to 1 and intercepts close to 0. Deviation from a 1:1 line is most likely due to surface or atmospheric changes; bias is likely due to bandwidth differences.

Table 4.1 Landsat 7 ETM+ to Landsat 8 OLI reflectance comparison results.

WRS-2 path/row (year)	Band	MAE (0 - +1)	Bias (-1 - +1)	OLI/TIRS Image Cloud %	ETM+ Image Cloud %	R^2	Slope	Intercept
019/026 (2013)	**Blue**	0.004	-0.003	0.09	0.00	0.88	0.872949	0.0019
	Green	0.004	0.002			0.93	0.904875	0.0055
	Red	0.005	0.003			0.94	0.902984	0.0060
	NIR	0.010	-0.002			0.96	1.029851	-0.0071
027/033 (2017)	**Blue**	0.009	-0.007	0.03	0.00	0.77	0.92032	-0.0018
	Green	0.007	0.000			0.79	0.975462	0.0013
	Red	0.008	0.003			0.77	1.045412	-0.0001
	NIR	0.018	0.014			0.96	1.037901	0.0035
041/035 (2015)	**Blue**	0.011	-0.010	0.03	0.00	0.89	0.868912	0.0021
	Green	0.007	-0.005			0.94	0.967219	-0.0012
	Red	0.007	-0.003			0.96	1.000485	-0.0035
	NIR	0.013	0.008			0.90	1.046385	-0.0018
041/035 (2016)	**Blue**	0.004	-0.002	0.10	0.00	0.95	0.972969	-0.0006
	Green	0.004	0.000			0.95	0.983628	0.0011
	Red	0.006	-0.002			0.95	0.989032	-0.0005
	NIR	0.013	0.009			0.92	1.065065	-0.0059
043/020 (2013)	**Blue**	0.004	0.004	1.96	0.00	0.57	0.604849	0.0168
	Green	0.007	0.007			0.72	0.892741	0.0104
	Red	0.007	0.007			0.72	0.925599	0.0085
	NIR	0.011	0.010			0.96	1.048194	0.0017

WRS-2 path/row (year)	Band	MAE (0 - +1)	Bias (-1 - +1)	OLI/TIRS Image Cloud %	ETM+ Image Cloud %	R^2	Slope	Intercept
047/018 (2013)	**Blue**	0.005	-0.004	6.96	0.00	0.59	0.857937	0.0008
	Green	0.002	-0.001			0.82	0.991456	-0.0003
	Red	0.003	0.000			0.86	1.02856	-0.0009
	NIR	0.009	0.005			0.95	1.089064	-0.0095
048/026 (2014)	**Blue**	0.005	-0.005	0.06	0.00	0.85	0.888758	-0.0014
	Green	0.002	0.000			0.93	1.000837	-0.0003
	Red	0.003	-0.001			0.94	0.95152	-0.0005
	NIR	0.017	0.014			0.99	1.107532	-0.0021

4.2 Regression types

For regressions of sampled chl-*a* concentration to all combinations, ratios or algorithms of Landsat band reflectance (n = 71) in all ecoregions (n = 7), linear regressions (no data transformations) had a mean and median R of 0.46 and 0.45 respectively, exponential regressions (natural log transformation of chl-*a* concentration) had a mean and median R of 0.49 and 0.51 respectively, logarithmic regressions (natural log transformation of reflectance) had a mean and median R of 0.46 and 0.48 respectively, and power regressions (natural log transformations of chl-*a* concentration and reflectance) had a mean and median R of 0.52 and 0.54 respectively.

Out of 497 possible models (71 combinations, ratios or algorithms of Landsat band reflectance × seven ecoregions), maximum R was found in 133 linear models (26.8%), 112 exponential models (22.5%), 59 logarithmic models (11.9%) and 193 power models (38.8%), and minimum R was found in 158 linear models (31.8%), 121 exponential models (24.3%), 161 logarithmic models (32.4%) and 57 power models (11.5%) (Figure 4.1).

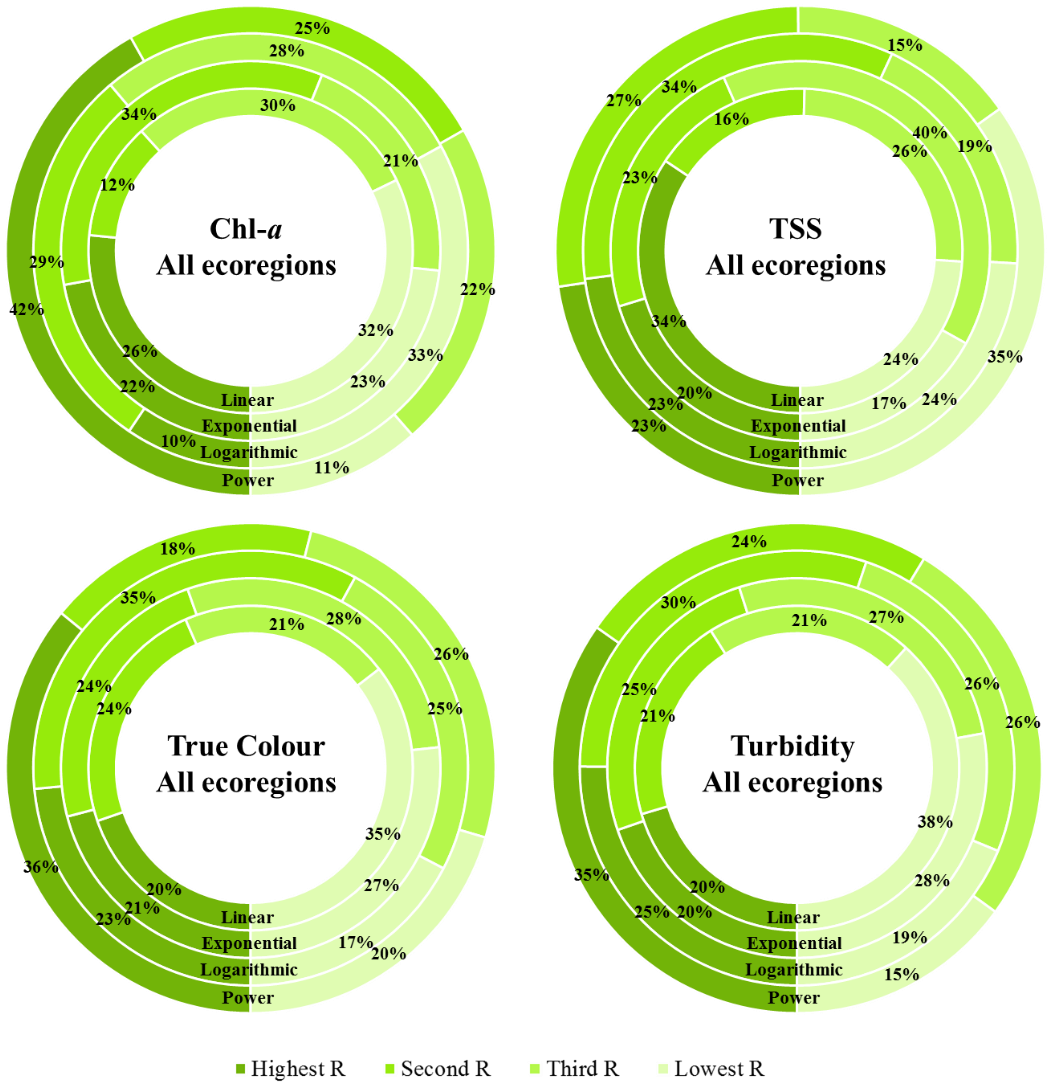

Figure 4.1 Combinations, ratios, or algorithms of Landsat band reflectance showing number of highest to lowest R with chl-*a* concentration and other optical constituents for all ecoregions.

For models with significant ($p < 0.05$) correlations between sampled chl-*a* concentration and combinations, ratios or algorithms of Landsat band reflectance, exponential and power models that predict chl-*a* concentration were least likely to be found with significant correlations between other freshwater optical constituents (true colour or DOC, turbidity and TSS) and combinations, ratios or algorithms of Landsat band reflectance. Out of 497 possible cases, linear regressions were significant for chl-*a* concentration and for no other optical constituents 131 times (26.4%), exponential regressions were significant for chl-*a* concentration and for no other optical constituents 142 times (28.6%), logarithmic regressions were significant for chl-*a* concentration and for no other optical constituents 132 times (26.6%), and power regressions were significant for chl-*a* concentration and for no other optical constituents 152 times (30.6%).

Of 188 models (significant correlations between sampled chl-*a* concentration and combinations, ratios or algorithms of Landsat band reflectances and no significant correlations between other freshwater optical constituents and combinations, ratios or algorithms of Landsat band reflectance), linear regressions had a mean and median R of 0.61 and 0.64 respectively, exponential regressions had a mean and median R of 0.64 and 0.65 respectively, logarithmic regressions had a mean and median R of 0.58 and 0.57 respectively, and power regressions had a mean and median R of 0.65 and 0.64 respectively. Maximum R was found in 59 linear models (31.4%), 53 exponential models (28.2%), 13 logarithmic models (6.9%) and 63 power models (33.5%), and minimum R was found in 42 linear models (22.3%), 37 exponential models (19.7%), 71 logarithmic models (37.8%) and 38 power models (20.2%).

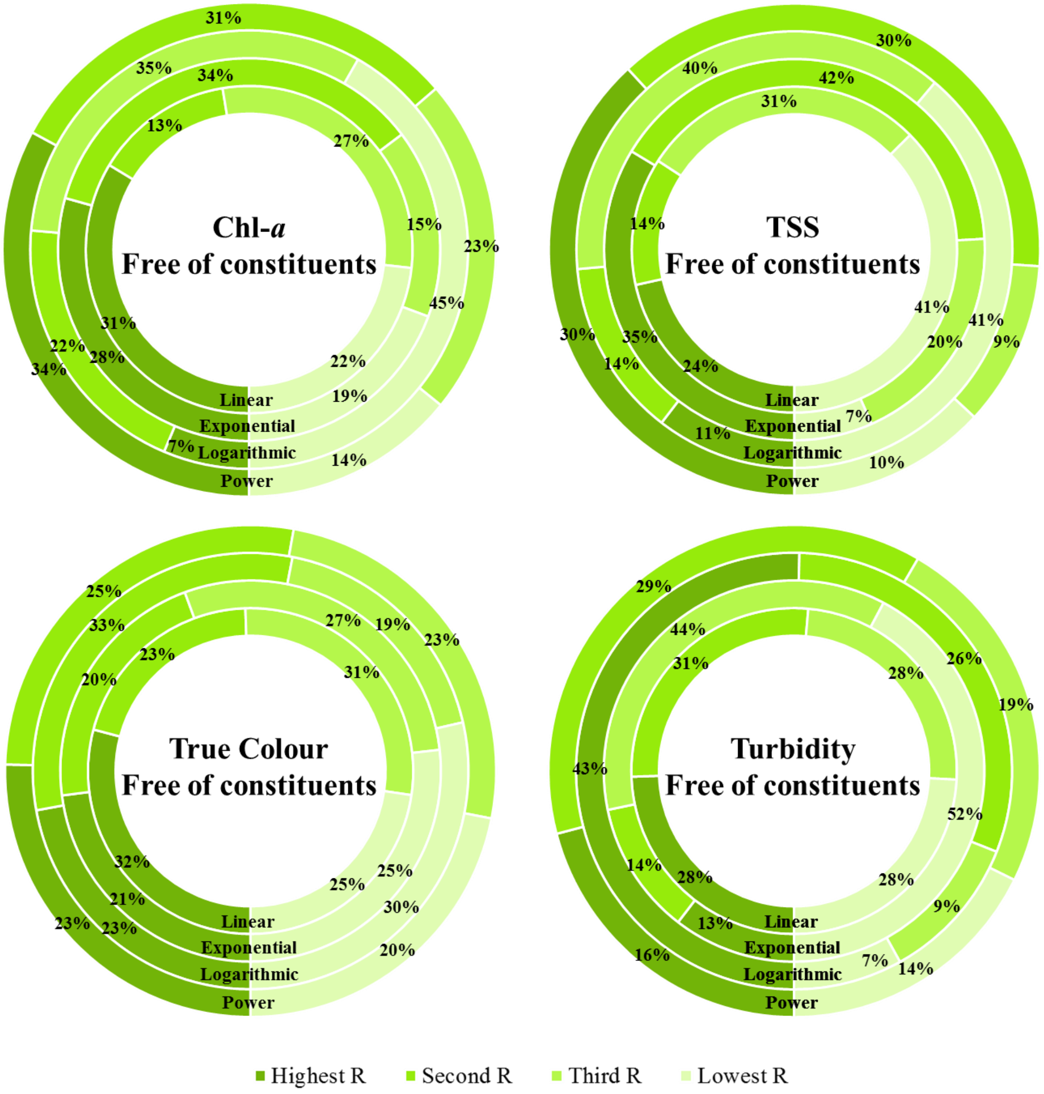

Figure 4.2 Combinations, ratios, or algorithms of Landsat band reflectance showing number of highest to lowest R with significant correlations for chl-a concentration and no significant correlations with other optical constituents for all ecoregions.

4.3 Landsat band reflectance combinations, ratios and algorithms

Of the four tested Landsat bands (Blue, Green, Red and NIR) across all ecoregions and for all regression types, NIR reflectance was found to have the strongest correlations with chl-*a* concentration. However, this was true only for linear and logarithmic models. Red reflectance was found to have the strongest correlations with chl-*a* concentration in exponential and power models (see table 4.2, and see Appendix F for full results of all algorithms).

Table 4.2 Pearson R correlation of chl-*a* to Blue, Green, Red and NIR bands. Shaded rows indicates highest median R for the corresponding regression. * = Significant ($p < 0.05$) and not significant for true colour, TSS and turbidity.

Band	Regression	PTW	BCF	TCF	TPS	TPD	SHF	TMF	Median
Blue	**Linear**	0.04	0.25	0.60*	0.46*	0.21	0.59*	0.44*	**0.44**
	Exponential	0.05	0.04	0.55*	0.46	0.19	0.52*	0.04	**0.19**
	Logarithmic	0.001	0.24	0.54*	0.49*	0.26	0.57*	0.36*	**0.36**
	Power	0.08	0.02	0.51*	0.52	0.26	0.51*	0.09	**0.26**
Green	**Linear**	0.41	0.77*	0.66	0.45	0.57	0.77	0.12	**0.57**
	Exponential	0.47*	0.79*	0.68	0.47	0.57	0.74	0.46*	**0.57**
	Logarithmic	0.44	0.74*	0.57	0.46	0.56	0.75	0.08	**0.56**
	Power	0.51*	0.79*	0.63*	0.52	0.62	0.74	0.47*	**0.62**
Red	**Linear**	0.56*	0.83*	0.69	0.40	0.46	0.80	0.24	**0.56**
	Exponential	0.64*	0.87*	0.71	0.40	0.48	0.76	0.32	**0.64**
	Logarithmic	0.53*	0.76*	0.59	0.43	0.50	0.77	0.17	**0.53**
	Power	0.64*	0.84*	0.66*	0.49	0.58	0.76	0.35	**0.64**
NIR	**Linear**	0.81*	0.80	0.54*	0.51	0.73	0.65*	0.72*	**0.72**
	Exponential	0.86*	0.76	0.50*	0.50	0.64	0.56*	0.44*	**0.56**
	Logarithmic	0.72*	0.71	0.46*	0.54	0.71	0.62*	0.59*	**0.62**
	Power	0.81*	0.76	0.44	0.62	0.70	0.56*	0.47*	**0.62**

Of the four tested Landsat bands (Blue, Green, Red and NIR) across all ecoregions and for all regression types, Green reflectance was found to have the strongest correlations with colour, which was true for all regressions (see table 4.3, and see Appendix F for full results of all algorithms).

Table 4.3 Pearson R correlation of true colour to Blue, Green, Red and NIR bands. Shaded rows indicates highest median R for the corresponding regression. * = Significant ($p < 0.05$) and not significant for chl-*a*.

Band	Regression	PTW	BCF	TCF	TPS	TPD	SHF	TMF	Median
Blue	**Linear**	0.01	0.23	0.02	N/A	0.54	0.17	0.17	**0.17**
	Exponential	0.10	0.28	0.08	N/A	0.47	0.10	0.18	**0.14**
	Logarithmic	0.02	0.27	0.05	N/A	0.53	0.17	0.18	**0.17**
	Power	0.10	0.30	0.03	N/A	0.44	0.10	0.18	**0.14**

Green	**Linear**	0.30	0.10	0.06	N/A	0.77	0.33	0.35	**0.32**
	Exponential	0.29	0.08	0.02	N/A	0.72	0.22	0.38	**0.25**
	Logarithmic	0.36	0.04	0.11	N/A	0.79	0.34	0.39	**0.35**
	Power	0.35	0.03	0.05	N/A	0.77	0.24	0.42	**0.30**
Red	**Linear**	0.19	0.14	0.00	N/A	0.84	0.21	0.34	**0.20**
	Exponential	0.18	0.13	0.09	N/A	0.78	0.05	0.37	**0.15**
	Logarithmic	0.23	0.06	0.01	N/A	0.86	0.20	0.37	**0.21**
	Power	0.21	0.04	0.02	N/A	0.86	0.03	0.40	**0.13**
NIR	**Linear**	0.04	0.49	0.06	N/A	0.56	0.05	0.10	**0.08**
	Exponential	0.06	0.50	0.00	N/A	0.60	0.04	0.22	**0.14**
	Logarithmic	0.07	0.54	0.12	N/A	0.66	0.03	0.10	**0.11**
	Power	0.01	0.55	0.14	N/A	0.72	0.06	0.25	**0.19**

Of the four tested Landsat bands (Blue, Green, Red and NIR), across all ecoregions, and for all regression types, Red reflectance was found to have the strongest correlations with turbidity, which was true for all regressions (see table 4.4, and see Appendix F for full results of all algorithms).

Table 4.4 Pearson R correlation of turbidity to Blue, Green, Red and NIR bands. Shaded rows indicates highest median R for the corresponding regression. * = Significant ($p < 0.05$) and not significant for chl-*a* and true colour.

Band	Regression	PTW	BCF	TCF	TPS	TPD	SHF	TMF	Median
Blue	**Linear**	N/A	0.29*	0.05	0.06	0.34	0.18	0.13	**0.15**
	Exponential	N/A	0.18	0.12	0.00	0.40	0.21	0.20	**0.19**
	Logarithmic	N/A	0.31	0.02	0.06	0.36	0.16	0.18	**0.17**
	Power	N/A	0.21	0.08	0.00	0.43*	0.20	0.24	**0.20**
Green	**Linear**	N/A	0.16	0.66	0.18	0.50	0.51	0.21	**0.35**
	Exponential	N/A	0.12	0.46	0.21	0.58	0.50	0.28	**0.37**
	Logarithmic	N/A	0.16	0.52	0.18	0.56	0.44	0.29	**0.37**
	Power	N/A	0.12	0.39	0.21	0.65	0.45	0.36	**0.37**
Red	**Linear**	N/A	0.44	0.68	0.34*	0.53	0.54	0.27	**0.48**
	Exponential	N/A	0.48	0.49	0.39*	0.60	0.56	0.33	**0.48**
	Logarithmic	N/A	0.44	0.55	0.35	0.60	0.51	0.37	**0.48**
	Power	N/A	0.49	0.42	0.41	0.69	0.54	0.41	**0.45**
NIR	**Linear**	N/A	0.20	0.10	0.49	0.25	0.11	0.28	**0.23**
	Exponential	N/A	0.33	0.23	0.47	0.33	0.19	0.33	**0.33**
	Logarithmic	N/A	0.21	0.13	0.50	0.27	0.10	0.38	**0.24**
	Power	N/A	0.34	0.25	0.48	0.36	0.18	0.43	**0.35**

Of the four tested Landsat bands (Blue, Green, Red and NIR) across all ecoregions and for all regression types, Green reflectance was found to have the strongest correlations with TSS, which was true for all regressions (see table 4.5, and see Appendix F for full results of all algorithms).

Table 4.5 Pearson R correlation of TSS to Blue, Green, Red and NIR bands. Shaded rows indicates highest median R for the corresponding regression. * = Significant ($p < 0.05$) and not significant for chl-*a* and true colour.

Band	Regression	PTW	BCF	TCF	TPS	TPD	SHF	TMF	Median
Blue	**Linear**	N/A	N/A	0.04	0.34	0.46	0.11	0.17	**0.17**
	Exponential	N/A	N/A	0.05	0.42	0.29	0.01	0.14	**0.14**
	Logarithmic	N/A	N/A	0.01	0.35	0.40	0.09	0.18	**0.18**
	Power	N/A	N/A	0.03	0.43	0.25	0.04	0.11	**0.11**
Green	**Linear**	N/A	N/A	0.27	0.69	0.66	0.67	0.27	**0.66**
	Exponential	N/A	N/A	0.19	0.76	0.48	0.53	0.28	**0.48**
	Logarithmic	N/A	N/A	0.26	0.62	0.58	0.58	0.31	**0.58**
	Power	N/A	N/A	0.18	0.72	0.43	0.46	0.30	**0.43**
Red	**Linear**	N/A	N/A	0.31	0.71*	0.67	0.64	0.31	**0.64**
	Exponential	N/A	N/A	0.26	0.80*	0.41	0.50	0.32	**0.41**
	Logarithmic	N/A	N/A	0.30	0.65	0.49	0.56	0.36	**0.49**
	Power	N/A	N/A	0.25	0.77	0.26	0.44	0.34	**0.34**
NIR	**Linear**	N/A	N/A	0.21	0.25	0.05	0.34	0.32	**0.25**
	Exponential	N/A	N/A	0.24	0.03	0.06	0.18	0.28	**0.18**
	Logarithmic	N/A	N/A	0.20	0.18	0.07	0.26	0.32	**0.20**
	Power	N/A	N/A	0.25	0.04	0.10	0.11	0.24	**0.11**

NIR reflectance was significantly correlated with chl-*a* concentration in four of the ecoregions (PTW, TCF, SHF and TMF) for all regression types (mean R = 0.68, 0.59, 0.60, 0.58, median R = 0.68, 0.54, 0.60, 0.52 for linear, exponential, logarithmic and power regressions respectively) where no other constituents (true colour, TSS and turbidity) are significant.

Red reflectance was significantly correlated with chl-*a* concentration in two of the ecoregions (PTW and BCF) for linear, exponential and logarithmic regression (mean R = 0.70, 0.75, 0.64, median R = 0.70, 0.75, 0.64), and 3 of the ecoregions (PTW, BCF, TCF) (mean R = 0.72, median R = 0.67) for power regression where no other constituents (true colour, TSS and turbidity) are significant.

Green reflectance was significantly correlated with chl-*a* concentration in one ecoregion (BCF) for linear and logarithmic regression (R = 0.77, 0.74), 3 of the ecoregions (PTW, BCF and TMF) for exponential regression (mean R = 0.57, median R = 0.47), and 4 of the ecoregions (PTW, BCF, TCF and TMF) for power regression (mean R = 0.61, median R = 0.58) where no other constituents (true colour, TSS and turbidity) are significant.

Blue reflectance was significantly correlated with chl-*a* concentration in 4 of the ecoregions (TCF, TPS, SHF and TMF) for all linear and logarithmic regression (mean R = 0.52, 0.49, median R = 0.52, 0.52), and 2 of the ecoregions (TCF and SHF) for all exponential and power regression (mean R = 0.54, 0.53, median R = 0.54, 0.53) where no other constituents (true colour, TSS and turbidity) are significant.

Correlations between sampled chl-*a* concentration, true colour or DOC, turbidity and TSS were tested for 78 combinations, ratios or algorithms of Landsat band reflectance in each ecoregion. Only certain combinations, ratios or algorithms are reported below based on (1) their performance (as indicated by correlation coefficient, significance and number of ecoregions where models had significant correlations with chl-*a* concentration but not with other freshwater optical constituents), and (2) common use in published studies (e.g., Red-to-Blue ratio, Green-to-Blue ratio). Full tables of results can be found in Appendix F. A heatmap overview of all Pearson R results can be seen in figure 4.2.

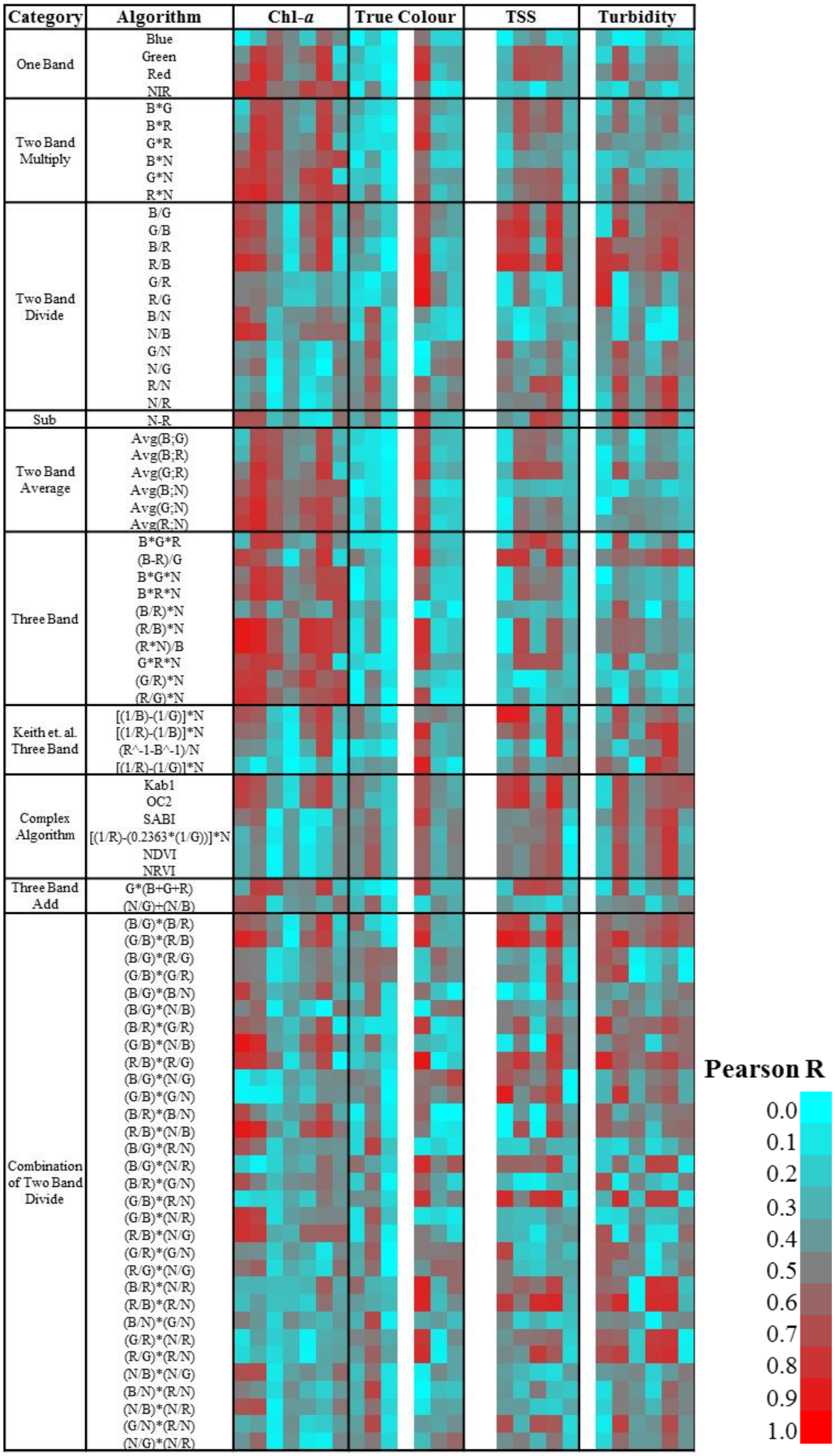

Figure 4.3 Overview of Pearson R correlation testing (linear regression). Cells within each column (left to right): PTW, BCF, TCF, TPS, TPD, SHF, and TMF.

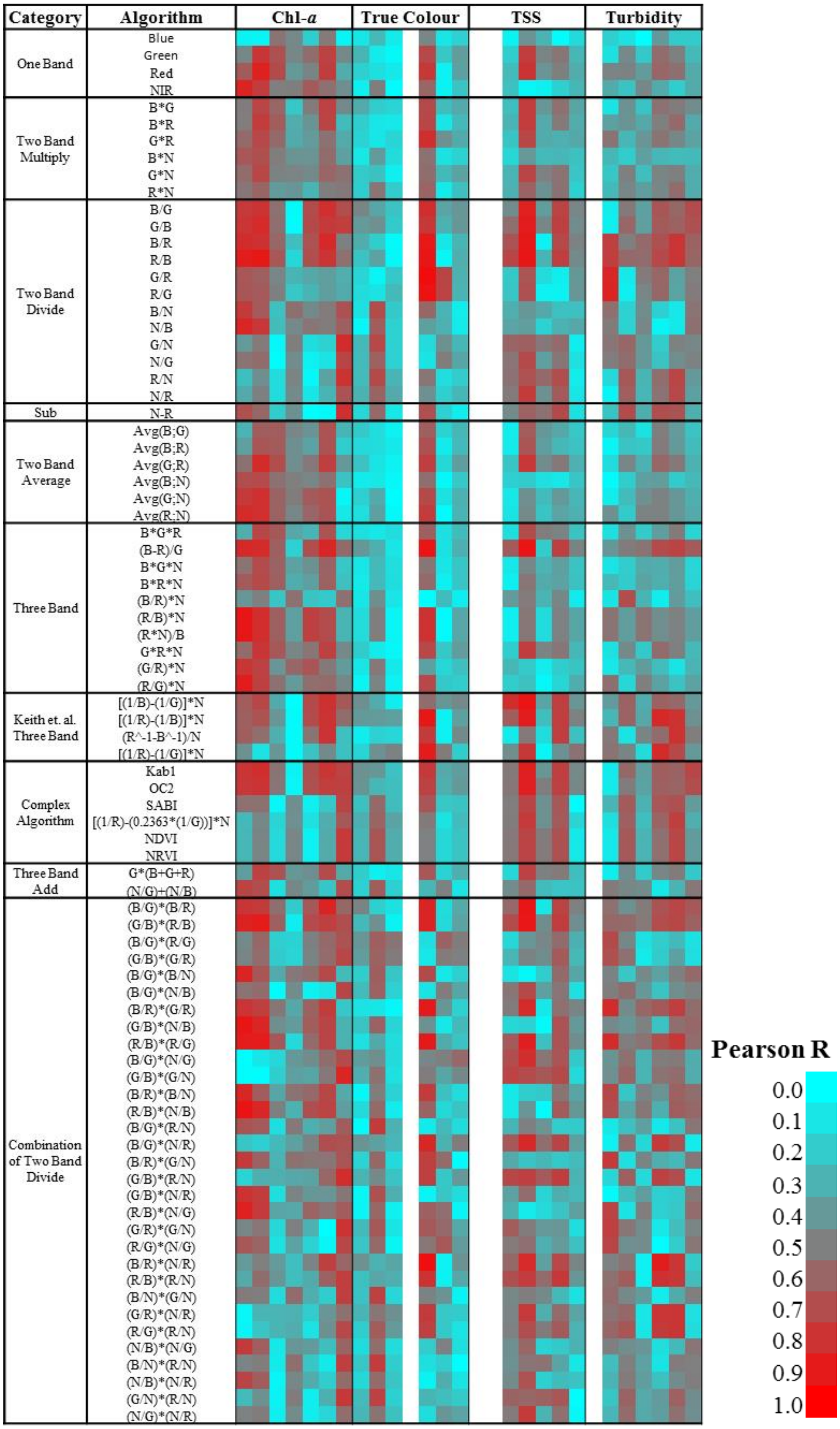

Figure 4.4 Overview of Pearson R correlation testing (exponential regression). Cells within each column (left to right): PTW, BCF, TCF, TPS, TPD, SHF, and TMF.

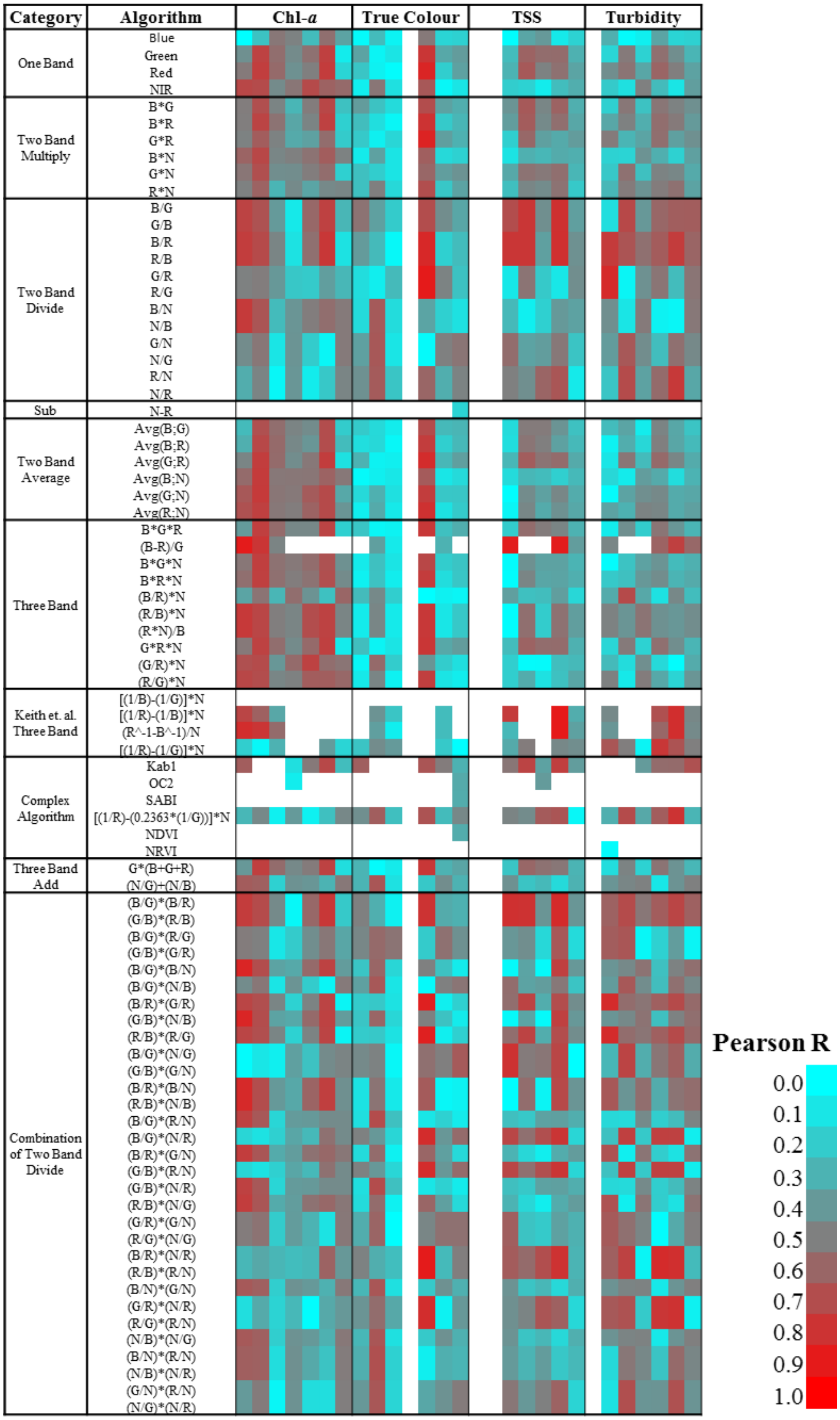

Figure 4.5 Overview of Pearson R correlation testing (logarithmic regression). Cells within each column (left to right): PTW, BCF, TCF, TPS, TPD, SHF, and TMF.

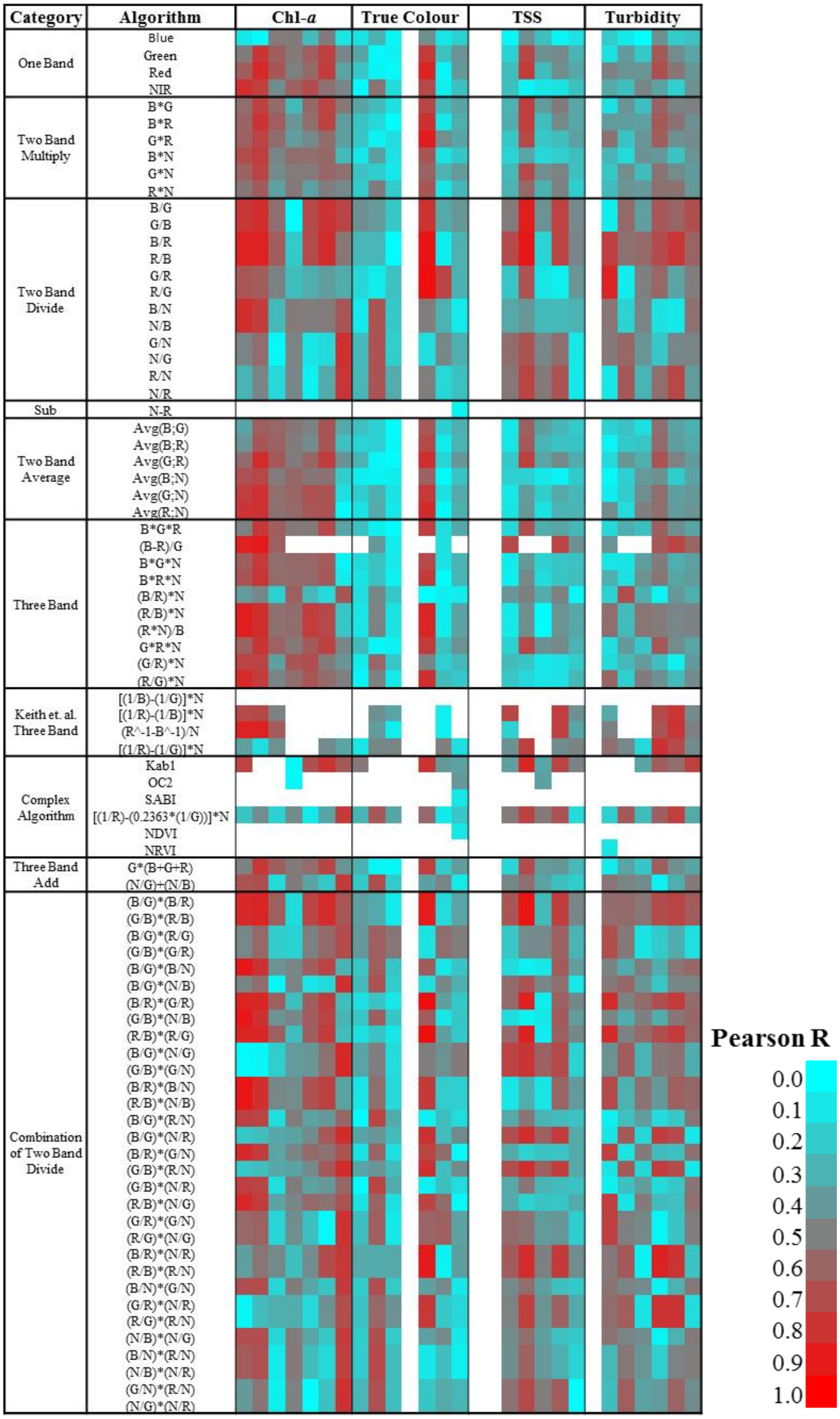

Figure 4.6 Overview of Pearson R correlation testing (power regression). Cells within each column (left to right): PTW, BCF, TCF, TPS, TPD, SHF, and TMF.

4.3.1 Red-to-Blue ratio (R ⁄ B)

Red-to-Blue ratio (R ⁄ B) of Landsat band reflectance had no significant correlations with non-chl-*a* optical constituents only in PTW for all regression types. Only DOC was tested in PTW (no turbidity or TSS samples were available). Across all ecoregions, R for correlations of (R ⁄ B) to chl-*a* concentration ranged from 0.08 ≤ R ≤ 0.83 for linear, 0.15 ≤ R ≤ 0.90 for exponential, 0.11 ≤ R ≤ 0.79 for logarithmic, and 0.21 ≤ R ≤ 0.86 for power regressions.

Significant correlations between true colour and (R ⁄ B) which had no corresponding significant correlations with chl-*a* concentration were not found in any ecoregions. Across all ecoregions, R for correlations of (R ⁄ B) to true colour ranged from 0.02 ≤ R ≤ 0.88 for linear, 0.003 ≤ R ≤ 0.91 for exponential, 0.03 ≤ R ≤ 0.84 for logarithmic, and 0.01 ≤ R ≤ 0.92 for power.

Significant correlations between turbidity and (R ⁄ B) which had no corresponding significant correlations with chl-*a* concentration or true colour were found in TPS and TMF for linear and logarithmic regressions. Across all ecoregions, R for correlations of (R ⁄ B) to turbidity ranged from 0.56 ≤ R ≤ 0.78 for linear regression, 0.57 ≤ R ≤ 0.79 for exponential, 0.56 ≤ R ≤ 0.77 for logarithmic, and 0.56 ≤ R ≤ 0.79 for power.

Significant correlations between TSS and (R ⁄ B), which had no corresponding significant correlations with chl-*a* concentration or true colour, were found only in TPS for all regression types. Across all ecoregions, R for correlations of (R ⁄ B) to TSS ranged from 0.02 ≤ R ≤ 0.88 for linear, 0.003 ≤ R ≤ 0.91 for exponential, 0.03 ≤ R ≤ 0.84 for logarithmic, and 0.01 ≤ R ≤ 0.92 for power (see table 4.6, and see Appendix F for full results of all algorithms).

Table 4.6 Pearson R correlation of all constituents to Red-to-Blue ratio (R ⁄ B). * = Significant ($p < 0.05$) and not significant for other constituents (chl-*a* to true colour, TSS and turbidity), (true colour to chl-*a*), (TSS to chl-*a* and true colour), (turbidity to chl-*a* and true colour).

Constituent	Regression	PTW	BCF	TCF	TPS	TPD	SHF	TMF	Median
Chl-*a*	**Linear**	0.83*	0.78	0.51	0.08	0.58	0.77	0.14	**0.58**
	Exponential	0.89*	0.90	0.66	0.15	0.69	0.79	0.56	**0.69**

	Logarithmic	0.76*	0.71	0.48	0.11	0.56	0.79	0.12	**0.56**
	Power	0.86*	0.86	0.64	0.21	0.70	0.83	0.53	**0.70**
True Colour	**Linear**	0.35	0.35	0.02	N/A	0.88	0.20	0.28	**0.31**
	Exponential	0.24	0.36	0.03	N/A	0.91	0.04	0.31	**0.28**
	Logarithmic	0.39	0.27	0.03	N/A	0.84	0.19	0.26	**0.27**
	Power	0.28	0.28	0.01	N/A	0.92	0.06	0.30	**0.28**
TSS	**Linear**	N/A	N/A	0.83	0.82*	0.50	0.85	0.42	**0.82**
	Exponential	N/A	N/A	0.73	0.91*	0.29	0.75	0.46	**0.73**
	Logarithmic	N/A	N/A	0.79	0.79*	0.38	0.81	0.43	**0.79**
	Power	N/A	N/A	0.70	0.91*	0.17	0.73	0.47	**0.70**
Turbidity	**Linear**	N/A	0.78	0.76	0.56*	0.66	0.78	0.60*	**0.71**
	Exponential	N/A	0.75	0.59	0.57*	0.71	0.79	0.60	**0.66**
	Logarithmic	N/A	0.77	0.67	0.56*	0.64	0.77	0.60*	**0.66**
	Power	N/A	0.75	0.56	0.58*	0.70	0.79	0.61	**0.66**

4.3.2 Green-to-Blue ratio (G ⁄ B)

The Green-to-Blue ratio (G ⁄ B) of Landsat band reflectance is commonly used water quality algorithm used for oligotrophic oceans and has been adapted to Landsat for inland waters on several occasions (Carder *et al.*, 2004). (G ⁄ B) had no significant correlations with non-chl-*a* optical constituents for only the PTW for exponential and power regression (R = 0.77 for exponential and 0.79 for power).

Significant correlations between true colour and (G ⁄ B), which had no corresponding significant correlations with chl-*a* concentration, were not found in any ecoregion. Across all ecoregions, R for correlations of (G ⁄ B) to true colour ranged from $0.20 \leq R \leq 0.69$ for linear regression, $0.20 \leq R \leq 0.78$ for exponential, $0.21 \leq R \leq 0.70$ for logarithmic, and $0.22 \leq R \leq 0.80$ for power.

Significant correlations between turbidity and (G ⁄ B) which had no corresponding significant correlations with chl-*a* concentration or true colour were found in TPS and TMF for linear and logarithmic regressions. Across all ecoregions, R for correlations of (G ⁄ B) to turbidity ranged from 0.13 – 0.78 for linear regression, $0.06 \leq R \leq 0.68$ for exponential, $0.13 \leq R \leq 0.72$ for logarithmic, and 0.06 – 0.69 for power.

Significant correlations between TSS and (G ⁄ B) which had no corresponding significant correlations with chl-*a* concentration or true colour were found in TPS for exponential and power regressions. Across all ecoregions, R for correlations of (G ⁄ B) to TSS ranged from $0.37 \leq R \leq 0.83$ for linear, $0.45 \leq R \leq 0.89$ for exponential, $0.38 \leq R \leq 0.81$ for logarithmic and $0.43 \leq R \leq 0.88$ for power (see table 4.7, and see Appendix F for full results of all algorithms).

Table 4.7 Pearson R correlation of all constituents to Green-to-Blue ratio (G ⁄ B). * = Significant ($p < 0.05$) and not significant for other constituents (chl-*a* to true colour, TSS and turbidity), (true colour to chl-*a*), (TSS to chl-*a* and true colour), (turbidity to chl-*a* and true colour).

Constituent	Regression	PTW	BCF	TCF	TPS	TPD	SHF	TMF	Median
Chl-a	**Linear**	0.77	0.71	0.40	0.10	0.61	0.74	0.31	**0.61**
	Exponential	0.79*	0.83	0.56	0.01	0.71	0.77	0.75	**0.75**
	Logarithmic	0.74	0.68	0.40	0.09	0.60	0.75	0.29	**0.60**
	Power	0.78*	0.82	0.56	0.00	0.71	0.80	0.73	**0.73**
True Colour	**Linear**	0.51	0.41	0.20	N/A	0.69	0.42	0.35	**0.41**
	Exponential	0.39	0.43	0.20	N/A	0.78	0.30	0.41	**0.40**
	Logarithmic	0.55	0.38	0.21	N/A	0.70	0.45	0.35	**0.41**
	Power	0.44	0.40	0.22	N/A	0.80	0.33	0.41	**0.40**
TSS	**Linear**	N/A	N/A	0.76	0.81*	0.46	0.83	0.37	**0.76**
	Exponential	N/A	N/A	0.57	0.89*	0.47	0.75	0.45	**0.57**
	Logarithmic	N/A	N/A	0.70	0.79*	0.44	0.81	0.38	**0.70**
	Power	N/A	N/A	0.51	0.88*	0.43	0.74	0.46	**0.51**
Turbidity	**Linear**	N/A	0.13	0.78	0.40*	0.58	0.65	0.63*	**0.61**
	Exponential	N/A	0.06	0.60	0.37*	0.64	0.62	0.68	**0.61**
	Logarithmic	N/A	0.13	0.72	0.41*	0.60	0.64	0.64*	**0.62**
	Power	N/A	0.06	0.58	0.37*	0.66	0.61	0.69	**0.60**

4.3.3 Blue and Near-Infrared combination (B × NIR)

The Blue and Near-Infrared combination (B × NIR) of Landsat band reflectance had no significant correlations with non-chl-*a* optical constituents in PTW, BCF, TCF, TDP, SHF and TMF for linear regression, PTW, BCF, TCF and SHF for exponential and power regression, and PTW, BCF, TCF, SHF and TMF, for logarithmic regression. Across all ecoregions, R for correlations of (B × NIR) to chl-*a* concentration ranged from $0.47 \leq R \leq 0.79$ for linear, $0.32 \leq R \leq 0.70$ for exponential, $0.52 \leq R \leq 0.72$ for logarithmic and $0.31 \leq R \leq 0.73$ for power.

Significant correlations between true colour and (B × NIR) which had no corresponding significant correlations with chl-*a* concentration were not found in any ecoregion. Across all ecoregions, R for correlations of (B × NIR) to true colour ranged from $0.003 \leq R \leq 0.52$ for linear, $0.02 \leq R \leq 0.50$ for exponential, $0.04 \leq R \leq 0.67$ for logarithmic and $0.005 \leq R \leq 0.67$ for power.

Significant correlations between turbidity and (B × NIR) which had no corresponding significant correlations with chl-*a* concentration or true colour were not found in any ecoregion. Across all ecoregions, R for correlations of (B × NIR) to turbidity ranged from $0.06 \leq R \leq 0.37$ for linear, $0.19 \leq R \leq 0.37$ for exponential, $0.05 \leq R \leq 0.41$ for logarithmic, and $0.18 \leq R \leq 0.43$ for power).

Significant correlations between TSS and (B × NIR) which had no corresponding significant correlations with chl-*a* concentration or true colour were not found in any ecoregion. Across all ecoregions, R for correlations of (B × NIR) to TSS ranged from $0.16 \leq R \leq 0.34$ for linear regression, $0.11 \leq R \leq 0.24$ for exponential, $0.14 \leq R \leq 0.28$ for logarithmic, and $0.04 \leq R \leq 0.34$ for power (see table 4.8, and see Appendix F for full results of all algorithms).

Table 4.8 Pearson R correlation of all constituents to Blue and Near-Infrared combination (B × NIR). * = Significant ($p < 0.05$) and not significant for other constituents (chl-*a* to true colour, TSS and turbidity), (true colour to chl-*a*), (TSS to chl-*a* and true colour), (turbidity to chl-*a* and true colour).

Constituent	Regression	PTW	BCF	TCF	TPS	TPD	SHF	TMF	Median
Chl-a	**Linear**	0.61*	0.79*	0.64*	0.47	0.53*	0.65*	0.73*	**0.64**
	Exponential	0.67*	0.70*	0.56*	0.42	0.42*	0.55*	0.32	**0.55**
	Logarithmic	0.57*	0.72*	0.52*	0.54	0.57*	0.61*	0.56	**0.57**
	Power	0.67*	0.73*	0.50*	0.60	0.56	0.55*	0.31	**0.56**
True Colour	**Linear**	0.03	0.33	0.00	N/A	0.52	0.11	0.13	**0.12**
	Exponential	0.07	0.33	0.09	N/A	0.50	0.02	0.19	**0.14**
	Logarithmic	0.04	0.34	0.10	N/A	0.67	0.09	0.15	**0.13**
	Power	0.04	0.33	0.09	N/A	0.67	0.00	0.23	**0.16**
TSS	**Linear**	N/A	N/A	0.16	0.34	0.26	0.31	0.23	**0.26**
	Exponential	N/A	N/A	0.17	0.21	0.11	0.15	0.24	**0.17**
	Logarithmic	N/A	N/A	0.14	0.27	0.24	0.20	0.28	**0.24**
	Power	N/A	N/A	0.19	0.16	0.04	0.06	0.21	**0.16**
Turbidity	**Linear**	N/A	0.06	0.08	0.37	0.27	0.15	0.15	**0.15**

	Exponential	N/A	0.19	0.21	0.37	0.33	0.21	0.22	**0.21**
	Logarithmic	N/A	0.05	0.09	0.41	0.33	0.13	0.32	**0.22**
	Power	N/A	0.18	0.20	0.41	0.43	0.19	0.37	**0.28**

4.3.4 Red-to-Near Infrared ratio (R⁄NIR)

The Red-to-Near-Infrared ratio (R⁄NIR) is a commonly used algorithm for determining chl-*a* in highly turbid waters (Dall'Olmo *et al*, 2003, Schalles, 2006). (R⁄NIR) of Landsat band reflectances had no significant correlations with non-chl-*a* optical constituents only in TMF for all regression types. Across all ecoregions, R for correlations of (R⁄NIR) to chl-*a* concentration ranged from $0.01 \leq R \leq 0.43$ for linear regression, $0.09 \leq R \leq 0.80$ for exponential, $0.03 \leq R \leq 0.48$ for logarithmic, and $0.09 \leq R \leq 0.78$ for power.

Significant correlations between true colour and (R⁄NIR) which had no corresponding significant correlations with chl-*a* concentration were found in TPD for linear and logarithmic regressions. Across all ecoregions, R for correlations of (R⁄NIR) to true colour ranged from $0.21 \leq R \leq 0.68$ for linear regression, $0.13 \leq R \leq 0.71$ for exponential, $0.23 \leq R \leq 0.65$ for logarithmic, and $0.15 \leq R \leq 0.67$ for power.

Significant correlations between turbidity and (R⁄NIR) which had no corresponding significant correlations with chl-*a* concentration or true colour were found in TCF and SHF for all regression types. Across all ecoregions, R for correlations of (R⁄NIR) to turbidity ranged from $0.29 \leq R \leq 0.79$ for linear, $0.15 \leq R \leq 0.72$ for exponential, $0.23 \leq R \leq 0.78$ for logarithmic and $0.09 \leq R \leq 0.62$ for power.

Significant correlations between TSS and (R⁄NIR) which had no corresponding significant correlations with chl-*a* concentration or true colour were found in TCF and SHF for all regression types. Across all ecoregions, R for correlations of (R⁄NIR) to TSS ranged from $0.09 \leq R \leq 0.71$ for linear, $0.07 \leq R \leq 0.70$ for exponential, $0.08 \leq R \leq 0.66$ for logarithmic, and $0.08 \leq R \leq 0.73$ for power regression (see table 4.9, and see Appendix F for full results of all algorithms).

Table 4.9 Pearson R correlation of all constituents to Red-to-Near Infrared ratio (R⁄NIR). * = Significant ($p < 0.05$) and not significant for other constituents (chl-*a* to true colour, TSS and turbidity), (true colour to chl-*a*), (TSS to chl-*a* and true colour), (turbidity to chl-*a* and true colour).

Constituent	Regression	PTW	BCF	TCF	TPS	TPD	SHF	TMF	Median
Chl-a	**Linear**	0.30	0.43	0.01	0.42	0.10	0.25	0.43*	**0.30**
	Exponential	0.25	0.44	0.14	0.48	0.03	0.36	0.80*	**0.36**
	Logarithmic	0.32	0.48	0.03	0.41	0.08	0.22	0.48*	**0.32**
	Power	0.29	0.48	0.15	0.47	0.05	0.33	0.78*	**0.33**
True Colour	**Linear**	0.41	0.68	0.21	N/A	0.63*	0.29	0.44	**0.43**
	Exponential	0.26	0.71	0.29	N/A	0.54	0.13	0.20	**0.28**
	Logarithmic	0.43	0.65	0.23	N/A	0.60*	0.32	0.49	**0.46**
	Power	0.28	0.67	0.32*	N/A	0.50	0.15	0.24	**0.30**
TSS	**Linear**	N/A	N/A	0.55	0.37*	0.71	0.68*	0.09	**0.55**
	Exponential	N/A	N/A	0.55*	0.68	0.58*	0.70	0.07	**0.58**
	Logarithmic	N/A	N/A	0.50*	0.44	0.60	0.66*	0.08	**0.50**
	Power	N/A	N/A	0.53	0.73	0.52*	0.68*	0.08	**0.53**
Turbidity	**Linear**	N/A	0.29	0.75*	0.36	0.60	0.79*	0.36	**0.48**
	Exponential	N/A	0.15	0.65*	0.29	0.57*	0.72	0.40	**0.48**
	Logarithmic	N/A	0.23	0.71*	0.37	0.58	0.78*	0.35	**0.48**
	Power	N/A	0.09	0.65	0.29	0.56*	0.72*	0.38	**0.47**

4.3.5 Three-band algorithm variant 1 [(G ⁄ R) × NIR]

The three-band algorithm variant 1 [(G ⁄ R) × NIR] as described by Gitelson *et al*, (2003; 2011) has seen promising results (Keith *et al*., 2018). [(G ⁄ R) × NIR] of Landsat band reflectance had no significant correlations with non-chl-*a* optical constituents in PTW, TCF, TPD, SHF, TMF for all regression types. Across all ecoregions, R for correlations of [(G ⁄ R) × NIR] to chl-*a* concentration ranged from $0.46 \leq R \leq 0.78$ for linear regression, $0.39 \leq R \leq 0.79$ for exponential, $0.42 \leq R \leq 0.73$ for logarithmic, and $0.39 \leq R \leq 0.74$ for power.

Significant correlations between true colour and [(G ⁄ R) × NIR] which had no corresponding significant correlations with chl-*a* concentration were not found in any ecoregion. Across all ecoregions, R for correlations of [(G ⁄ R) × NIR] to true colour ranged from $0.02 \leq R \leq 0.52$ for linear, $0.09 \leq R \leq 0.53$ for exponential, $0.04 \leq R \leq 0.59$ for logarithmic, and $0.07 \leq R \leq 0.59$ for power.

Significant correlations between turbidity and [(G ⁄ R) × NIR] which had no corresponding significant correlations with chl-*a* concentration or true colour were not found in any ecoregion. Across all ecoregions, R for correlations of [(G ⁄ R) × NIR] to turbidity ranged from $0.06 \leq R \leq 0.43$ for linear, $0.09 \leq R \leq 0.38$ for exponential, $0.01 \leq R \leq 0.44$ for logarithmic, and $0.05 \leq R \leq 0.39$ for power.

Significant correlations between TSS and [(G ⁄ R) × NIR] which had no corresponding significant correlations with chl-*a* concentration or true colour were not found in any ecoregion. Across all ecoregions, R for correlations of [(G ⁄ R) × NIR] to TSS ranged from $0.04 \leq R \leq 0.35$ for linear, $0.07 \leq R \leq 0.28$ for exponential, $0.02 \leq R \leq 0.28$ for logarithmic, and $0.09 \leq R \leq 0.26$ for power (see table 4.10, and see Appendix F for full results of all algorithms).

Table 4.10 Pearson R correlation of all constituents to Three-band algorithm variant 1 [(G ⁄ R) × NIR]. * = Significant ($p < 0.05$) and not significant for other constituents (chl-*a* to true colour, TSS and turbidity), (true colour to chl-*a*), (TSS to chl-*a* and true colour), (turbidity to chl-*a* and true colour).

Constituent	Regression	PTW	BCF	TCF	TPS	TPD	SHF	TMF	Median
Chl-a	**Linear**	0.76*	0.78	0.46*	0.58	0.77*	0.61*	0.66*	**0.66**
	Exponential	0.79*	0.74	0.42*	0.59	0.66*	0.52*	0.39*	**0.59**
	Logarithmic	0.69*	0.71	0.41*	0.58	0.74*	0.57*	0.54*	**0.58**
	Power	0.74*	0.73	0.37*	0.67	0.69*	0.51*	0.41*	**0.67**
True Colour	**Linear**	0.02	0.52	0.12	N/A	0.31	0.20	0.12	**0.16**
	Exponential	0.10	0.53	0.09	N/A	0.37	0.16	0.25	**0.20**
	Logarithmic	0.04	0.59	0.20	N/A	0.42	0.20	0.13	**0.20**
	Power	0.07	0.59	0.22	N/A	0.48	0.18	0.27	**0.25**
TSS	**Linear**	N/A	N/A	0.23	0.04	0.05	0.35	0.27	**0.23**
	Exponential	N/A	N/A	0.28	0.20	0.07	0.19	0.23	**0.20**
	Logarithmic	N/A	N/A	0.19	0.02	0.02	0.26	0.28	**0.19**
	Power	N/A	N/A	0.26	0.22	0.09	0.11	0.19	**0.19**
Turbidity	**Linear**	N/A	0.21	0.13	0.43	0.17	0.06	0.23	**0.19**
	Exponential	N/A	0.09	0.27	0.38	0.26	0.11	0.29	**0.27**
	Logarithmic	N/A	0.27	0.14	0.44	0.15	0.01	0.33	**0.21**
	Power	N/A	0.14	0.27	0.39	0.25	0.05	0.39	**0.26**

4.3.6 Modified three-band algorithm $[((1/R) - (1/B)) \times NIR]$

Directly adapted from Gilterson by Kieth *et al.* (2018), this algorithm subtracts the blue reflectance peak in Landsat TM Band 1 (OLI Band 2) from the red absorption peak and multiplies the difference by the NIR reflectance peak. In many cases, the algorithm returned negative values as there were higher measured blue reflectances than those of Red, which limits the scope of regression tests available to only the linear and exponential. Modified three-band algorithm $[((1/R) - (1/B)) \times NIR]$ of Landsat band reflectances had no significant correlations with non-chl-*a* optical constituents only in PTW for exponential. Across all ecoregions, R for correlations of $[((1/R) - (1/B)) \times NIR]$ to chl-*a* concentration ranged from $0.05 \le R \le 0.73$ for linear and $0.08 \le R \le 0.80$ for exponential (logarithmic and power regression not possible due to negative x-axis values).

Significant correlations between true colour and $[((1/R) - (1/B)) \times NIR]$ which had no corresponding significant correlations with chl-*a* concentration were not found in any ecoregion. Across all ecoregions, R for correlations of $[((1/R) - (1/B)) \times NIR]$ to true colour ranged from $0.24 \le R \le 0.83$ for linear regression and $0.05 \le R \le 0.90$ for exponential.

Significant correlations between turbidity and $[((1/R) - (1/B)) \times NIR]$ which had no corresponding significant correlations with chl-*a* concentration or true colour was found in TPS for the exponential regression. Across all ecoregions, R for correlations of $[((1/R) - (1/B)) \times NIR]$ to turbidity ranged from = $0.29 \le R \le 0.80$ for linear and $0.28 \le R \le 0.83$ for exponential.

Significant correlations between TSS and $[((1/R) - (1/B)) \times NIR]$ which had no corresponding significant correlations with chl-*a* concentration or true colour were not found in any ecoregion. Across all ecoregions, R for correlations of $[((1/R) - (1/B)) \times NIR]$ to TSS ranged from $0.35 \le R \le 0.81$ for linear, and $0.26 \le R \le 0.89$ for exponential (see table 4.11, and see Appendix F for full results of all algorithms).

Table 4.11 Pearson R correlation of all constituents to modified three-band algorithm $[((1/R) - (1/B)) \times NIR]$. * = Significant ($p < 0.05$) and not significant for other constituents (chl-*a* to true colour, TSS and turbidity), (true colour to chl-*a*), (TSS to chl-*a* and true colour), (turbidity to chl-*a* and true colour).

Constituent	**Regression**	**PTW**	**BCF**	**TCF**	**TPS**	**TPD**	**SHF**	**TMF**	**Median**
Chl-a	**Linear**	0.57	0.56	0.30	0.05	0.56	0.73	0.25	**0.56**
	Exponential	0.62*	0.67	0.41	0.02	0.70	0.80	0.57	**0.62**
	Logarithmic	0.73	0.62	0.35	N/A	N/A	N/A	N/A	**0.62**
	Power	0.70	0.72	0.49	N/A	N/A	N/A	N/A	**0.70**
True Colour	**Linear**	0.54	0.39	0.24	N/A	0.83	0.29	0.36	**0.37**
	Exponential	0.40	0.40	0.37	N/A	0.90	0.05	0.37	**0.39**
	Logarithmic	N/A	0.42	0.23	N/A	N/A	0.27	N/A	**0.27**
	Power	N/A	0.44	0.35	N/A	N/A	0.06	N/A	**0.35**
TSS	**Linear**	N/A	N/A	0.58	0.72*	0.35	0.81	0.37	**0.58**
	Exponential	N/A	N/A	0.63	0.89*	0.26	0.75	0.49	**0.63**
	Logarithmic	N/A	N/A	0.77	N/A	N/A	0.91	0.32	**0.77**
	Power	N/A	N/A	0.72	N/A	N/A	0.75	0.43	**0.72**
Turbidity	**Linear**	N/A	0.40	0.66	0.29	0.75	0.80	0.46	**0.56**
	Exponential	N/A	0.28	0.61	0.34*	0.84	0.80	0.43	**0.52**
	Logarithmic	N/A	0.46	N/A	N/A	0.69	0.82	0.47	**0.58**
	Power	N/A	0.34	N/A	N/A	0.71	0.79	0.45	**0.58**

4.3.7 Three-band algorithm variant 2 (G × R × NIR)

A variant of the three-band algorithm where Green and Red reflectances are multiplied instead of using a ratio was found to be significantly correlated with chl-*a* concentration in 6 of the 7 ecoregions using linear and logarithmic regressions, and in all ecoregions using exponential and power regressions. (G × R × NIR) of Landsat band reflectances had no significant correlations with non-chl-*a* optical constituents only in PTW and BCF for linear and logarithmic regression, PTW, BCF and TMF for exponential regression and PTW, BCF, TCF and TMF for power regression. Across all ecoregions, R for correlations of (G × R × NIR) to chl-*a* concentration ranged from $0.12 \leq R \leq 0.77$ for linear regression, $0.46 \leq R \leq 0.79$ for exponential, $0.08 \leq R \leq 0.75$ for logarithmic, and $0.47 \leq R \leq 0.79$ for power).

Significant correlations between true colour and (G × R × NIR) which had no corresponding significant correlations with chl-*a* concentration were not found in any ecoregion. Across all ecoregions, R for correlations of (G × R × NIR) to true colour ranged from 0.06 ≤ R ≤ 0.77 for linear regression, 0.02 ≤ R ≤ 0.72 for exponential, 0.04 ≤ R ≤ 0.79 for logarithmic, and 0.03 ≤ R ≤ 0.77 for power.

Significant correlations between turbidity and (G × R × NIR) which had no corresponding significant correlations with chl-*a* concentration or true colour were found in TCF, TPD and SHF for linear, logarithmic and power regressions, and TPD and SFH for power regressions. Across all ecoregions, R for correlations of (G × R × NIR) to turbidity ranged from 0.16 ≤ R ≤ 0.66 for linear regression, 0.12 ≤ R ≤ 0.58 for exponential, 0.16 ≤ R ≤ 0.56 for logarithmic, and 0.12 ≤ R ≤ 0.65 for power.

Significant correlations between TSS and (G × R × NIR) which had no corresponding significant correlations with chl-*a* concentration or true colour were not found in any ecoregion. Across all ecoregions, R for correlations of (G × R × NIR) to TSS ranged from 0.27 ≤ R ≤ 0.69 for linear regression, 0.19 ≤ R ≤ 0.76 for exponential, 0.26 ≤ R ≤ 0.62 for logarithmic and 0.18 ≤ R ≤ 0.72 for power (see table 4.12, and see Appendix F for full results of all algorithms).

Table 4.12 Pearson R correlation of all constituents to three-band algorithm variant 2 (G × R × NIR). * = Significant ($p < 0.05$) and not significant for other constituents (chl-*a* to true colour, TSS and turbidity), (true colour to chl-*a*), (TSS to chl-*a* and true colour), (turbidity to chl-*a* and true colour).

Constituent	Regression	PTW	BCF	TCF	TPS	TPD	SHF	TMF	Median
Chl-a	**Linear**	0.70*	0.77*	0.73	0.45	0.63	0.77	0.12	**0.70**
	Exponential	0.69*	0.79*	0.63	0.47	0.51	0.74	0.46*	**0.63**
	Logarithmic	0.62*	0.74*	0.57	0.46	0.61	0.75	0.08	**0.61**
	Power	0.72*	0.79*	0.61*	0.52	0.66	0.74	0.47*	**0.66**
True Colour	**Linear**	0.08	0.10	0.06	N/A	0.77	0.33	0.35	**0.21**
	Exponential	0.11	0.08	0.02	N/A	0.72	0.22	0.38	**0.17**
	Logarithmic	0.15	0.04	0.11	N/A	0.79	0.34	0.39	**0.25**
	Power	0.18	0.03	0.05	N/A	0.77	0.24	0.42	**0.21**
TSS	**Linear**	N/A	N/A	0.27	0.69	0.66	0.67	0.27	**0.66**
	Exponential	N/A	N/A	0.19	0.76	0.48	0.53	0.28	**0.48**
	Logarithmic	N/A	N/A	0.26	0.62	0.58	0.58	0.31	**0.58**
	Power	N/A	N/A	0.18	0.72	0.43	0.46	0.30	**0.43**
Turbidity	**Linear**	N/A	0.16	0.66	0.18	0.50	0.51	0.21	**0.35**
	Exponential	N/A	0.12	0.46	0.21	0.58	0.50	0.28	**0.37**
	Logarithmic	N/A	0.16	0.52	0.18	0.56	0.44	0.29	**0.37**

	Power	N/A	0.12	0.39	0.21	0.65	0.45	0.36	**0.37**

4.3.8 Green and Red combination (G × R)

The Green and Red combination (G × R) of Landsat band reflectances had no significant correlations with non-chl-*a* optical constituents in BCF for linear regression, PTW and BCF for exponential and logarithmic regression and PTW, BCF, TCF, and TMF for power regression. Across all ecoregions, R for correlations of (G × R) to chl-*a* concentration ranged from $0.25 \leq R \leq 0.81$ for linear regression, $0.35 \leq R \leq 0.81$ for exponential, $0.12 \leq R \leq 0.77$ for logarithmic, and $0.42 \leq R \leq 0.83$ for power.

Significant correlations between true colour and (G × R) which had no corresponding significant correlations with chl-*a* concentration were found in the not found in any ecoregion. Across all ecoregions, R for correlations of (G × R) to true colour ranged from $0.01 \leq R \leq 0.78$ for linear regression, $0.11 \leq R \leq 0.69$ for exponential, $0.05 \leq R \leq 0.83$ for logarithmic and $0.01 \leq R \leq 0.83$ for power.

Significant correlations between turbidity and (G × R) which had no corresponding significant correlations with chl-*a* concentration or true colour were not found in any regions. Across all ecoregions, R for correlations of (G × R) to turbidity ranged from $0.16 \leq R \leq 0.73$ for linear regression, $0.23 \leq R \leq 0.56$ for exponential, $0.20 \leq R \leq 0.59$ for logarithmic, and $0.25 \leq R \leq 0.68$ for power.

Significant correlations between true colour and (G × R) which had no corresponding significant correlations with chl-*a* concentration or true colour were found in TPS for all regression types. Across all ecoregions, R for correlations of (G × R) to TSS ranged from $0.24 \leq R \leq 0.77$ for linear, $0.24 \leq R \leq 0.78$ for exponential, $0.29 \leq R \leq 0.64$ for logarithmic, and $0.22 \leq R \leq 0.75$ for power (see table 4.13, and see Appendix F for full results of all algorithms).

Table 4.13 Pearson R correlation of all constituents to Green and Red combination (G × R). * = Significant ($p < 0.05$) and not significant for other constituents (chl-*a* to true colour, TSS and turbidity), (true colour to chl-*a*), (TSS to chl-*a* and true colour), (turbidity to chl-*a* and true colour).

Constituent	Regression	PTW	BCF	TCF	TPS	TPD	SHF	TMF	Median

Chl-a	**Linear**	0.49*	0.49	0.38*	0.25	0.23	0.38	0.28	**0.38**
	Exponential	0.66*	0.63	0.47*	0.29	0.34	0.38	0.32	**0.38**
	Logarithmic	0.50*	0.51	0.40*	0.22	0.21	0.38	0.28	**0.38**
	Power	0.66*	0.64	0.49*	0.25	0.31	0.38	0.32	**0.38**
True Colour	**Linear**	0.15	0.04	0.25	N/A	0.88*	0.48	0.24	**0.25**
	Exponential	0.17	0.04	0.21	N/A	0.95*	0.73	0.30	**0.26**
	Logarithmic	0.13	0.07	0.27	N/A	0.90*	0.49	0.24	**0.26**
	Power	0.15	0.07	0.25	N/A	0.94*	0.73	0.30	**0.27**
TSS	**Linear**	N/A	N/A	0.10	0.54	0.17	0.10*	0.44	**0.17**
	Exponential	N/A	N/A	0.22	0.66	0.14	0.07*	0.41	**0.22**
	Logarithmic	N/A	N/A	0.09	0.55	0.21	0.10*	0.45	**0.21**
	Power	N/A	N/A	0.22	0.67	0.10	0.06*	0.41	**0.22**
Turbidity	**Linear**	N/A	0.82	0.04	0.45*	0.54	0.27	0.53*	**0.49**
	Exponential	N/A	0.85	0.08	0.52*	0.60	0.36	0.50*	**0.51**
	Logarithmic	N/A	0.84	0.04	0.43*	0.54	0.26	0.54*	**0.49**
	Power	N/A	0.86	0.07	0.50*	0.59	0.36	0.51*	**0.50**

4.3.9 Three-band algorithm variant 3 [(R ⁄ B) × NIR]

The three-band algorithm variant 3 [(R ⁄ B) × NIR] of Landsat band reflectances had no significant correlations with non-chl-*a* optical constituents in all regions for logarithmic regression, PTW, BCF, TCF, TPD, SHF, and TMF for linear regression, PTW, BCF, TCF, TPD, and SHF for exponential regression and PTW, BCF, TCF, TPS, TPD, and SHF for power regression. Across all ecoregions, R for correlations of [(R ⁄ B) × NIR] to chl-*a* concentration ranged from $0.39 \leq R \leq 0.90$ for linear regression, $0.29 \leq R \leq 0.91$ for exponential, $0.48 \leq R \leq 0.78$ for logarithmic, and $0.22 \leq R \leq 0.87$ for power.

Significant correlations between true colour and [(R ⁄ B) × NIR] which had no corresponding significant correlations with chl-*a* concentration were not found in any ecoregion. Across all ecoregions, R for correlations of [(R ⁄ B) × NIR] to true colour ranged from $0.04 \leq R \leq 0.82$ for linear regression, $0.02 \leq R \leq 0.80$ for exponential, $0.08 \leq R \leq 0.72$ for logarithmic and $0.07 \leq R \leq 0.85$ for power.

Significant correlations between turbidity and [(R ⁄ B) × NIR] which had no corresponding significant correlations with chl-*a* concentration or true colour were found in TPS for exponential and power regressions. Across all ecoregions, R for correlations of [(R ⁄ B) × NIR] to turbidity ranged from 0.33 ≤ R ≤ 0.59 for linear, 0.38 ≤ R ≤ 0.54 for exponential, 0.41 ≤ R ≤ 0.55 and 0.27 ≤ R ≤ 0.57 for power.

Significant correlations between true colour and [(R ⁄ B) × NIR] which had no corresponding significant correlations with chl-*a* concentration or true colour were found in TPS for linear and exponential regressions. Across all ecoregions, R for correlations of [(R ⁄ B) × NIR] to TSS ranged from 0.04 ≤ R ≤ 0.71 for linear regression, 0.06 ≤ R ≤ 0.53 for exponential, 0.01 ≤ R ≤ 0.57 for logarithmic and 0.01 ≤ R ≤ 0.44 for power (see table 4.14, and see Appendix F for full results of all algorithms).

Table 4.14 Pearson R correlation of all constituents to **t**hree-band algorithm variant 3 [(R ⁄ B) × NIR]. * = Significant ($p < 0.05$) and not significant for other constituents (chl-*a* to true colour, TSS and turbidity), (true colour to chl-*a*), (TSS to chl-*a* and true colour), (turbidity to chl-*a* and true colour).

Constituent	Regression	PTW	BCF	TCF	TPS	TPD	SHF	TMF	Median
Chl-a	**Linear**	0.90*	0.86	0.64	0.39	0.81	0.78	0.67*	**0.78**
	Exponential	0.91*	0.82	0.62*	0.37	0.75	0.70	0.29	**0.70**
	Logarithmic	0.78*	0.73	0.51*	0.48	0.70	0.74	0.48*	**0.70**
	Power	0.87*	0.82	0.55*	0.57	0.76	0.72	0.22	**0.72**
True Colour	**Linear**	0.11	0.49	0.04	N/A	0.82	0.14	0.23	**0.18**
	Exponential	0.14	0.50	0.04	N/A	0.80	0.02	0.34	**0.24**
	Logarithmic	0.08	0.47	0.08	N/A	0.78	0.10	0.22	**0.16**
	Power	0.10	0.49	0.10	N/A	0.85	0.07	0.36	**0.23**
TSS	**Linear**	N/A	N/A	0.04	0.71*	0.27	0.65	0.35	**0.35**
	Exponential	N/A	N/A	0.06	0.53*	0.13	0.49	0.35	**0.35**
	Logarithmic	N/A	N/A	0.01	0.57	0.20	0.55	0.38	**0.38**
	Power	N/A	N/A	0.08	0.44	0.01	0.42	0.34	**0.34**
Turbidity	**Linear**	N/A	0.47	0.59*	0.56*	0.36	0.44	0.33	**0.45**
	Exponential	N/A	0.54	0.38	0.54*	0.44	0.49	0.38	**0.47**
	Logarithmic	N/A	0.49	0.42	0.55	0.43	0.41	0.45	**0.44**
	Power	N/A	0.57	0.27	0.54	0.52	0.47	0.49	**0.50**

4.4 Spatial cross-validation results

Spatial cross validation was employed to determine if the removal of randomly selected spatial clusters reduced the predictive capabilities of the selected models. Models were selected based on the highest R of significant ($p < 0.05$) correlations between algorithms and chl-*a* concentration where correlations to other constituents were not significant ($p \geq 0.05$) Models selected for testing were also those that provided a robust explanation across as many ecoregions as possible. Chl-*a* concentration is the only variable of interest for modelling and therefore true colour, TSS and turbidity do not have models developed for testing. Initial model tests were done prior to outlier removal to assess the initial predictive power. Each model was tested using spatial cross-validation (folds = 30%, iterations = 100) to assess the model's predictive capabilities. Since $[((1/R) - (1/B)) \times NIR]$ and (G/B) returned poor results (low R), spatial cross-validation was not performed on these models.

4.4.1 Selected Landsat band reflectance combinations, ratios and algorithms

Those band reflectance combinations, ratios and algorithms selected as having the highest R in significant correlations to chl-*a* concentration with no significant correlations to other constituents are as follows:

- $(R/B) \times (NIR/B)$ in PTW with $R = 0.92$ for exponential regression;
- Red band in BCF with $R = 0.87$ for exponential regression;
- $[(B \times R) \times NIR]$ in TCF with $R = 0.74$ for linear regression;
- $[(B/R) \times NIR]$ in TPS with $R = 0.55$ for linear regression;
- $[(G/R) \times NIR]$ in TPD with $R = 0.76$ for linear regression;
- $[(R/G) \times NIR]$ in SHF with $R = 0.67$ for linear regression and
- (G/NIR) in TMF with $R = 0.83$ for exponential regression.

Spatial cross-validation results of models predicting chl-*a* concentration developed from these band reflectance combinations, ratios and algorithms for each ecoregion are found in Figure 4.3. Due to poor validation results for some of these models, other algorithms that were most often free of significant correlations with other constituents were also validated for all ecoregions.

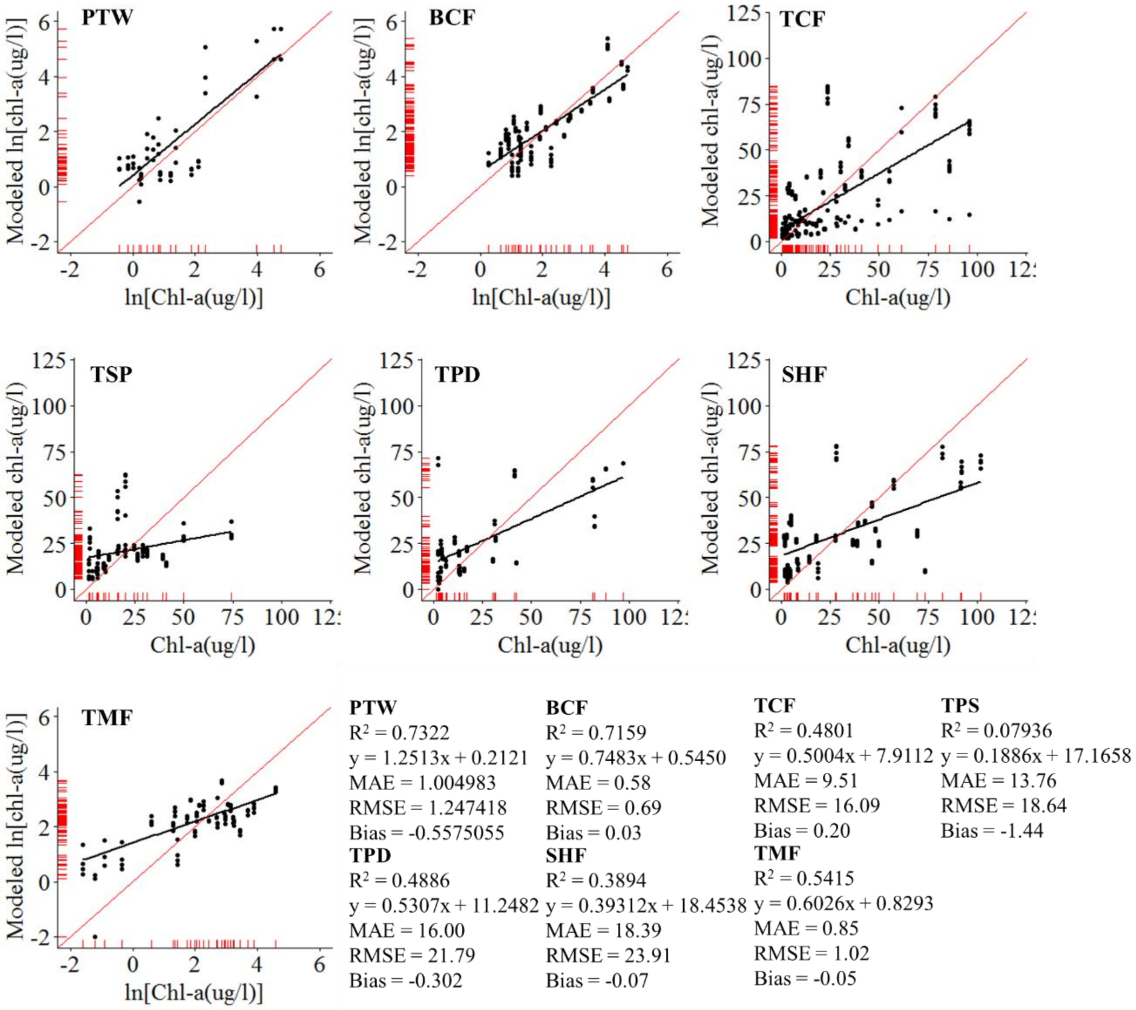

PTW
$R^2 = 0.7322$
$y = 1.2513x + 0.2121$
MAE = 1.004983
RMSE = 1.247418
Bias = -0.5575055

BCF
$R^2 = 0.7159$
$y = 0.7483x + 0.5450$
MAE = 0.58
RMSE = 0.69
Bias = 0.03

TCF
$R^2 = 0.4801$
$y = 0.5004x + 7.9112$
MAE = 9.51
RMSE = 16.09
Bias = 0.20

TPS
$R^2 = 0.07936$
$y = 0.1886x + 17.1658$
MAE = 13.76
RMSE = 18.64
Bias = -1.44

TPD
$R^2 = 0.4886$
$y = 0.5307x + 11.2482$
MAE = 16.00
RMSE = 21.79
Bias = -0.302

SHF
$R^2 = 0.3894$
$y = 0.39312x + 18.4538$
MAE = 18.39
RMSE = 23.91
Bias = -0.07

TMF
$R^2 = 0.5415$
$y = 0.6026x + 0.8293$
MAE = 0.85
RMSE = 1.02
Bias = -0.05

Figure 4.7 Spatial cross-validation of best models in each ecoregion. The black line represents the trend between the modeled and the in situ chl-a, the red line represents the 1:1, and the red dashes represent the position of each point on the axis. A good model is represented by low error (MAE and RMSE), follow the 1:1, and have a slope close to 1 and an intercept close to 0.

4.4.2 Blue and Near-Infrared combination (B × NIR)

(B × NIR) models were free of significant correlations with non-chl-*a* optical constituents in 6 of 7 ecoregions and featured relatively high R ($0.47 \leq R \leq 0.79$ using linear regression. The linear model, however, showed poor predictive power ($17.76 \leq$ RMSE ≤ 47.91 µg L^{-1}, median RMSE = 20.16 µg L^{-1}) and high average predictive error

(10.94 ≤ MAE ≤ 32.3 μg L^{-1} median MAE = 15.23 μg L^{-1}) at high chl-*a* concentrations (increased spectral variability) (Figure 4.4).

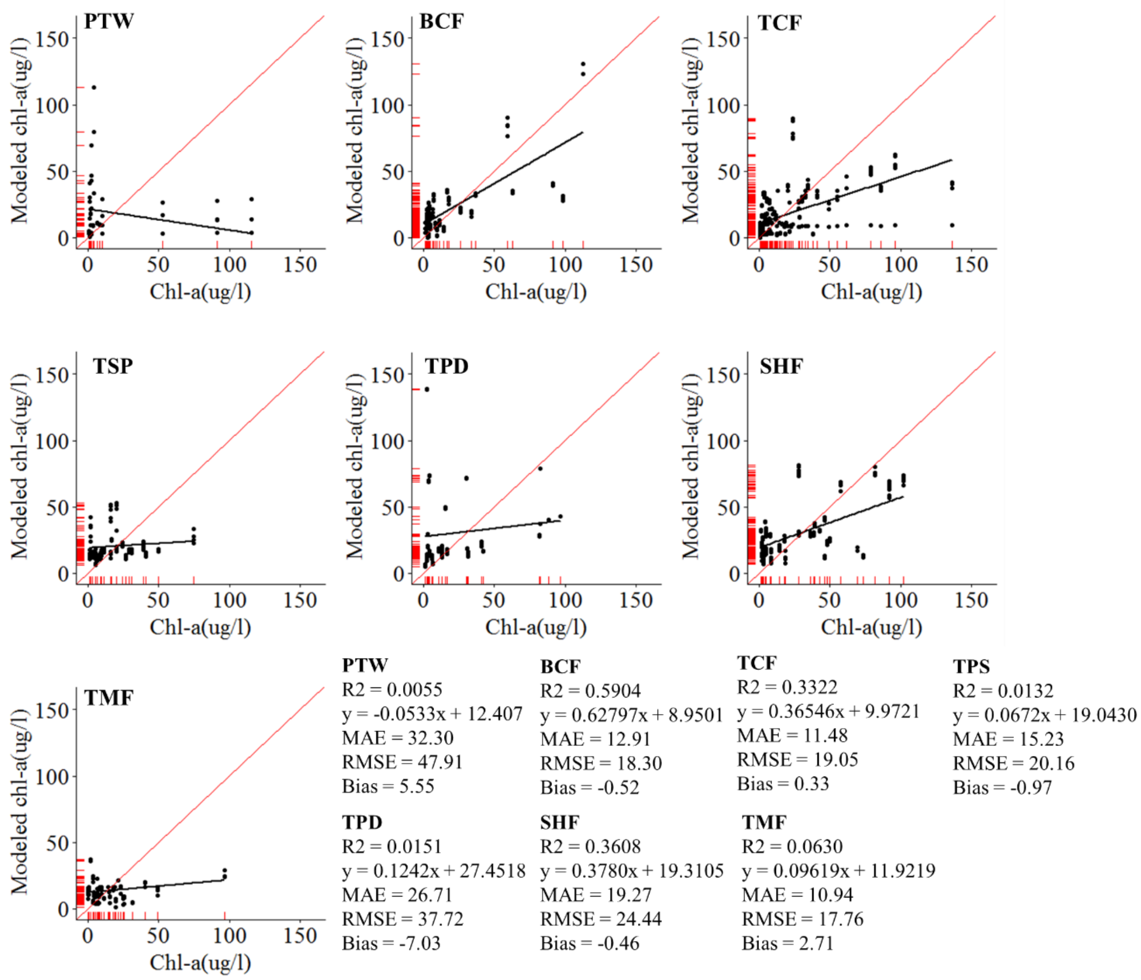

PTW
R2 = 0.0055
y = -0.0533x + 12.407
MAE = 32.30
RMSE = 47.91
Bias = 5.55

BCF
R2 = 0.5904
y = 0.62797x + 8.9501
MAE = 12.91
RMSE = 18.30
Bias = -0.52

TCF
R2 = 0.3322
y = 0.36546x + 9.9721
MAE = 11.48
RMSE = 19.05
Bias = 0.33

TPS
R2 = 0.0132
y = 0.0672x + 19.0430
MAE = 15.23
RMSE = 20.16
Bias = -0.97

TPD
R2 = 0.0151
y = 0.1242x + 27.4518
MAE = 26.71
RMSE = 37.72
Bias = -7.03

SHF
R2 = 0.3608
y = 0.3780x + 19.3105
MAE = 19.27
RMSE = 24.44
Bias = -0.46

TMF
R2 = 0.0630
y = 0.09619x + 11.9219
MAE = 10.94
RMSE = 17.76
Bias = 2.71

Figure 4.8 Spatial cross-validation of linear models of Blue and Near Infrared combination (B × NIR) in each ecoregion.

4.4.3 Red-to-Near-Infrared ratio (R ⁄ NIR)

(R ⁄ NIR) models were free of significant correlations with non-chl-*a* optical constituents in 1 of 7 ecoregions and featured relatively low R (0.03 ≤ R ≤ 0.80) using exponential regression. The linear model, however, showed poorer predictive power (1.11 ≤ RMSE ≤ 2.15 ln(μg L^{-1}), median RMSE = ln(μg L^{-1})) and higher average predictive error (0.82 ≤ MAE ≤ 1.80 ln(µg L^{-1}) median MAE = 1.18 ln(µg L^{-1})) at both high and low chl-*a* concentrations (increased spectral variability) (Figure 4.5).

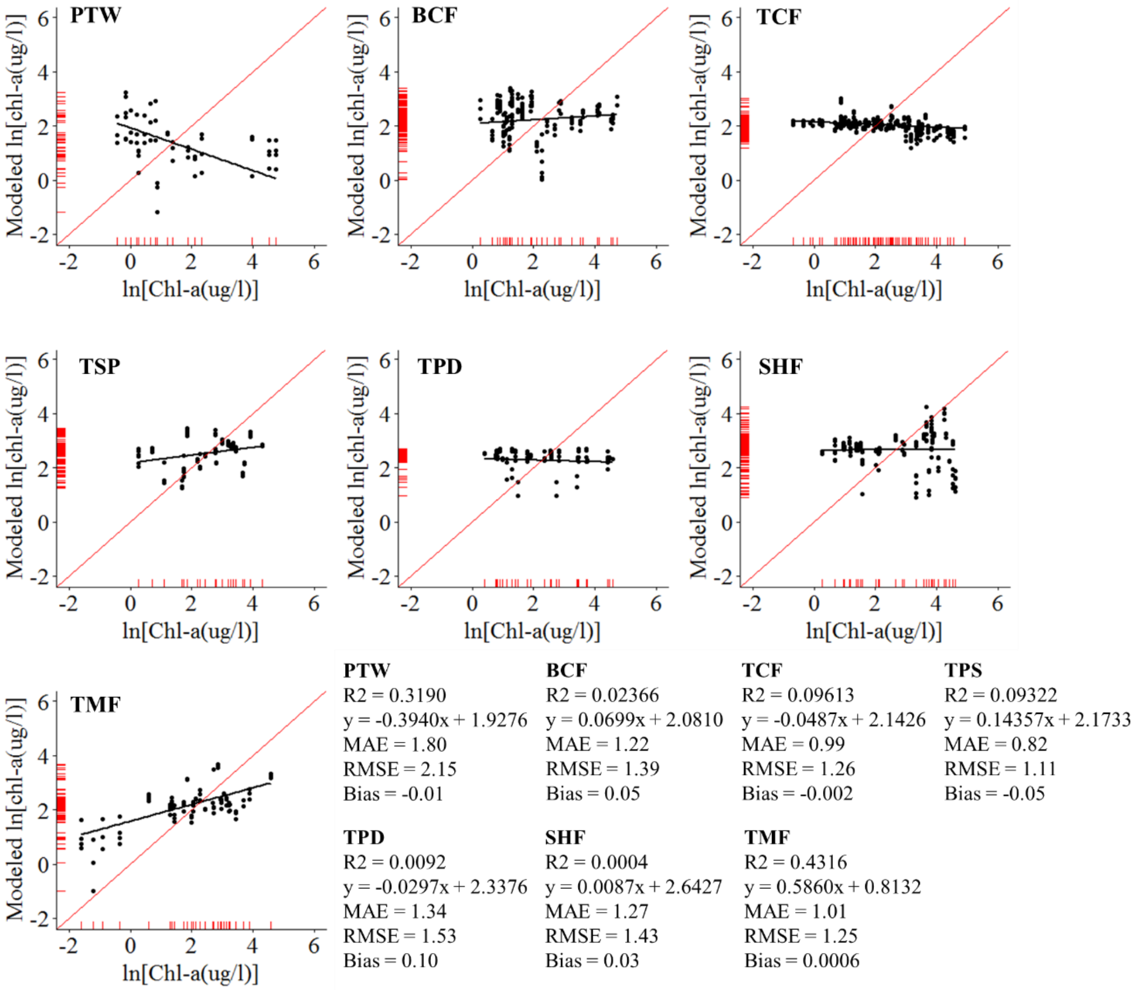

PTW
R2 = 0.3190
y = -0.3940x + 1.9276
MAE = 1.80
RMSE = 2.15
Bias = -0.01

BCF
R2 = 0.02366
y = 0.0699x + 2.0810
MAE = 1.22
RMSE = 1.39
Bias = 0.05

TCF
R2 = 0.09613
y = -0.0487x + 2.1426
MAE = 0.99
RMSE = 1.26
Bias = -0.002

TPS
R2 = 0.09322
y = 0.14357x + 2.1733
MAE = 0.82
RMSE = 1.11
Bias = -0.05

TPD
R2 = 0.0092
y = -0.0297x + 2.3376
MAE = 1.34
RMSE = 1.53
Bias = 0.10

SHF
R2 = 0.0004
y = 0.0087x + 2.6427
MAE = 1.27
RMSE = 1.43
Bias = 0.03

TMF
R2 = 0.4316
y = 0.5860x + 0.8132
MAE = 1.01
RMSE = 1.25
Bias = 0.0006

Figure 4.9 Spatial cross-validation of linear models of Red-to-Near-Infrared (R/NIR) in each ecoregion.

4.4.4 Three-band algorithm variant 1 [(G ⁄ R) × NIR]

[(G ⁄ R) × NIR] models were free of significant correlations with non-chl-*a* optical constituents in five of seven ecoregions and featured relatively high R (0.37 ≤ R ≤ 0.74 using power regression. The linear model, however, showed moderate predictive power (0.91 ≤ RMSE ≤ 1.74 ln(µg L^{-1}), median RMSE = 1.13 ln(µg L^{-1})) and high average predictive error (0.79 ≤ MAE ≤ 1.46 ln(µg L^{-1}), median MAE = ln(µg L^{-1})), varying by ecoregion (Figure 4.6).

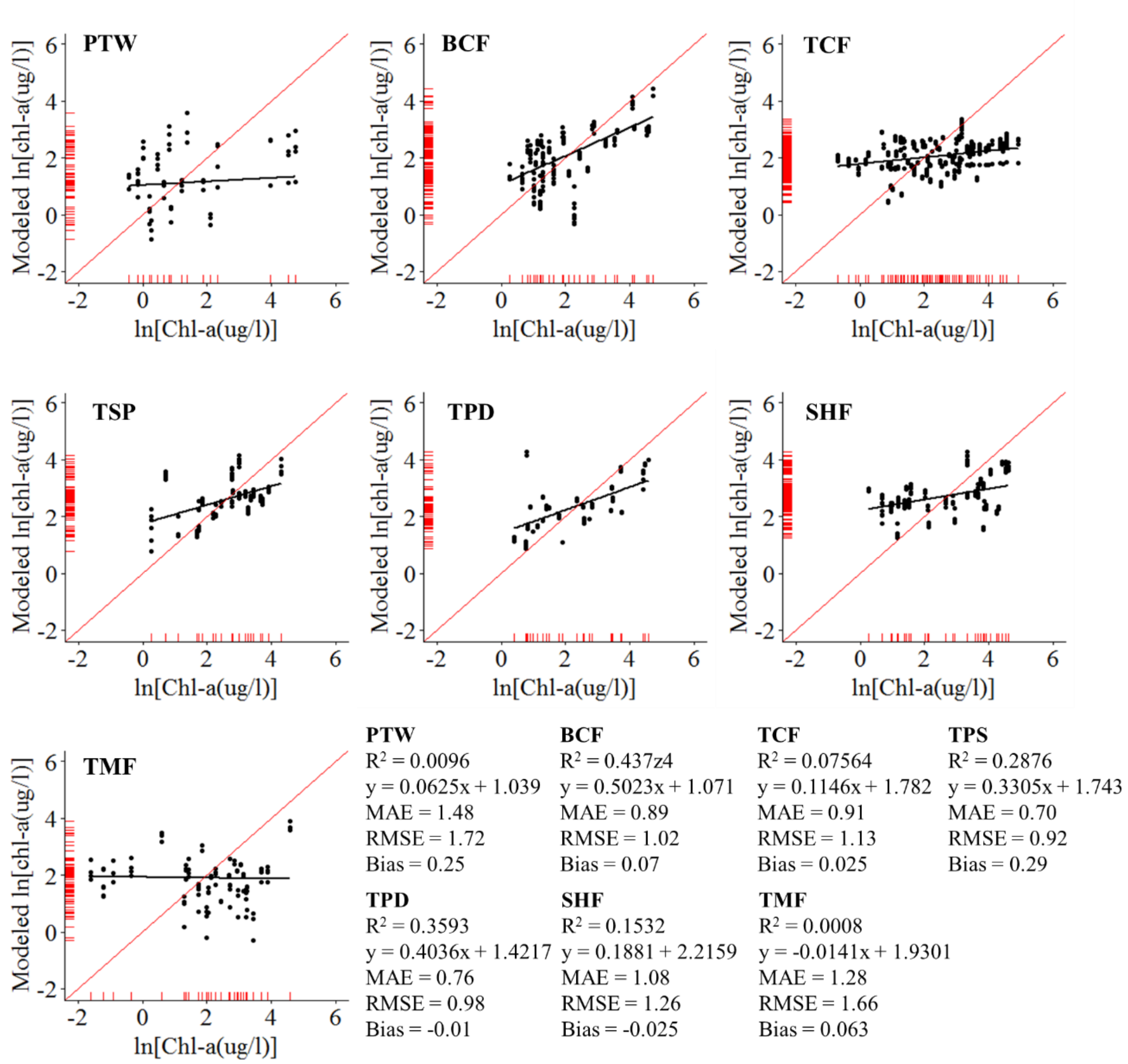

PTW
$R^2 = 0.0096$
y = 0.0625x + 1.039
MAE = 1.48
RMSE = 1.72
Bias = 0.25

BCF
R^2 = 0.437z4
y = 0.5023x + 1.071
MAE = 0.89
RMSE = 1.02
Bias = 0.07

TCF
$R^2 = 0.07564$
y = 0.1146x + 1.782
MAE = 0.91
RMSE = 1.13
Bias = 0.025

TPS
$R^2 = 0.2876$
y = 0.3305x + 1.743
MAE = 0.70
RMSE = 0.92
Bias = 0.29

TPD
$R^2 = 0.3593$
y = 0.4036x + 1.4217
MAE = 0.76
RMSE = 0.98
Bias = -0.01

SHF
$R^2 = 0.1532$
y = 0.1881 + 2.2159
MAE = 1.08
RMSE = 1.26
Bias = -0.025

TMF
$R^2 = 0.0008$
y = -0.0141x + 1.9301
MAE = 1.28
RMSE = 1.66
Bias = 0.063

Figure 4.10 Spatial cross-validation of linear models of the three-band algorithm variant 1 [(G ⁄ R) × NIR] in each ecoregion.

4.4.5 Three-band algorithm variant 2 (G × R × NIR)

(G × R × NIR) models were free of significant correlations with non-chl-*a* optical constituents in 4 of 7 ecoregions and featured relatively high R (0.47 ≤ R ≤ 0.79) using power regression. The linear model, however, showed moderate predictive power (0.81 ≤

RMSE ≤ 1.97 µg L^{-1}, median RMSE = 1.06 ln(µg L^{-1})) and low average predictive error (0.67 ≤ MAE ≤ 1.63 ln(µg L^{-1})median MAE = 0.71 ln(µg L^{-1})) (Figure 4.7).

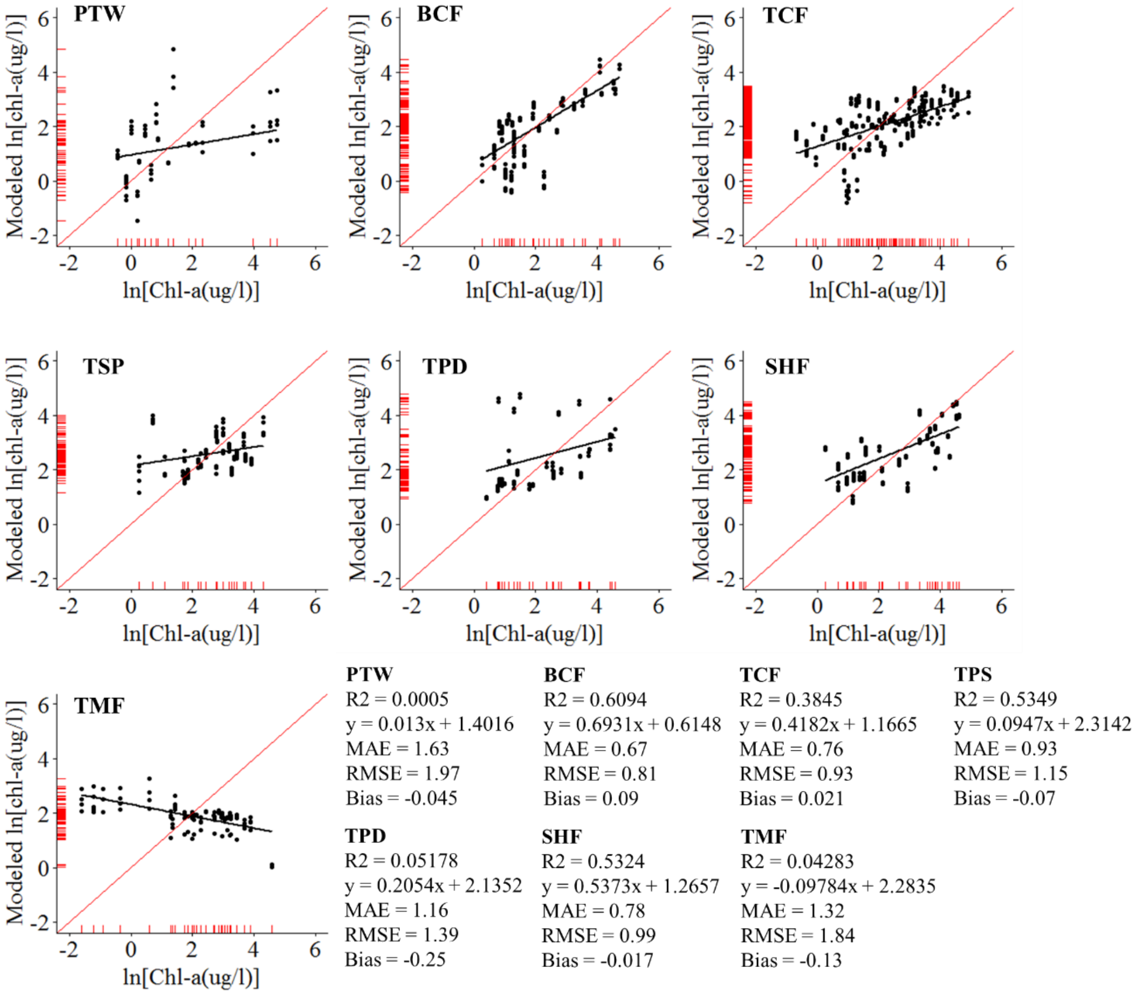

PTW
R2 = 0.0005
y = 0.013x + 1.4016
MAE = 1.63
RMSE = 1.97
Bias = -0.045

BCF
R2 = 0.6094
y = 0.6931x + 0.6148
MAE = 0.67
RMSE = 0.81
Bias = 0.09

TCF
R2 = 0.3845
y = 0.4182x + 1.1665
MAE = 0.76
RMSE = 0.93
Bias = 0.021

TPS
R2 = 0.5349
y = 0.0947x + 2.3142
MAE = 0.93
RMSE = 1.15
Bias = -0.07

TPD
R2 = 0.05178
y = 0.2054x + 2.1352
MAE = 1.16
RMSE = 1.39
Bias = -0.25

SHF
R2 = 0.5324
y = 0.5373x + 1.2657
MAE = 0.78
RMSE = 0.99
Bias = -0.017

TMF
R2 = 0.04283
y = -0.09784x + 2.2835
MAE = 1.32
RMSE = 1.84
Bias = -0.13

Figure 4.11 Spatial cross-validation of linear models of the three-band algorithm variant 2 (G×R×NIR] in each ecoregion.

4.4.6 Green and Red combination (G × R)

(G × R) models were free of significant correlations with non-chl-*a* optical constituents in four of seven ecoregions and featured relatively low R (0.29 ≤ R ≤ 0.66) using exponential regression. The linear model, however, showed moderate predictive power (0.86 ≤ RMSE ≤ 2.82 ln(µg L^{-1}), median RMSE = 1.25 ln(µg L^{-1})) and moderate average predictive error (0.69 ≤ MAE ≤ 2.21 ln(µg L^{-1}) median MAE = 0.99 ln(µg L^{-1})) at high chl-*a* concentrations (increased spectral variability) (Figure 4.8).

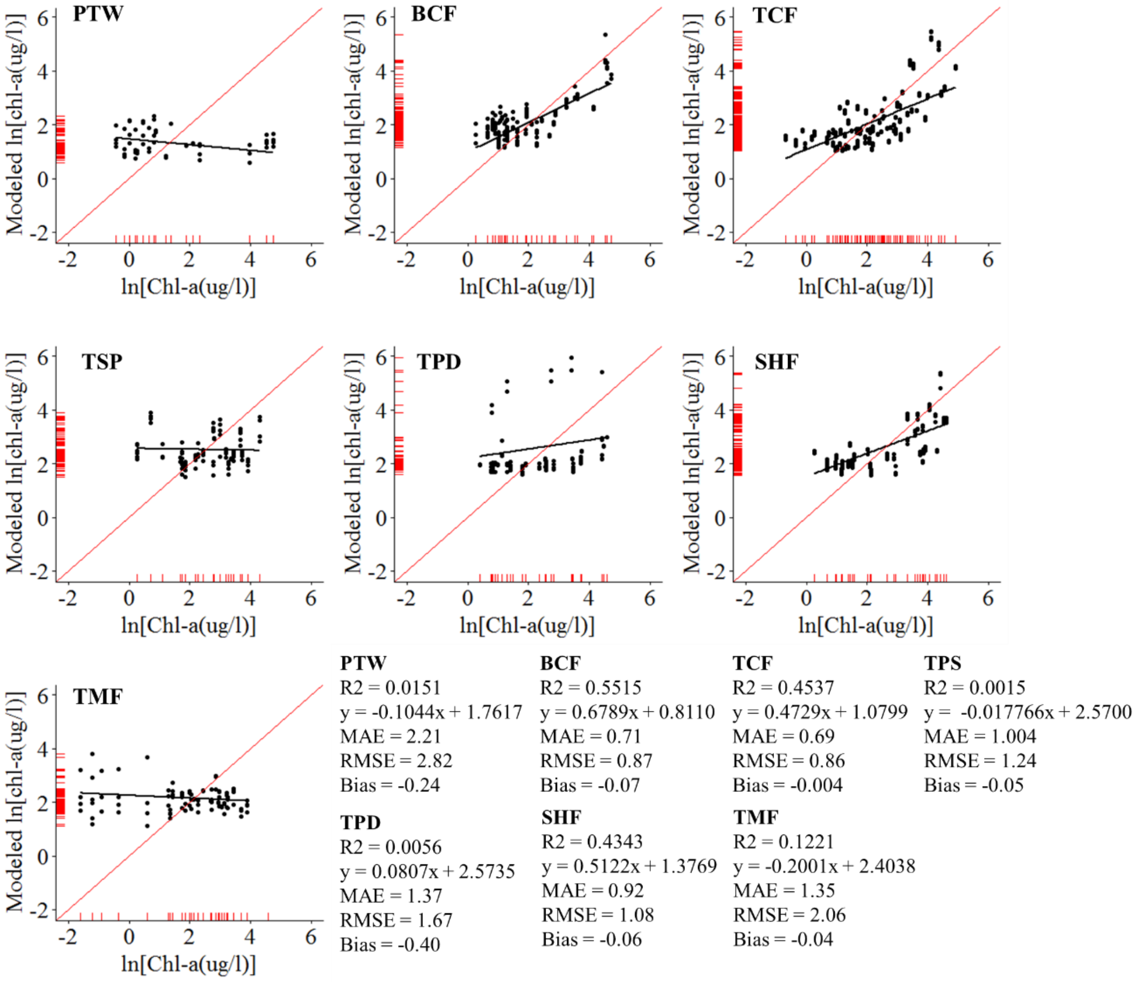

PTW
R2 = 0.0151
y = -0.1044x + 1.7617
MAE = 2.21
RMSE = 2.82
Bias = -0.24

BCF
R2 = 0.5515
y = 0.6789x + 0.8110
MAE = 0.71
RMSE = 0.87
Bias = -0.07

TCF
R2 = 0.4537
y = 0.4729x + 1.0799
MAE = 0.69
RMSE = 0.86
Bias = -0.004

TPS
R2 = 0.0015
y = -0.017766x + 2.5700
MAE = 1.004
RMSE = 1.24
Bias = -0.05

TPD
R2 = 0.0056
y = 0.0807x + 2.5735
MAE = 1.37
RMSE = 1.67
Bias = -0.40

SHF
R2 = 0.4343
y = 0.5122x + 1.3769
MAE = 0.92
RMSE = 1.08
Bias = -0.06

TMF
R2 = 0.1221
y = -0.2001x + 2.4038
MAE = 1.35
RMSE = 2.06
Bias = -0.04

Figure 4.12 Spatial cross-validation of linear models of the Green and Red combination (G×R) in each ecoregion.

4.4.7 Three-band algorithm variant 3 [(R ⁄ B) × NIR]

[(R ⁄ B) × NIR] models were free of significant correlations with non-chl-*a* optical constituents in two of seven ecoregions and featured relatively high R (0.22 ≤ R ≤ 0.87) using power regression. The linear model, however, showed high predictive power (0.86 ≤ RMSE ≤ 1.82 ln(µg L^{-1}), median RMSE = 1.02 ln(µg L^{-1})) and low average predictive error ($0.74 \leq$ MAE ≤ 1.44 ln(μg L^{-1}) median MAE = 0.81 ln(μg L^{-1})) at high chl-*a* concentrations (increased spectral variability) (Figure 4.9).

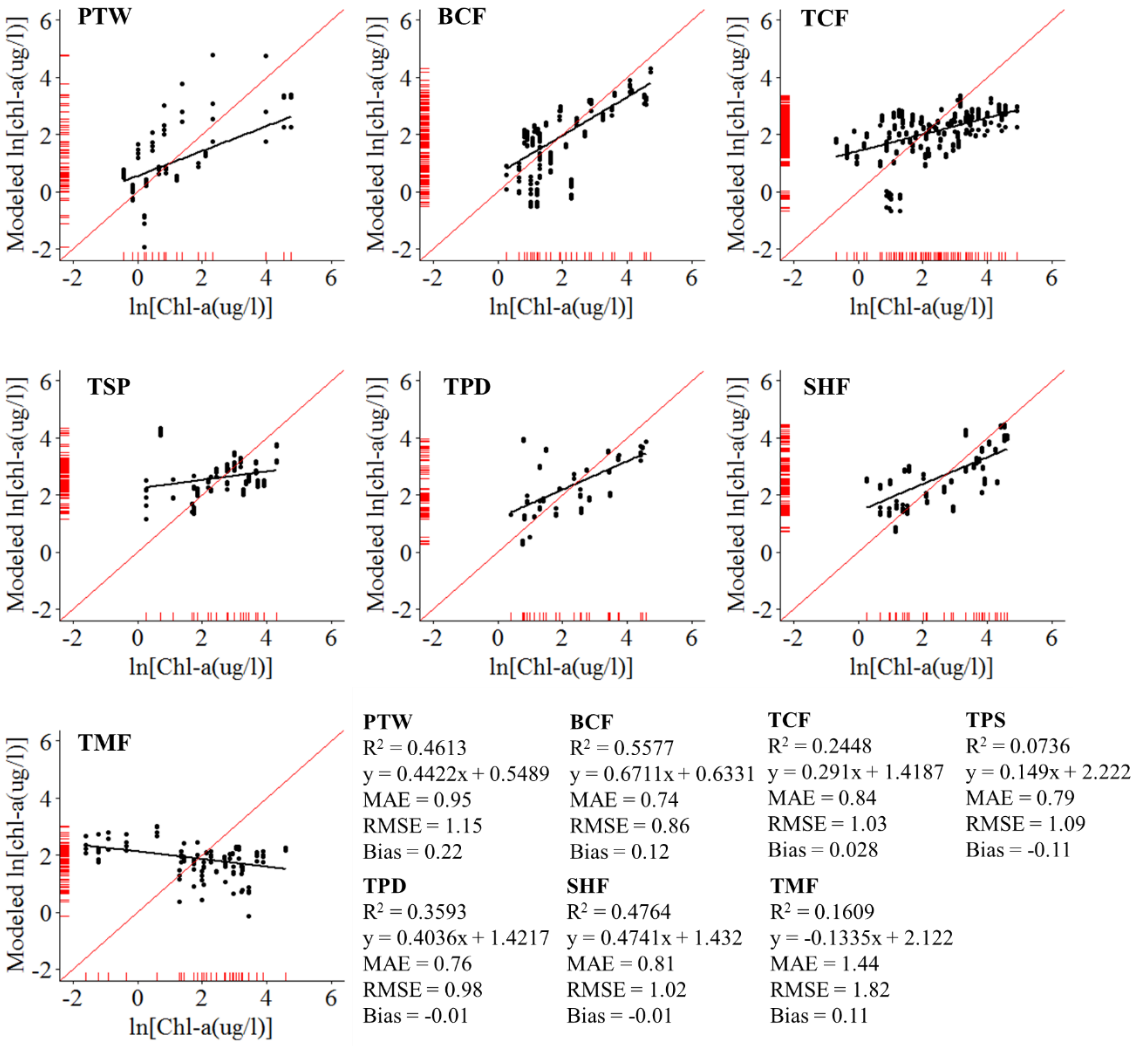

Figure 4.13 Spatial cross-validation of linear models of the three-band algorithm variant 3 [(**R⁄B**) × **NIR**] in each ecoregion.

4.4.8 Identifying the best algorithm per ecoregion

Of the chl-*a* results, figure 4.10 identifies the number of ecoregions in which chl-a is significant ($p < 0.05$), and not significant for true colour, TSS, and turbidity for all tested algorithms. It was found that no algorithm was significant for all regions, and only one to five algorithms were significant for at least five of seven ecoregions, depending on regression curve.

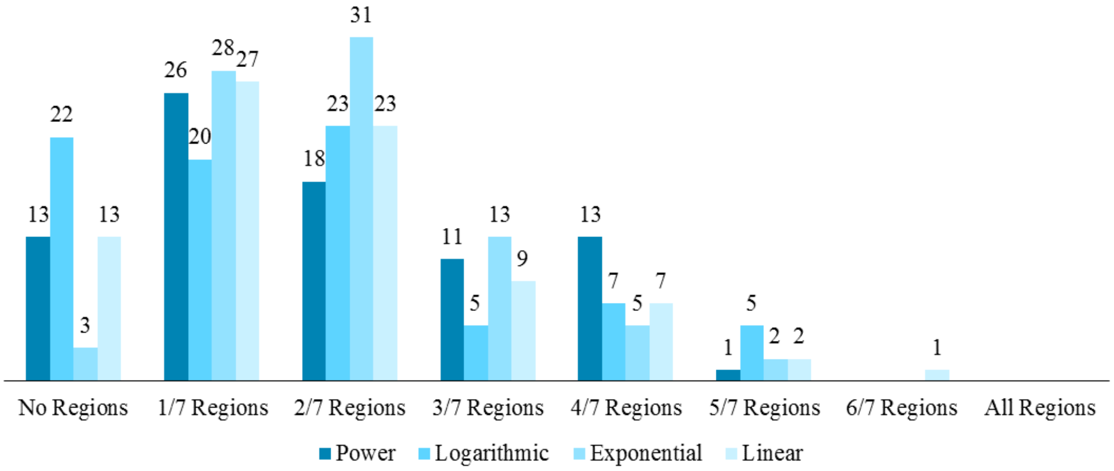

Figure 4.14 Number of ecoregions in which chl-*a* is significant ($p < 0.05$) and other optical constituents (true colour, TSS and turbidity) are not significant ($p > 0.05$) for all regressions. Values given are the total number of algorithms which meet this significance criteria.

Of the algorithms representing at least five of seven ecoregions where the significance criteria is true, linear regression using (B × NIR) was significant for six of seven regions, and [(G ⁄ R) × NIR] for five of seven regardless of regression. It was found that (B × NIR) using linear regression has high error and would be an unfit model. [(G ⁄ R) × NIR] provided a better fit for most regions, in which the same bands using [(G × R) × NIR] provided a strong fit for many regions as well, and met the significance criteria in four of seven regions.

For each ecoregion, a model was selected based on (1) the highest predictive power from spatial cross-validation results, (2) robustness (lowest average MAE across all other ecoregions), and (3) highest R in correlation to chl-*a* concentration with no significant correlations to other constituents:

- [(R ⁄ B) × NIR] in PTW;

- (G × R × NIR) in BCF, TCF and SHF;
- [(G ⁄ R) × NIR] in TPS and TPD; and
- (R ⁄ NIR) in TMF.

One outlier was removed after one iteration in PTW, TPD and SHF; three outliers were removed after three iterations in BCF; eight outliers were removed after three iterations in TCF; four outliers were removed after two iterations in TPS; and five outliers were removed after three iterations in TMF. After outliers were removed, the models were applied to obtain chl-*a* concentrations (Figure 4.11). While the predictive bias of the model (average error) is close to zero, there is an over-prediction at chl-*a* concentrations less than 2.0-3.0 ln(µg L^{-1}), and an under-prediction at chl-*a* concentrations greater than 2.0-3.0 ln(µg L^{-1}), as indicated by the trend line. All models pass the Shapiro-Wilks normality test, and are normally distributed. Spatial cross-validation results for the selected chl-*a* algorithms applied in each ecoregion are found in Figure 4.12.

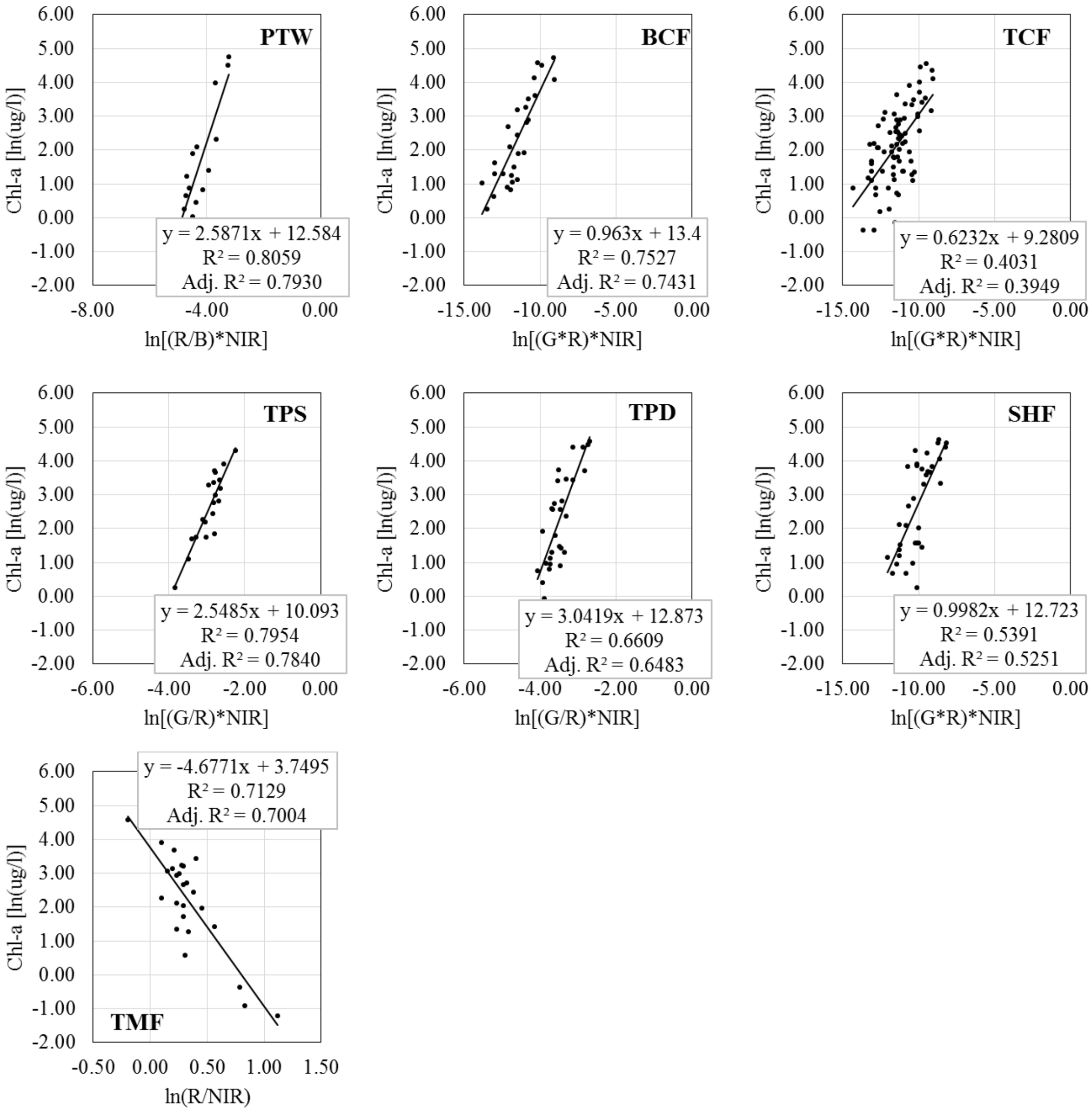

Figure 4.15 Selected chl-*a* algorithm regression plots in each ecoregion.

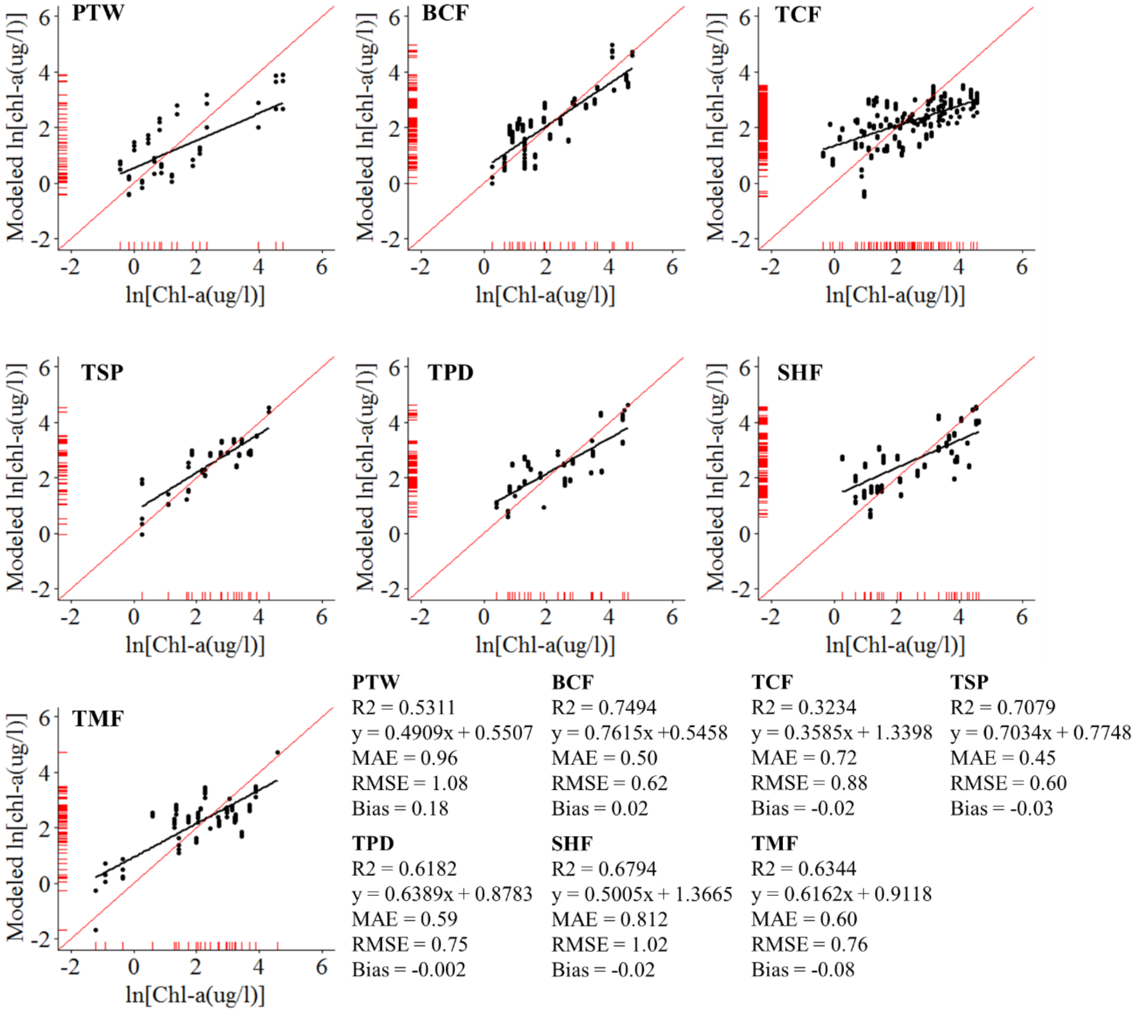

Figure 4.16 Selected models: Spatial cross validation.

Chapter 5

5 Discussion

This study was designed to identify methods in which we can create accurate predictive models for chl-*a* concentration retrieval. This requires appropriate atmospheric correction for Landsat level-1 images of freshwaters, and empirical model correlation tests, where chl-*a* is significant and other optical constituents (true colour, TSS and turbidity) are not. This was done by identifying correlations between *in situ* surface chl-*a* concentrations to various Landsat band ratios, combinations and algorithms, and the regression type that provided the best fit (i.e. linear, exponential, logarithmic and power).

5.1 The impact of atmospheric correction

Appropriate atmospheric correction methods for Landsat and other sensor satellite images have been in constant development, with the radiative transfer equation presented in section 1.2.2 being one of the standard methods for terrestrial and marine applications (Pathak *et al*, 2014). The 6SV algorithm is a terrestrial model, and as such is not applicable to inland waters. It is very difficult to predict atmospheric contribution over water as they are often the darkest pixels, and changes to inherent optical properties can change the spectral response, and shift the distribution of aerosols, particularly for large waterbodies (Slade *et al*, 2010). Studies typically find better results with that of TOA radiance (Toming *et al*, 2016; Martins *et al.*, 2017). Typically, atmospheric correction attempts perform poorly for the Blue band due to inefficient modelling of aerosols (Guanter *et al*, 2010; Lobo *et al*, 2015). The atmosphere also makes up the majority of radiance seen in dark pixels (Martins *et al*, 2017), making the removal of Rayleigh scatter more important for inland waters. Rayleigh scatter correction should provide a better fit for true colour parameters, as they have strong absorption of blue and green light and rely heavily on the removal of scattering effects from the atmosphere (Kutser *et al*, 2005). It was seen that the chl-*a* algorithms which make use of the Blue and Green bands provided an improved R, as chl-*a* absorption and reflectance are also associated with the Red to NIR edge of the spectrum, which are less influenced by the atmosphere. Rayleigh scatter path radiance was found to be higher for the Blue bands than that of the NIR (see appendix C), suggesting that correction for Rayleigh scatter in the Blue band, when, for example Red-to-Blue ratio is used, would provide a better correlation to chl-*a*. It was found that water colour had comparable levels of change in correlation to band reflectance when applying Rayleigh scatter correction. However, colour did not show as high of a magnitude of change. The effects of Rayleigh scatter correction on performance improvement for water colour bands is negligible.

5.2 Differences in Landsat ETM+ to OLI reflectance

One of the common skepticisms when building empirical models with the Landsat series is the inclusion of reflectance measured from both TM/ETM+ and OLI sensors given the differences in bandwidths introduced in the OLI sensor (Table 1.3). The different sensors will measure different peaks along the electromagnetic spectrum, in which a comparison of reflectance between OLI and ETM+ can help demonstrate the magnitude of these differences. A significant difference was not found across the results presented, particularly with the Red and NIR, as measured MAE and bias is similar across all bands. There was a near perfect 1:1 correlation between the two sensors, where the slope was close to 1 and the intercept 0. Differences that occurred between the sensors are most likely due to shifts in the atmosphere as a result of the 8-day time lag between ETM+ and OLI. The variation was not likely due to bandwidth differences as there is comparable error with the Blue band, where the bandwidths do not vary to as high of a magnitude (OLI: 452-512 nm; ETM+: 450-520 nm). The Blue band was the most heavily influenced by the atmosphere (Vermote *et al*, 2016), and as R^2 (table 4.1) is lower than the Red and NIR, this suggests the differences seen are due to shifts in the atmosphere.

The data presented suggests difference in the reflectance measured between the sensors, which would in turn suggest similar predictive capabilities that has been confirmed in other remote sensing of water quality studies (Tu *et al.*, 2018; Mishra *et al*, 2014; Pahlevan & Schott, 2014). Moving forward with the use of these models for in situ modelling will not be impacted to a significant degree by the shift in radiometric bandwidths between sensors.

5.3 Regression types

The majority of studies regarding water quality analysis which implement empirical modelling use either a linear or exponential regression through the use of a natural log transform of the chl-*a* data. There is typically greater predictive power to that of chl-*a* when using an exponential curve within the literature (Feng *et al*, 2015). This is because models require a wide range of trophic state to provide effective prediction of chl-*a* at a given reflectance, from oligotrophic to hyper-eutrophic. As chl-*a* data are not normally distributed, there is an increased predictive error (MAE and RMSE) when using linear or logarithmic regression. By transforming the chl-*a* samples there is most often a resulting normal distribution, which may be a result of the observed high predictive error of linear regression when implementing cross validation of the optimal algorithms (highest Pearson R, $P < 0.05$, true colour/DOC, TSS and turbidity). Using linear regression produced MAE ranging from 9.51-18.39 µg/l and RMSE ranging from 16.09-23.91 µg/l. This study found that exponential and power curves provided a somewhat better fit than linear and logarithmic regression for most algorithms tested, both in the correlation and tests, and in comparison of the 1:1 plots.

Logarithmic regression (represented as a natural-log transformation of the reflectance) consistently provided poor correlations (with some exceptions), as there was typically less variability in the reflectance at higher chl-*a* concentrations when transformed. A natural-log transformation of the reflectance does not help in establishing a linear trend when lowering the discernable values between high reflectance. This depends on the algorithm, as combinations (multiplication of bands) provided increased distance between points at higher reflectance compared to band ratios (division of bands). For this reason, logarithmic and power regression provide a better fit than that of linear or exponential. Due to the improvement we get by transforming the dependent variable (chl-*a*), and the independent variable (reflectance) (when multiplying reflectance, as the majority of algorithms involve a combination in some form), power regression provided the best results regardless of region or algorithm.

Here, the assumption that the sampling location water chemistry was representative of the entire, surficial lake was accepted. While a standard deviation threshold will limit some of the variability expected between the in situ sample and reflectance, there was an introduction of increased variability in the measured reflectance. For this reason, power regression provided a stronger fit more often, as the natural-transformation of both axes can help reduce the variability.

There are additional variables that may affect the relationship between freshwater chemistry and the observed reflectance. Mixed linear models allow for the addition of fixed and random factors, such as spatial and temporal components of latitude, longitude, and month of sampling. Mixed linear models however, require that the inputs for prediction, meet the same criteria as the model inputs, which severely limits its application. For this reason, two-dimensional regression remains the best option of the application of this study.

5.4 Selecting an optimal algorithm

The primary purpose of this study is to identify key algorithms that provided a strong fit for chl-*a*, and not for other optical constituents (based on R and P). Schalles (2006) found that the application of the NIR limits the influence of sediments and DOM. Step-wise addition of suspended white kaolin clay sediments in a mesocosm showed little to no effect on the reflectance spectra of chl-*a* from 750-900 nm (Figure 5.1). Step-wise addition of humic acid (to simulate DOM) also found little to no distinction from 825-900 nm (see Figure 5.2). The study reports peaks in chl-*a* absorption at 685 nm and 750 nm are not influenced by the presence of sediments and DOM and are indicative of chl-*a*. These absorbent Red and NIR (685 nm and 750 nm) chl-*a* signals have a narrow wavelength range in which to capitalize, where the application to Landsat may not be possible due to its broad bandwidths. Schalles, among others, presented the importance of the NIR, in which the Red-to-NIR ratio is to provide a strong indication of chl-*a* in turbid waters. Often it is assumed that many inland waters are turbid (Mobley, 1994; Schalles, 2006) and therefore the Red-to-NIR ratio should be applied, as the NIR is less affected by presence of DOM and sediments. The tests done here provided a poor correlation using the Red-to-NIR ratio with chl-*a* concentrations, with the exception of the TMF ecoregion. The TMF ecoregion is known to have high precipitation (Schneider *et al.* 2011) and growth productivity, so there would be an increase in the run-off of organic matter in the waters.

The correlation of chl-*a* to individual Landsat bands can help in assessing how constituents (sediments and DOM measured through true colour, TSS and turbidity) will confound any chl-*a* predictions that may arise when using retrieval models. There is a large increase in the reflectance of water (highest at shorter wavelengths) with the inclusion of sediments, and a decrease with the inclusion of DOM (see Figures 5.1 and 5.2). The increase in turbidity and TSS will result in increased reflectance due to backscattering of suspended matter. True colour is a result of dissolved humic and fluvic acids, due to DOM. Waters with a high measured true colour, have increased DOM, and therefore a lower reflectance than that of chl-*a*. For individual bands, Green and Red most consistently provide the greatest fit for true colour, TSS and turbidity, with Blue and NIR bands providing the lowest fit. This is consistent with what is seen in Figures 5.1 and 5.2, where the greater the concentration of sediments, the higher the reflectance at the corresponding wavelength bands, where Green and Red exhibit the highest change in reflectance as a result of DOM, and Blue and Green as a result of sediments. The greater the peak reflectance, the more indicative reflectance measurements are a result of that constituent. Chl-*a* shows highest reflectance in the Green band (Figure 5.3), with more absorption in the Red and NIR. Many algorithms use the Green-to-Red and Red-to-Blue to better predict for chl-*a*, however the effects of sediments and DOM on the Green and Blue band may confound the results.

The Red-to-Blue ratio is typically reported to have high correlation with chl-*a* concentrations (Han & Jordan 2005; Sass *et a'l*, 2007). One of the potential issues presented was the influence of sediments as they strongly impact the Blue band. It was found that despite having a high correlation across all regions, it also provided a strong fit for that of TSS and turbidity, with a relatively low fit to true colour. It may be possible that some of the TSS and turbidity samples have a high chl-*a* concentration, and that the chl-*a* signal is being isolated, and so the associated sediments and DOM is not impactful. However, when we multiply this ratio by the NIR band (which we know is less impacted by the presence of sediments and DOM), there was an improvement between the chl-*a* concentration and surface reflectance, and a sharp decrease in the Pearson R for TSS and turbidity.

The NIR plays a key role in isolating for the chl-*a* signal, as Gilterson *et al.* (2003; 2011) demonstrated which utilizes NIR reflectance peak at 710 nm, and the NIR absorbent peak at 750 nm. The equation was adapted to Landsat by Keith *et al.* (2018), however, due to the broad bandwidths, the algorithm was modified heavily. The algorithms presented by Keith (available in the appendices), typically provided a strong correlation with true colour/DOC, TSS and turbidity. The algorithms also provided a negative reflectance for some regions, in which logarithmic and power regressions were not possible. This may be in part due to the differences in atmospheric correction methods between this and the Keith *et al.* study. Additional three band algorithms such as the [(B-R)/G] and [(R^{-1}) - (B^{-1})/N], provided a similar range of results ($0.62 \leq R \leq 0.90$ and $0.64 \leq R \leq 0.87$) for power regression. These results are based on only three of the seven regions, due to negative reflectance. When compared to the range in R within the same ecoregions (using linear and exponential), we see that power regression has comparable results ($0.46 \leq R \leq 0.84$ and $0.23 \leq R \leq 0.63$ respectively).

The NIR-to-Blue combination provided the highest number of ecoregions free from optical constituents, and provided a reasonable R. This was interesting as the Blue band is the most influenced by sediments and atmospheric aerosols, and so it was expected to exhibit similar results to that of the Red-to-Blue ratio. These results further suggest that the inclusion of the NIR is vitally important, regardless of turbid conditions. Typically, it is assumed that the NIR is not useful at resolving low chl-*a* concentrations compared to other wavelengths more sensitive to changes in water, which is consistent with our results for the PTW and TCF, where a majority of lakes were oligotrophic (see Figure 3.1). The Blue and NIR combination did not provide a strong predictive model, as there were very poor validation results, as the chl-*a* concentrations are not often normally distributed using linear regression.

In addition to using the NIR band, there was a strong performance of the Green and Red bands, as a means of providing an adequate correlation for chl-*a*, and not additional optical constituents. As a ratio, combination and three-band algorithm, the Green and Red bands produced a correlation in almost all regions. There have been only a few studies that have tested the relationship of the Green-to-Red and NIR bands (Keith *et al.*, 2018; Bonansea *et al.*, 2018). While it was free of optical constituents and had a comparable R with algorithms for the respective tested regions, it provided a poor correlation in the TCF and TMF regions. The TMF would theoretically have the most turbid conditions of inland waters compared to the other regions, due to high precipitation (and subsequent run-off of sediments and organic matter). While Green-to-Red is cited by some to be useful for turbid waters (Ha *et al*., 2018), a higher proportion of sources reference the Red-to-NIR ratio instead (Dekker *et al*, 1991; Gitelson *et al*., 2000; Gons *et al*., 2002; Dall'Olmo *et al*., 2003; Schalles, 2006; Signh *et al*., 2014). The TCF region has the largest number of samples from differing sources and therefore had increased variability in the reflectance spectra, which may have caused the lower correlation. The TCF also has the highest number of oligotrophic to mesotrophic lakes, in which lakes with <20µg/l, show a much more varied response in the chl-*a* signal than that of the high chl-*a* samples. This may be due to the Landsats low pixel depth, which does not discern the subtle changes in oligotrophic waters. While the [(G ⁄ R) × NIR] algorithm does not provide the best results for the TCF region, the (G × R) and the (G × R × NIR) algorithms provided a strong fit. The (G × R × NIR) algorithm provided adequate levels of error prior to the removal of outliers for all regions. The algorithm was significant for chl-a and not for the other tested constituents in four regions, and of those not significant for chl-*a*, it was a result of TSS and turbidity. The Green-to-Red ratio provided promising results in remote sensing of phytoplankton, along with the addition of the NIR. This also has to do with the relationship between the expected absorbance and reflectance of chl-*a*. It is expected that the Red band will be most affected by the absorbance of chl-*a*, where the Green band is most affected by the reflectance of chl-*a*. The NIR is highly by the presence of chl-*a* fluorescence, therefore an interaction of these three bands will help to best describe for the presence of chl-*a*, whereas the presence of higher or lower reflectance of each individual band may be a result of some other variable.

The [(R ⁄ B) × N] may provide a better fit for lakes with less turbid conditions. For this reason, the [(R ⁄ B × NIR] algorithm was selected as the preferable model for the PTW as it provided a stronger fit than what is seen with the [(G ⁄ R) × NIR] algorithm. The (G × R × NIR) was selected for the BCF, TCF and SHF regions, while the TPS and TPD regions had a preferable correlation with the G/R × NIR algorithm. While there is a performance difference between the two algorithms, the difference in R is negligible across all regions and regressions (R difference = 0.16), and even more so for power regression (R difference = 0.13). The difference was dependent on the dataset and is most likely due to variability and error. While the Green band does show good correlation to sediments and DOM, (from both the theory and from the results), it is indicative of the peak chl-*a* reflectance. As a ratio with Red that is multiplied by the NIR, we see an improvement to the correlation, which is not significant for true colour, TSS and turbidity. The Red-to-NIR ratio had the strongest fit of chl-*a* concentration and Landsat reflectances for the TMF region, most likely due to highly turbid waters.

There were an additional 31 band combinations which tested the correlation of the product of two ratios, six of which included all four tested bands. Of these 31 algorithms, power regression was the dominant curve of fit, in which there were some comparative results to other more commonly used algorithms. These algorithms were tested to determine if there were any additional combinations that could be used to explain levels of chl-*a*. The results were variable, and when a correlation was found to be free of optical constituents that had a high correlation, it is almost always exclusive to that tested region. Since we do not see any consistency with these algorithms across multiple tested datasets, they did not provide sufficient physical evidence to explain the chl-*a* concentration to Landsat reflectance relationship. Several of these algorithms, typically those containing a ratio of Green-to-Blue, provided a stronger correlation for that of water colour.

5.5 The application of selected models

Spatial cross validation is highly important for determining predictive error. By removing spatial clusters of data, we simulate the application of the model to locations where we do not have data. Removing the data spatially helps ensure that the model works well, as spatial clusters of lakes may be more related (eutrophic or oligotrophic) than what is represented in the total distribution of chl-*a* within the model. Lakes that are closer together spatially are more likely to be related, and if we can still predict the values accurately with low error, we have greater confidence in the model. In order to provide an improved historical context for phytoplankton blooms and lake trophic state moving forward, the models need to be applied to a large geographic region, which has been demonstrated in other studies. Of the algorithms tested, it is apparent that linear regression models such as the Blue and NIR combination, provide a poor predictive model, with a very high RMSE and MAE value measured. When either exponential or power regressions was tested, the comparative plots of the selected models indicate better overall fit.

The empirical models that have been developed are to be applied to a wide range of lakes, and as we may not have in situ information, there is a need for validation. The cross-validation results suggest that the models do provide sufficient predictive capabilities.

The models have the capacity to predict for surface chl-*a* concentrations, which serve as a proxy for surface algal biomass. There is a distinct lack of complete historical lake chemistry data, in which these models may serve to fill. A universal model was not identified, which may be a result of regional differences, differences in individual lake compositions, or additional variables present in the data (see table 3.4). The use of these models may provide insight into changes in lake phytoplankton biomass overtime. It will be possible to create a 30+ year time series, and identify whether trends are increasing or decreasing. This lends to the question of whether lakes are becoming more or less eutrophic overtime. Shifts to more eutrophic conditions could lend credibility to the perceived increase in blooming events. The Landsat satellite sensor is limited in this capacity however, due to the poor temporal resolution. The sensor can only image a lake every 16 days, the presence of clouds, wind shear, or any other factor that may invalidate the images, can create an even greater gap in data. A single snapshot of conditions may not translate to annual conditions of the lake. While other sensors such as MODIS and MERIS provide daily images, the spatial resolution is far too coarse to measure inland waters (table 1.1). Sentinal-2a does provide daily images at an even finer spatial scale compared to Landsat (10-20m), however the sensor was launched in 2015, and so it would be impossible to build an historical time series. If a researcher is looking to provide more recent daily monitoring, then Sentinal-2a should be used. This research provides some insight into what bands may provide a strong fit, in which the algorithms presented here will need to be adapted to that sensor.

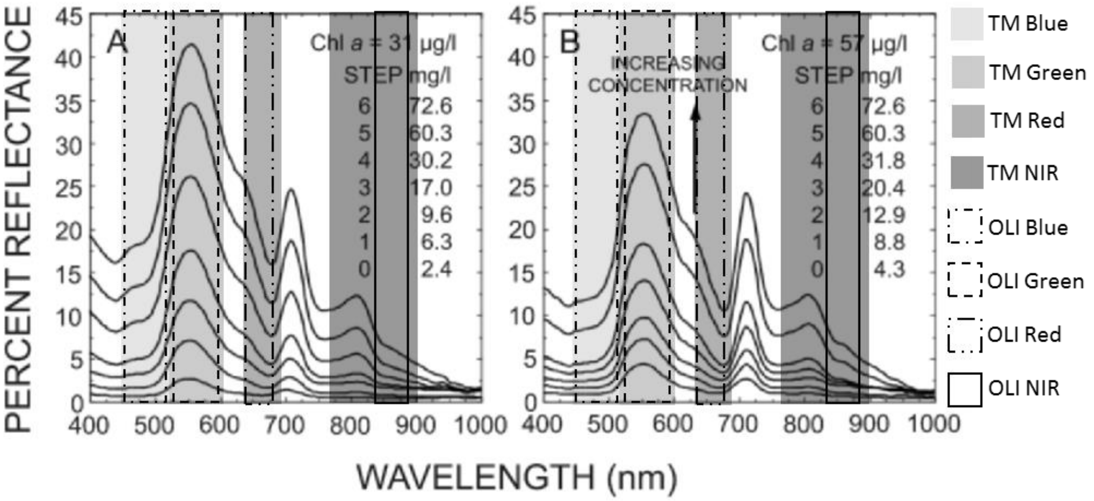

Figure 5.1; Adapted from Schalles (2006): Reflectance spectra of water during stepwise addition of white kaolin clay at a constant chl-*a* concentration (31 and 57 µg L^{-1}) in replicate tank mesocosms. Black bars indicate Landsat TM bandwidths

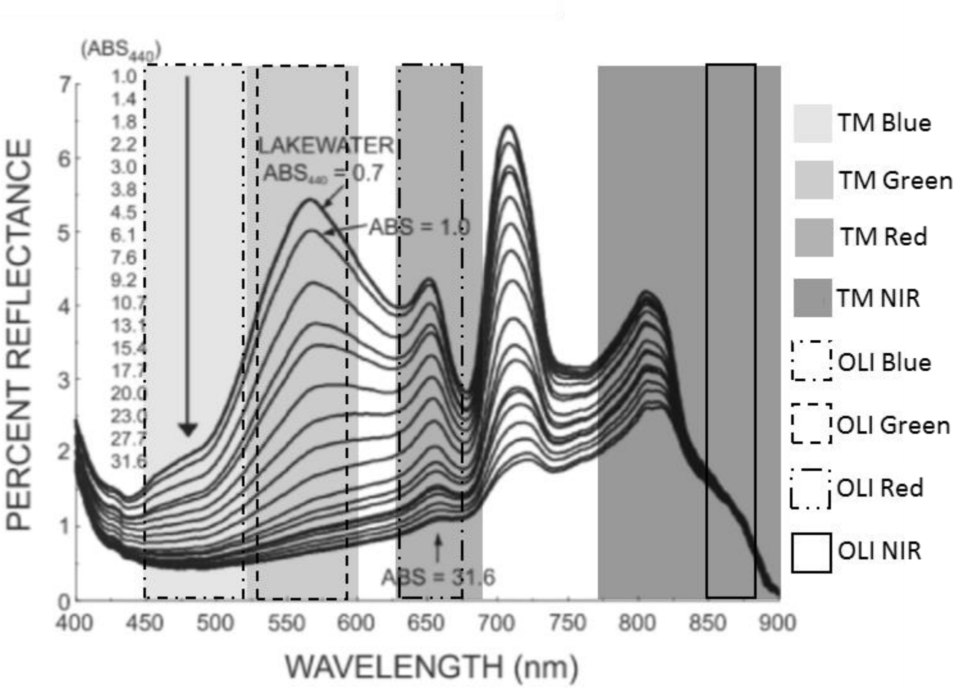

Figure 5.2: Adapted from Schalles (2006); Reflectance spectra of a 16-liter water sample during stepwise addition of humic acid (absorption at 440 nm). Samples contain *Anabaena* sp. bloom with 116.3 µg L^{-1}. Landsat TM bandwidths

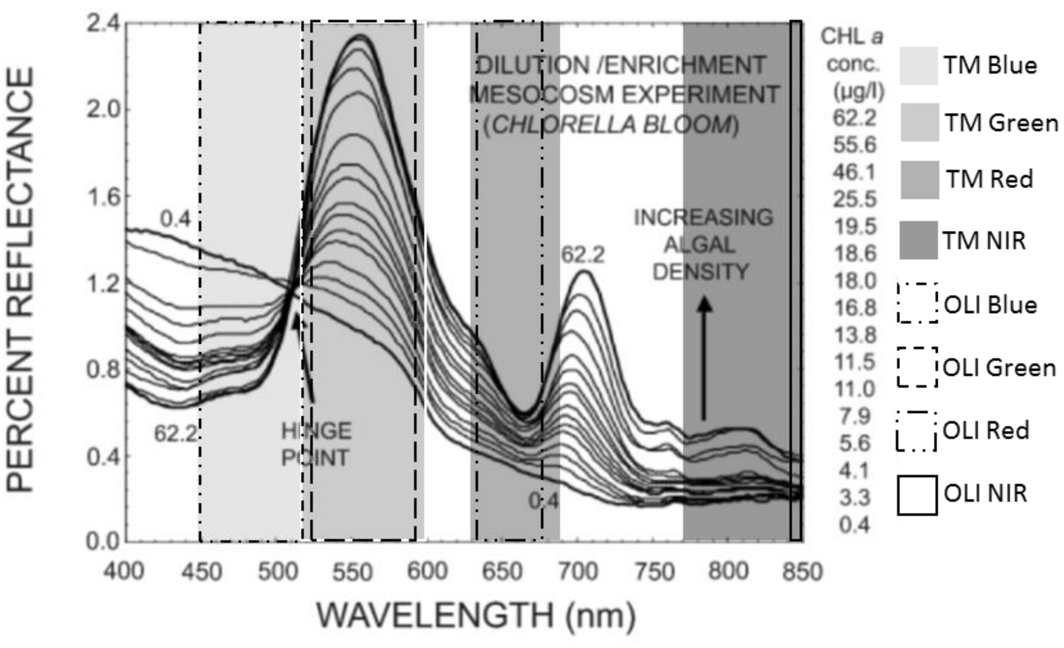

Figure 5.3 Adapted from Schalles (2006); Graded reflectance spectr*a* for different chl-*a* levels (0.4 to 62.2 µg L^{-1}).

Chapter 6

6 Conclusion

6.1 Research Findings

The objective of this research was to identify combinations, ratios or algorithms of Landsat band reflectances and the regression types that to create models for predicting chl-*a* concentrations in freshwater lakes across a range of geographic regions with limited confusion from the presence of other freshwater optical constituents.

It was found that the inclusion of both Landsat ETM+ and OLI within the same model is appropriate due to low measured error, and highly correlated reflectance measurements. The use of logarithmic regression provided low predictive power across most algorithms and constituents, while linear regression was identified as a strong fit for chl-*a* but provided significant error during validation. Exponential and power regression provided better fit and lower error, with power regression slightly out performing exponential regression. Three band algorithms were the preferable algorithms across all regions for chl-*a*. The (G/R)×NIR and the G×R×NIR provided the best fit of these algorithms, by providing a weak fit on average for colour, TSS and turbidity, and one of the highest correlations with linear regression. The NIR band is theoretically the band which is least influenced by other optical constituents and is made evident in the presented results. The application of the NIR to that of other band ratios and combinations that are commonly used for detecting chl-*a*, provided an improved correlation and a lower correlation with other optical constituents.

It was found that water colour was most often correlated with the Green-to-Blue ratio, and other tested two-ratio algorithms, however specific water colour algorithms were not tested. Water colour is the most important of the tested parameters to isolate from (as it does not include phytoplankton as a measurement, and instead predominately DOM), in which the inclusion of the NIR is found to do.

While it was found that chl-*a* was best fit using a three-band algorithm, a universal algorithm was not identified. While the (G/R×NIR and the G×R×NIR did provide the best fit for most ecoregions, it is not consistent across all ecoregions. This may be a result of chance, in which further testing may be needed (e.g. the TMF region was poorly correlated and instead exhibited a high fit Red-to-NIR ratio, for turbid conditions).

6.2 Research Significance

There is an ever growing need to improve our understanding of baseline lake trophic conditions, to better determine the implications of future scenarios on water resources. In addition, we see an ever-growing list of increased phytoplankton bloom reporting, pushing the need for greater monitoring. Robust remote sensing algorithms can help researchers and policy makers and water quality experts in maintaining an up to date inventory of lake surface conditions. Extensive in situ monitoring can be costly and inefficient, in which the application of robust predicative algorithms can provide a much cheaper alternative, particularly for remote and hard to reach lakes. This research also paves way for further analysis to better understand the potential covariates that are driving the trend of increased phytoplankton bloom formation on a global scale. Water security is an ever-pressing issue with future climate projections (Hanjra & Qureshi, 2010), particularly in the developing world. Additional stressors that can drive increased algal blooms, can place a greater hold on freshwater resources. It is imperative to monitor these resources, identify drivers, and find meaningful and impactful solutions.

Previous research in this field has primarily been limited in spatial scale, where models are typically developed for single lakes. This research aimed to identify correlations between chl-*a* concentrations and reflectances, over wide geographic regions. This research is aimed to apply these best fit models to lakes within similar regional boundaries, however further validation efforts are needed to determine the predictive accuracy of the models. The models provide the ability to identify peak algal biomass during the growing season, typically during the months of August, September and October, depending on latitude. This process provides researchers with the tools to better understand the potential shift of local and even global freshwater resources.

6.3 Future Research Direction

It is commonly theorized that climate change is one of the major drivers of phytoplankton bloom formation, as Paerl and Huisman (2008) identify higher growth rates of cyanobacteria (commonly toxin producing phytoplankton), compared to diatoms and green algae in warmer waters as part of the aptly named “blooms like it hot” paper. There is however, a lack of global representation in this study, as climactic changes such as temperature, precipitation, and nutrient concentration vary spatially, in which the use of singular lakes do not address the global effect climate change presents. The effects of climate change vary spatially, where greater rates of change exist at high latitudes, and changes in precipitation events vary greatly. There is also a lack of *in situ* data to provide conclusive evidence of increased algal biomass accumulation in lakes globally over time. The application of the models presented can be used to answer such a question, in which we may fill in the gaps by predicting surface chl-*a* concentration as a proxy for phytoplankton biomass. Climate change impact on these lakes can be assessed as we can measure conditions such as surface water temperature through an algorithm in development by Schaffer *et al.* (2018). Other drivers of phytoplankton blooms such as DOM can be estimated in the same method as chl-*a*, while precipitation grids can identify the potential of runoff within each lake. Statistical analysis of the resulting information can help in determining if what we are seeing now is a result of increased reporting, or if there is a correlation with climate related variables, and algal biomass concentration. Spectral coherence wavelet analysis techniques can help determine if the trends that are being identified are a result of anthropogenic influence, or instead due to climactic oscillation patterns (such as El Niño). There is much that can be built upon with the application of these models, and further research is required to help determine if algal blooms do in fact like it hot.

References

Alberta Environment and Parks (AEP) (2017). Surface Water Quality Data. Last accessed 11/14/2018 at URL: http://aep.alberta.ca/water/reports-data/surface-water-quality-data/default.aspx

Allan, M. G., Hamilton, D. P., Hicks, B. J., & Brabyn, L. (2011). Landsat remote sensing of chlorophyll a concentrations in central north island lakes of New Zealand. International Journal of Remote Sensing, 32(7), 2037-2055. doi:10.1080/01431161003645840

Allan, M. G., Hamilton, D. P., Hicks, B., & Brabyn, L. (2015). Empirical and semi-analytical chlorophyll a algorithms for multi-temporal monitoring of New Zealand lakes using Landsat. Environmental Monitoring and Assessment, 187(6), 1-24. doi:10.1007/s10661-015-4585-4

Allee, R. J., & Johnson, J. E. (1999). Use of satellite imagery to estimate surface chlorophyll a and secchi disc depth of Bull Shoals Reservoir, Arkansas, USA. International Journal of Remote Sensing, 20(6), 1057-1072. doi:10.1080/014311699212849

Alparslan, E., Aydöner, C., Tufekci, V., & Tüfekci, H. (2007). Water quality assessment at Ömerli dam using remote sensing techniques. Environmental Monitoring and Assessment, 135(1), 391-398. doi:10.1007/s10661-007-9658-6

Almanza, E., & Melack, J. M. (1985). Chlorophyll differences in Mono Lake (California) observable on Landsat imagery. Hydrobiologia, 122(1), 13-17. doi:10.1007/BF00018955

Alawadi, F. (2010). Detection of surface algal blooms using the newly developed algorithm surface algal bloom index (SABI). In Remote Sensing of the Ocean, Sea Ice, and Large Water Regions 2010 (Vol. 7825, p. 782506). International Society for Optics and Photonics.

Anderson, C.W. (2005). Chapter 6.7: Turbidity. National Field Manual for the Collection of Water-Quality Data, USGS. Accessed on Oct 24, 2018 at: https://water.usgs.gov/owq/FieldManual/Chapter6/Section6.7_v2.1.pdf

Anderson, D. (2014). HABs in a changing world: a perspective on harmful algal blooms, their impacts, and research and management in a dynamic era of climactic and environmental change. In Harmful algae 2012: Proceedings of the 15th International Conference on Harmful Algae: October 29-November 2, 2012, CECO, Changwon, Gyeongnam, Korea/editors, H- G. Kim, B. Reguera, G.M. Hallegraeff, Chang Kyu Lee, M. (Vol. 2012, p. 3). NIH Public Access.

Baghdadi, N., & Zribi, M. (2016). Optical remote sensing of land surfaces: Techniques and methods. London, UK; ISTE Press Ltd.

Bilotta, G. S., & Brazier, R. E. (2008). Understanding the influence of suspended solids on water quality and aquatic biota. Water Research, 42(12), 2849-2861.

Bernd B., Lang, M., Kotthoff, L., Schiffner, J., Richter, J., Studerus, E., Casalicchio, G., & Jones, Z.M. (2016) MLR: Machine Learning in R. Journal of Machine Learning Research. 17(170), 1-5.

Beinroth, F. H. (1982). Some highly weathered soils of Puerto Rico, 1. Morphology, formation and classification. Geoderma, 27(1-2), 1-73.

Bodhaine, B. A., Wood, N. B., Dutton, E. G., and Slusser, J. R. (1999) On Rayleigh optical depth calculations, J. Atmos. Ocean. Tech., 16, 1854–1861, doi:10.1175/1520-0426(1999)016<1854:ORODC>2.0.CO;2.

Boucher, J., Weathers, K. C., Norouzi, H., & Steele, B. (2018). Assessing the effectiveness of Landsat 8 chlorophyll a retrieval algorithms for regional freshwater monitoring. Ecological Applications. 28(4) 1044-1054.

Bonansea, M., Rodriguez, C., & Pinotti, L. (2018). Assessing the potential of integrating Landsat sensors for estimating chlorophyll-a concentration in a reservoir. Hydrology Research, 49(5), 1608-1617.

Brezonik, P., Menken, K. D., & Bauer, M. (2005). Landsat-based remote sensing of lake water quality characteristics, including chlorophyll and colored dissolved organic matter (CDOM). Lake and Reservoir Management, 21(4), 373-382. doi:10.1080/07438140509354442

Callieri, C., Bertoni, R., Contesini, M., Bertoni, F. (2014). Lake level fluctuations boost toxic cyanobacterial “oligotrophic blooms.” PloS One, 9: e109526. https://doi.org/10.1371/journal.pone.0109526.

Camps-Valls, G. (2012). Remote Sensing Image Processing (1st ed.). San Rafael, Calif. (1537 Fourth Street, San Rafael, CA 94901 USA): Morgan & Claypool.

Carder, K. L., Chen, F. R., Cannizzaro, J. P., Campbell, J. W., & Mitchell, B. G. (2004). Performance of the MODIS semi-analytical ocean color algorithm for chlorophyll-a. Advances in Space Research, 33(7), 1152-1159.

Carlson R.E. and J. Simpson (1996) A Co-ordinator's Guide to Volunteer Lake Monitoring Methods. North American Lake Management Society. 96 pp.

Carpenter, S. M., & Carpenter, D. J. (1983). Modeling inland water quality using Landsat data. Remote Sensing of Environment, 13(4), 345-352. doi:10.1016/0034-4257(83)90035-4

Carr, N.G., Whitton B.A., (1982). The Biology of Cyanobacteria. Botanical Monographs, Vol. 19, University of California Press, Blackwell Scientific Publications, Blackwell, Oxford.

CEC (Commission for Environmental Cooperation). 1997. Ecological regions of North America: Toward a common perspective. Commission for Environmental Cooperation, Montreal, Quebec, Canada, 71 pp.

Chander, G., Markham, B. L., & Helder, D. L. (2009). Summary of current radiometric calibration coefficients for Landsat MSS, TM, ETM+, and EO-1 ALI sensors. Remote Sensing of Environment, 113(5), 893-903.

Chandrasekhar, S. (1960). Radiative Transfer. New York: Dover Publications. 393 p.

Chavez, P. S. (1988). An improved dark-object subtraction technique for atmospheric scattering correction of multispectral data. Remote Sensing of Environment, 24(3), 459-479. doi:10.1016/0034-4257(88)90019-3

Chavez, P.S. (1996) Image-based atmospheric corrections – revisited and revised. Photogrammetric Engineering and Remote Sensing, 62, 1025–1036

Chen, L., Tan, C., Kao, S., & Wang, T. (2008). Improvement of remote monitoring on water quality in a subtropical reservoir by incorporating grammatical evolution with parallel genetic algorithms into satellite imagery. Water Research, 42(1), 296-306. doi:10.1016/j.watres.2007.07.014

Chen, J., Zhang, X., & Quan, W. (2013). Retrieval chlorophyll-a concentration from coastal waters: three-band semi-analytical algorithms comparison and development. Optics Express, 21(7), 9024-9042.

Cottingham, K. L., Ewing, H. A., Greer, M. L., Carey, C. C., Weathers, K. C. 2015. Cyanobacteria as biological drivers of lake nitrogen and phosphorus cycling. Ecosphere, 6: 1-19. https://doi.org/10.1890/ES14-00174.1.

Dall'Olmo, G., Gitelson, A. A., & Rundquist, D. C. (2003). Towards a unified approach for remote estimation of chlorophyll-a in both terrestrial vegetation and turbid productive waters. Geophysical Research Letters, 30(18).

Dekker, A. G., Malthus, T. J. and Seyhan, E. (1991) Quantitative modeling of inland water quality for high-resolution MSS systems. IEEE Trans. Geosci. Remote Sens. , 29, 89–95

DeVries, B., Huang, C., Lang, M., Jones, J., Huang, W., Creed, I., & Carroll, M. (2017). Automated quantification of surface water inundation in wetlands using optical satellite imagery. Remote Sensing, 9(8), 807. doi:10.3390/rs9080807

Dorset Environmental Science Center (DESC) (2017). A-Lakes: Lake Phytoplankton/Chlorophyll. Accessed 14 July 2017. Available upon request at: https://desc.ca/data

Duan, H., Zhang, Y., Zhang, B., Song, K., & Wang, Z. (2007). Assessment of chlorophyll-a concentration and trophic state for Lake Chagan using Landsat TM and field spectral data. Environmental Monitoring and Assessment, 129(1), 295-308. doi:10.1007/s10661-006-9362-y

Fadel, A., Faour, G., & Slim, K. (2016). Assessment of the trophic state and chlorophyll-a concentrations using Landsat OLI in Karaoun Reservoir, Lebanon. Lebanese Science Journal, 17, 130-145.

Falkowski, P.G. and J.A. Raven. 2007. Aquatic Photosynthesis. Princeton University Press, Princeton, N.J. USA. 488 p

Fallu, M., & Pienitz, R. (1999). Lacustrine diatoms in the Hudson Bay and James Bay area of Quebec - reconstruction of dissolved organic carbon concentrations. Écoscience, 6(4), 603-620.

Fan, Y., & van den Dool, H. (2008). A global monthly land surface air temperature analysis for 1948-present, Journal of Geophysical Research, 113, D01103, doi:10.1029/2007JD008470. Last accessed 12/05/2018 at: https://www.esrl.noaa.gov/psd/data/gridded/data.ghcncams.html

Feng, L., Hu, C., Han, X., Chen, X., & Qi, L. (2015). Long-term distribution patterns of chlorophyll-a concentration in China's largest freshwater lake: MERIS full-resolution observations with a practical approach. Remote Sensing, 7(1), 275-299. doi:10.3390/rs70100275

Fisher Scientific (2007). American Public Health Association (APHA) Standard Operating Procedure for: Total Suspended Solids. Fisher Scientific. Accessed on Oct 24th, 2018 at: https://beta-static.fishersci.com/content/dam/fishersci/en_US/documents/programs/scientific/technical-documents/white-papers/apha-total-suspended-solids-procedure-white-paper.pdf

Giardino, C., Pepe, M., Brivio, P. A., Ghezzi, P., & Zilioli, E. (2001). Detecting chlorophyll, secchi disk depth and surface temperature in a sub-alpine lake using Landsat imagery. Science of the Total Environment, 268(1), 19-29. doi:10.1016/S0048-9697(00)00692-6

Giblin, A., Kling, G. (1992). Chlorophyll a and primary productivity data for various lakes near Toolik Research Station, Arctic LTER. Summer 1990 to 1999. Environmental Data Initiative.

Gilabert, M.A., Conese, C., Maselli, F. (1994). An atmospheric correction method for the automatic retrieval of surface reflectances from TM images. International Journal of Remote Sensing, 15(10), 2065-2086. DOI:10.1080/01431169408954228

Gitelson, A. A., Gao, B. C., Li, R. R., Berdnikov, S., & Saprygin, V. (2011). Estimation of chlorophyll-a concentration in productive turbid waters using a Hyperspectral

Imager for the Coastal Ocean—the Azov Sea case study. Environmental Research Letters, 6(2), 024023.

Gitelson, A. A., Gritz, Y., & Merzlyak, M. N. (2003). Relationships between leaf chlorophyll content and spectral reflectance and algorithms for non-destructive chlorophyll assessment in higher plant leaves. Journal of plant physiology, 160(3), 271-282.

Gitelson, A. A., Schalles, J. F., & Hladik, C. M. (2007). Remote chlorophyll-a retrieval in turbid, productive estuaries: Chesapeake Bay case study. Remote Sensing of Environment, 109(4), 464-472.

Gons, H. J., Rijkeboer, M., & Ruddick, K. G. (2002). A chlorophyll-retrieval algorithm for satellite imagery (Medium Resolution Imaging Spectrometer) of inland and coastal waters. Journal of Plankton Research, 24(9), 947-951.

Gray, J. R., Glysson, G. D., Turcios, L. M., & Schwarz, G. E. (2000). Comparability of suspended-sediment concentration and total suspended solids data. US Geological Survey Water-Resources Investigations Report 00-4191, 20.

Guan, X. (2009). Monitoring Lake Simcoe water quality using Landsat TM images.(Master's thesis, University of Waterloo).

Guanter, L., Ruiz-Verdú, A., Odermatt, D., Giardino, C., Simis, S., Estellés, V., . . . Moreno, J. (2010). Atmospheric correction of ENVISAT/MERIS data over inland waters: Validation for european lakes. Remote Sensing of Environment, 114(3), 467-480. doi:10.1016/j.rse.2009.10.004

Ha, N., Thao, N., Koike, K., & Nhuan, M. (2017). Selecting the best band ratio to estimate chlorophyll-a concentration in a tropical freshwater lake using sentinel 2A images from a case study of Lake Ba Be (Northern Vietnam). ISPRS International Journal of Geo-Information, 6(9), 290. doi:10.3390/ijgi6090290

Han, L. & Jordan, K., (2005). Estimating and mapping chlorophyll a concentration in Pensacola Bay, Florida using Landsat ETM data. International Journal of Remote Sensing, 26, pp. 5245–5254.

Han, L., Rundquist, D. C., Liu, L. L., Fraser, R. N., & Schalles, J. F. (1994). The spectral responses of algal chlorophyll in water with varying levels of suspended sediment. International Journal of Remote Sensing, 15(18), 3707-3718.

Hanjra, M. A., & Qureshi, M. E. (2010). Global water crisis and future food security in an era of climate change. Food Policy, 35(5), 365-377.

Hambrook-Berkman, J.A., & Canova, M.G. (2007). Chapter 7.4: Algal Biomass Indicators. National Field Manual for the Collection of Water-Quality Data, USGS. Accessed on Oct 24, 2018 at: https://water.usgs.gov/owq/FieldManual/Chapter7/7.4.pdf

Hansen, J. E. and Travis, L. D. (1974) Light scattering in planetary atmospheres, Space Science Review, 16, 527–610, doi:10.1007/BF00168069.

Hellweger, F.L., Schlosser, P., Lall, U. And Weissel, J.K., (2004). Use of satellite imagery for water quality studies in New York Harbor. Estuarine, Coastal and Shelf Science, 61, pp. 437–448.

Ho, J. C., Stumpf, R. P., Bridgeman, T. B., & Michalak, A. M. (2017). Using Landsat to extend the historical record of lacustrine phytoplankton blooms: A Lake Erie case study. Remote Sensing of Environment, 191, 273-285.

Huisman, J., Codd, G. A., Paerl, H. W., Ibelings, B. W., Verspagen, J. M. H., Visser, P. M. 2018. Cyanobacterial blooms. Nature Reviews. Microbiology, 16: 471-483. https://doi.org/10.1038/s41579-018-0040-1.

International Organization for Standardization, (1999). Water quality — determination of turbidity: Geneva, Switzerland, International Organization for Standardization, ISO 7027, 10

Jeffrey, S. W., & Humphrey, G. F. (1975). New spectrophotometric equations for determining chlorophylls a, b, c1 and c2 in higher-plants, algae and natural phytoplankton. Biochemie Und Physiologie Der Pflanzen, 167, 191–194

Jones, J.W. (2015). Efficient wetland surface water detection and monitoring via Landsat: Comparison with in situ data from the Everglades Depth Estimation Network. Remote Sensing 7(9):12503-12538, doi:10.3390/rs70912503

Jorge, D., Barbosa, C., De Carvalho, L., Affonso, A., Lobo, F., Novo, E., Adriana Affonso. (2017). SNR (signal-to-noise ratio) impact on water constituent retrieval from simulated images of optically complex amazon lakes. Remote Sensing, 9(7), 644. doi:10.3390/rs9070644

Kabbara, N., Benkhelil, J., Awad, M., & Barale, V. (2008). Monitoring water quality in the coastal area of Tripoli (Lebanon) using high-resolution satellite data. ISPRS Journal of Photogrammetry and Remote Sensing, 63(5), 488-495.

Kallio, K., Attila, J., Härmä, P., Koponen, S., Pulliainen, J., Hyytiäinen, U., & Pyhälahti, T. (2008). Landsat ETM+ images in the estimation of seasonal lake water quality in boreal river basins. Environmental Management, 42(3), 511-522. doi:10.1007/s00267-008-9146-y

Kaufman, Y. J., Wald, A. E., Remer, L. A., Gao, B., Li, R., & Flynn, L. (1997). The MODIS 2.1-micrometer channel-correlation with visible reflectance for use in remote sensing of aerosol. IEEE Transactions on Geoscience and Remote Sensing, 35(5), 1286.

Kaye, C. A. (1959). Coastal Geology of Puerto Rico. US Government Printing Office.

Keith, D., Rover, J., Green, J., Zalewsky, B., Charpentier, M., Thursby, G., & Bishop, J. (2018). Monitoring algal blooms in drinking water reservoirs using the Landsat-8 operational land imager. International Journal of Remote Sensing, 39(9), 2818-2846. doi:10.1080/01431161.2018.1430912

Khalil, M. T., Saad, A. E. H. A., Fishar, M. R., & Bedir, T. Z. (2013). Ecological Studies on Macrobenthic Invertebrates of Bardawil Wetland, Egypt. World Environment, 3(1), 1-8.

Kim, H. H., Ko, B. C., & Nam, J. Y. (2016). Predicting chlorophyll-ausing Landsat 8 OLI sensor data and the non-linear RANSAC method – a case study of Nakdong River, south korea. International Journal of Remote Sensing, 37(14), 3255-3271. doi:10.1080/01431161.2016.1196839

Kloiber, S. M., Brezonik, P. L., Olmanson, L. G., & Bauer, M. E. (2002). A procedure for regional lake water clarity assessment using Landsat multispectral data. Remote Sensing of Environment, 82(1), 38-47. doi:10.1016/S0034-4257(02)00022-6

Kutser, T. (2012). The possibility of using the Landsat image archive for monitoring long time trends in coloured dissolved organic matter concentration in lake waters. Remote Sensing of Environment, 123, 334-338. doi:10.1016/j.rse.2012.04.004anagement, 42(3), 511-522. doi:10.1007/s00267-008-9146-y

Kutser, T., Pierson, D. C., Kallio, K. Y., Reinart, A., & Sobek, S. (2005). Mapping lake CDOM by satellite remote sensing. Remote Sensing of Environment, 94(4), 535-540. doi:10.1016/j.rse.2004.11.009

Lathrop, R.G. & Lillesand, T.M., (1986) Use of thematic mapper data to assess water quality in Green Bay and Central Lake Michigan. Photogrammetric Engineering and Remote Sensing, 52, pp. 671–680.

Li, Y. (2001). Calcareous soils in Miami-Dade County. University of Florida Cooperative Extension Service, Institute of Food and Agriculture Sciences, EDIS

Lim, H. S., MatJafri, M. Z., & Abdullah, K. (2009). Chlorophyll measurement from landsat TM imagery. Paper presented at the 1-4. doi:10.1109/OCEANSE.2009.5278182

Lin, S. (2017). Climate Change and Algal Blooms. Michigan State University, Doctoral Dissertation.

Lin, S., Qi, J., Jones, J. R., & Stevenson, R. J. (2018). Effects of sediments and coloured dissolved organic matter on remote sensing of chlorophyll-a using Landsat TM/ETM+ over turbid waters. International Journal of Remote Sensing, 39(5), 1421-1440.

Lobo, F. L., Costa, M. P. F., & Novo, E. M. L. M. (2015). Time-series analysis of Landsat-MSS/TM/OLI images over Amazonian waters impacted by gold mining activities. Remote Sensing of Environment, 157, 170-184. doi:10.1016/j.rse.2014.04.030

Lopez, C.B., Jewett, E.B., Dortch, Q., Walton, B.T., Hudnell, H.K. 2008. Scientific Assessment of Freshwater Harmful Algal Blooms. Interagency Working Group on Harmful Algal Blooms, Hypoxia, and Human Health of the Joint Subcommittee on Ocean Science and Technology. Washington, DC.

Lymburner, L., Botha, E., Hestir, E., Anstee, J., Sagar, S., Dekker, A., & Malthus, T. (2016). Landsat 8: Providing continuity and increased precision for measuring multi-decadal time series of total suspended matter. Remote Sensing of Environment, 185, 108-118. doi:10.1016/j.rse.2016.04.011

Martins, V., Barbosa, C., de Carvalho, L., Jorge, D., Lobo, F., & Novo, E. (2017). Assessment of atmospheric correction methods for sentinel-2 MSI images applied to amazon floodplain lakes. Remote Sensing, 9(4), 322. doi:10.3390/rs9040322

Masek, J.G., E.F. Vermote, N. Saleous, R. Wolfe, F.G. Hall, F. Huemmrich, F. Gao, J. Kutler, and T.K. Lim. (2013). LEDAPS Calibration, Reflectance, Atmospheric Correction Preprocessing Code, Version 2. ORNL DAAC, Oak Ridge, Tennessee, USA. http://dx.doi.org/10.3334/ORNLDAAC/1146

Matthews, M. W. (2011). A current review of empirical procedures of remote sensing in inland and near-coastal transitional waters. International Journal of Remote Sensing, 32(21), 6855-6899. doi:10.1080/01431161.2010.512947

Mayo, M., Gitelson, A., Yacobi, Y. Z., & Ben-Avraham, Z. (1995). Chlorophyll distribution in Lake Kinneret determined from Landsat Thematic Mapper data. Remote Sensing, 16(1), 175-182.

MECP (2017). The Chemical Water Quality of Lake Nipissing. Ontario Ministry of Environment, Conservation, and Parks. Accessed on Oct 24, 2018 at: https://www.ontario.ca/page/chemical-water-quality-lake-nipissing

Medeiros, A. S., Biastoch, R. G., Luszczek, C. E., Wang, X. A., Muir, D. C. G., & Quinlan, R. (2012). Patterns in the limnology of lakes and ponds across multiple local and regional environmental gradients in the eastern Canadian arctic. Inland Waters, 2(2), 59-76. doi:10.5268/IW-2.2.427.

Menken, K. D., Brezonik, P. L., & Bauer, M. E. (2006). Influence of chlorophyll and colored dissolved organic matter (CDOM) on lake reflectance spectra: Implications for measuring lake properties by remote sensing. Lake and Reservoir Management, 22(3), 179-190.

Mishra, N., Haque, M. O., Leigh, L., Aaron, D., Helder, D., & Markham, B. (2014). Radiometric cross calibration of Landsat 8 operational land imager (OLI) and

Landsat 7 enhanced thematic mapper plus (ETM+). Remote Sensing, 6(12), 12619-12638. doi:10.3390/rs61212619

Mobley, C. D. (1994). Light and water: Radiative transfer in natural waters. San Diego: Academic Press.

Molot, L, Watson SB, Creed, I.F., Trick, C.G., McCabe, S.K., Verschoor, M.J., Sorichetti R.J., Powe, C., Venkiteswan, J.J., & Schiff, S.L. (2014). A novel model for cyanobacteria b,loom formation: The critical role of anoxia and ferrous iron. Freshwater Biology 59: 1323-1340.

Moses, W. J., Bowles, J. H., & Corson, M. R. (2015). Expected improvements in the quantitative remote sensing of optically complex waters with the use of an optically fast hyperspectral spectrometer—a modeling study. Sensors (Switzerland), 15(3), 6152-6173. doi:10.3390/s150306152

Moses, W. J., Gitelson, A. A., Berdnikov, S., & Povazhnyy, V. (2009). Estimation of chlorophyll-a concentration in case II waters using MODIS and MERIS data—successes and challenges. Environmental Research Letters, 4(4), 045005.

Nazeer, M., Nichol, J. E., & Yung, Y. (2014). Evaluation of atmospheric correction models and Landsat surface reflectance product in an urban coastal environment. International Journal of Remote Sensing, 35(16), 6271-6291. doi:10.1080/01431161.2014.951742

O'Reilly, J. E., Maritorena, S., Mitchell, B. G., Siegel, D. A., Carder, K. L., Garver, S. A., . . . McClain, C. (1998). Ocean color chlorophyll algorithms for SeaWiFS. Journal of Geophysical Research: Oceans, 103(C11), 24937-24953. doi:10.1029/98JC02160

Olmanson, L. G., Brezonik, P. L., Finlay, J. C., & Bauer, M. E. (2016). Comparison of Landsat 8 and Landsat 7 for regional measurements of CDOM and water clarity in lakes. Remote Sensing of Environment, 185, 119-128.

Östlund, C., Flink, P., Strombeck, N., Pierson, D. And Lindell, T., (2001) Mapping of the water quality of Lake Erken, Sweden, from imaging spectrometry and Landsat Thematic Mapper. The Science of the Total Environment, 268, pp. 139–154.

Paerl, H. W., & Huisman, J. (2008). Climate: blooms like it hot. Science, 320(5872), 57-58. doi:10.1126/science.1155398

Paerl, H. W., & Otten, T. G. (2013). Harmful cyanobacterial blooms: Causes, consequences, and controls. Microbial Ecology, 65(4), 995-1010. doi:10.1007/s00248-012-0159-y

Pahlevan, N., & Schott, J. R. (2013). Leveraging EO-1 to evaluate capability of new generation of landsat sensors for coastal/inland water studies. IEEE Journal of

Selected Topics in Applied Earth Observations and Remote Sensing, 6(2), 360-374. doi:10.1109/JSTARS.2012.2235174

Pathak, V. N., Pandya, M. R., Shah, D. B., Trivedi, H. J., Patel, K. D., Sridhar, V. N., & Singh, R. P. (2014). Inter Comparison of Atmospheric Correction Models-SACRS2, FLAASH and 6SV Using Resourcesat-2 AWiFS Data. The International Archives of Photogrammetry, Remote Sensing and Spatial Information Sciences, 40(8), 881.

Patra, P. P., Dubey, S. K., Trivedi, R. K., Sahu, S. K., & Rout, S. K. (2017). Estimation of chlorophyll-a concentration and trophic states in Nalban lake of East Kolkata wetland, India from Landsat 8 OLI data. Spatial Information Research, 25(1), 75-87. doi:10.1007/s41324-016-0069-z

Pick, F. R. (2016). Blooming algae: a Canadian perspective on the rise of toxic cyanobacteria. Canadian Journal of Fisheries and Aquatic Sciences, 73(7), 1149-1158.

Potter, B.B., & Wimsatt, J.C. (2005). Method 415.3 - measurement of total organic carbon, dissolved organic carbon and specific UV absorbance at 254 nm in source water and drinking water. U.S. Environmental Protection Agency, Washington, DC.

Ritche, J. C., Cooper, C. M., & Schiebe, F. R., (1990). The relationship of MSS and TM digital data with suspended sediments, chlorophyll, and temperature in Moon Lake, Mississippi (USA). Remote Sensing of Environment, 33, 137-148.

Salem, S. I., Higa, H., Kim, H., Kobayashi, H., Oki, K., & Oki, T. (2017). Assessment of chlorophyll-a algorithms considering different trophic statuses and optimal bands. Sensors (Basel, Switzerland), 17(8), 1746. doi:10.3390/s17081746

Sass G, I.F. Creed, S.E. Bayley, and K.J. Devito. (2007) Understanding variation in trophic status of lakes on the Boreal Plain: a 20 year retrospective using Landsat TM imagery. Remote Sensing of Environment.109, 127-141.

Schaeffer, B. A., Iiames, J., Dwyer, J., Urquhart, E., Salls, W., Rover, J., & Seegers, B. (2018). An initial validation of Landsat 5 and 7 derived surface water temperature for US lakes, reservoirs, and estuaries. International Journal of Remote Sensing, 1-17.

Schalles, J. F. (2006). Optical remote sensing techniques to estimate phytoplankton chlorophyll a concentrations in coastal. In: Remote Sensing of Aquatic Coastal Ecosystem Processes. L. Richardson & E.LeDrew (eds.), Springer, Dordrecht. pp. 27-79

Schlesinger, W.H. 1997. Biogeochemistry – An Analysis of Global Change. Academic Press, Ny, NY, USA. 595 p.

Schneider, U., Becker, A., Finger, P., Meyer-Christoffer, A., Rudolf, B., & Ziese, M. (2011): GPCC Full Data Reanalysis Version 6.0 at 0.5°: Monthly Land-Surface Precipitation from Rain-Gauges built on GTS-based and Historic Data. DOI: 10.5676/DWD_GPCC/FD_M_V7_050. Last accessed on 12/05/2018 at: https://www.esrl.noaa.gov/psd/data/gridded/data.gpcc.html

Siegel, D. A., Wang, M., Maritorena, S., & Robinson, W. (2000). Atmospheric correction of satellite ocean color imagery: The black pixel assumption. Applied Optics, 39(21), 3582-3591. doi:10.1364/AO.39.003582

Simons, H., Soto, X., Zhu, Z., Singh, K.D., Bellan, M.F., Iremonger, S., Hirvonen, H., Smith, B., Watson, V., Tosi, J. and Morales, L., (2001). Global Ecological Zoning for the Global Forest Resources Assessment 2000-Final Report.

Singh, K., Ghosh, M., Sharma, S. R., & Kumar, P. (2014). Blue-red-NIR model for chlorophyll-α retrieval in hypersaline-alkaline water using Landsat ETM+ sensor. IEEE Journal of Selected Topics in Applied Earth Observations and Remote Sensing, 7(8), 3553-3559. doi:10.1109/JSTARS.2014.2340856

Slade, J. H., VanReken, T. M., Mwaniki, G. R., Bertman, S., Stirm, B., & Shepson, P. B. (2010). Aerosol production from the surface of the Great Lakes. Geophysical Research Letters, 37(18).

Sorichetti, R. J., I. F. Creed, and C. G. Trick. 2014a. Evidence for iron-regulated cyanobacterial predominance in oligotrophic lakes. Freshwater Biol. 59 (4): 679-691, doi:10.1111/fwb.12295

Sturm, B., (1981). The atmospheric correction of remotely sensed data and the quantitative determination of suspended matter in marine water surface layers. In Remote Sensing in Meteorology, Oceanography and Hydrology, edited by A. P. Cracknell (Chichester: Ellis Horwood Limited), Chapter 11.

Sudheer, K.P., Chaubey, I. & Garg, V., (2006). Lake water quality assessment from Landsat thematic mapper data using neural network: an approach to optimal band combination selection. Journal of the American Water Resources Association, 42, pp. 1683–1695.

Swedish University of Agricultural Sciences (SLU) (2018). Miljödata MVM Environmental Data. Last accessed at 11/14/2018 at URL http://miljodata.slu.se/mvm

Symons, C. C., Arnott, S. E., & Sweetman, J. N. (2012). Nutrient limitation of phytoplankton communities in subarctic lakes and ponds in Wapusk National Park, Canada. Polar Biology, 35(4), 481-489. doi:10.1007/s00300-011-1092-0

Taranu, Z. E. Gregory-Eaves, I., Leavitt, P.R., *et al*. 2015. Acceleration of cyanobacterial dominance in north temperate-subarctic lakes during the Anthropocene. Ecology Letters, 18: 375-384. doi: 10.1111/ele.12420.

Tebbs, E. J., Remedios, J. J., & Harper, D. M. (2013). Remote sensing of chlorophyll-a as a measure of cyanobacterial biomass in Lake Bogoria, a hypertrophic, saline-alkaline, flamingo lake, using Landsat ETM. Remote Sensing of Environment, 135, 92-106. doi:10.1016/j.rse.2013.03.024

Teixeira, L. C., de Paiva, J. B. D., da Silva Pereira, J. E., & de Moura Lisbôa, R. (2016). Relationship between turbidity and suspended sediment concentration from a small hydrographic basin in Santa Maria (Rio Grande do Sul, Brazil). International Journal of River Basin Management, 14(4), 393-399.

The Government of British Columbia (2018) Environmental Monitoring System (EMS) Surface water monitoring. Last accessed 11/14/2018 at URL https://www2.gov.bc.ca/gov/content/environment/research-monitoring-reporting/monitoring/environmental-monitoring-system

Toming, K., Kutser, T., Laas, A., Sepp, M., Paavel, B., & Noges, T. (2016). First experiences in mapping lake water quality parameters with sentinel-2 MSI imagery. Remote Sensing, 8(8), 640. doi:10.3390/rs8080640

Trinh, R. C., Fichot, C. G., Gierach, M. M., Holt, B., Malakar, N. K., Hulley, G., & Smith, J. (2017). Application of Landsat 8 for monitoring impacts of wastewater discharge on coastal water quality. Frontiers in Marine Science, 4, 329.

Tu, M., Smith, P., & Filippi, A. (2018). Hybrid forward-selection method-based water-quality estimation via combining Landsat TM, ETM+, and OLI/TIRS images and ancillary environmental data. PloS One, 13(7), e0201255. doi:10.1371/journal.pone.0201255

Tucker, C. J. (1979). Red and photographic infrared linear combinations for monitoring vegetation. Remote sensing of Environment, 8(2), 127-150.

Tyler, A.N., Svab, E., Preston, T., Présing, M. & Kovács, W.A., (2006). Remote sensing of the water quality of shallow lakes: a mixture modelling approach to quantifying phytoplankton in water characterized by high-suspended sediment. International Journal of Remote Sensing, 27, pp. 1521–1537.

United Nations Environment Programme (2017). GEMStat database of the Global Environment Monitoring System for freshwater (GEMS/Water) Programme. International Centre for Water Resources and Global Change, Koblenz. Accessed 26 October 2017. Available upon request from GEMS/Water Data Centre: data-request@gemstat.org

U.S. Environmental Protection Agency, (1993). Methods for the determination of inorganic substances in environmental samples: Cincinnati, Ohio, U.S. Environmental Protection Agency EPA/600/R–93/100, 178.

U.S. Geological Survey (2017). Landsat Collection 1 level 1 product definition. U.S. Geological Survey. Accessed on 12/03/2018 at:

https://landsat.usgs.gov/sites/default/files/documents/LSDS-1656_Landsat_Level-1_Product_Collection_Definition.pdf

U.S. Geological Survey (2018a), Environmental Protection Agency: Storage and Retrieval (STORET). Data available on the World Wide Web (USGS Water Data for the Nation). Last accessed 11/14/2018, at URL https://www.waterqualitydata.us/portal/

U.S. Geological Survey (2018b), National Water Information System (NWIS). Data available on the World Wide Web (USGS Water Data for the Nation). Last accessed 11/14/2018, at URL https://www.waterqualitydata.us/portal/

U.S. Geological Survey (2018c). Landsat 4-7 Surface reflectance (LEDAPS) product. U.S. Geological Surey. Accessed on 12/03/2018 at: https://landsat.usgs.gov/sites/default/files/documents/ledaps_product_guide.pdf

U.S. Geological Survey (2018d). Landsat 8 surface reflectance code (LaSRC) product. U.S. Geological Survey. Accessed on 12/03/2018 at: https://landsat.usgs.gov/sites/default/files/documents/lasrc_product_guide.pdf

Veblen, T. T., Young, K. R., & Orme, A. R. (Eds.). (2015). The Physical Geography of South America. Oxford University Press

Vermote, E.F., and El Saleous, N. (2007). LEDAPS surface reflectance product description v.2. https://landsat.usgs.gov/sites/default/files/documents/ledaps_add.pdf, last accessed November 11, 2018

Vermote, E., Justice, C., Claverie, M., & Franch, B. (2016). Preliminary analysis of the performance of the Landsat 8/OLI land surface reflectance product. Remote Sensing of Environment, 185, 46-56. doi:10.1016/j.rse.2016.04.008

Vermote E., Tanré, D., Deuzé, J. L., Herman, M., Morcrette, J. J., & Kotchenova S. Y. (2006). Second Simulation of a Satellite Signal in the Solar Spectrum - Vector (6SV). MODIS land surface reflectance science computing facility, user manual part two.

Vincent R.K., X. Qin, R.M.L. Mckay, J. Miner, K. Czajkowski, J. Savino, T. Bridgeman (2004) Phycocyanin detection from Landsat TM data for mapping cyanobacterial blooms in Lake Erie. Remote Sensing of Environment. 89, 381–392

Watts, C. D., Naden, P. S., Machell, J., & Banks, J. (2001). Long term variation in water colour from Yorkshire catchments. Science of the Total Environment, 278(1-3), 57-72.

Wang, D., Feng, X., Ma, R., Kang, G. (2007). A method for retrieving water-leaving radiance from Landsat TM image in Taihu Lake, East China. Chinese Geographical Science, 17(4), 364-369. doi:10.1007/s11769-007-0364-7

Wagner, C., & Adrian, R. (2009). Cyanobacteria dominance: Quantifying the effects of climate change. Limnology and Oceanography, 54(6, part2), 2460-2468. doi:10.4319/lo.2009.54.6_part_2.2460

Wehr, J.D., Sheath, R.G., Kociolek, J.P. (2015) Freshwater Algae of North America: Ecology and Classification. Elsevier Inc.

Winter, J. G., DeSellas, A. M., Fletcher, R., Heintsch, L., Morley, A., Nakamoto, L., Utsumi, K. (2011). Algal blooms in Ontario, Canada: Increases in reports since 1994. Lake and Reservoir Management, 27: 107-114. https://doi.org/10.1080/07438141.2011.557765.

Yacobi, Y. Z., Yacobi, Y. Z., Gitelson, A., Gitelson, A., Mayo, M., & Mayo, M. (1995). Remote sensing of chlorophyll in Lake Kinneret using high spectral-resolution radiometer and Landsat TM: Spectral features of reflectance and algorithm development. Journal of Plankton Research, 17(11), 2155-2173. doi:10.1093/plankt/17.11.2155

Yip, H. D., Johansson, J., & Hudson, J. J. (2015;2014;). A 29-year assessment of the water clarity and chlorophyll-a concentration of a large reservoir: Investigating spatial and temporal changes using Landsat imagery. Journal of Great Lakes Research, 41, 34-44. doi:10.1016/j.jglr.2014.11.022

Young, A. T. (1980). Revised depolarization corrections for atmospheric extinction. Applied Optics, 19(20), 3427. doi:10.1364/AO.19.003427

Young, A. T. (1981). Rayleigh scattering. Applied optics, 20(4), 533-535.

Appendices

Appendix A: Supplementary information on Landsat remote sensing studies

Table A1: Chronological overview of Landsat remote sensing of phytoplankton biomass. B1 = Band 1, B2 = Band 2, B3 = Band 3, B4 = Band 4, and B5 = Band 5.

Author	Year	Satellite	Bands	# Lakes	Locations	Modelled Parameters	Atmospheric Correction Method	Statistical Model	Highest Chl-*a* R^2
Carpenter S.M, & Carpenter D.J.	1983	Landsat 1 MSS	B4, B5	1	Canberra, Australia	Chl-*a*	Rad	MLR	0.90
Almanza, E., & Melack J.M.	1984	Landsat 1 MSS	B4	1	Yosemite National Park, CA	Chl-*a* SD	Rad	None	0.42
Lathrop, R.G., & Lillesand, T.M	1986	Landsat 5 TM	B2	1	Green Bay/ Lake Michigan	Chl-*a* Turb SWT SD	Rad	Power	0.99
Ritchie, J.C., *et al*.	1990	Landsat 1 MSS Landsat 5 TM	B1	1	Moon Lake, MS	Chl-*a* TSS	Rad	Linear	0.51
Yacobi Y.Z., *et al*.	1995	Landsat 5 TM	B4 ⁄ B3	1	Lake Kinneret, Israel	Chl-*a* SD	Rad	Linear	0.98
Allee, R.J., & Johnson, J.E.	1999	Landsat 5 TM	B1, B2, B3, B5	1	Bull Shoals Reservoir, AR	Chl-*a* SD	DP-H	SW Polynomial	0.8 (SW) 0.84 (Polynomial)
Östlund C., *et al*.	2001	Landsat 5 TM	B2	1	Lake Erken, Sweden	Chl-*a* TSS	6S	Linear	0.93
Giardino, C., *et al*.	2001	Landsat 5 TM	B1 − B2	1	Lombardia, Italy	Chl-*a* SD SWT	DOS	Linear	0.99
Kloiber, S.M., *et al*.	2002	Landsat 5 TM	B1	450	Twin City, MN	Chl-*a* SD	Rad	MSW	0.95
Hellweger, F.L., *et al*.	2004	Landsat 5 TM	B2 ⁄ B3	1	New York Harbor, NY	Chl-*a* SD	Rad	Linear	0.78
Han L. & Jordan K.J.	2005	Landsat 7 ETM+	B1 ⁄ B3	1	Pensacola Bay, FL	Chl-*a* TSS	COST	Linear	0.67

Author	Year	Satellite	Bands	# Lakes	Locations	Modelled Parameters	Atmospheric Correction Method	Statistical Model	Highest Chl-*a* R^2
Brezonik, P., *et al*.	2005	Landsat 5 TM	B3 + B1⁄B3	15	East-Central Minnesota	Chl-*a* CDOM	Rad	Linear	0.89
Tyler, A.N., *et al*.	2006	Landsat 5 TM	B3	1	Lake Balaton, Hungary	Chl-*a* TSS	DOS	Multivariate	0.95
Sudheer, K.P., *et al*.	2006	Landsat 5 TM	B1⁄B2	1	Beaver Lake, AR	Chl-*a* TSS	Rad	ANN	0.31
Sass, G.Z. *et al*.	2007	Landsat 5 TM Landsat 7 ETM+	B3⁄B1	76	Utikuma Uplands, AB	Chl-*a*	Rad	Linear	0.83
Duan, H., *et al*.	2007	Landsat 5 TM	B4⁄B3	1	Lake Chagan, China	Chl-*a*	FLAASH	Linear	0.69
Alparslan, E., *et al*.	2007	Landsat 7 ETM+	B1, B2, B3, B4	1	Ömerli Dam, Turkey	Chl-*a* TSS SD	DOS	MLR	0.92
Chen L., *et al*.	2008	Landsat 7 ETM+	B1, B4, B5, B7	1	Feitsui Reservoir, Taiwan	Chl-*a*	DN	GEGA MLR	0.89 (GEGA) 0.82 (MLR)
Lim, H.S., *et al*.	2009	Landsat 5 TM	N/A	1	Penang Island, Malaysia	Chl-*a*	ATCOR2	Two-Term Par	0.83
Allan M.G., *et al*.	2011	Landsat 7 ETM+	B3	10	Rotorua lakes, New Zealand	Chl-*a* SD Turb	6S COST DOS	Linear	0.89
Tebbs E.J., *et al*.	2013	Landsat 7 ETM+	B4⁄B1	1	Eastern Rift Valley, Kenya	Chl-*a* TSS/ISS SD	FLAASH	Linear	0.88
Singh, K., *et al*.	2014	Landsat 7 ETM+	B3 − B1 × B4	1	Sambhar Lake, India	Chl-*a*	DOS	Linear	0.88
Allan, M.G., *et al*.	2015	Landsat 7 ETM+	B3	12	Rotorua lakes, New Zealand	Chl-*a* SD Turb	MODTRAN 4	Semi-*a*nalytic Linear	0.68 (SA) 0.68 (Linear)
Yip, H.D., *et al*.	2015	Landsat 4 TM Landsat 5 TM Landsat 7 EMT+	B4 + B3	1	Lake Diefenbaker, SK	Chl-*a* SD	DOS	Linear MLR (SD)	0.58
Kim, H.H., *et al*.	2016	Landsat 8 OLI	B4 − B2 × B5	1	Nakdong River, South Korea	Chl-*a*	FLAASH	NL-RANSAC	0.89

Author	**Year**	**Satellite**	**Bands**	**# Lakes**	**Locations**	**Modelled Parameters**	**Atmospheric Correction Method**	**Statistical Model**	**Highest Chl-*a* R^2**
Fadel, A., *et al*.	2016	Landsat 8 OLI	B2 ⁄ B4 × B5	1	Karaoun Reservoir, Lebanon	Chl-*a*	FLAASH	Linear	0.72
Patra, P.P., *et al*.,	2017	Landsat 8 OLI	B5 ⁄ B4	1	Nalban Lake, India	Chl-*a*	DOS	Linear	0.85
Lin, S.	2017	Landsat 5 TM Landsat 7 ETM+ Landsat 8 OLI	Ratios of all bands (no thermal bands)	1157	Continental USA	Chl-*a* CDOM TSS SWT	6S	BRT RF MLR GAM	0.33

Satellites: ETM+ = Enhanced Thematic Mapper Plus, MSS = Multispectral Scanner System, OLI = Operational Land Imager, TM = Thematic Mapper.
Modelled Parameters: CDOM = Coloured Dissolved Organic Matter, Chl-*a* = Chlorophyll-*a*, ISS = Inorganic Suspended Solids, SD = Secchi Disk Depth, SWT = Surface Water Temperature, TSS = Total Suspended Solids
Atmospheric Correction Method: 6S = 6S Radiative Transfer Code, ATCOR2 = Atmospheric Correction for Flat Terrain, COST = Cosine of the Zenith Angle Method, DOS = Dark Object Subtraction, DP-H = Dark Pixel Haze Correction, FLAASH = Fast Line-of-sight Atmospheric Analysis of Hypercubes, MODTRAN4 = Moderate Resolution Transmission Model, Rad = Radiometric Correction/Rectification, DN = Digital Numbers
Regression Methods: ANN = Artificial Neural Networks, BRT = Boosted Regression Trees, GAM = Generalized Additive Model ,GEGA = Grammatical Evolution and Genetic Algorithm, MLR = Multiple Linear Regression, MSW = Multiple Step-wise Regression, NL-RANSAC = Non-Linear Random Sample Consensus Model, RF = Random Forest Model, SW = Step-wise Regression, Two-Term Par = Two-Term Parameter Equation

Appendix B: Landsat scene WRS codes

Table B1: WRS Landsat scenes used in this study, number of images per scene, and number of chl-*a* samples per image

Region	WRS	Chl-a samples (n)	Images (n)	WRS	Chl-a samples (n)	Images (n)
PTW	P:073 R:012	8	4	P:019 R:023	1	1
	P:018 R:024	2	1	P:047 R:018	4	1
	P:019 R:021	2	1	P:069 R:017	1	1
BCF	P:194 R:014	4	4	P:042 R:022	12	11
	P:194 R:015	10	5	P:043 R:020	4	1
TCF	P:028 R:027	7	4	P:022 R:027	1	1
	P:025 R:028	31	13	P:052 R:022	1	1
	P:046 R:026	2	2	P:048 R:026	6	3
	P:018 R:029	14	8	P:050 R:022	1	1
	P:048 R:023	2	2	P:044 R:021	15	2
	P:048 R:024	2	2			
TPS	P:027 R:033	18	14	P:033 R:032	6	5
TPD	P:037 R:032	7	5	P:041 R:032	1	1
	P:041 R:030	1	1	P:042 R:033	1	1
	P:043 R:028	1	1	P:043 R:033	1	1
	P:043 R:029	4	4	P:044 R:028	1	1
	P:038 R:032	10	10	P:045 R:025	1	1
	P:039 R:034	1	1	P:045 R:026	1	1
SHF	P:016 R:040	23	6	P:016 R:041	13	5
TMF	P:225 R:079	7	7	P:005 R:047	1	1
	P:015 R:042	22	22			

Table B2: WRS Landsat scenes used in this study, number of images per scene, and number of true colour samples per image

Region	WRS	True Colour samples (n)	Images (n)	WRS	True Colour samples (n)	Images (n)
PTW	P:035 R:018	1	1	P:033 R:019	1	1
	P:033 R:016	6	1	P:033 R:017	4	1
	P:033 R:018	3	1	P:036 R:015	3	1
BCF	P:195 R:018	28	8			
TCF	P:018 R:029	34	17			

TPD	P:048 R:026	2	2	P:041 R:032	3	3
	P:028 R:027	7	4	P:042 R:033	4	4
	P:050 R:022	1	1	P:039 R:034	1	1
	P:041 R:031	3	3	P:043 R:032	2	2
SHF	P:043 R:033	1	1	P:016 R:041	17	3
	P:016 R:040	17	4			
TMF	P:015 R:042	14	6			

Table B3: WRS Landsat scenes used in this study, number of images per scene, and number of TSS samples per image

Region	**WRS**	**TSS samples (n)**	**Images (n)**	**WRS**	**TSS samples (n)**	**Images (n)**
TCF	P:025 R:028	5	2	P:028 R:027	13	3
TPS	P:028 R:027	32	3	P:028 R:029	8	4
TPD	P:043 R:033	7	6	P:043 R:028	1	1
	P:045 R:029	2	2	P:041 R:032	1	1
	P:041 R:031	2	2	P:042 R:033	4	4
SHF	P:016 R:040	26	4	P:016 R:041	2	2
TMF	P:015 R:042	15	9	P:015 R:041	1	1

Table B4: WRS Landsat scenes used in this study, number of images per scene, and number of turbidity samples per image

Region	**WRS**	**Turbidity samples (n)**	**Images (n)**	**WRS**	**Turbidity samples (n)**	**Images (n)**
BCF	P:194 R:015	16	1			
TCF	P:052 R:022	3	2	P:048 R:026	9	3
	P:044 R:026	1	1	P:050 R:022	1	1
	P:048 R:024	1	1	P:025 R:028	5	1
	P:048 R:025	1	1			
TPS	P:027 R:035	1	1	P:027 R:031	1	1
	P:032 R:027	8	5	P:030 R:029	1	1
	P:027 R:034	1	1	P:028 R:030	3	3
	P:028 R:029	5	5	P:028 R:031	4	2
	P:031 R:027	2	2	P:029 R:030	1	1
	P:032 R:029	2	2	P:029 R:034	1	1
	P:036 R:027	1	1	P:033 R:032	2	2
	P:043 R:028	5	4			

TPD	P:041 R:030	3	3	P:043 R:029	1	1
	P:041 R:032	3	3	P:043 R:032	1	1
	P:042 R:033	4	4	P:044 R:028	1	1
	P:036 R:032	1	1	P:045 R:029	2	2
	P:037 R:032	1	1	P:036 R:034	1	1
	P:041 R:031	2	2			
SHF	P:016 R:040	19	3	P:016 R:041	16	2
TMF	P:015 R:042	16	6			

Appendix C: Comparison of TOA reflectance and partial atmospheric correction (PAC)

Table C1: Comparison of TOA reflectance and partial atmospheric correction (PAC) method as proposed in this study. Average path radiance contributed by Rayleigh scattering measured by total radiance measured by the sensor. Chl-*a* data set.

Region	Band	TOA Reflectance	PAC Reflectance	Difference	Avg. Rayleigh Radiance [W/(m^2×srad×µm)]	n
PTW	Blue	-0.06	-0.04	0.02	21.26 (66%)	18
	Green	0.35	0.41	0.06	10.96 (59%)	
	Red	0.53	0.56	0.03	5.42 (52%)	
	NIR	0.80	0.81	0.01	1.51 (23%)	
BCF	Blue	-0.32	0.25	0.56	18.73 (63%)	30
	Green	0.56	0.77	0.20	9.64 (53%)	
	Red	0.75	0.83	0.08	4.90 (50%)	
	NIR	0.80	0.80	0.00	1.33 (21%)	
TCF	Blue	0.56	0.60	0.04	21.55 (62%)	82
	Green	0.67	0.66	-0.01	11.11 (53%)	
	Red	0.68	0.69	0.01	5.49 (48%)	
	NIR	0.54	0.54	0.00	1.49 (19%)	
TPS	Blue	0.45	0.46	0.00	24.74 (49%)	24
	Green	0.45	0.45	0.00	12.55 (33%)	
	Red	0.40	0.40	0.00	6.29 (26%)	
	NIR	0.51	0.51	0.00	1.70 (11%)	
TPD	Blue	0.17	0.21	0.05	22.78 (63%)	30
	Green	0.54	0.57	0.03	11.63 (43%)	
	Red	0.45	0.46	0.01	5.81 (37%)	
	NIR	0.73	0.73	0.00	1.60 (21%)	
SHF	Blue	0.59	0.59	-0.01	25.73 (51%)	36
	Green	0.77	0.77	-0.01	13.03 (38%)	
	Red	0.80	0.80	0.00	6.54 (34%)	
	NIR	0.64	0.65	0.00	1.69 (15%)	
TMF	Blue	0.38	0.44	0.07	23.90 (50%)	30
	Green	0.09	0.12	0.03	12.24 (39%)	
	Red	0.22	0.24	0.02	6.06 (32%)	
	NIR	0.71	0.72	0.00	1.67 (20%)	

Table C2: Comparison of TOA reflectance and partial atmospheric correction (PAC) method as proposed in this study. Average path radiance contributed by Rayleigh scattering measured by total radiance measured by the sensor. True colour data set.

Region	Band	TOA Reflectance	PAC Reflectance	Difference	Avg. Rayleigh Radiance [W/(m^2×srad ×µm)]	n
PTW	Blue	-0.03	-0.01	0.02	23.03 (60%)	18
	Green	-0.31	-0.30	0.01	11.67 (47%)	
	Red	-0.20	-0.19	0.01	5.89 (41%)	
	NIR	0.03	0.04	0.00	1.61 (22%)	
BCF	Blue	0.48	0.23	-0.25	18.24 (65%)	28
	Green	0.34	-0.10	-0.44	9.46 (64%)	
	Red	0.31	-0.14	-0.45	4.79 (61%)	
	NIR	-0.40	-0.49	-0.09	1.16 (39%)	
TCF	Blue	-0.01	-0.02	-0.01	22.13 (64%)	44
	Green	-0.05	-0.06	-0.01	11.24 (57%)	
	Red	0.01	0.00	-0.01	5.68 (54%)	
	NIR	-0.06	-0.06	0.00	1.49 (21%)	
TPD	Blue	0.55	0.56	0.01	22.92 (54%)	16
	Green	0.78	0.78	0.00	11.78 (37%)	
	Red	0.84	0.84	0.00	5.81 (29%)	
	NIR	0.60	0.60	0.00	1.61 (21%)	
SHF	Blue	-0.16	-0.17	-0.01	24.98 (51%)	34
	Green	-0.32	-0.33	0.00	12.65 (39%)	
	Red	-0.21	-0.21	0.00	6.36 (35%)	
	NIR	-0.06	-0.05	0.01	1.71 (16%)	
TMF	Blue	-0.17	-0.17	0.00	25.55 (45%)	14
	Green	-0.35	-0.35	0.00	12.92 (31%)	
	Red	-0.34	-0.34	0.00	6.49 (23%)	
	NIR	-0.10	-0.10	0.00	1.77 (8%)	

Table C3: Comparison of TOA reflectance and partial atmospheric correction (PAC) method as proposed in this study. Average path radiance contributed by Rayleigh scattering measured by total radiance measured by the sensor. TSS data set.

Region	Band	TOA Reflectance	PAC Reflectance	Difference	Avg. Rayleigh Radiance [W/(m^2×srad ×µm)]	n

BCF	Blue	-0.29	-0.29	0.00	15.18 (69%)	16
	Green	-0.16	-0.16	0.00	7.87 (70%)	
	Red	0.44	0.44	0.00	4.17 (74%)	
	NIR	0.20	0.20	0.00	0.95 (59%)	
TCF	Blue	-0.16	-0.05	0.11	21.36 (68%)	21
	Green	0.61	0.66	0.05	10.90 (60%)	
	Red	0.59	0.68	0.09	5.49 (56%)	
	NIR	-0.14	-0.10	0.04	1.51 (26%)	
TPS	Blue	-0.09	-0.06	0.03	24.08 (54%)	37
	Green	0.17	0.18	0.01	12.27 (39%)	
	Red	0.33	0.34	0.01	6.12 (34%)	
	NIR	0.49	0.49	0.00	1.67 (15%)	
TPD	Blue	0.33	0.34	0.00	23.90 (54%)	21
	Green	0.50	0.50	0.00	12.24 (39%)	
	Red	0.54	0.53	0.00	06.06 (34%)	
	NIR	0.25	0.25	0.00	01.67 (21%)	
SHF	Blue	0.18	0.18	-0.01	24.50 (52%)	35
	Green	0.51	0.51	-0.01	12.41 (40%)	
	Red	0.55	0.54	-0.01	6.24 (36%)	
	NIR	0.11	0.11	0.00	1.68 (17%)	
TMF	Blue	0.15	0.13	-0.01	24.50 (47%)	16
	Green	0.22	0.21	-0.01	12.46 (37%)	
	Red	0.27	0.27	0.00	6.23 (29%)	
	NIR	0.28	0.28	0.00	1.64 (12%)	

Table C4: Comparison of TOA reflectance and partial atmospheric correction (PAC) method as proposed in this study. Average path radiance contributed by Rayleigh scattering measured by total radiance measured by the sensor. Turbidity data set.

Region	Band	TOA Reflectance	PAC Reflectance	Difference	Avg. Rayleigh Radiance [W/(m^2×srad ×µm)]	n
TCF	Blue	-0.01	-0.04	-0.03	24.31 (63%)	18
	Green	0.31	0.27	-0.04	12.33 (53%)	
	Red	0.33	0.31	-0.02	6.20 (48%)	
	NIR	-0.21	-0.21	0.00	1.61 (17%)	
TPS	Blue	0.36	0.34	-0.02	24.74 (60%)	27
	Green	0.69	0.69	0.00	12.55 (46%)	
	Red	0.71	0.71	0.00	6.30 (40%)	

	NIR	0.25	0.25	0.01	1.60 (15%)	
TPD	Blue	0.46	0.46	0.00	25.87 (55%)	17
	Green	0.66	0.66	0.00	13.16 (38%)	
	Red	0.67	0.67	0.00	6.55 (31%)	
	NIR	0.06	0.05	0.00	1.79 (17%)	
SHF	Blue	0.11	0.11	0.00	23.99 (53%)	28
	Green	0.67	0.67	0.00	12.15 (41%)	
	Red	0.64	0.64	0.00	6.12 (37%)	
	NIR	0.34	0.34	0.00	1.65 (17%)	
TMF	Blue	0.12	0.17	0.05	23.17 (51%)	16
	Green	0.24	0.27	0.03	11.88 (43%)	
	Red	0.31	0.31	0.01	5.89 (35%)	
	NIR	0.31	0.32	0.01	1.56 (16%)	

Appendix D: Results summary tables

Table D1: Chl-*a* algorithm results summary. Constituent free region indicates the corresponding constituents are not statistically significant (true colour, TSS and turbidity) (P>0.05) with the algorithm

Algorithm	**Regression**	**Range**	**Average**	**Median**	**# Constituent Free Regions**
Blue	Linear	0.04 - 0.60	0.37	0.44	4
	Exponential	0.04 - 0.55	0.26	0.19	2
	Logarithmic	0.00 - 0.57	0.35	0.36	4
	Power	0.02 - 0.52	0.29	0.26	2
Green	Linear	0.12 - 0.77	0.53	0.57	1
	Exponential	0.46 - 0.79	0.60	0.57	3
	Logarithmic	0.08 - 0.75	0.51	0.56	1
	Power	0.47 - 0.79	0.61	0.62	4
Red	Linear	0.24 - 0.83	0.57	0.56	2
	Exponential	0.32 - 0.87	0.60	0.64	2
	Logarithmic	0.17 - 0.77	0.53	0.53	2
	Power	0.35 - 0.84	0.62	0.64	3
NIR	Linear	0.51 - 0.81	0.68	0.72	4
	Exponential	0.44 - 0.86	0.61	0.56	4
	Logarithmic	0.46 - 0.72	0.62	0.62	4
	Power	0.44 - 0.81	0.62	0.62	4
B×G	Linear	0.18 - 0.73	0.49	0.43	1
	Exponential	0.22 - 0.67	0.45	0.42	2
	Logarithmic	0.20 - 0.70	0.48	0.48	2
	Power	0.34 - 0.67	0.52	0.53	2
B×R	Linear	0.30 - 0.78	0.53	0.43	2
	Exponential	0.13 - 0.75	0.47	0.38	2
	Logarithmic	0.25 - 0.74	0.51	0.47	2
	Power	0.26 - 0.75	0.54	0.52	3
B×NIR	Linear	0.47 - 0.79	0.63	0.64	6
	Exponential	0.32 - 0.70	0.52	0.55	5
	Logarithmic	0.52 - 0.72	0.58	0.57	5
	Power	0.31 - 0.73	0.56	0.56	4
G×R	Linear	0.25 - 0.81	0.56	0.46	1
	Exponential	0.35 - 0.81	0.55	0.51	2
	Logarithmic	0.12 - 0.77	0.53	0.53	2
	Power	0.42 - 0.83	0.62	0.60	4

G×NIR	Linear	0.12 - 0.77	0.53	0.57	1
	Exponential	0.46 - 0.79	0.60	0.57	3
	Logarithmic	0.08 - 0.75	0.51	0.56	1
	Power	0.47 - 0.79	0.61	0.62	4
R×NIR	Linear	0.42 - 0.84	0.70	0.71	3
	Exponential	0.25 - 0.82	0.58	0.63	3
	Logarithmic	0.47 - 0.74	0.61	0.63	4
	Power	0.13 - 0.81	0.60	0.67	3
B⁄G	Linear	0.08 - 0.75	0.49	0.57	1
	Exponential	0.02 - 0.81	0.62	0.71	1
	Logarithmic	0.09 - 0.75	0.51	0.60	0
	Power	0.00 - 0.82	0.63	0.73	1
B⁄R	Linear	0.10 - 0.78	0.47	0.51	1
	Exponential	0.26 - 0.84	0.64	0.68	1
	Logarithmic	0.11 - 0.79	0.51	0.56	1
	Power	0.21 - 0.86	0.66	0.70	1
B⁄NIR	Linear	0.24 - 0.72	0.48	0.45	4
	Exponential	0.24 - 0.77	0.55	0.56	3
	Logarithmic	0.27 - 0.77	0.53	0.52	3
	Power	0.27 - 0.82	0.58	0.52	4
G⁄B	Linear	0.10 - 0.77	0.52	0.61	0
	Exponential	0.01 - 0.83	0.63	0.75	1
	Logarithmic	0.09 - 0.75	0.51	0.60	0
	Power	0.00 - 0.82	0.63	0.73	1
G⁄R	Linear	0.23 - 0.49	0.36	0.38	2
	Exponential	0.29 - 0.66	0.44	0.38	2
	Logarithmic	0.21 - 0.51	0.36	0.38	2
	Power	0.25 - 0.66	0.44	0.38	2
G⁄NIR	Linear	0.07 - 0.46	0.31	0.40	1
	Exponential	0.03 - 0.83	0.37	0.39	1
	Logarithmic	0.04 - 0.54	0.33	0.42	0
	Power	0.03 - 0.82	0.37	0.48	2
R⁄B	Linear	0.08 - 0.83	0.53	0.58	1
	Exponential	0.15 - 0.90	0.66	0.69	1
	Logarithmic	0.11 - 0.79	0.51	0.56	1
	Power	0.21 - 0.86	0.66	0.70	1
R⁄G	Linear	0.19 - 0.53	0.36	0.39	2
	Exponential	0.22 - 0.66	0.43	0.38	2
	Logarithmic	0.21 - 0.51	0.36	0.38	2

	Power	0.25 - 0.66	0.44	0.38	2
R⁄NIR	Linear	0.01 - 0.43	0.28	0.30	1
	Exponential	0.03 - 0.80	0.36	0.36	1
	Logarithmic	0.03 - 0.48	0.29	0.32	1
	Power	0.05 - 0.78	0.36	0.33	1
NIR⁄B	Linear	0.25 - 0.81	0.56	0.58	3
	Exponential	0.26 - 0.85	0.58	0.54	4
	Logarithmic	0.27 - 0.77	0.53	0.52	3
	Power	0.27 - 0.82	0.58	0.52	4
NIR⁄G	Linear	0.00 - 0.60	0.32	0.40	1
	Exponential	0.01 - 0.73	0.35	0.45	2
	Logarithmic	0.04 - 0.54	0.33	0.42	0
	Power	0.03 - 0.82	0.37	0.48	2
NIR⁄R	Linear	0.05 - 0.53	0.29	0.33	0
	Exponential	0.09 - 0.68	0.35	0.33	1
	Logarithmic	0.03 - 0.48	0.29	0.32	1
	Power	0.05 - 0.78	0.36	0.33	1
B×G×R[1]	Linear	0.26 - 0.76	0.52	0.43	2
	Exponential	0.15 - 0.72	0.45	0.34	2
	Logarithmic	0.19 - 0.75	0.51	0.47	1
	Power	0.35 - 0.78	0.57	0.52	3
B×G×NIR[1]	Linear	0.43 - 0.78	0.63	0.69	4
	Exponential	0.22 - 0.70	0.50	0.55	4
	Logarithmic	0.43 - 0.76	0.58	0.56	5
	Power	0.04 - 0.77	0.55	0.60	4
B×R×NIR[1]	Linear	0.41 - 0.81	0.64	0.72	4
	Exponential	0.24 - 0.71	0.50	0.61	3
	Logarithmic	0.46 - 0.75	0.58	0.56	5
	Power	0.08 - 0.78	0.56	0.58	3
G×R×NIR[1]	Linear	0.12 - 0.77	0.53	0.57	1
	Exponential	0.46 - 0.79	0.60	0.57	3
	Logarithmic	0.08 - 0.75	0.51	0.56	1
	Power	0.47 - 0.79	0.61	0.62	4
Avg(B;G)[1,2]	Linear	0.23 - 0.72	0.49	0.46	1
	Exponential	0.29 - 0.67	0.49	0.47	2
	Logarithmic	0.20 - 0.70	0.48	0.48	2
	Power	0.33 - 0.67	0.51	0.53	2
Avg(B;R)[1,2]	Linear	0.29 - 0.73	0.51	0.44	2
	Exponential	0.19 - 0.67	0.48	0.44	2

	Logarithmic	0.26 - 0.72	0.50	0.47	2
	Power	0.25 - 0.67	0.51	0.51	2
Avg(B;NIR)[1,2]	Linear	0.50 - 0.79	0.62	0.61	5
	Exponential	0.24 - 0.70	0.53	0.55	4
	Logarithmic	0.53 - 0.77	0.59	0.54	5
	Power	0.19 - 0.72	0.54	0.55	4
Avg(G;R)[1,2]	Linear	0.18 - 0.81	0.55	0.52	2
	Exponential	0.40 - 0.83	0.60	0.55	3
	Logarithmic	0.12 - 0.76	0.53	0.53	2
	Power	0.42 - 0.82	0.62	0.60	4
Avg(G;NIR)[1,2]	Linear	0.48 - 0.84	0.66	0.69	3
	Exponential	0.03 - 0.81	0.58	0.64	3
	Logarithmic	0.34 - 0.77	0.60	0.65	3
	Power	0.12 - 0.81	0.60	0.68	3
Avg(R;NIR)[1,2]	Linear	0.47 - 0.84	0.66	0.63	4
	Exponential	0.09 - 0.83	0.58	0.61	3
	Logarithmic	0.42 - 0.75	0.60	0.62	4
	Power	0.01 - 0.81	0.58	0.66	3
N-R[3,4]	Linear	0.08 - 0.68	0.40	0.44	2
	Exponential	0.00 - 0.81	0.39	0.42	2
	Logarithmic	0.00 - 0.00	0.00	N/A	0
	Power	0.00 - 0.00	0.00	N/A	0
Kab1[5,6]	Linear	0.14 - 0.75	0.51	0.57	0
	Exponential	0.05 - 0.82	0.63	0.74	1
	Logarithmic	0.13 - 0.72	0.45	0.53	0
	Power	0.03 - 0.80	0.58	0.68	0
NDVI	Linear	0.03 - 0.49	0.29	0.32	1
	Exponential	0.05 - 0.78	0.36	0.33	1
	Logarithmic	0.00 - 0.00	0.00	N/A	0
	Power	0.00 - 0.00	0.00	N/A	0
NRVI	Linear	0.03 - 0.49	0.29	0.32	1
	Exponential	0.05 - 0.78	0.36	0.33	1
	Logarithmic	0.00 - 0.00	0.00	N/A	0
	Power	0.00 - 0.00	0.00	N/A	0
OC2[7]	Linear	0.11 - 0.74	0.50	0.60	1
	Exponential	0.03 - 0.80	0.62	0.75	2
	Logarithmic	0.07 - 0.07	0.07	0.07	0
	Power	0.03 - 0.03	0.03	0.03	0
SABI[5,8]	Linear	0.02 - 0.61	0.32	0.40	2

	Exponential	0.03 - 0.73	0.37	0.44	2
	Logarithmic	0.00 - 0.00	0.00	N/A	0
	Power	0.00 - 0.00	0.00	N/A	0
(B-R)/G[4,9]	Linear	0.09 - 0.79	0.49	0.54	1
	Exponential	0.18 - 0.85	0.66	0.69	2
	Logarithmic	0.48 - 0.89	0.72	0.80	0
	Power	0.62 - 0.90	0.80	0.87	0
(NIR/G)+(NIR/B)	Linear	0.14 - 0.70	0.46	0.44	2
	Exponential	0.12 - 0.73	0.47	0.46	2
	Logarithmic	0.18 - 0.64	0.45	0.43	2
	Power	0.14 - 0.77	0.48	0.51	2
G×(B+G+R)	Linear	0.26 - 0.76	0.53	0.47	1
	Exponential	0.33 - 0.74	0.53	0.44	1
	Logarithmic	0.13 - 0.75	0.51	0.52	1
	Power	0.42 - 0.78	0.59	0.57	4
[(1/B)-(1/G)]×NIR[10]	Linear	0.08 - 0.76	0.47	0.63	1
	Exponential	0.00 - 0.81	0.55	0.65	3
	Logarithmic	0.00 - 0.00	0.00	N/A	0
	Power	0.00 - 0.00	0.00	N/A	0
[(1/R)-(1/G)]×NIR[10]	Linear	0.01 - 0.40	0.17	0.10	0
	Exponential	0.02 - 0.46	0.27	0.25	0
	Logarithmic	0.03 - 0.39	0.22	0.19	0
	Power	0.12 - 0.45	0.35	0.37	0
[(1/R)-(1/B)]×NIR[10]	Linear	0.05 - 0.73	0.43	0.56	0
	Exponential	0.02 - 0.80	0.54	0.62	1
	Logarithmic	0.35 - 0.73	0.57	0.62	0
	Power	0.49 - 0.72	0.64	0.70	0
[(1/R)-(0.2363×(1/G))]×NIR[11]	Linear	0.03 - 0.51	0.28	0.29	1
	Exponential	0.12 - 0.65	0.35	0.32	1
	Logarithmic	0.06 - 0.47	0.28	0.28	1
	Power	0.08 - 0.77	0.36	0.35	1
(R^-1-B^-1)/NIR[12]	Linear	0.05 - 0.73	0.33	0.33	2
	Exponential	0.02 - 0.80	0.44	0.54	2
	Logarithmic	0.58 - 0.83	0.73	0.80	0
	Power	0.64 - 0.87	0.79	0.86	0
(B/R)×NIR	Linear	0.31 - 0.71	0.47	0.41	3
	Exponential	0.21 - 0.56	0.38	0.41	1
	Logarithmic	0.24 - 0.60	0.43	0.43	2
	Power	0.14 - 0.66	0.39	0.39	1

(G⁄R)×NIR	Linear	0.46 - 0.78	0.66	0.66	5
	Exponential	0.39 - 0.79	0.59	0.59	5
	Logarithmic	0.41 - 0.74	0.61	0.58	5
	Power	0.37 - 0.74	0.59	0.67	5
(R⁄B)×NIR	Linear	0.39 - 0.90	0.72	0.78	2
	Exponential	0.29 - 0.91	0.64	0.70	2
	Logarithmic	0.48 - 0.78	0.63	0.70	3
	Power	0.22 - 0.87	0.64	0.72	2
(R⁄G)×NIR	Linear	0.42 - 0.82	0.67	0.67	4
	Exponential	0.39 - 0.89	0.60	0.57	4
	Logarithmic	0.47 - 0.72	0.61	0.63	4
	Power	0.48 - 0.83	0.63	0.58	4
(R×NIR)⁄B[13]	Linear	0.39 - 0.90	0.72	0.78	2
	Exponential	0.29 - 0.91	0.64	0.70	2
	Logarithmic	0.48 - 0.78	0.63	0.70	3
	Power	0.22 - 0.87	0.64	0.72	2
(B⁄G)×(B⁄R)	Linear	0.07 - 0.78	0.45	0.48	0
	Exponential	0.20 - 0.86	0.63	0.66	0
	Logarithmic	0.03 - 0.79	0.51	0.59	0
	Power	0.13 - 0.86	0.67	0.73	1
(B⁄G)×(B⁄NIR)	Linear	0.28 - 0.76	0.49	0.49	2
	Exponential	0.27 - 0.86	0.56	0.56	2
	Logarithmic	0.34 - 0.86	0.57	0.59	2
	Power	0.29 - 0.91	0.61	0.63	2
(B⁄G)×(R⁄G)	Linear	0.11 - 0.53	0.37	0.44	1
	Exponential	0.17 - 0.68	0.45	0.50	2
	Logarithmic	0.10 - 0.53	0.38	0.45	1
	Power	0.17 - 0.71	0.46	0.50	3
(B⁄G)×(R⁄NIR)	Linear	0.17 - 0.68	0.43	0.42	3
	Exponential	0.12 - 0.67	0.47	0.53	2
	Logarithmic	0.16 - 0.75	0.47	0.46	4
	Power	0.13 - 0.75	0.50	0.51	3
(B⁄G)×(NIR⁄B)	Linear	0.00 - 0.60	0.32	0.40	1
	Exponential	0.01 - 0.73	0.35	0.45	2
	Logarithmic	0.04 - 0.54	0.33	0.42	0
	Power	0.03 - 0.82	0.37	0.48	2
(B⁄G)×(NIR⁄G)	Linear	0.04 - 0.46	0.27	0.27	0
	Exponential	0.00 - 0.71	0.34	0.40	0
	Logarithmic	0.02 - 0.48	0.25	0.24	0

	Power	0.02 - 0.84	0.35	0.39	0
(B⁄G)×(NIR⁄R)	Linear	0.03 - 0.57	0.29	0.29	0
	Exponential	0.18 - 0.69	0.41	0.37	1
	Logarithmic	0.11 - 0.56	0.30	0.27	0
	Power	0.21 - 0.83	0.44	0.36	1
(B⁄R)×(B⁄NIR)	Linear	0.28 - 0.72	0.48	0.48	2
	Exponential	0.34 - 0.85	0.57	0.59	2
	Logarithmic	0.34 - 0.84	0.58	0.61	2
	Power	0.36 - 0.91	0.63	0.68	2
(B⁄R)×(G⁄R)	Linear	0.06 - 0.71	0.43	0.44	1
	Exponential	0.21 - 0.79	0.57	0.62	1
	Logarithmic	0.04 - 0.74	0.48	0.49	1
	Power	0.25 - 0.86	0.60	0.63	1
(B⁄R)×(G⁄NIR)	Linear	0.26 - 0.69	0.48	0.47	2
	Exponential	0.30 - 0.77	0.57	0.56	2
	Logarithmic	0.33 - 0.76	0.55	0.55	2
	Power	0.35 - 0.84	0.60	0.59	2
(B⁄R)×(NIR⁄R)	Linear	0.26 - 0.64	0.34	0.30	0
	Exponential	0.25 - 0.75	0.48	0.48	2
	Logarithmic	0.26 - 0.61	0.35	0.29	1
	Power	0.25 - 0.78	0.51	0.46	1
(B⁄NIR)×(G⁄NIR)	Linear	0.16 - 0.51	0.36	0.40	2
	Exponential	0.14 - 0.75	0.43	0.51	1
	Logarithmic	0.19 - 0.65	0.45	0.43	2
	Power	0.16 - 0.77	0.48	0.51	1
(B⁄NIR)×(R⁄NIR)	Linear	0.13 - 0.50	0.34	0.39	2
	Exponential	0.08 - 0.75	0.38	0.48	1
	Logarithmic	0.13 - 0.63	0.42	0.44	2
	Power	0.08 - 0.75	0.44	0.53	1
(G⁄B)×(G⁄R)	Linear	0.08 - 0.54	0.38	0.43	3
	Exponential	0.17 - 0.72	0.46	0.48	3
	Logarithmic	0.10 - 0.53	0.38	0.45	1
	Power	0.17 - 0.71	0.46	0.50	3
(G⁄B)×(G⁄NIR)	Linear	0.02 - 0.45	0.22	0.19	0
	Exponential	0.00 - 0.85	0.33	0.35	1
	Logarithmic	0.02 - 0.48	0.25	0.24	0
	Power	0.02 - 0.84	0.35	0.39	0
(G⁄B)×(R⁄B)	Linear	0.01 - 0.86	0.53	0.61	1
	Exponential	0.07 - 0.89	0.66	0.71	1

	Logarithmic	0.03 - 0.79	0.51	0.59	0
	Power	0.13 - 0.86	0.67	0.73	1
(G/B)×(R/NIR)	Linear	0.11 - 0.53	0.27	0.20	1
	Exponential	0.17 - 0.82	0.42	0.34	1
	Logarithmic	0.11 - 0.56	0.30	0.27	0
	Power	0.21 - 0.83	0.44	0.36	1
(G/B)×(NIR/B)	Linear	0.29 - 0.92	0.61	0.62	2
	Exponential	0.30 - 0.92	0.61	0.64	3
	Logarithmic	0.34 - 0.86	0.57	0.59	2
	Power	0.29 - 0.91	0.61	0.63	2
(G/B)×(NIR/R)	Linear	0.13 - 0.80	0.49	0.47	3
	Exponential	0.13 - 0.80	0.50	0.48	3
	Logarithmic	0.16 - 0.75	0.47	0.46	4
	Power	0.13 - 0.75	0.50	0.51	3
(G/R)×(G/NIR)	Linear	0.08 - 0.46	0.34	0.42	0
	Exponential	0.00 - 0.80	0.40	0.47	2
	Logarithmic	0.11 - 0.55	0.37	0.39	1
	Power	0.02 - 0.80	0.41	0.44	1
(G/R)×(NIR/R)	Linear	0.05 - 0.37	0.24	0.27	0
	Exponential	0.03 - 0.55	0.30	0.29	1
	Logarithmic	0.01 - 0.41	0.24	0.28	1
	Power	0.04 - 0.70	0.31	0.31	1
(G/NIR)×(R/NIR)	Linear	0.06 - 0.44	0.28	0.32	1
	Exponential	0.05 - 0.78	0.34	0.31	1
	Logarithmic	0.04 - 0.52	0.31	0.40	1
	Power	0.01 - 0.81	0.36	0.40	1
(R/B)×(R/G)	Linear	0.01 - 0.81	0.49	0.54	1
	Exponential	0.15 - 0.89	0.60	0.66	1
	Logarithmic	0.04 - 0.74	0.48	0.49	1
	Power	0.25 - 0.86	0.60	0.63	1
(R/B(×(R/NIR)	Linear	0.18 - 0.56	0.32	0.26	1
	Exponential	0.25 - 0.75	0.47	0.41	1
	Logarithmic	0.26 - 0.61	0.35	0.29	1
	Power	0.25 - 0.78	0.51	0.46	1
(R/B)×(NIR/B)	Linear	0.24 - 0.91	0.63	0.66	2
	Exponential	0.30 - 0.92	0.62	0.69	2
	Logarithmic	0.34 - 0.84	0.58	0.61	2
	Power	0.36 - 0.91	0.63	0.68	2
(R/B)×(NIR/G)	Linear	0.30 - 0.80	0.58	0.61	3

	Exponential	0.34 - 0.87	0.59	0.61	2
	Logarithmic	0.33 - 0.76	0.55	0.55	2
	Power	0.35 - 0.84	0.60	0.59	2
(R⁄G)×(R⁄NIR)	Linear	0.02 - 0.38	0.23	0.28	1
	Exponential	0.04 - 0.72	0.31	0.29	1
	Logarithmic	0.01 - 0.41	0.24	0.28	1
	Power	0.04 - 0.70	0.31	0.31	1
(R⁄G)×(NIR⁄G)	Linear	0.13 - 0.62	0.37	0.33	1
	Exponential	0.04 - 0.72	0.38	0.36	1
	Logarithmic	0.11 - 0.55	0.37	0.39	1
	Power	0.02 - 0.80	0.41	0.44	1
(NIR⁄B)×(NIR⁄G)	Linear	0.08 - 0.70	0.46	0.45	2
	Exponential	0.09 - 0.77	0.45	0.41	2
	Logarithmic	0.19 - 0.65	0.45	0.43	2
	Power	0.16 - 0.77	0.48	0.51	1
(NIR⁄B)×(NIR⁄R)	Linear	0.04 - 0.69	0.43	0.40	3
	Exponential	0.04 - 0.73	0.42	0.46	1
	Logarithmic	0.13 - 0.63	0.42	0.44	2
	Power	0.08 - 0.75	0.44	0.53	1
(NIR⁄G)×(NIR⁄R)	Linear	0.04 - 0.59	0.29	0.41	0
	Exponential	0.06 - 0.57	0.33	0.45	2
	Logarithmic	0.04 - 0.52	0.31	0.40	1
	Power	0.01 - 0.81	0.36	0.40	1

(1) Fadel *et al.*, 2016; (2) Patra *et al.*, 2015; (3) Tucker, 1979; (4) Ho *et al.*, 2017; (5) Boucher ***et al.,*** 2018; (6) Kabbara ***et al.,*** 2008; (7) Trinh **et a**l., 2017; (8) Alawadi *et al.*, 2010; (9) Mayo *et al.*, 1995; (10) Keith *et al.*, 2018; (11) Chen *et al.*, 2013; (12) Singh *et a.l*, 2014; Guan *et al.*, 2009.

Kab1 = 1.67-3.94×ln(B)+3.78×ln(G)
NDVI = (NIR-R)⁄(NIR+R)
NRVI = [(R⁄NIRIR)-1]⁄[(R⁄NIRIR)+1)
SABI = (NIR-R)⁄(B+G)

$$\boldsymbol{OC2 = 0.1977 + \left(-1.8117\left(log_{10}\left(\frac{B}{G}\right)\right)\right)^{1} + \left(1.9743\left(log_{10}\left(\frac{B}{G}\right)\right)\right)^{2} + \left(2.5635\left(log_{10}\left(\frac{B}{G}\right)\right)\right)^{3} + \left(-0.7218\left(log_{10}\left(\frac{B}{G}\right)\right)\right)^{4}}$$

Table D2: True colour algorithm results summary. Constituent free region indicates the corresponding constituents (chl-*a*) are not statistically significant (P>0.05) with the algorithm

Algorithm	**Regression**	**Range**	**Average**	**Median**	**# Constituent Free Regions**
Blue	Linear	0.01 - 0.54	0.19	0.17	0
	Exponential	0.08 - 0.47	0.20	0.14	0
	Logarithmic	0.02 - 0.53	0.20	0.17	0
	Power	0.03 - 0.44	0.19	0.14	0
Green	Linear	0.06 - 0.77	0.32	0.32	0
	Exponential	0.02 - 0.72	0.29	0.25	0
	Logarithmic	0.04 - 0.79	0.34	0.35	0
	Power	0.03 - 0.77	0.31	0.30	0
Red	Linear	0.00 - 0.84	0.29	0.20	0
	Exponential	0.05 - 0.78	0.27	0.15	0
	Logarithmic	0.01 - 0.86	0.29	0.21	0
	Power	0.02 - 0.86	0.26	0.13	0
NIR	Linear	0.04 - 0.56	0.22	0.08	0
	Exponential	0.00 - 0.60	0.24	0.14	0
	Logarithmic	0.03 - 0.66	0.25	0.11	0
	Power	0.01 - 0.72	0.29	0.19	0
B×G	Linear	0.00 - 0.66	0.22	0.19	1
	Exponential	0.04 - 0.60	0.22	0.18	1
	Logarithmic	0.08 - 0.70	0.28	0.26	0
	Power	0.02 - 0.64	0.26	0.23	0
B×R	Linear	0.02 - 0.73	0.22	0.15	1
	Exponential	0.01 - 0.65	0.21	0.13	1
	Logarithmic	0.03 - 0.77	0.25	0.17	0
	Power	0.03 - 0.74	0.23	0.14	0
B×NIR	Linear	0.00 - 0.52	0.19	0.12	0
	Exponential	0.02 - 0.50	0.20	0.14	0
	Logarithmic	0.04 - 0.67	0.23	0.13	0
	Power	0.00 - 0.67	0.23	0.16	0
G×R	Linear	0.01 - 0.78	0.29	0.23	0
	Exponential	0.11 - 0.69	0.27	0.17	0
	Logarithmic	0.05 - 0.83	0.31	0.28	0
	Power	0.01 - 0.83	0.28	0.21	0
G×NIR	Linear	0.06 - 0.77	0.32	0.32	0

	Exponential	0.02 - 0.72	0.29	0.25	0
	Logarithmic	0.04 - 0.79	0.34	0.35	0
	Power	0.03 - 0.77	0.31	0.30	0
R×NIR	Linear	0.01 - 0.73	0.26	0.19	0
	Exponential	0.03 - 0.67	0.26	0.20	0
	Logarithmic	0.07 - 0.79	0.28	0.18	0
	Power	0.01 - 0.82	0.28	0.22	0
B⁄G	Linear	0.21 - 0.70	0.44	0.41	0
	Exponential	0.24 - 0.82	0.44	0.38	0
	Logarithmic	0.21 - 0.70	0.44	0.41	0
	Power	0.22 - 0.80	0.43	0.40	0
B⁄R	Linear	0.03 - 0.78	0.31	0.22	0
	Exponential	0.02 - 0.90	0.30	0.24	0
	Logarithmic	0.03 - 0.84	0.33	0.27	0
	Power	0.01 - 0.92	0.31	0.28	0
B⁄NIR	Linear	0.11 - 0.68	0.28	0.18	0
	Exponential	0.07 - 0.70	0.33	0.25	0
	Logarithmic	0.12 - 0.65	0.27	0.17	0
	Power	0.07 - 0.67	0.31	0.26	0
G⁄B	Linear	0.20 - 0.69	0.43	0.41	0
	Exponential	0.20 - 0.78	0.42	0.40	0
	Logarithmic	0.21 - 0.70	0.44	0.41	0
	Power	0.22 - 0.80	0.43	0.40	0
G⁄R	Linear	0.04 - 0.88	0.34	0.25	1
	Exponential	0.04 - 0.95	0.40	0.26	1
	Logarithmic	0.07 - 0.90	0.35	0.26	1
	Power	0.07 - 0.94	0.41	0.27	1
G⁄NIR	Linear	0.01 - 0.69	0.35	0.41	1
	Exponential	0.14 - 0.71	0.34	0.28	1
	Logarithmic	0.02 - 0.66	0.37	0.44	1
	Power	0.12 - 0.68	0.34	0.29	1
R⁄B	Linear	0.02 - 0.88	0.35	0.31	0
	Exponential	0.03 - 0.91	0.31	0.28	0
	Logarithmic	0.03 - 0.84	0.33	0.27	0
	Power	0.01 - 0.92	0.31	0.28	0
R⁄G	Linear	0.10 - 0.91	0.36	0.26	1
	Exponential	0.10 - 0.93	0.41	0.29	1
	Logarithmic	0.07 - 0.90	0.35	0.26	1
	Power	0.07 - 0.94	0.41	0.27	1

R⁄NIR	Linear	0.21 - 0.68	0.44	0.43	1
	Exponential	0.13 - 0.71	0.35	0.28	0
	Logarithmic	0.23 - 0.65	0.45	0.46	1
	Power	0.15 - 0.67	0.36	0.30	1
NIR⁄B	Linear	0.11 - 0.61	0.23	0.17	0
	Exponential	0.03 - 0.63	0.27	0.24	0
	Logarithmic	0.12 - 0.65	0.27	0.17	0
	Power	0.07 - 0.67	0.31	0.26	0
NIR⁄G	Linear	0.04 - 0.60	0.37	0.46	1
	Exponential	0.10 - 0.62	0.34	0.30	1
	Logarithmic	0.02 - 0.66	0.37	0.44	1
	Power	0.12 - 0.68	0.34	0.29	1
NIR⁄R	Linear	0.23 - 0.59	0.45	0.49	1
	Exponential	0.19 - 0.61	0.36	0.32	1
	Logarithmic	0.23 - 0.65	0.45	0.46	1
	Power	0.15 - 0.67	0.36	0.30	1
B×G×R[1]	Linear	0.04 - 0.71	0.24	0.18	1
	Exponential	0.09 - 0.62	0.23	0.13	1
	Logarithmic	0.04 - 0.78	0.28	0.24	0
	Power	0.00 - 0.75	0.25	0.18	0
B×G×NIR[1]	Linear	0.02 - 0.58	0.22	0.19	0
	Exponential	0.10 - 0.54	0.23	0.17	0
	Logarithmic	0.08 - 0.72	0.27	0.22	0
	Power	0.08 - 0.72	0.26	0.19	0
B×R×NIR[1]	Linear	0.01 - 0.65	0.22	0.17	0
	Exponential	0.06 - 0.58	0.22	0.18	1
	Logarithmic	0.06 - 0.77	0.25	0.18	0
	Power	0.01 - 0.77	0.24	0.17	0
G×R×NIR[1]	Linear	0.06 - 0.77	0.32	0.32	0
	Exponential	0.02 - 0.72	0.29	0.25	0
	Logarithmic	0.04 - 0.79	0.34	0.35	0
	Power	0.03 - 0.77	0.31	0.30	0
Avg(B;G)[1,2]	Linear	0.04 - 0.69	0.26	0.22	0
	Exponential	0.05 - 0.63	0.25	0.19	1
	Logarithmic	0.08 - 0.70	0.28	0.24	0
	Power	0.01 - 0.65	0.26	0.21	0
Avg(B;R)[1,2]	Linear	0.01 - 0.75	0.24	0.15	1
	Exponential	0.08 - 0.68	0.23	0.14	1
	Logarithmic	0.03 - 0.76	0.26	0.17	0

	Power	0.03 - 0.71	0.24	0.17	1
Avg(B;NIR)[1,2]	Linear	0.02 - 0.59	0.17	0.11	0
	Exponential	0.03 - 0.56	0.17	0.08	0
	Logarithmic	0.02 - 0.64	0.18	0.10	0
	Power	0.02 - 0.62	0.17	0.06	0
Avg(G;R)[1,2]	Linear	0.04 - 0.81	0.31	0.27	0
	Exponential	0.05 - 0.75	0.28	0.19	0
	Logarithmic	0.05 - 0.83	0.32	0.29	0
	Power	0.02 - 0.82	0.29	0.22	0
Avg(G;NIR)[1,2]	Linear	0.07 - 0.73	0.29	0.22	0
	Exponential	0.01 - 0.71	0.28	0.24	0
	Logarithmic	0.12 - 0.76	0.30	0.22	0
	Power	0.11 - 0.78	0.30	0.25	0
Avg(R;NIR)[1,2]	Linear	0.04 - 0.80	0.27	0.17	0
	Exponential	0.00 - 0.76	0.26	0.21	0
	Logarithmic	0.06 - 0.81	0.27	0.16	0
	Power	0.02 - 0.83	0.28	0.21	0
N-R[3,4]	Linear	0.12 - 0.80	0.39	0.31	1
	Exponential	0.07 - 0.69	0.29	0.17	1
	Logarithmic	0.17 - 0.17	0.00	0.17	0
	Power	0.05 - 0.05	0.00	0.05	0
Kab1[5,6]	Linear	0.21 - 0.66	0.43	0.42	0
	Exponential	0.24 - 0.77	0.43	0.39	0
	Logarithmic	0.30 - 0.67	0.53	0.57	0
	Power	0.36 - 0.80	0.52	0.46	0
NDVI	Linear	0.23 - 0.64	0.45	0.46	1
	Exponential	0.15 - 0.67	0.36	0.30	0
	Logarithmic	0.33 - 0.33	0.00	0.33	0
	Power	0.10 - 0.10	0.00	0.10	0
NRVI	Linear	0.23 - 0.64	0.45	0.46	1
	Exponential	0.15 - 0.67	0.36	0.30	1
	Logarithmic	0.00 - 0.00	0.00	N/A	0
	Power	0.00 - 0.00	0.00	N/A	0
OC2[7]	Linear	0.21 - 0.66	0.41	0.39	0
	Exponential	0.25 - 0.74	0.40	0.36	0
	Logarithmic	0.34 - 0.34	0.34	0.34	1
	Power	0.40 - 0.40	0.40	0.40	1
SABI[5,8]	Linear	0.19 - 0.76	0.46	0.44	2
	Exponential	0.22 - 0.67	0.37	0.25	1

	Logarithmic	0.33 - 0.33	0.00	0.33	1
	Power	0.09 - 0.09	0.00	0.09	1
(B-R)⁄G[4,9]	Linear	0.07 - 0.84	0.39	0.31	0
	Exponential	0.10 - 0.92	0.36	0.31	0
	Logarithmic	0.08 - 0.38	0.26	0.30	0
	Power	0.07 - 0.40	0.19	0.12	0
(NIR⁄G)+(NIR⁄B)	Linear	0.12 - 0.61	0.32	0.31	1
	Exponential	0.10 - 0.64	0.31	0.23	1
	Logarithmic	0.12 - 0.67	0.34	0.30	1
	Power	0.08 - 0.69	0.34	0.29	1
G×(B+G+R)	Linear	0.00 - 0.73	0.26	0.24	0
	Exponential	0.06 - 0.66	0.25	0.18	0
	Logarithmic	0.02 - 0.79	0.31	0.30	0
	Power	0.03 - 0.76	0.28	0.25	0
[(1⁄B)-(1⁄G)]×NIR[10]	Linear	0.06 - 0.55	0.39	0.44	0
	Exponential	0.06 - 0.57	0.38	0.42	0
	Logarithmic	0.00 - 0.00	0.00	N/A	1
	Power	0.00 - 0.00	0.00	N/A	0
[(1⁄R)-(1⁄G)]×NIR[10]	Linear	0.06 - 0.88	0.37	0.33	2
	Exponential	0.16 - 0.89	0.45	0.46	2
	Logarithmic	0.01 - 0.45	0.26	0.23	1
	Power	0.09 - 0.50	0.33	0.47	1
[(1⁄R)-(1⁄B)]×NIR[10]	Linear	0.24 - 0.83	0.44	0.37	0
	Exponential	0.05 - 0.90	0.42	0.39	0
	Logarithmic	0.23 - 0.42	0.31	0.27	0
	Power	0.06 - 0.44	0.28	0.35	0
[(1⁄R)-(0.2363×(1⁄G))]×NIR[11]	Linear	0.25 - 0.61	0.45	0.49	2
	Exponential	0.10 - 0.60	0.36	0.33	0
	Logarithmic	0.25 - 0.68	0.46	0.46	1
	Power	0.08 - 0.66	0.36	0.32	1
(R^-1-B^-1)⁄NIR[12]	Linear	0.04 - 0.62	0.27	0.24	0
	Exponential	0.05 - 0.77	0.28	0.17	0
	Logarithmic	0.07 - 0.38	0.24	0.27	0
	Power	0.06 - 0.38	0.17	0.06	0
(B⁄R)×NIR	Linear	0.02 - 0.44	0.19	0.19	0
	Exponential	0.00 - 0.44	0.16	0.10	0
	Logarithmic	0.00 - 0.46	0.17	0.12	0
	Power	0.00 - 0.46	0.16	0.10	0
(G⁄R)×NIR	Linear	0.02 - 0.52	0.21	0.16	0

	Exponential	0.09 - 0.53	0.25	0.20	0
	Logarithmic	0.04 - 0.59	0.26	0.20	0
	Power	0.07 - 0.59	0.30	0.25	0
(R⁄B)×NIR	Linear	0.04 - 0.82	0.30	0.18	0
	Exponential	0.02 - 0.80	0.31	0.24	0
	Logarithmic	0.08 - 0.78	0.29	0.16	0
	Power	0.07 - 0.85	0.33	0.23	0
(R⁄G)×NIR	Linear	0.02 - 0.71	0.23	0.08	0
	Exponential	0.04 - 0.71	0.28	0.20	0
	Logarithmic	0.06 - 0.76	0.26	0.10	0
	Power	0.03 - 0.81	0.31	0.24	0
(R×NIR)⁄B[13]	Linear	0.04 - 0.82	0.30	0.18	0
	Exponential	0.02 - 0.80	0.31	0.24	0
	Logarithmic	0.08 - 0.78	0.29	0.16	0
	Power	0.07 - 0.85	0.33	0.23	0
(B⁄G)×(B⁄R)	Linear	0.05 - 0.72	0.36	0.31	0
	Exponential	0.12 - 0.86	0.35	0.26	0
	Logarithmic	0.06 - 0.80	0.39	0.32	0
	Power	0.08 - 0.89	0.36	0.34	0
(B⁄G)×(B⁄NIR)	Linear	0.03 - 0.61	0.29	0.22	0
	Exponential	0.08 - 0.71	0.34	0.21	0
	Logarithmic	0.08 - 0.60	0.30	0.23	0
	Power	0.09 - 0.64	0.34	0.22	0
(B⁄G)×(R⁄G)	Linear	0.21 - 0.60	0.48	0.52	0
	Exponential	0.12 - 0.63	0.47	0.53	0
	Logarithmic	0.20 - 0.59	0.47	0.51	0
	Power	0.11 - 0.62	0.46	0.52	0
(B⁄G)×(R⁄NIR)	Linear	0.08 - 0.74	0.24	0.17	0
	Exponential	0.01 - 0.76	0.26	0.20	0
	Logarithmic	0.08 - 0.70	0.24	0.16	0
	Power	0.01 - 0.73	0.25	0.19	0
(B⁄G)×(NIR⁄B)	Linear	0.04 - 0.60	0.37	0.46	1
	Exponential	0.10 - 0.62	0.34	0.30	1
	Logarithmic	0.02 - 0.66	0.37	0.44	1
	Power	0.12 - 0.68	0.34	0.29	1
(B⁄G)×(NIR⁄G)	Linear	0.04 - 0.73	0.47	0.52	2
	Exponential	0.14 - 0.58	0.42	0.46	1
	Logarithmic	0.03 - 0.65	0.45	0.50	2
	Power	0.14 - 0.53	0.41	0.47	1

(B⁄G)×(NIR⁄R)	Linear	0.17 - 0.83	0.51	0.51	2
	Exponential	0.28 - 0.85	0.46	0.40	1
	Logarithmic	0.16 - 0.83	0.48	0.45	3
	Power	0.26 - 0.81	0.43	0.39	2
(B⁄R)×(B⁄NIR)	Linear	0.00 - 0.61	0.20	0.06	0
	Exponential	0.03 - 0.76	0.31	0.21	0
	Logarithmic	0.04 - 0.65	0.25	0.10	0
	Power	0.09 - 0.77	0.33	0.19	0
(B⁄R)×(G⁄R)	Linear	0.09 - 0.76	0.23	0.13	0
	Exponential	0.03 - 0.90	0.29	0.14	0
	Logarithmic	0.06 - 0.88	0.28	0.20	0
	Power	0.09 - 0.94	0.33	0.22	0
(B⁄R)×(G⁄NIR)	Linear	0.04 - 0.60	0.32	0.28	0
	Exponential	0.01 - 0.75	0.37	0.37	0
	Logarithmic	0.06 - 0.60	0.32	0.26	0
	Power	0.02 - 0.73	0.36	0.35	0
(B⁄R)×(NIR⁄R)	Linear	0.25 - 0.87	0.48	0.44	3
	Exponential	0.05 - 0.95	0.42	0.39	1
	Logarithmic	0.26 - 0.90	0.46	0.41	2
	Power	0.05 - 0.90	0.39	0.33	2
(B⁄NIR)×(G⁄NIR)	Linear	0.06 - 0.71	0.35	0.32	1
	Exponential	0.04 - 0.74	0.35	0.33	1
	Logarithmic	0.13 - 0.66	0.34	0.30	1
	Power	0.09 - 0.69	0.33	0.29	1
(B⁄NIR)×(R⁄NIR)	Linear	0.01 - 0.74	0.28	0.25	0
	Exponential	0.00 - 0.76	0.25	0.19	0
	Logarithmic	0.07 - 0.69	0.31	0.30	0
	Power	0.06 - 0.71	0.26	0.23	0
(G⁄B)×(G⁄R)	Linear	0.19 - 0.58	0.45	0.49	0
	Exponential	0.09 - 0.62	0.44	0.51	0
	Logarithmic	0.20 - 0.59	0.47	0.51	0
	Power	0.11 - 0.62	0.46	0.52	0
(G⁄B)×(G⁄NIR)	Linear	0.02 - 0.56	0.42	0.48	2
	Exponential	0.12 - 0.55	0.38	0.41	1
	Logarithmic	0.03 - 0.65	0.45	0.50	2
	Power	0.14 - 0.53	0.41	0.47	1
(G⁄B)×(R⁄B)	Linear	0.08 - 0.84	0.39	0.36	0
	Exponential	0.05 - 0.86	0.35	0.32	0
	Logarithmic	0.06 - 0.80	0.39	0.32	0

	Power	0.08 - 0.89	0.36	0.34	0
(G⁄B)×(R⁄NIR)	Linear	0.15 - 0.80	0.45	0.44	2
	Exponential	0.21 - 0.75	0.39	0.35	2
	Logarithmic	0.16 - 0.83	0.48	0.45	3
	Power	0.26 - 0.81	0.43	0.39	2
(G⁄B)×(NIR⁄B)	Linear	0.13 - 0.58	0.28	0.24	0
	Exponential	0.09 - 0.61	0.30	0.25	0
	Logarithmic	0.08 - 0.60	0.30	0.23	0
	Power	0.09 - 0.64	0.34	0.22	0
(G⁄B)×(NIR⁄R)	Linear	0.08 - 0.65	0.23	0.14	0
	Exponential	0.03 - 0.68	0.24	0.18	0
	Logarithmic	0.08 - 0.70	0.24	0.16	0
	Power	0.01 - 0.73	0.25	0.19	0
(G⁄R)×(G⁄NIR)	Linear	0.00 - 0.63	0.42	0.52	1
	Exponential	0.10 - 0.65	0.43	0.46	1
	Logarithmic	0.01 - 0.61	0.42	0.52	1
	Power	0.09 - 0.63	0.43	0.48	2
(G⁄R)×(NIR⁄R)	Linear	0.06 - 0.78	0.44	0.46	3
	Exponential	0.20 - 0.77	0.41	0.36	3
	Logarithmic	0.05 - 0.83	0.44	0.41	3
	Power	0.15 - 0.78	0.40	0.33	3
(G⁄NIR)×(R⁄NIR)	Linear	0.10 - 0.71	0.39	0.38	1
	Exponential	0.18 - 0.74	0.32	0.26	0
	Logarithmic	0.16 - 0.66	0.42	0.42	1
	Power	0.22 - 0.68	0.34	0.28	0
(R⁄B)×(R⁄G)	Linear	0.03 - 0.92	0.30	0.21	0
	Exponential	0.12 - 0.90	0.34	0.28	0
	Logarithmic	0.06 - 0.88	0.28	0.20	0
	Power	0.09 - 0.94	0.33	0.22	0
(R⁄B(×(R⁄NIR)	Linear	0.25 - 0.86	0.42	0.36	1
	Exponential	0.05 - 0.80	0.35	0.33	1
	Logarithmic	0.26 - 0.90	0.46	0.41	2
	Power	0.05 - 0.90	0.39	0.33	1
(R⁄B)×(NIR⁄B)	Linear	0.07 - 0.56	0.25	0.13	0
	Exponential	0.07 - 0.61	0.30	0.19	0
	Logarithmic	0.04 - 0.65	0.25	0.10	0
	Power	0.09 - 0.77	0.33	0.19	0
(R⁄B)×(NIR⁄G)	Linear	0.06 - 0.57	0.29	0.26	0
	Exponential	0.04 - 0.62	0.32	0.31	0

	Logarithmic	0.06 - 0.60	0.32	0.26	0
	Power	0.02 - 0.73	0.36	0.35	0
(R⁄G)×(R⁄NIR)	Linear	0.04 - 0.82	0.43	0.36	3
	Exponential	0.11 - 0.74	0.38	0.30	2
	Logarithmic	0.05 - 0.83	0.44	0.41	3
	Power	0.15 - 0.78	0.40	0.33	2
(R⁄G)×(NIR⁄G)	Linear	0.00 - 0.60	0.41	0.49	1
	Exponential	0.04 - 0.65	0.40	0.46	1
	Logarithmic	0.01 - 0.61	0.42	0.52	1
	Power	0.09 - 0.63	0.43	0.48	2
(NIR⁄B)×(NIR⁄G)	Linear	0.06 - 0.54	0.30	0.30	0
	Exponential	0.13 - 0.57	0.28	0.17	1
	Logarithmic	0.13 - 0.66	0.34	0.30	1
	Power	0.09 - 0.69	0.33	0.29	1
(NIR⁄B)×(NIR⁄R)	Linear	0.09 - 0.55	0.30	0.32	1
	Exponential	0.05 - 0.58	0.24	0.19	0
	Logarithmic	0.07 - 0.69	0.31	0.30	0
	Power	0.06 - 0.71	0.26	0.23	0
(NIR⁄G)×(NIR⁄R)	Linear	0.15 - 0.60	0.41	0.46	1
	Exponential	0.13 - 0.54	0.33	0.32	1
	Logarithmic	0.16 - 0.66	0.42	0.42	1
	Power	0.22 - 0.68	0.34	0.28	0

(1) Fadel *et al*., 2016; (2) Patra *et al*., 2015; (3) Tucker, 1979; (4) Ho *et al.*, 2017; (5) Boucher ***et al.,*** 2018; (6) Kabbara ***et al.,*** 2008; (7) Trinh *et al*., 2017; (8) Alawadi *et al*, 2010; (9) Mayo *et al*, 1995; (10) Keith *et al*, 2018; (11) Chen *et al*., 2013; (12) Singh *et al*., 2014; Guan *et al*., 2009.

Kab1 = 1.67-3.94×ln(B)+3.78×ln(G)
NDVI = (NIR-R)⁄(NIR+R)
NRVI = [(R⁄NIRIR)-1]⁄[(R⁄NIRIR)+1)
SABI = (NIR-R)⁄(B+G)

$$\boldsymbol{OC2 = 0.1977 + \left(-1.8117\left(log_{10}\left(\frac{B}{G}\right)\right)\right)^{1} + \left(1.9743\left(log_{10}\left(\frac{B}{G}\right)\right)\right)^{2} + \left(2.5635\left(log_{10}\left(\frac{B}{G}\right)\right)\right)^{3} + \left(-0.7218\left(log_{10}\left(\frac{B}{G}\right)\right)\right)^{4}}$$

Table D3: TSS algorithm results summary. Constituent free region indicates the corresponding constituents (chl-*a*, true colour) are not statistically significant (P>0.05) with the algorithm

Algorithm	Regression	Range	Average	Median	# Constituent Free Regions
Blue	Linear	0.04 - 0.46	0.22	0.17	0
	Exponential	0.01 - 0.42	0.18	0.14	0
	Logarithmic	0.01 - 0.40	0.21	0.18	0
	Power	0.03 - 0.43	0.17	0.11	0
Green	Linear	0.27 - 0.69	0.51	0.66	0
	Exponential	0.19 - 0.76	0.45	0.48	0
	Logarithmic	0.26 - 0.62	0.47	0.58	0
	Power	0.18 - 0.72	0.42	0.43	0
Red	Linear	0.31 - 0.71	0.53	0.64	1
	Exponential	0.26 - 0.80	0.46	0.41	1
	Logarithmic	0.30 - 0.65	0.47	0.49	0
	Power	0.25 - 0.77	0.41	0.34	0
NIR	Linear	0.05 - 0.34	0.23	0.25	0
	Exponential	0.03 - 0.28	0.16	0.18	0
	Logarithmic	0.07 - 0.32	0.21	0.20	0
	Power	0.04 - 0.25	0.15	0.11	0
B×G	Linear	0.09 - 0.63	0.41	0.53	0
	Exponential	0.06 - 0.64	0.35	0.39	0
	Logarithmic	0.14 - 0.52	0.37	0.41	0
	Power	0.09 - 0.61	0.31	0.28	0
B×R	Linear	0.12 - 0.68	0.43	0.52	0
	Exponential	0.10 - 0.69	0.37	0.37	1
	Logarithmic	0.16 - 0.56	0.38	0.41	0
	Power	0.13 - 0.66	0.32	0.27	0
B×NIR	Linear	0.16 - 0.34	0.26	0.26	0
	Exponential	0.11 - 0.24	0.18	0.17	0
	Logarithmic	0.14 - 0.28	0.23	0.24	0
	Power	0.04 - 0.21	0.13	0.16	0
G×R	Linear	0.24 - 0.77	0.55	0.71	0
	Exponential	0.24 - 0.78	0.47	0.51	1
	Logarithmic	0.29 - 0.64	0.47	0.54	0
	Power	0.22 - 0.75	0.42	0.34	0
G×NIR	Linear	0.27 - 0.69	0.51	0.66	0

	Exponential	0.19 - 0.76	0.45	0.48	0
	Logarithmic	0.26 - 0.62	0.47	0.58	0
	Power	0.18 - 0.72	0.42	0.43	0
R×NIR	Linear	0.05 - 0.67	0.40	0.47	0
	Exponential	0.06 - 0.54	0.31	0.28	1
	Logarithmic	0.01 - 0.51	0.32	0.34	0
	Power	0.07 - 0.46	0.24	0.29	0
B⁄G	Linear	0.38 - 0.78	0.59	0.62	1
	Exponential	0.38 - 0.87	0.58	0.47	1
	Logarithmic	0.38 - 0.81	0.62	0.70	1
	Power	0.43 - 0.88	0.61	0.51	1
B⁄R	Linear	0.26 - 0.77	0.59	0.74	1
	Exponential	0.05 - 0.90	0.56	0.67	1
	Logarithmic	0.38 - 0.81	0.64	0.79	1
	Power	0.17 - 0.91	0.60	0.70	1
B⁄NIR	Linear	0.07 - 0.36	0.24	0.24	0
	Exponential	0.24 - 0.41	0.31	0.31	0
	Logarithmic	0.06 - 0.40	0.26	0.28	0
	Power	0.27 - 0.40	0.32	0.30	0
G⁄B	Linear	0.37 - 0.83	0.65	0.76	1
	Exponential	0.45 - 0.89	0.62	0.57	1
	Logarithmic	0.38 - 0.81	0.62	0.70	1
	Power	0.43 - 0.88	0.61	0.51	1
G⁄R	Linear	0.10 - 0.54	0.27	0.17	1
	Exponential	0.07 - 0.66	0.30	0.22	1
	Logarithmic	0.09 - 0.55	0.28	0.21	1
	Power	0.06 - 0.67	0.29	0.22	1
G⁄NIR	Linear	0.20 - 0.66	0.43	0.43	1
	Exponential	0.06 - 0.62	0.48	0.58	2
	Logarithmic	0.23 - 0.57	0.42	0.39	1
	Power	0.09 - 0.67	0.47	0.56	1
R⁄B	Linear	0.42 - 0.85	0.68	0.82	1
	Exponential	0.29 - 0.91	0.63	0.73	1
	Logarithmic	0.38 - 0.81	0.64	0.79	1
	Power	0.17 - 0.91	0.60	0.70	1
R⁄G	Linear	0.08 - 0.55	0.29	0.26	1
	Exponential	0.05 - 0.68	0.28	0.22	1
	Logarithmic	0.09 - 0.55	0.28	0.21	1
	Power	0.06 - 0.67	0.29	0.22	1

R⁄NIR	Linear	0.09 - 0.71	0.48	0.55	2
	Exponential	0.07 - 0.70	0.52	0.58	2
	Logarithmic	0.08 - 0.66	0.46	0.50	2
	Power	0.08 - 0.73	0.51	0.53	2
NIR⁄B	Linear	0.03 - 0.44	0.26	0.30	0
	Exponential	0.17 - 0.38	0.31	0.34	0
	Logarithmic	0.06 - 0.40	0.26	0.28	0
	Power	0.27 - 0.40	0.32	0.30	0
NIR⁄G	Linear	0.26 - 0.50	0.40	0.41	1
	Exponential	0.12 - 0.71	0.45	0.53	1
	Logarithmic	0.23 - 0.57	0.42	0.39	1
	Power	0.09 - 0.67	0.47	0.56	1
NIR⁄R	Linear	0.07 - 0.63	0.43	0.48	0
	Exponential	0.10 - 0.77	0.49	0.52	1
	Logarithmic	0.08 - 0.66	0.46	0.50	2
	Power	0.08 - 0.73	0.51	0.53	2
B×G×R[1]	Linear	0.15 - 0.76	0.48	0.64	1
	Exponential	0.12 - 0.70	0.41	0.48	1
	Logarithmic	0.20 - 0.58	0.42	0.48	0
	Power	0.15 - 0.69	0.36	0.32	0
B×G×NIR[1]	Linear	0.08 - 0.58	0.37	0.47	0
	Exponential	0.09 - 0.47	0.29	0.29	1
	Logarithmic	0.02 - 0.43	0.30	0.37	0
	Power	0.08 - 0.40	0.22	0.23	0
B×R×NIR[1]	Linear	0.06 - 0.64	0.39	0.53	0
	Exponential	0.06 - 0.53	0.31	0.33	1
	Logarithmic	0.01 - 0.48	0.30	0.35	0
	Power	0.06 - 0.46	0.23	0.22	0
G×R×NIR[1]	Linear	0.27 - 0.69	0.51	0.66	0
	Exponential	0.19 - 0.76	0.45	0.48	0
	Logarithmic	0.26 - 0.62	0.47	0.58	0
	Power	0.18 - 0.72	0.42	0.43	0
Avg(B;G)[1,2]	Linear	0.12 - 0.59	0.39	0.48	0
	Exponential	0.07 - 0.64	0.34	0.34	0
	Logarithmic	0.14 - 0.52	0.37	0.42	0
	Power	0.09 - 0.61	0.31	0.29	0
Avg(B;R)[1,2]	Linear	0.11 - 0.61	0.39	0.42	0
	Exponential	0.08 - 0.66	0.33	0.28	0
	Logarithmic	0.13 - 0.54	0.36	0.37	0

	Power	0.10 - 0.64	0.30	0.23	0
Avg(B;NIR)[1,2]	Linear	0.15 - 0.32	0.25	0.26	0
	Exponential	0.09 - 0.23	0.16	0.18	0
	Logarithmic	0.14 - 0.29	0.23	0.26	0
	Power	0.05 - 0.20	0.14	0.18	0
Avg(G;R)[1,2]	Linear	0.29 - 0.70	0.52	0.66	0
	Exponential	0.22 - 0.78	0.46	0.45	0
	Logarithmic	0.28 - 0.64	0.48	0.55	0
	Power	0.21 - 0.75	0.42	0.35	0
Avg(G;NIR)[1,2]	Linear	0.04 - 0.55	0.37	0.44	0
	Exponential	0.09 - 0.44	0.30	0.29	0
	Logarithmic	0.01 - 0.47	0.33	0.37	0
	Power	0.09 - 0.39	0.26	0.28	0
Avg(R;NIR)[1,2]	Linear	0.07 - 0.56	0.38	0.45	0
	Exponential	0.11 - 0.46	0.29	0.30	0
	Logarithmic	0.04 - 0.47	0.32	0.34	0
	Power	0.11 - 0.40	0.24	0.29	0
N-R[3,4]	Linear	0.24 - 0.75	0.49	0.43	1
	Exponential	0.11 - 0.71	0.49	0.55	1
	Logarithmic	0.00 - 0.00	0.00	N/A	0
	Power	0.00 - 0.00	0.00	N/A	0
Kab1[5,6]	Linear	0.37 - 0.81	0.62	0.71	1
	Exponential	0.41 - 0.88	0.60	0.52	1
	Logarithmic	0.37 - 0.75	0.56	0.54	1
	Power	0.34 - 0.84	0.55	0.48	1
NDVI	Linear	0.08 - 0.67	0.46	0.50	1
	Exponential	0.08 - 0.73	0.51	0.53	1
	Logarithmic	0.00 - 0.00	0.00	N/A	0
	Power	0.00 - 0.00	0.00	N/A	0
NRVI	Linear	0.08 - 0.67	0.46	0.50	1
	Exponential	0.08 - 0.73	0.51	0.53	1
	Logarithmic	0.00 - 0.00	0.00	N/A	0
	Power	0.00 - 0.00	0.00	N/A	0
OC2[7]	Linear	0.38 - 0.84	0.65	0.73	2
	Exponential	0.47 - 0.88	0.63	0.53	2
	Logarithmic	0.40 - 0.40	0.40	0.40	1
	Power	0.37 - 0.37	0.37	0.37	1
SABI[5,8]	Linear	0.17 - 0.64	0.45	0.46	1
	Exponential	0.01 - 0.73	0.47	0.51	2

	Logarithmic	0.00 - 0.00	0.00	N/A	0
	Power	0.00 - 0.00	0.00	N/A	0
(B-R)⁄G[4,9]	Linear	0.40 - 0.81	0.64	0.77	1
	Exponential	0.20 - 0.92	0.60	0.64	1
	Logarithmic	0.39 - 0.89	0.72	0.89	0
	Power	0.43 - 0.73	0.62	0.71	0
(NIR⁄G)+(NIR⁄B)	Linear	0.14 - 0.41	0.27	0.26	0
	Exponential	0.23 - 0.58	0.35	0.26	0
	Logarithmic	0.15 - 0.43	0.28	0.28	0
	Power	0.19 - 0.56	0.36	0.36	0
G×(B+G+R)	Linear	0.21 - 0.72	0.50	0.67	0
	Exponential	0.16 - 0.74	0.43	0.50	0
	Logarithmic	0.23 - 0.60	0.44	0.53	0
	Power	0.16 - 0.70	0.39	0.39	0
[(1⁄B)-(1⁄G)]×NIR[10]	Linear	0.26 - 0.88	0.61	0.81	2
	Exponential	0.36 - 0.92	0.65	0.75	1
	Logarithmic	0.00 - 0.00	0.00	N/A	0
	Power	0.00 - 0.00	0.00	N/A	0
[(1⁄R)-(1⁄G)]×NIR[10]	Linear	0.31 - 0.57	0.43	0.45	1
	Exponential	0.03 - 0.78	0.45	0.44	2
	Logarithmic	0.34 - 0.51	0.44	0.46	0
	Power	0.43 - 0.75	0.53	0.47	0
[(1⁄R)-(1⁄B)]×NIR[10]	Linear	0.35 - 0.81	0.57	0.58	1
	Exponential	0.26 - 0.89	0.61	0.63	1
	Logarithmic	0.32 - 0.91	0.67	0.77	0
	Power	0.43 - 0.75	0.63	0.72	0
[(1⁄R)-(0.2363×(1⁄G))]×NIR[11]	Linear	0.01 - 0.64	0.43	0.51	2
	Exponential	0.16 - 0.77	0.50	0.51	1
	Logarithmic	0.03 - 0.67	0.46	0.48	2
	Power	0.14 - 0.74	0.52	0.52	0
(R^-1-B^-1)⁄NIR[12]	Linear	0.08 - 0.81	0.37	0.31	1
	Exponential	0.08 - 0.75	0.35	0.24	1
	Logarithmic	0.28 - 0.91	0.52	0.37	0
	Power	0.18 - 0.75	0.42	0.34	0
(B⁄R)×NIR	Linear	0.17 - 0.36	0.29	0.30	0
	Exponential	0.07 - 0.51	0.35	0.40	1
	Logarithmic	0.16 - 0.38	0.29	0.26	1
	Power	0.03 - 0.50	0.35	0.41	1
(G⁄R)×NIR	Linear	0.04 - 0.35	0.19	0.23	0

	Exponential	0.07 - 0.28	0.20	0.20	0
	Logarithmic	0.02 - 0.28	0.15	0.19	0
	Power	0.09 - 0.26	0.17	0.19	0
(R/B)×NIR	Linear	0.04 - 0.71	0.40	0.35	1
	Exponential	0.06 - 0.53	0.31	0.35	1
	Logarithmic	0.01 - 0.57	0.34	0.38	0
	Power	0.01 - 0.44	0.26	0.34	0
(R/G)×NIR	Linear	0.12 - 0.44	0.28	0.31	0
	Exponential	0.03 - 0.32	0.19	0.20	0
	Logarithmic	0.12 - 0.35	0.25	0.25	0
	Power	0.10 - 0.28	0.17	0.15	0
(R×NIR)/B[13]	Linear	0.04 - 0.71	0.40	0.35	1
	Exponential	0.06 - 0.53	0.31	0.35	1
	Logarithmic	0.01 - 0.57	0.34	0.38	0
	Power	0.01 - 0.44	0.26	0.34	0
(B/G)×(B/R)	Linear	0.26 - 0.77	0.58	0.71	1
	Exponential	0.09 - 0.91	0.56	0.59	1
	Logarithmic	0.42 - 0.83	0.66	0.81	1
	Power	0.27 - 0.92	0.62	0.66	1
(B/G)×(B/NIR)	Linear	0.02 - 0.66	0.26	0.23	0
	Exponential	0.03 - 0.58	0.25	0.20	0
	Logarithmic	0.02 - 0.75	0.31	0.36	0
	Power	0.05 - 0.64	0.26	0.14	0
(B/G)×(R/G)	Linear	0.16 - 0.60	0.34	0.34	1
	Exponential	0.16 - 0.57	0.38	0.41	1
	Logarithmic	0.14 - 0.66	0.36	0.41	1
	Power	0.22 - 0.62	0.41	0.45	1
(B/G)×(R/NIR)	Linear	0.18 - 0.49	0.29	0.29	1
	Exponential	0.20 - 0.49	0.32	0.29	0
	Logarithmic	0.22 - 0.37	0.31	0.32	0
	Power	0.24 - 0.54	0.33	0.29	0
(B/G)×(NIR/B)	Linear	0.26 - 0.50	0.40	0.41	0
	Exponential	0.12 - 0.71	0.45	0.53	0
	Logarithmic	0.23 - 0.57	0.42	0.39	0
	Power	0.09 - 0.67	0.47	0.56	0
(B/G)×(NIR/G)	Linear	0.03 - 0.68	0.48	0.57	1
	Exponential	0.21 - 0.82	0.59	0.66	2
	Logarithmic	0.00 - 0.81	0.52	0.54	1
	Power	0.18 - 0.79	0.60	0.71	2

(B⁄G)×(NIR⁄R)	Linear	0.20 - 0.74	0.54	0.60	1
	Exponential	0.37 - 0.84	0.63	0.65	1
	Logarithmic	0.16 - 0.79	0.59	0.69	1
	Power	0.33 - 0.82	0.65	0.70	1
(B⁄R)×(B⁄NIR)	Linear	0.01 - 0.62	0.29	0.38	1
	Exponential	0.08 - 0.54	0.27	0.21	0
	Logarithmic	0.01 - 0.72	0.35	0.42	1
	Power	0.10 - 0.60	0.30	0.31	0
(B⁄R)×(G⁄R)	Linear	0.16 - 0.68	0.48	0.49	2
	Exponential	0.09 - 0.83	0.49	0.51	2
	Logarithmic	0.32 - 0.74	0.56	0.57	2
	Power	0.07 - 0.87	0.52	0.58	2
(B⁄R)×(G⁄NIR)	Linear	0.06 - 0.34	0.22	0.30	0
	Exponential	0.21 - 0.33	0.26	0.26	0
	Logarithmic	0.07 - 0.39	0.25	0.30	0
	Power	0.18 - 0.33	0.26	0.23	0
(B⁄R)×(NIR⁄R)	Linear	0.32 - 0.73	0.54	0.53	2
	Exponential	0.37 - 0.83	0.60	0.59	1
	Logarithmic	0.30 - 0.81	0.60	0.64	2
	Power	0.44 - 0.83	0.63	0.64	1
(B⁄NIR)×(G⁄NIR)	Linear	0.18 - 0.47	0.27	0.23	0
	Exponential	0.12 - 0.50	0.36	0.46	0
	Logarithmic	0.15 - 0.42	0.28	0.29	0
	Power	0.21 - 0.56	0.37	0.37	0
(B⁄NIR)×(R⁄NIR)	Linear	0.21 - 0.54	0.32	0.25	1
	Exponential	0.09 - 0.55	0.39	0.43	1
	Logarithmic	0.22 - 0.40	0.32	0.30	0
	Power	0.16 - 0.62	0.39	0.40	0
(G⁄B)×(G⁄R)	Linear	0.13 - 0.71	0.38	0.47	1
	Exponential	0.28 - 0.65	0.43	0.45	1
	Logarithmic	0.14 - 0.66	0.36	0.41	1
	Power	0.22 - 0.62	0.41	0.45	1
(G⁄B)×(G⁄NIR)	Linear	0.03 - 0.89	0.54	0.62	2
	Exponential	0.14 - 0.73	0.59	0.70	3
	Logarithmic	0.00 - 0.81	0.52	0.54	2
	Power	0.18 - 0.79	0.60	0.71	3
(G⁄B)×(R⁄B)	Linear	0.39 - 0.88	0.71	0.85	2
	Exponential	0.44 - 0.91	0.65	0.71	2
	Logarithmic	0.42 - 0.83	0.66	0.81	2

	Power	0.27 - 0.92	0.62	0.66	2
(G⁄B)×(R⁄NIR)	Linear	0.12 - 0.84	0.61	0.79	2
	Exponential	0.29 - 0.76	0.63	0.72	2
	Logarithmic	0.16 - 0.79	0.59	0.69	2
	Power	0.33 - 0.82	0.65	0.70	2
(G⁄B)×(NIR⁄B)	Linear	0.01 - 0.81	0.36	0.42	1
	Exponential	0.02 - 0.67	0.28	0.18	0
	Logarithmic	0.02 - 0.75	0.31	0.36	0
	Power	0.05 - 0.64	0.26	0.14	0
(G⁄B)×(NIR⁄R)	Linear	0.25 - 0.44	0.32	0.29	0
	Exponential	0.16 - 0.57	0.34	0.32	0
	Logarithmic	0.22 - 0.37	0.31	0.32	0
	Power	0.24 - 0.54	0.33	0.29	0
(G⁄R)×(G⁄NIR)	Linear	0.17 - 0.74	0.35	0.25	0
	Exponential	0.13 - 0.64	0.42	0.41	0
	Logarithmic	0.21 - 0.63	0.35	0.31	0
	Power	0.19 - 0.58	0.42	0.41	0
(G⁄R)×(NIR⁄R)	Linear	0.18 - 0.59	0.45	0.53	2
	Exponential	0.31 - 0.78	0.50	0.48	1
	Logarithmic	0.16 - 0.67	0.47	0.48	1
	Power	0.33 - 0.75	0.52	0.49	1
(G⁄NIR)×(R⁄NIR)	Linear	0.14 - 0.68	0.48	0.64	2
	Exponential	0.00 - 0.66	0.50	0.61	2
	Logarithmic	0.17 - 0.61	0.45	0.50	2
	Power	0.02 - 0.71	0.48	0.55	2
(R⁄B)×(R⁄G)	Linear	0.43 - 0.78	0.63	0.64	2
	Exponential	0.24 - 0.88	0.57	0.64	2
	Logarithmic	0.32 - 0.74	0.56	0.57	2
	Power	0.07 - 0.87	0.52	0.58	2
(R⁄B(×(R⁄NIR)	Linear	0.27 - 0.85	0.64	0.77	1
	Exponential	0.41 - 0.78	0.64	0.69	1
	Logarithmic	0.30 - 0.81	0.60	0.64	1
	Power	0.44 - 0.83	0.63	0.64	1
(R⁄B)×(NIR⁄B)	Linear	0.03 - 0.78	0.39	0.43	1
	Exponential	0.01 - 0.64	0.31	0.41	1
	Logarithmic	0.01 - 0.72	0.35	0.42	1
	Power	0.10 - 0.60	0.30	0.31	0
(R⁄B)×(NIR⁄G)	Linear	0.08 - 0.43	0.28	0.29	0
	Exponential	0.08 - 0.37	0.23	0.24	0

	Logarithmic	0.07 - 0.39	0.25	0.30	0
	Power	0.18 - 0.33	0.26	0.23	0
(R⁄G)×(R⁄NIR)	Linear	0.13 - 0.78	0.48	0.46	1
	Exponential	0.30 - 0.69	0.53	0.51	1
	Logarithmic	0.16 - 0.67	0.47	0.48	1
	Power	0.33 - 0.75	0.52	0.49	1
(R⁄G)×(NIR⁄G)	Linear	0.21 - 0.53	0.34	0.35	1
	Exponential	0.25 - 0.56	0.41	0.39	2
	Logarithmic	0.21 - 0.63	0.35	0.31	1
	Power	0.19 - 0.58	0.42	0.41	1
(NIR⁄B)×(NIR⁄G)	Linear	0.13 - 0.39	0.27	0.28	0
	Exponential	0.17 - 0.59	0.34	0.30	0
	Logarithmic	0.15 - 0.42	0.28	0.29	0
	Power	0.21 - 0.56	0.37	0.37	0
(NIR⁄B)×(NIR⁄R)	Linear	0.18 - 0.39	0.30	0.34	0
	Exponential	0.18 - 0.68	0.36	0.26	0
	Logarithmic	0.22 - 0.40	0.32	0.30	0
	Power	0.16 - 0.62	0.39	0.40	0
(NIR⁄G)×(NIR⁄R)	Linear	0.19 - 0.53	0.39	0.44	0
	Exponential	0.03 - 0.76	0.43	0.52	1
	Logarithmic	0.17 - 0.61	0.45	0.50	2
	Power	0.02 - 0.71	0.48	0.55	3

(1) Fadel *et al.*, 2016; (2) Patra *et al.*, 2015; (3) Tucker, 1979; (4) Ho *et al.*, 2017; (5) Boucher ***et al.,*** 2018; (6) Kabbara ***et al.,*** 2008; (7) Trinh *et al.*, 2017; (8) Alawadi *et al.*, 2010; (9) Mayo *et al.*, 1995; (10) Keith *et al.*, 2018; (11) Chen *et al.*, 2013; (12) Singh *et al.*, 2014; Guan *et al.*, 2009.

Kab1 = 1.67-3.94×ln(B)+3.78×ln(G)
NDVI = (NIR-R)⁄(NIR+R)
NRVI = [(R⁄NIRIR)-1]⁄[(R⁄NIRIR)+1]
SABI = (NIR-R)⁄(B+G)

$$\boldsymbol{OC2 = 0.1977 + \left(-1.8117\left(log_{10}\left(\frac{B}{G}\right)\right)\right)^{1} + \left(1.9743\left(log_{10}\left(\frac{B}{G}\right)\right)\right)^{2} + \left(2.5635\left(log_{10}\left(\frac{B}{G}\right)\right)\right)^{3} + \left(-0.7218\left(log_{10}\left(\frac{B}{G}\right)\right)\right)^{4}}$$

Table D4: Turbidity algorithm results summary. Constituent free region indicates the corresponding constituents (chl-*a* and true colour) are not statistically significant (P>0.05) with the algorithm

Algorithm	Regression	Range	Average	Median	# Constituent Free Regions
Blue	Linear	0.05 - 0.34	0.17	0.15	1
	Exponential	0.00 - 0.40	0.19	0.19	0
	Logarithmic	0.02 - 0.36	0.18	0.17	0
	Power	0.00 - 0.43	0.19	0.20	1
Green	Linear	0.16 - 0.66	0.37	0.35	0
	Exponential	0.12 - 0.58	0.36	0.37	0
	Logarithmic	0.16 - 0.56	0.36	0.37	0
	Power	0.12 - 0.65	0.36	0.37	0
Red	Linear	0.27 - 0.68	0.47	0.48	1
	Exponential	0.33 - 0.60	0.47	0.48	1
	Logarithmic	0.35 - 0.60	0.47	0.48	0
	Power	0.41 - 0.69	0.49	0.45	0
NIR	Linear	0.10 - 0.49	0.24	0.23	0
	Exponential	0.19 - 0.47	0.31	0.33	0
	Logarithmic	0.10 - 0.50	0.26	0.24	0
	Power	0.18 - 0.48	0.34	0.35	0
B×G	Linear	0.07 - 0.54	0.29	0.29	0
	Exponential	0.10 - 0.43	0.27	0.26	0
	Logarithmic	0.07 - 0.48	0.29	0.29	0
	Power	0.12 - 0.57	0.29	0.27	0
B×R	Linear	0.14 - 0.54	0.31	0.28	0
	Exponential	0.21 - 0.46	0.32	0.29	0
	Logarithmic	0.19 - 0.53	0.33	0.33	0
	Power	0.26 - 0.61	0.36	0.31	0
B×NIR	Linear	0.06 - 0.37	0.18	0.15	0
	Exponential	0.19 - 0.37	0.25	0.21	0
	Logarithmic	0.05 - 0.41	0.22	0.22	0
	Power	0.18 - 0.43	0.30	0.28	0
G×R	Linear	0.16 - 0.73	0.39	0.36	0
	Exponential	0.23 - 0.56	0.39	0.40	0
	Logarithmic	0.20 - 0.59	0.41	0.41	0
	Power	0.25 - 0.68	0.43	0.40	0
G×NIR	Linear	0.16 - 0.66	0.37	0.35	0

	Exponential	0.12 - 0.58	0.36	0.37	0
	Logarithmic	0.16 - 0.56	0.36	0.37	0
	Power	0.12 - 0.65	0.36	0.37	0
R×NIR	Linear	0.17 - 0.51	0.36	0.35	0
	Exponential	0.24 - 0.46	0.36	0.38	1
	Logarithmic	0.33 - 0.48	0.39	0.36	0
	Power	0.19 - 0.55	0.41	0.43	0
B⁄G	Linear	0.14 - 0.64	0.50	0.61	2
	Exponential	0.07 - 0.70	0.49	0.56	1
	Logarithmic	0.13 - 0.72	0.52	0.62	2
	Power	0.06 - 0.69	0.50	0.60	1
B⁄R	Linear	0.56 - 0.76	0.64	0.61	2
	Exponential	0.50 - 0.79	0.65	0.65	1
	Logarithmic	0.56 - 0.77	0.67	0.66	2
	Power	0.56 - 0.79	0.67	0.66	1
B⁄NIR	Linear	0.03 - 0.51	0.29	0.30	0
	Exponential	0.09 - 0.56	0.33	0.31	0
	Logarithmic	0.04 - 0.53	0.28	0.27	0
	Power	0.09 - 0.56	0.32	0.33	0
G⁄B	Linear	0.13 - 0.78	0.53	0.61	2
	Exponential	0.06 - 0.68	0.49	0.61	1
	Logarithmic	0.13 - 0.72	0.52	0.62	2
	Power	0.06 - 0.69	0.50	0.60	1
G⁄R	Linear	0.04 - 0.82	0.44	0.49	2
	Exponential	0.08 - 0.85	0.48	0.51	2
	Logarithmic	0.04 - 0.84	0.44	0.49	2
	Power	0.07 - 0.86	0.48	0.50	2
G⁄NIR	Linear	0.24 - 0.70	0.47	0.44	1
	Exponential	0.20 - 0.60	0.45	0.48	1
	Logarithmic	0.26 - 0.66	0.46	0.46	1
	Power	0.22 - 0.59	0.45	0.47	1
R⁄B	Linear	0.56 - 0.78	0.69	0.71	2
	Exponential	0.57 - 0.79	0.67	0.66	1
	Logarithmic	0.56 - 0.77	0.67	0.66	2
	Power	0.56 - 0.79	0.67	0.66	1
R⁄G	Linear	0.04 - 0.85	0.44	0.48	2
	Exponential	0.06 - 0.86	0.47	0.49	2
	Logarithmic	0.04 - 0.84	0.44	0.49	2
	Power	0.07 - 0.86	0.48	0.50	2

R⁄NIR	Linear	0.29 - 0.79	0.53	0.48	2
	Exponential	0.15 - 0.72	0.46	0.48	2
	Logarithmic	0.23 - 0.78	0.50	0.48	2
	Power	0.09 - 0.72	0.45	0.47	2
NIR⁄B	Linear	0.03 - 0.54	0.28	0.27	1
	Exponential	0.04 - 0.56	0.31	0.32	0
	Logarithmic	0.04 - 0.53	0.28	0.27	0
	Power	0.09 - 0.56	0.32	0.33	0
NIR⁄G	Linear	0.27 - 0.59	0.45	0.46	1
	Exponential	0.23 - 0.57	0.44	0.46	1
	Logarithmic	0.26 - 0.66	0.46	0.46	1
	Power	0.22 - 0.59	0.45	0.47	1
NIR⁄R	Linear	0.17 - 0.76	0.47	0.46	2
	Exponential	0.04 - 0.71	0.43	0.46	2
	Logarithmic	0.23 - 0.78	0.50	0.48	2
	Power	0.09 - 0.72	0.45	0.47	2
B×G×R^{1}	Linear	0.05 - 0.68	0.31	0.25	0
	Exponential	0.12 - 0.52	0.30	0.29	0
	Logarithmic	0.08 - 0.54	0.33	0.35	0
	Power	0.14 - 0.63	0.35	0.33	0
B×G×NIR^{1}	Linear	0.00 - 0.42	0.24	0.30	0
	Exponential	0.11 - 0.38	0.25	0.26	1
	Logarithmic	0.01 - 0.42	0.27	0.29	0
	Power	0.10 - 0.51	0.29	0.34	0
B×R×NIR^{1}	Linear	0.09 - 0.42	0.28	0.31	0
	Exponential	0.17 - 0.38	0.28	0.29	1
	Logarithmic	0.21 - 0.45	0.32	0.32	0
	Power	0.12 - 0.54	0.36	0.36	0
G×R×NIR^{1}	Linear	0.16 - 0.66	0.37	0.35	0
	Exponential	0.12 - 0.58	0.36	0.37	0
	Logarithmic	0.16 - 0.56	0.36	0.37	0
	Power	0.12 - 0.65	0.36	0.37	0
Avg(B;G)^{1,2}	Linear	0.07 - 0.46	0.29	0.32	0
	Exponential	0.12 - 0.50	0.28	0.26	0
	Logarithmic	0.08 - 0.48	0.29	0.30	0
	Power	0.12 - 0.57	0.29	0.27	0
Avg(B;R)^{1,2}	Linear	0.05 - 0.45	0.27	0.29	0
	Exponential	0.04 - 0.51	0.28	0.25	0
	Logarithmic	0.05 - 0.50	0.28	0.30	0

	Power	0.04 - 0.59	0.29	0.28	0
Avg(B;NIR)[1,2]	Linear	0.08 - 0.37	0.21	0.18	0
	Exponential	0.02 - 0.38	0.24	0.24	0
	Logarithmic	0.08 - 0.39	0.23	0.23	0
	Power	0.03 - 0.43	0.26	0.27	0
Avg(G;R)[1,2]	Linear	0.09 - 0.68	0.39	0.39	0
	Exponential	0.14 - 0.59	0.39	0.39	0
	Logarithmic	0.10 - 0.59	0.38	0.40	0
	Power	0.14 - 0.67	0.40	0.40	0
Avg(G;NIR)[1,2]	Linear	0.01 - 0.48	0.33	0.39	0
	Exponential	0.07 - 0.49	0.33	0.36	0
	Logarithmic	0.02 - 0.47	0.33	0.36	0
	Power	0.07 - 0.56	0.34	0.38	0
Avg(R;NIR)[1,2]	Linear	0.27 - 0.49	0.38	0.38	0
	Exponential	0.20 - 0.49	0.39	0.42	0
	Logarithmic	0.30 - 0.49	0.39	0.37	0
	Power	0.14 - 0.57	0.41	0.44	0
N-R[3,4]	Linear	0.26 - 0.80	0.54	0.54	1
	Exponential	0.23 - 0.70	0.49	0.50	1
	Logarithmic	0.00 - 0.00	0.00	N/A	0
	Power	0.00 - 0.00	0.00	N/A	0
Kab1[5,6]	Linear	0.15 - 0.72	0.53	0.61	2
	Exponential	0.08 - 0.72	0.50	0.60	1
	Logarithmic	0.39 - 0.68	0.56	0.58	2
	Power	0.35 - 0.74	0.58	0.60	1
NDVI	Linear	0.22 - 0.78	0.50	0.47	1
	Exponential	0.08 - 0.72	0.45	0.47	1
	Logarithmic	0.00 - 0.00	0.00	N/A	0
	Power	0.00 - 0.00	0.00	N/A	0
NRVI	Linear	0.22 - 0.78	0.50	0.47	1
	Exponential	0.08 - 0.72	0.45	0.47	1
	Logarithmic	0.01 - 0.01	0.00	0.01	0
	Power	0.10 - 0.10	0.00	0.10	0
OC2[7]	Linear	0.15 - 0.71	0.51	0.60	3
	Exponential	0.08 - 0.69	0.48	0.56	2
	Logarithmic	0.00 - 0.00	0.00!	N/A	1
	Power	0.00 - 0.00	0.00!	N/A	1
SABI[5,8]	Linear	0.36 - 0.75	0.55	0.55	2
	Exponential	0.29 - 0.68	0.50	0.52	2

	Logarithmic	0.00 - 0.00	0.00	N/A	0
	Power	0.00 - 0.00	0.00	N/A	0
(B-R)/G[4,9]	Linear	0.47 - 0.73	0.60	0.61	2
	Exponential	0.41 - 0.74	0.59	0.59	1
	Logarithmic	0.48 - 0.75	0.61	0.60	0
	Power	0.42 - 0.73	0.60	0.62	0
(NIR/G)+(NIR/B)	Linear	0.15 - 0.51	0.41	0.43	1
	Exponential	0.09 - 0.53	0.39	0.46	0
	Logarithmic	0.10 - 0.50	0.40	0.45	0
	Power	0.04 - 0.54	0.39	0.46	0
G×(B+G+R)	Linear	0.13 - 0.69	0.34	0.29	1
	Exponential	0.06 - 0.51	0.32	0.33	1
	Logarithmic	0.13 - 0.55	0.34	0.36	0
	Power	0.07 - 0.63	0.34	0.35	0
[(1/B)-(1/G)]×NIR[10]	Linear	0.26 - 0.69	0.47	0.44	2
	Exponential	0.32 - 0.61	0.49	0.49	0
	Logarithmic	0.00 - 0.00	0.00	N/A	0
	Power	0.00 - 0.00	0.00	N/A	0
[(1/R)-(1/G)]×NIR[10]	Linear	0.04 - 0.77	0.51	0.55	0
	Exponential	0.14 - 0.83	0.52	0.51	0
	Logarithmic	0.04 - 0.79	0.53	0.59	1
	Power	0.14 - 0.81	0.52	0.52	0
[(1/R)-(1/B)]×NIR[10]	Linear	0.29 - 0.80	0.56	0.56	0
	Exponential	0.28 - 0.84	0.55	0.52	1
	Logarithmic	0.46 - 0.82	0.61	0.58	0
	Power	0.34 - 0.79	0.57	0.58	0
[(1/R)-(0.2363×(1/G))]×NIR[11]	Linear	0.25 - 0.79	0.48	0.47	2
	Exponential	0.13 - 0.75	0.45	0.46	2
	Logarithmic	0.29 - 0.80	0.52	0.49	2
	Power	0.18 - 0.75	0.47	0.48	0
(R^-1-B^-1)/NIR[12]	Linear	0.17 - 0.80	0.47	0.47	1
	Exponential	0.10 - 0.80	0.50	0.52	2
	Logarithmic	0.42 - 0.82	0.57	0.53	1
	Power	0.49 - 0.79	0.61	0.58	0
(B/R)×NIR	Linear	0.00 - 0.68	0.32	0.29	2
	Exponential	0.07 - 0.70	0.30	0.27	2
	Logarithmic	0.12 - 0.71	0.37	0.34	2
	Power	0.04 - 0.69	0.32	0.31	2
(G/R)×NIR	Linear	0.06 - 0.43	0.20	0.19	0

	Exponential	0.09 - 0.38	0.23	0.27	0
	Logarithmic	0.01 - 0.44	0.22	0.21	0
	Power	0.05 - 0.39	0.25	0.26	0
(R/B)×NIR	Linear	0.33 - 0.59	0.46	0.45	2
	Exponential	0.38 - 0.54	0.46	0.47	1
	Logarithmic	0.41 - 0.55	0.46	0.44	0
	Power	0.27 - 0.57	0.48	0.50	0
(R/G)×NIR	Linear	0.06 - 0.51	0.30	0.30	0
	Exponential	0.16 - 0.56	0.36	0.36	1
	Logarithmic	0.09 - 0.52	0.34	0.38	0
	Power	0.19 - 0.60	0.41	0.44	0
(R×NIR)/B[13]	Linear	0.33 - 0.59	0.46	0.45	1
	Exponential	0.38 - 0.54	0.46	0.47	1
	Logarithmic	0.41 - 0.55	0.46	0.44	0
	Power	0.27 - 0.57	0.48	0.50	0
(B/G)×(B/R)	Linear	0.47 - 0.71	0.58	0.60	2
	Exponential	0.43 - 0.72	0.59	0.61	1
	Logarithmic	0.54 - 0.73	0.64	0.63	2
	Power	0.53 - 0.73	0.63	0.61	1
(B/G)×(B/NIR)	Linear	0.31 - 0.55	0.43	0.44	2
	Exponential	0.22 - 0.59	0.43	0.47	1
	Logarithmic	0.25 - 0.57	0.46	0.48	1
	Power	0.32 - 0.60	0.46	0.49	1
(B/G)×(R/G)	Linear	0.05 - 0.66	0.31	0.26	0
	Exponential	0.12 - 0.71	0.31	0.23	0
	Logarithmic	0.03 - 0.67	0.32	0.28	0
	Power	0.10 - 0.69	0.33	0.26	0
(B/G)×(R/NIR)	Linear	0.14 - 0.49	0.28	0.24	0
	Exponential	0.09 - 0.54	0.26	0.24	0
	Logarithmic	0.15 - 0.49	0.28	0.23	1
	Power	0.06 - 0.53	0.26	0.23	0
(B/G)×(NIR/B)	Linear	0.27 - 0.59	0.45	0.46	0
	Exponential	0.23 - 0.57	0.44	0.46	0
	Logarithmic	0.26 - 0.66	0.46	0.46	0
	Power	0.22 - 0.59	0.45	0.47	0
(B/G)×(NIR/G)	Linear	0.28 - 0.58	0.43	0.42	2
	Exponential	0.29 - 0.55	0.43	0.46	1
	Logarithmic	0.29 - 0.73	0.47	0.43	1
	Power	0.29 - 0.63	0.46	0.48	1

(B/G)×(NIR/R)	Linear	0.06 - 0.73	0.41	0.39	1
	Exponential	0.05 - 0.77	0.38	0.36	0
	Logarithmic	0.07 - 0.75	0.46	0.50	0
	Power	0.08 - 0.76	0.41	0.40	0
(B/R)×(B/NIR)	Linear	0.31 - 0.66	0.48	0.52	2
	Exponential	0.22 - 0.72	0.50	0.53	1
	Logarithmic	0.33 - 0.66	0.52	0.56	1
	Power	0.30 - 0.71	0.53	0.57	1
(B/R)×(G/R)	Linear	0.49 - 0.81	0.61	0.58	3
	Exponential	0.45 - 0.83	0.64	0.62	3
	Logarithmic	0.54 - 0.83	0.65	0.61	3
	Power	0.49 - 0.83	0.66	0.63	3
(B/R)×(G/NIR)	Linear	0.07 - 0.69	0.36	0.38	0
	Exponential	0.12 - 0.77	0.42	0.40	0
	Logarithmic	0.06 - 0.68	0.36	0.37	1
	Power	0.11 - 0.76	0.41	0.39	0
(B/R)×(NIR/R)	Linear	0.03 - 0.81	0.50	0.56	1
	Exponential	0.05 - 0.88	0.49	0.52	0
	Logarithmic	0.04 - 0.83	0.56	0.68	2
	Power	0.05 - 0.86	0.52	0.59	0
(B/NIR)×(G/NIR)	Linear	0.04 - 0.47	0.38	0.45	0
	Exponential	0.07 - 0.58	0.39	0.42	0
	Logarithmic	0.09 - 0.51	0.40	0.46	0
	Power	0.04 - 0.54	0.39	0.46	0
(B/NIR)×(R/NIR)	Linear	0.12 - 0.61	0.38	0.44	1
	Exponential	0.11 - 0.51	0.37	0.43	1
	Logarithmic	0.15 - 0.59	0.41	0.47	1
	Power	0.18 - 0.53	0.40	0.45	1
(G/B)×(G/R)	Linear	0.01 - 0.74	0.34	0.31	0
	Exponential	0.08 - 0.68	0.33	0.28	0
	Logarithmic	0.03 - 0.67	0.32	0.28	0
	Power	0.10 - 0.69	0.33	0.26	0
(G/B)×(G/NIR)	Linear	0.29 - 0.80	0.49	0.44	1
	Exponential	0.29 - 0.61	0.46	0.49	2
	Logarithmic	0.29 - 0.73	0.47	0.43	2
	Power	0.29 - 0.63	0.46	0.48	2
(G/B)×(R/B)	Linear	0.52 - 0.81	0.66	0.64	3
	Exponential	0.52 - 0.72	0.62	0.60	2
	Logarithmic	0.54 - 0.73	0.64	0.63	3

	Power	0.53 - 0.73	0.63	0.61	2
(G/B)×(R/NIR)	Linear	0.09 - 0.82	0.49	0.53	1
	Exponential	0.10 - 0.74	0.41	0.39	1
	Logarithmic	0.07 - 0.75	0.46	0.50	1
	Power	0.08 - 0.76	0.41	0.40	1
(G/B)×(NIR/B)	Linear	0.15 - 0.60	0.47	0.54	2
	Exponential	0.23 - 0.59	0.46	0.48	2
	Logarithmic	0.25 - 0.57	0.46	0.48	2
	Power	0.32 - 0.60	0.46	0.49	1
(G/B)×(NIR/R)	Linear	0.12 - 0.48	0.28	0.24	1
	Exponential	0.02 - 0.52	0.26	0.23	0
	Logarithmic	0.15 - 0.49	0.28	0.23	1
	Power	0.06 - 0.53	0.26	0.23	0
(G/R)×(G/NIR)	Linear	0.05 - 0.65	0.44	0.46	0
	Exponential	0.09 - 0.75	0.43	0.46	0
	Logarithmic	0.02 - 0.65	0.43	0.49	1
	Power	0.04 - 0.75	0.41	0.48	0
(G/R)×(NIR/R)	Linear	0.05 - 0.79	0.50	0.61	1
	Exponential	0.10 - 0.79	0.49	0.57	0
	Logarithmic	0.06 - 0.80	0.53	0.67	0
	Power	0.10 - 0.80	0.51	0.60	0
(G/NIR)×(R/NIR)	Linear	0.07 - 0.74	0.46	0.43	1
	Exponential	0.22 - 0.62	0.44	0.42	1
	Logarithmic	0.12 - 0.69	0.46	0.42	1
	Power	0.26 - 0.63	0.45	0.42	1
(R/B)×(R/G)	Linear	0.51 - 0.85	0.66	0.65	3
	Exponential	0.50 - 0.83	0.65	0.64	3
	Logarithmic	0.54 - 0.83	0.65	0.61	3
	Power	0.49 - 0.83	0.66	0.63	3
(R/B(×(R/NIR)	Linear	0.04 - 0.83	0.58	0.74	0
	Exponential	0.05 - 0.81	0.52	0.60	0
	Logarithmic	0.04 - 0.83	0.56	0.68	1
	Power	0.05 - 0.86	0.52	0.59	0
(R/B)×(NIR/B)	Linear	0.23 - 0.65	0.52	0.57	1
	Exponential	0.31 - 0.69	0.52	0.56	1
	Logarithmic	0.33 - 0.66	0.52	0.56	1
	Power	0.30 - 0.71	0.53	0.57	1
(R/B)×(NIR/G)	Linear	0.06 - 0.67	0.34	0.32	1
	Exponential	0.11 - 0.73	0.39	0.36	1

	Logarithmic	0.06 - 0.68	0.36	0.37	1
	Power	0.11 - 0.76	0.41	0.39	0
(R⁄G)×(R⁄NIR)	Linear	0.07 - 0.81	0.55	0.72	0
	Exponential	0.10 - 0.79	0.51	0.62	0
	Logarithmic	0.06 - 0.80	0.53	0.67	0
	Power	0.10 - 0.80	0.51	0.60	0
(R⁄G)×(NIR⁄G)	Linear	0.07 - 0.64	0.41	0.47	2
	Exponential	0.01 - 0.73	0.39	0.44	2
	Logarithmic	0.02 - 0.65	0.43	0.49	2
	Power	0.04 - 0.75	0.41	0.48	1
(NIR⁄B)×(NIR⁄G)	Linear	0.18 - 0.53	0.40	0.41	1
	Exponential	0.13 - 0.54	0.38	0.43	1
	Logarithmic	0.09 - 0.51	0.40	0.46	1
	Power	0.04 - 0.54	0.39	0.46	1
(NIR⁄B)×(NIR⁄R)	Linear	0.18 - 0.55	0.41	0.46	1
	Exponential	0.24 - 0.52	0.40	0.42	2
	Logarithmic	0.15 - 0.59	0.41	0.47	2
	Power	0.18 - 0.53	0.40	0.45	2
(NIR⁄G)×(NIR⁄R)	Linear	0.16 - 0.63	0.43	0.41	1
	Exponential	0.29 - 0.58	0.43	0.41	1
	Logarithmic	0.12 - 0.69	0.46	0.42	1
	Power	0.26 - 0.63	0.45	0.42	2

(1) Fadel *et al*., 2016; (2) Patra *et al*., 2015; (3) Tucker, 1979; (4) Ho *et al*., 2017; (5) Boucher ***et al*.,** 2018; (6) Kabbara ***et al*.,** 2008; (7) Trinh *et al*., 2017; (8) Alawadi *et al*., 2010; (9) Mayo *et al*., 1995; (10) Keith *et al*., 2018; (11) Chen *et al*., 2013; (12) Singh *et al*., 2014; Guan *et al*., 2009.

Kab1 = 1.67-3.94×ln(B)+3.78×ln(G)
NDVI = (NIR-R)⁄(NIR+R)
NRVI = [(R⁄NIRIR)-1]⁄[(R⁄NIRIR)+1]
SABI = (NIR-R)⁄(B+G)

$$\boldsymbol{OC2 = 0.1977 + \left(-1.8117\left(log_{10}\left(\frac{B}{G}\right)\right)\right)^{1} + \left(1.9743\left(log_{10}\left(\frac{B}{G}\right)\right)\right)^{2} + \left(2.5635\left(log_{10}\left(\frac{B}{G}\right)\right)\right)^{3} + \left(-0.7218\left(log_{10}\left(\frac{B}{G}\right)\right)\right)^{4}}$$

Appendix E: Algorithms by region and regression without confounding signals

Table E1: Chl-*a* statistically significant algorithms free of additional optical constituents (Colour, TSS and Turbidity). A = Linear, B = Exponential, C = Logarithmic, D = Power, 1 = PTW, 2 = BCF, 3 = TCF, 4 = TPS, 5 = TPD, 6 = SHF, 7 = TMF.

Algorithm	**A 1**	**A 2**	**A 3**	**A 4**	**A 5**	**A 6**	**A 7**	**B 1**	**B 2**	**B 3**	**B 4**	**B 5**	**B 6**	**B 7**	**C 1**	**C 2**	**C 3**	**C 4**	**C 5**	**C 6**	**C 7**	**D 1**	**D 2**	**D 3**	**D 4**	**D 5**	**D 6**	**D 7**	**# A**	**# B**	**# C**	**# D**
Blue			x	x		x	x			x			x				x	x		x	x			x			x		4	2	4	2
Green		x						x	x					x		x						x	x	x				x	1	3	1	4
Red	x	x						x	x						x	x						x	x	x					2	2	2	3
NIR	x		x			x	x	x		x			x	x	x		x			x	x	x		x			x	x	4	4	4	4
B×G		x							x	x						x	x						x	x					1	2	2	2
B×R		x					x		x	x						x	x					x	x	x					2	2	2	3
B×NIR	x	x	x		x	x	x	x	x	x		x	x		x	x	x			x	x	x	x	x			x		6	5	5	4
G×R		x						x	x						x	x						x	x	x				x	1	2	2	4
G×NIR	x	x						x	x					x	x	x						x	x	x				x	2	3	2	4
R×NIR	x	x					x	x	x	x					x	x	x				x	x	x	x					3	3	4	3
B⁄G		x							x													x							1	1	0	1
B⁄R	x							x							x							x							1	1	1	1
B⁄NIR	x		x		x	x		x		x			x		x		x		x			x		x		x	x		4	3	3	4
G⁄B								x														x							0	1	0	1
G⁄R	x		x					x		x					x		x					x		x					2	2	2	2
G⁄NIR							x							x								x						x	1	1	0	2
R⁄B	x							x							x							x							1	1	1	1
R⁄G	x		x					x		x					x		x					x		x					2	2	2	2
R⁄NIR							x							x							x							x	1	1	1	1
NIR⁄B	x		x		x			x		x		x	x		x		x		x			x		x		x	x		3	4	3	4
NIR⁄G	x							x						x								x						x	1	2	0	2

NIR⁄R													x							x							x	0	1	1	1
B×G×R		x					x		x	x						x						x	x	x					2	2	1	3
B×G×NIR	x	x	x				x	x	x	x		x			x	x	x			x	x	x	x	x			x		4	4	5	4
B×R×NIR	x	x	x				x	x	x	x					x	x	x			x	x	x	x	x					4	3	5	3
G×R×NIR	x	x						x	x					x	x	x						x	x	x				x	2	3	2	4
Avg(B;G)		x							x	x						x	x						x	x					1	2	2	2
Avg(B;R)		x	x						x	x						x	x						x	x					2	2	2	2
Avg(B;N)	x	x	x			x	x	x	x	x			x		x	x	x			x	x	x	x	x			x		5	4	5	4
Avg(G;R)	x	x						x	x					x	x	x						x	x	x				x	2	3	2	4
Avg(G;N)	x	x					x	x	x	x					x	x	x					x	x	x					3	3	3	3
Avg(R;N)	x	x	x				x	x	x	x					x	x	x				x	x	x	x					4	3	4	3
N-R	x						x	x						x															2	2	0	0
Kab1								x																					0	1	0	0
NDVI							x							x															1	1	0	0
NRVI							x							x															1	1	0	0
OC2		x						x	x																				1	2	0	0
SABI	x						x	x						x															2	2	0	0
(B-R)⁄G		x						x	x																				1	2	0	0
(NIR⁄G)+(NIR⁄B)	x				x			x				x			x				x			x				x			2	2	2	2
G×(B+G+R)		x							x							x						x	x	x				x	1	1	1	4
[(1⁄B)-(1⁄G)]×NIR		x						x	x					x															1	3	0	0
[(1⁄R)-(1⁄G)]×NIR																													0	0	0	0
[(1⁄R)-(1⁄B)]×NIR								x																					0	1	0	0
[(1⁄R)-(0.2363×(1⁄G))]×NIR							x							x							x							x	1	1	1	1
(R^-1-B^-1)⁄NIR		x	x					x		x																			2	2	0	0

(B/R)×NIR				x	x		x							x					x		x							x	3	1	2	1
(G/R)×NIR	x		x		x	x	x	x		x		x	x	x	x		x		x	x	x	x		x		x	x	x	5	5	5	5
(R/B)×NIR	x						x	x		x					x		x				x	x		x					2	2	3	2
(R/G)×NIR	x		x			x	x	x		x			x	x	x		x			x	x	x		x			x	x	4	4	4	4
(R×NIR)/B	x						x	x		x					x		x				x	x		x					2	2	3	2
(B/G)×(B/R)																						x							0	0	0	1
(B/G)×(B/NIR)	x		x					x		x					x				x			x		x					2	2	2	2
(B/G)×(R/G)					x							x		x					x			x				x		x	1	2	1	3
(B/G)×(R/NIR)	x					x	x	x					x		x				x	x	x	x				x	x		3	2	4	3
(B/G)×(NIR/B)	x							x						x								x						x	1	2	0	2
(B/G)×(NIR/G)																													0	0	0	0
(B/G)×(NIR/R)														x														x	0	1	0	1
(B/R)×(B/NIR)	x		x					x		x					x		x					x		x					2	2	2	2
(B/R)×(G/R)	x							x							x							x							1	1	1	1
(B/R)×(G/NIR)	x		x					x		x					x		x					x		x					2	2	2	2
(B/R)×(NIR/R)									x					x							x							x	0	2	1	1
(B/NIR)×(G/NIR)	x						x	x							x				x			x							2	1	2	1
(B/NIR)×(R/NIR)	x						x	x							x						x	x							2	1	2	1
(G/B)×(G/R)	x				x		x	x				x		x					x			x				x		x	3	3	1	3
(G/B)×(G/NIR)														x															0	1	0	0
(G/B)×(R/B)	x							x														x							1	1	0	1
(G/B)×(R/NIR)							x							x														x	1	1	0	1
(G/B)×(NIR/B)	x				x			x		x		x			x				x			x		x					2	3	2	2
(G/B)×(NIR/R)	x				x		x	x				x	x		x				x	x	x	x				x	x		3	3	4	3
(G/R)×(G/NIR)								x						x	x							x							0	2	1	1
(G/R)×(NIR/R)														x							x							x	0	1	1	1

(G⁄NIR)×(R⁄NIR)							x							x							x							x	1	1	1	1
(R⁄B)×(R⁄G)	x							x							x							x							1	1	1	1
(R⁄B(×(R⁄NIR)							x							x							x							x	1	1	1	1
(R⁄B)×(NIR⁄B)	x				x			x		x					x		x					x		x					2	2	2	2
(R⁄B)×(NIR⁄G)	x		x		x			x		x					x		x					x		x					3	2	2	2
(R⁄G)×(R⁄NIR)							x							x							x							x	1	1	1	1
(R⁄G)×(NIR⁄G)	x							x							x							x							1	1	1	1
(NIR⁄B)×(NIR⁄G)	x				x			x				x			x				x			x							2	2	2	1
(NIR⁄B)×(NIR⁄R)	x				x		x	x							x						x	x							3	1	2	1
(NIR⁄G)×(NIR⁄R)								x						x							x							x	0	2	1	1

Table E2: True colour statistically significant algorithms free of additional optical constituents (Chl-*a*). A = Linear, B = Exponential, C = Logarithmic, D = Power, 1 = PTW, 2 = BCF, 3 = TCF, 4 = TPS, 5 = TPD, 6 = SHF, 7 = TMF.

Algorithm	A 1	A 2	A 3	A 4	A 5	A 6	A 7	B 1	B 2	B 3	B 4	B 5	B 6	B 7	C 1	C 2	C 3	C 4	C 5	C 6	C 7	D 1	D 2	D 3	D 4	D 5	D 6	D 7	# A	# B	# C	# D
Blue																													0	0	0	0
Green																													0	0	0	0
Red																													0	0	0	0
NIR																													0	0	0	0
B×G					x							x																	1	1	0	0
B×R					x							x																	1	1	0	0
B×N																													0	0	0	0
G×R																													0	0	0	0
G×N																													0	0	0	0
R×N																													0	0	0	0
B/G																													0	0	0	0
B/R																													0	0	0	0
B/N																													0	0	0	0
G/B																													0	0	0	0
G/R					x							x							x							x			1	1	1	1
G/N						x							x							x							x		1	1	1	1
R/B																													0	0	0	0
R/G					x							x							x							x			1	1	1	1
R/N					x														x					x					1	0	1	1
NIR/B																													0	0	0	0
NIR/G						x							x							x							x		1	1	1	1
NIR/R						x				x									x					x					1	1	1	1
B×G×R					x							x																	1	1	0	0

B×G×N																													0	0	0	0
B×R×N												x																	0	1	0	0
G×R×N																													0	0	0	0
Avg(B;G)												x																	0	1	0	0
Avg(B;R)					x							x														x			1	1	0	1
Avg(B;N)																													0	0	0	0
Avg(G;R)																													0	0	0	0
Avg(G;N)																													0	0	0	0
Avg(R;N)																													0	0	0	0
N-R					x							x																	1	1	0	0
Kab1																													0	0	0	0
NDVI					x																								1	0	0	0
NRVI					x					x																			1	1	0	0
OC2																	x							x					0	0	1	1
SABI					x	x						x					x							x					2	1	1	1
(B-R)⁄G																													0	0	0	0
(NIR⁄G)+(NIR⁄B)						x							x							x							x		1	1	1	1
G×(B+G+R)																													0	0	0	0
[(1⁄B)-(1⁄G)]×N																	x												0	0	1	0
[(1⁄R)-(1⁄G)]×N		x			x				x			x				x							x						2	2	1	1
[(1⁄R)-(1⁄B)]×N																													0	0	0	0
[(1⁄R)-(0.2363×(1⁄G))]×N	x				x														x							x			2	0	1	1
(R^-1-B^-1)⁄N																													0	0	0	0
(B⁄R)×N																													0	0	0	0
(G⁄R)×N																													0	0	0	0

(R/B)×N																													0	0	0	0
(R/G)×N																													0	0	0	0
(R×N)/B																													0	0	0	0
(B/G)×(B/R)																													0	0	0	0
(B/G)×(B/N)																													0	0	0	0
(B/G)×(R/G)																													0	0	0	0
(B/G)×(R/N)																													0	0	0	0
(B/G)×(NIR/B)						x							x							x							x		1	1	1	1
(B/G)×(NIR/G)	x	x							x							x			x				x						2	1	2	1
(B/G)×(NIR/R)	x				x							x			x	x			x				x			x			2	1	3	2
(B/R)×(B/N)																													0	0	0	0
(B/R)×(G/R)																													0	0	0	0
(B/R)×(G/N)																													0	0	0	0
(B/R)×(NIR/R)	x				x		x			x					x				x					x		x			3	1	2	2
(B/N)×(G/N)						x							x							x							x		1	1	1	1
(B/N)×(R/N)																													0	0	0	0
(G/B)×(G/R)																													0	0	0	0
(G/B)×(G/N)		x			x				x							x			x				x						2	1	2	1
(G/B)×(R/B)																													0	0	0	0
(G/B)×(R/N)		x			x				x			x			x	x			x				x			x			2	2	3	2
(G/B)×(NIR/B)																													0	0	0	0
(G/B)×(NIR/R)																													0	0	0	0
(G/R)×(G/N)						x							x							x						x	x		1	1	1	2
(G/R)×(NIR/R)	x		x		x				x	x		x				x	x		x				x	x		x			3	3	3	3
(G/N)×(R/N)						x														x									1	0	1	0
(R/B)×(R/G)																													0	0	0	0

(R⁄B(×(R⁄N)					x							x			x				x							x			1	1	2	1
(R⁄B)×(NIR⁄B)																													0	0	0	0
(R⁄B)×(NIR⁄G)																													0	0	0	0
(R⁄G)×(R⁄N)		x	x		x				x			x				x	x		x				x			x			3	2	3	2
(R⁄G)×(NIR⁄G)						x							x							x						x	x		1	1	1	2
(NIR⁄B)×(NIR⁄G)													x							x							x		0	1	1	1
(NIR⁄B)×(NIR⁄R)						x																							1	0	0	0
(NIR⁄G)×(NIR⁄R)						x							x							x									1	1	1	0

Table E3: TSS statistically significant algorithms free of additional optical constituents (Chl-*a* and true colour). A = Linear, B = Exponential, C = Logarithmic, D = Power, 1 = PTW, 2 = BCF, 3 = TCF, 4 = TPS, 5 = TPD, 6 = SHF, 7 = TMF.

Algorithm	A 1	A 2	A 3	A 4	A 5	A 6	A 7	B 1	B 2	B 3	B 4	B 5	B 6	B 7	C 1	C 2	C 3	C 4	C 5	C 6	C 7	D 1	D 2	D 3	D 4	D 5	D 6	D 7	# A	# B	# C	# D
Blue																													0	0	0	0
Green																													0	0	0	0
Red				x							x																		1	1	0	0
NIR																													0	0	0	0
B×G																													0	0	0	0
B×R											x																		0	1	0	0
B×N																													0	0	0	0
G×R											x																		0	1	0	0
G×N																													0	0	0	0
R×N											x																		0	1	0	0
B⁄G				x							x							x							x				1	1	1	1
B⁄R				x							x							x							x				1	1	1	1
B⁄N																													0	0	0	0
G⁄B				x							x							x							x				1	1	1	1
G⁄R				x							x							x							x				1	1	1	1
G⁄N			x							x		x					x							x					1	2	1	1
R⁄B				x							x							x							x				1	1	1	1
R⁄G				x							x							x							x				1	1	1	1
R⁄N			x			x				x		x					x			x						x	x		2	2	2	2
NIR⁄B																													0	0	0	0
NIR⁄G			x							x							x							x					1	1	1	1
NIR⁄R													x				x			x						x	x		0	1	2	2
B×G×R				x							x																		1	1	0	0

B×G×N											x																		0	1	0	0
B×R×N											x																		0	1	0	0
G×R×N																													0	0	0	0
Avg(B;G)																													0	0	0	0
Avg(B;R)																													0	0	0	0
Avg(B;N)																													0	0	0	0
Avg(G;R)																													0	0	0	0
Avg(G;N)																													0	0	0	0
Avg(R;N)																													0	0	0	0
N-R						x							x																1	1	0	0
Kab1				x							x							x							x				1	1	1	1
NDVI						x						x																	1	1	0	0
NRVI						x						x																	1	1	0	0
OC2			x	x						x	x							x							x				2	2	1	1
SABI				x						x			x																1	2	0	0
(B-R)⁄G				x							x																		1	1	0	0
(NIR⁄G)+(NIR⁄B)																													0	0	0	0
G×(B+G+R)																													0	0	0	0
[(1⁄B)-(1⁄G)]×N			x	x							x																		2	1	0	0
[(1⁄R)-(1⁄G)]×N				x							x			x															1	2	0	0
[(1⁄R)-(1⁄B)]×N				x							x																		1	1	0	0
[(1⁄R)-(0.2363×(1⁄G))]×N				x		x							x					x		x									2	1	2	0
(R^-1-B^-1)⁄N				x							x																		1	1	0	0
(B⁄R)×N													x							x							x		0	1	1	1
(G⁄R)×N																													0	0	0	0

(R/B)×N				x							x																		1	1	0	0
(R/G)×N																													0	0	0	0
(R×N)/B				x							x																		1	1	0	0
(B/G)×(B/R)				x							x							x							x				1	1	1	1
(B/G)×(B/N)																													0	0	0	0
(B/G)×(R/G)				x							x							x							x				1	1	1	1
(B/G)×(R/N)					x																								1	0	0	0
(B/G)×(NIR/B)																													0	0	0	0
(B/G)×(NIR/G)				x							x	x						x							x	x			1	2	1	2
(B/G)×(NIR/R)				x							x							x							x				1	1	1	1
(B/R)×(B/N)				x														x											1	0	1	0
(B/R)×(G/R)			x	x						x	x						x	x						x	x				2	2	2	2
(B/R)×(G/N)																													0	0	0	0
(B/R)×(NIR/R)			x	x							x						x	x							x				2	1	2	1
(B/N)×(G/N)																													0	0	0	0
(B/N)×(R/N)					x							x																	1	1	0	0
(G/B)×(G/R)				x							x							x							x				1	1	1	1
(G/B)×(G/N)			x	x						x	x	x					x	x						x	x	x			2	3	2	3
(G/B)×(R/B)			x	x						x	x						x	x						x	x				2	2	2	2
(G/B)×(R/N)			x	x						x	x						x	x						x	x				2	2	2	2
(G/B)×(NIR/B)				x																									1	0	0	0
(G/B)×(NIR/R)																													0	0	0	0
(G/R)×(G/N)																													0	0	0	0
(G/R)×(NIR/R)				x		x					x							x							x				2	1	1	1
(G/N)×(R/N)			x		x							x	x				x		x							x	x		2	2	2	2
(R/B)×(R/G)			x	x						x	x						x	x						x	x				2	2	2	2

(R⁄B(×(R⁄N)				x							x							x							x				1	1	1	1
(R⁄B)×(NIR⁄B)				x							x							x											1	1	1	0
(R⁄B)×(NIR⁄G)																													0	0	0	0
(R⁄G)×(R⁄N)				x							x							x							x				1	1	1	1
(R⁄G)×(NIR⁄G)			x							x	x						x							x					1	2	1	1
(NIR⁄B)×(NIR⁄G)																													0	0	0	0
(NIR⁄B)×(NIR⁄R)																													0	0	0	0
(NIR⁄G)×(NIR⁄R)										x							x		x					x		x	x		0	1	2	3

Table E4: Turbidity statistically significant algorithms free of additional optical constituents (Chl-*a* and true colour). A = Linear, B = Exponential, C = Logarithmic, D = Power, 1 = PTW, 2 = BCF, 3 = TCF, 4 = TPS, 5 = TPD, 6 = SHF, 7 = TMF.

Algorithm	**A 1**	**A 2**	**A 3**	**A 4**	**A 5**	**A 6**	**A 7**	**B 1**	**B 2**	**B 3**	**B 4**	**B 5**	**B 6**	**B 7**	**C 1**	**C 2**	**C 3**	**C 4**	**C 5**	**C 6**	**C 7**	**D 1**	**D 2**	**D 3**	**D 4**	**D 5**	**D 6**	**D 7**	**# A**	**# B**	**# C**	**# D**
Blue		x																								x			1	0	0	1
Green																													0	0	0	0
Red				x							x																		1	1	0	0
NIR																													0	0	0	0
B×G																													0	0	0	0
B×R																													0	0	0	0
B×N																													0	0	0	0
G×R																													0	0	0	0
G×N																													0	0	0	0
R×N											x																		0	1	0	0
B⁄G				x			x				x							x			x				x				2	1	2	1
B⁄R				x			x				x							x			x				x				2	1	2	1
B⁄N																													0	0	0	0
G⁄B				x			x				x							x			x				x				2	1	2	1
G⁄R				x			x				x			x				x			x				x			x	2	2	2	2
G⁄N			x							x							x							x					1	1	1	1
R⁄B				x			x				x							x			x				x				2	1	2	1
R⁄G				x			x				x			x				x			x				x			x	2	2	2	2
R⁄N			x			x				x		x					x			x						x	x		2	2	2	2
NIR⁄B				x																									1	0	0	0
NIR⁄G			x							x							x							x					1	1	1	1
NIR⁄R			x		x							x	x				x			x						x	x		2	2	2	2
B×G×R																													0	0	0	0

B×G×N											x																		0	1	0	0
B×R×N											x																		0	1	0	0
G×R×N																													0	0	0	0
Avg(B;G)																													0	0	0	0
Avg(B;R)																													0	0	0	0
Avg(B;N)																													0	0	0	0
Avg(G;R)																													0	0	0	0
Avg(G;N)																													0	0	0	0
Avg(R;N)																													0	0	0	0
N-R						x							x																1	1	0	0
Kab1				x			x				x							x			x				x				2	1	2	1
NDVI						x						x																	1	1	0	0
NRVI						x						x																	1	1	0	0
OC2			x	x			x			x	x							x							x				3	2	1	1
SABI			x	x						x			x																2	2	0	0
(B-R)⁄G				x			x				x																		2	1	0	0
(NIR⁄G)+(NIR⁄B)				x																									1	0	0	0
G×(B+G+R)			x							x																			1	1	0	0
[(1⁄B)-(1⁄G)]×N			x	x																									2	0	0	0
[(1⁄R)-(1⁄G)]×N																					x								0	0	1	0
[(1⁄R)-(1⁄B)]×N											x																		0	1	0	0
[(1⁄R)-(0.2363×(1⁄G))]×N				x		x						x	x					x		x									2	2	2	0
(R^-1-B^-1)⁄N				x							x			x			x												1	2	1	0
(B⁄R)×N			x			x				x			x				x			x				x			x		2	2	2	2
(G⁄R)×N																													0	0	0	0

(R⁄B)×N			x	x							x																		2	1	0	0
(R⁄G)×N											x																		0	1	0	0
(R×N)⁄B				x							x																		1	1	0	0
(B⁄G)×(B⁄R)				x			x				x							x			x				x				2	1	2	1
(B⁄G)×(B⁄N)				x			x							x				x										x	2	1	1	1
(B⁄G)×(R⁄G)																													0	0	0	0
(B⁄G)×(R⁄N)																		x											0	0	1	0
(B⁄G)×(NIR⁄B)																													0	0	0	0
(B⁄G)×(NIR⁄G)				x	x							x						x								x			2	1	1	1
(B⁄G)×(NIR⁄R)		x																											1	0	0	0
(B⁄R)×(B⁄N)				x			x							x				x										x	2	1	1	1
(B⁄R)×(G⁄R)			x	x			x			x	x			x			x	x			x			x	x			x	3	3	3	3
(B⁄R)×(G⁄N)																		x											0	0	1	0
(B⁄R)×(NIR⁄R)			x													x	x												1	0	2	0
(B⁄N)×(G⁄N)																													0	0	0	0
(B⁄N)×(R⁄N)						x							x							x							x		1	1	1	1
(G⁄B)×(G⁄R)																													0	0	0	0
(G⁄B)×(G⁄N)			x							x		x					x	x						x		x			1	2	2	2
(G⁄B)×(R⁄B)			x	x			x			x	x						x	x			x			x	x				3	2	3	2
(G⁄B)×(R⁄N)			x							x							x							x					1	1	1	1
(G⁄B)×(NIR⁄B)			x	x							x			x			x	x										x	2	2	2	1
(G⁄B)×(NIR⁄R)				x														x											1	0	1	0
(G⁄R)×(G⁄N)																		x											0	0	1	0
(G⁄R)×(NIR⁄R)						x																							1	0	0	0
(G⁄N)×(R⁄N)			x										x				x										x		1	1	1	1
(R⁄B)×(R⁄G)			x	x			x			x	x			x			x	x			x			x	x			x	3	3	3	3

(R⁄B(×(R⁄N)																x													0	0	1	0
(R⁄B)×(NIR⁄B)				x							x							x										x	1	1	1	1
(R⁄B)×(NIR⁄G)				x							x							x											1	1	1	0
(R⁄G)×(R⁄N)																													0	0	0	0
(R⁄G)×(NIR⁄G)			x	x						x	x						x	x							x				2	2	2	1
(NIR⁄B)×(NIR⁄G)				x						x							x								x				1	1	1	1
(NIR⁄B)×(NIR⁄R)			x							x			x				x			x					x			x	1	2	2	2
(NIR⁄G)×(NIR⁄R)			x							x							x								x			x	1	1	1	2

Appendix F: Full R and significance results per ecoregion

Table F1: PTW Pearson R results: A = Chl-*a* (µg/l), B = DOC (mg/l), C = TSS (mg/l), D = Turbidity (NTU), 1 = Linear curve, 2 = Exponential Curve, 3 = Logarithmic Curve, 4 = Power curve. *P-value < 0.05

Algorithm	**A1**	**A2**	**A3**	**A4**	**B1**	**B2**	**B3**	**B4**	**C1**	**C2**	**C3**	**C4**	**D1**	**D2**	**D3**	**D4**
Blue	-0.04	0.05	0.00	0.08	-0.01	-0.10	-0.02	-0.10	N/A	N/A	N/A	N/A	N/A	N/A	N/A	N/A
Green	0.41	0.47*	0.44	0.51*	-0.30	-0.29	-0.36	-0.35	N/A	N/A	N/A	N/A	N/A	N/A	N/A	N/A
Red	0.56*	0.64*	0.53*	0.64*	-0.19	-0.18	-0.23	-0.21	N/A	N/A	N/A	N/A	N/A	N/A	N/A	N/A
NIR	0.81*	0.86*	0.72*	0.81*	0.04	-0.06	0.07	-0.01	N/A	N/A	N/A	N/A	N/A	N/A	N/A	N/A
B×G	0.18	0.25	0.28	0.37	-0.15	-0.18	-0.23	-0.26	N/A	N/A	N/A	N/A	N/A	N/A	N/A	N/A
B×R	0.30	0.38	0.36	0.47*	-0.10	-0.13	-0.16	-0.18	N/A	N/A	N/A	N/A	N/A	N/A	N/A	N/A
B×N	0.61*	0.67*	0.57*	0.67*	0.03	-0.07	0.04	-0.04	N/A	N/A	N/A	N/A	N/A	N/A	N/A	N/A
G×R	0.46	0.51*	0.49*	0.58*	-0.19	-0.17	-0.29	-0.28	N/A	N/A	N/A	N/A	N/A	N/A	N/A	N/A
G×N	0.75*	0.76*	0.65*	0.74*	-0.08	-0.14	-0.10	-0.15	N/A	N/A	N/A	N/A	N/A	N/A	N/A	N/A
R×N	0.81*	0.82*	0.67*	0.78*	-0.06	-0.12	-0.07	-0.10	N/A	N/A	N/A	N/A	N/A	N/A	N/A	N/A
B⁄G	-0.70*	-0.77*	-0.74*	-0.78*	0.58*	0.48*	0.55*	0.44	N/A	N/A	N/A	N/A	N/A	N/A	N/A	N/A
B⁄R	-0.69*	-0.82*	-0.76*	-0.86*	0.44	0.32	0.39	0.28	N/A	N/A	N/A	N/A	N/A	N/A	N/A	N/A
B⁄N	-0.72*	-0.77*	-0.77*	-0.82*	-0.18	-0.12	-0.14	-0.08	N/A	N/A	N/A	N/A	N/A	N/A	N/A	N/A
G⁄B	0.77*	0.79*	0.74*	0.78*	-0.51*	-0.39	-0.55*	-0.44	N/A	N/A	N/A	N/A	N/A	N/A	N/A	N/A
G⁄R	-0.49*	-0.66*	-0.50*	-0.66*	-0.15	-0.17	-0.13	-0.15	N/A	N/A	N/A	N/A	N/A	N/A	N/A	N/A
G⁄N	-0.40	-0.39	-0.45	-0.48*	-0.37	-0.27	-0.38	-0.27	N/A	N/A	N/A	N/A	N/A	N/A	N/A	N/A
R⁄B	0.83*	0.89*	0.76*	0.86*	-0.35	-0.24	-0.39	-0.28	N/A	N/A	N/A	N/A	N/A	N/A	N/A	N/A
R⁄G	0.49*	0.66*	0.50*	0.66*	0.12	0.14	0.13	0.15	N/A	N/A	N/A	N/A	N/A	N/A	N/A	N/A
R⁄N	-0.30	-0.25	-0.32	-0.29	-0.41	-0.26	-0.43	-0.28	N/A	N/A	N/A	N/A	N/A	N/A	N/A	N/A
NIR⁄B	0.81*	0.85*	0.77*	0.82*	0.11	0.03	0.14	0.08	N/A	N/A	N/A	N/A	N/A	N/A	N/A	N/A
NIR⁄G	0.47*	0.54*	0.45	0.48*	0.38	0.26	0.38	0.27	N/A	N/A	N/A	N/A	N/A	N/A	N/A	N/A
NIR⁄R	0.33	0.33	0.32	0.29	0.45	0.30	0.43	0.28	N/A	N/A	N/A	N/A	N/A	N/A	N/A	N/A

B×G×R	0.26	0.32	0.39	0.49*	-0.12	-0.13	-0.23	-0.24	N/A	N/A	N/A	N/A	N/A	N/A	N/A	N/A
B×G×N	0.51*	0.55*	0.54*	0.63*	-0.02	-0.10	-0.08	-0.14	N/A	N/A	N/A	N/A	N/A	N/A	N/A	N/A
B×R×N	0.61*	0.64*	0.56*	0.67*	-0.01	-0.08	-0.06	-0.10	N/A	N/A	N/A	N/A	N/A	N/A	N/A	N/A
G×R×N	0.70*	0.69*	0.62*	0.72*	-0.08	-0.11	-0.15	-0.18	N/A	N/A	N/A	N/A	N/A	N/A	N/A	N/A
Avg(B;G)	0.23	0.30	0.27	0.35	-0.18	-0.21	-0.21	-0.24	N/A	N/A	N/A	N/A	N/A	N/A	N/A	N/A
Avg(B;R)	0.29	0.37	0.32	0.42	-0.11	-0.15	-0.13	-0.16	N/A	N/A	N/A	N/A	N/A	N/A	N/A	N/A
Avg(B;N)	0.61*	0.69*	0.58*	0.68*	0.02	-0.08	0.02	-0.06	N/A	N/A	N/A	N/A	N/A	N/A	N/A	N/A
Avg(G;R)	0.48*	0.55*	0.48*	0.58*	-0.25	-0.24	-0.30	-0.29	N/A	N/A	N/A	N/A	N/A	N/A	N/A	N/A
Avg(G;N)	0.71*	0.77*	0.66*	0.75*	-0.13	-0.18	-0.15	-0.19	N/A	N/A	N/A	N/A	N/A	N/A	N/A	N/A
Avg(R;N)	0.77*	0.83*	0.69*	0.79*	-0.07	-0.12	-0.06	-0.10	N/A	N/A	N/A	N/A	N/A	N/A	N/A	N/A
N-R	0.68*	0.68*	N/A	N/A	0.32	0.15	N/A	N/A	N/A	N/A	N/A	N/A	N/A	N/A	N/A	N/A
Kab1	0.75*	0.79*	0.64*	0.74*	-0.55*	-0.43	-0.63*	-0.53*	N/A	N/A	N/A	N/A	N/A	N/A	N/A	N/A
NDVI	0.32	0.28	N/A	N/A	0.43	0.28	N/A	N/A	N/A	N/A	N/A	N/A	N/A	N/A	N/A	N/A
NRVI	-0.32	-0.28	N/A	N/A	-0.43	-0.28	N/A	N/A	N/A	N/A	N/A	N/A	N/A	N/A	N/A	N/A
OC2	0.74*	0.78*	N/A	N/A	-0.54*	-0.42	N/A	N/A	N/A	N/A	N/A	N/A	N/A	N/A	N/A	N/A
SABI	0.53*	0.56*	N/A	N/A	0.40	0.24	N/A	N/A	N/A	N/A	N/A	N/A	N/A	N/A	N/A	N/A
(B-R)⁄G	-0.73*	-0.84*	-0.89*	-0.87*	0.52*	0.41	N/A	N/A	N/A	N/A	N/A	N/A	N/A	N/A	N/A	N/A
(NIR⁄G)+(NIR⁄B)	0.67*	0.73*	0.64*	0.67*	0.28	0.18	0.30	0.21	N/A	N/A	N/A	N/A	N/A	N/A	N/A	N/A
G×(B+G+R)	0.32	0.38	0.41	0.49*	-0.20	-0.20	-0.30	-0.30	N/A	N/A	N/A	N/A	N/A	N/A	N/A	N/A
[(1⁄B)-(1⁄G)]×N	0.68*	0.64*	N/A	N/A	-0.55*	-0.44	N/A	N/A	N/A	N/A	N/A	N/A	N/A	N/A	N/A	N/A
[(1⁄R)-(1⁄G)]×N	-0.26	-0.43	-0.19	-0.37	0.31	0.16	0.23	0.09	N/A	N/A	N/A	N/A	N/A	N/A	N/A	N/A
[(1⁄R)-(1⁄B)]×N	-0.57*	-0.62*	-0.73*	-0.70*	0.54*	0.40	N/A	N/A	N/A	N/A	N/A	N/A	N/A	N/A	N/A	N/A
[(1⁄R)-(0.2363×(1⁄G))]×N	0.29	0.27	0.28	0.24	0.47*	0.31	0.44	0.28	N/A	N/A	N/A	N/A	N/A	N/A	N/A	N/A
(R^-1-B^-1)⁄N	-0.46	-0.63*	-0.83*	-0.87*	0.10	0.06	N/A	N/A	N/A	N/A	N/A	N/A	N/A	N/A	N/A	N/A
(B⁄R)×N	0.36	0.41	0.36	0.39	0.25	0.09	0.27	0.13	N/A	N/A	N/A	N/A	N/A	N/A	N/A	N/A
(G⁄R)×N	0.76*	0.79*	0.69*	0.74*	0.02	-0.10	0.04	-0.07	N/A	N/A	N/A	N/A	N/A	N/A	N/A	N/A

(R/B)×N	0.90*	0.91*	0.78*	0.87*	-0.11	-0.14	-0.08	-0.10	N/A	N/A	N/A	N/A	N/A	N/A	N/A	N/A
(R/G)×N	0.82*	0.89*	0.72*	0.83*	0.04	-0.04	0.09	0.03	N/A	N/A	N/A	N/A	N/A	N/A	N/A	N/A
(R×N)/B	0.90*	0.91*	0.78*	0.87*	-0.11	-0.14	-0.08	-0.10	N/A	N/A	N/A	N/A	N/A	N/A	N/A	N/A
(B/G)×(B/R)	-0.65*	-0.79*	-0.77*	-0.84*	0.60*	0.48*	0.50*	0.38	N/A	N/A	N/A	N/A	N/A	N/A	N/A	N/A
(B/G)×(B/N)	-0.76*	-0.86*	-0.86*	-0.91*	0.21	0.19	0.23	0.22	N/A	N/A	N/A	N/A	N/A	N/A	N/A	N/A
(B/G)×(R/G)	-0.51*	-0.46	-0.52*	-0.47*	0.48*	0.41	0.47*	0.40	N/A	N/A	N/A	N/A	N/A	N/A	N/A	N/A
(B/G)×(R/N)	-0.68*	-0.67*	-0.75*	-0.75*	-0.15	-0.01	-0.13	0.01	N/A	N/A	N/A	N/A	N/A	N/A	N/A	N/A
(B/G)×(NIR/B)	0.47*	0.54*	0.45	0.48*	0.38	0.26	0.38	0.27	N/A	N/A	N/A	N/A	N/A	N/A	N/A	N/A
(B/G)×(NIR/G)	-0.04	0.00	-0.02	-0.02	0.50*	0.39	0.46	0.35	N/A	N/A	N/A	N/A	N/A	N/A	N/A	N/A
(B/G)×(NIR/R)	-0.19	-0.22	-0.16	-0.21	0.56*	0.42	0.50*	0.36	N/A	N/A	N/A	N/A	N/A	N/A	N/A	N/A
(B/R)×(B/N)	-0.72*	-0.85*	-0.84*	-0.91*	0.05	0.03	0.11	0.09	N/A	N/A	N/A	N/A	N/A	N/A	N/A	N/A
(B/R)×(G/R)	-0.63*	-0.79*	-0.73*	-0.86*	0.20	0.11	0.20	0.12	N/A	N/A	N/A	N/A	N/A	N/A	N/A	N/A
(B/R)×(G/N)	-0.69*	-0.77*	-0.76*	-0.84*	-0.19	-0.17	-0.14	-0.11	N/A	N/A	N/A	N/A	N/A	N/A	N/A	N/A
(B/R)×(NIR/R)	-0.30	-0.39	-0.29	-0.38	0.59*	0.43	0.49*	0.33	N/A	N/A	N/A	N/A	N/A	N/A	N/A	N/A
(B/N)×(G/N)	-0.51*	-0.51*	-0.65*	-0.69*	-0.30	-0.23	-0.29	-0.20	N/A	N/A	N/A	N/A	N/A	N/A	N/A	N/A
(B/N)×(R/N)	-0.50*	-0.48*	-0.63*	-0.64*	-0.32	-0.22	-0.31	-0.20	N/A	N/A	N/A	N/A	N/A	N/A	N/A	N/A
(G/B)×(G/R)	0.52*	0.48*	0.52*	0.47*	-0.46	-0.38	-0.47*	-0.40	N/A	N/A	N/A	N/A	N/A	N/A	N/A	N/A
(G/B)×(G/N)	-0.02	0.01	0.02	0.02	-0.43	-0.31	-0.46	-0.35	N/A	N/A	N/A	N/A	N/A	N/A	N/A	N/A
(G/B)×(R/B)	0.86*	0.86*	0.77*	0.84*	-0.40	-0.27	-0.50*	-0.38	N/A	N/A	N/A	N/A	N/A	N/A	N/A	N/A
(G/B)×(R/N)	0.11	0.17	0.16	0.21	-0.44	-0.29	-0.50*	-0.36	N/A	N/A	N/A	N/A	N/A	N/A	N/A	N/A
(G/B)×(NIR/B)	0.92*	0.92*	0.86*	0.91*	-0.24	-0.23	-0.23	-0.22	N/A	N/A	N/A	N/A	N/A	N/A	N/A	N/A
(G/B)×(NIR/R)	0.80*	0.80*	0.75*	0.75*	0.11	-0.03	0.13	-0.01	N/A	N/A	N/A	N/A	N/A	N/A	N/A	N/A
(G/R)×(G/N)	-0.45	-0.47*	-0.52*	-0.58*	-0.33	-0.27	-0.32	-0.25	N/A	N/A	N/A	N/A	N/A	N/A	N/A	N/A
(G/R)×(NIR/R)	0.11	0.03	0.13	0.04	0.48*	0.29	0.42	0.24	N/A	N/A	N/A	N/A	N/A	N/A	N/A	N/A
(G/N)×(R/N)	-0.32	-0.26	-0.40	-0.40	-0.38	-0.26	-0.41	-0.28	N/A	N/A	N/A	N/A	N/A	N/A	N/A	N/A
(R/B)×(R/G)	0.81*	0.89*	0.73*	0.86*	-0.20	-0.12	-0.20	-0.12	N/A	N/A	N/A	N/A	N/A	N/A	N/A	N/A

(R⁄B(×(R⁄N)	0.25	0.34	0.29	0.38	-0.40	-0.24	-0.49*	-0.33	N/A	N/A	N/A	N/A	N/A	N/A	N/A	N/A
(R⁄B)×(NIR⁄B)	0.91*	0.92*	0.84*	0.91*	-0.15	-0.14	-0.11	-0.09	N/A	N/A	N/A	N/A	N/A	N/A	N/A	N/A
(R⁄B)×(NIR⁄G)	0.80*	0.87*	0.76*	0.84*	0.09	0.04	0.14	0.11	N/A	N/A	N/A	N/A	N/A	N/A	N/A	N/A
(R⁄G)×(R⁄N)	-0.15	-0.04	-0.13	-0.04	-0.37	-0.19	-0.42	-0.24	N/A	N/A	N/A	N/A	N/A	N/A	N/A	N/A
(R⁄G)×(NIR⁄G)	0.54*	0.65*	0.52*	0.58*	0.31	0.23	0.32	0.25	N/A	N/A	N/A	N/A	N/A	N/A	N/A	N/A
(NIR⁄B)×(NIR⁄G)	0.69*	0.77*	0.65*	0.69*	0.24	0.13	0.29	0.20	N/A	N/A	N/A	N/A	N/A	N/A	N/A	N/A
(NIR⁄B)×(NIR⁄R)	0.67*	0.73*	0.63*	0.64*	0.29	0.15	0.31	0.20	N/A	N/A	N/A	N/A	N/A	N/A	N/A	N/A
(NIR⁄G)×(NIR⁄R)	0.41	0.49*	0.40	0.40	0.42	0.29	0.41	0.28	N/A	N/A	N/A	N/A	N/A	N/A	N/A	N/A

Table F2: BCF Pearson R results: A = Chl-*a* (µg/l), B = Water Colour (TCU), C = TSS (mg/l), D = Turbidity (NTU), 1 = Linear curve, 2 = Exponential Curve, 3 = Logarithmic Curve, 4 = Power curve. *P-value < 0.05

Algorithm	A1	A2	A3	A4	B1	B2	B3	B4	C1	C2	C3	C4	D1	D2	D3	D4
Blue	0.25	0.04	0.24	0.02	0.23	0.28	0.27	0.30	N/A	N/A	N/A	N/A	-0.29	-0.18	-0.31	-0.21
Green	0.77*	0.79*	0.74*	0.79*	-0.10	-0.08	-0.04	-0.03	N/A	N/A	N/A	N/A	-0.16	-0.12	-0.16	-0.12
Red	0.83*	0.87*	0.76*	0.84*	-0.14	-0.13	-0.06	-0.04	N/A	N/A	N/A	N/A	0.44	0.48	0.44	0.49
NIR	0.80*	0.76*	0.71*	0.76*	-0.49*	-0.50*	-0.54*	-0.55*	N/A	N/A	N/A	N/A	0.20	0.33	0.21	0.34
B×G	0.70*	0.65*	0.70*	0.67*	0.00	0.04	0.11	0.13	N/A	N/A	N/A	N/A	-0.21	-0.14	-0.24	-0.16
B×R	0.78*	0.75*	0.74*	0.75*	-0.04	-0.01	0.08	0.10	N/A	N/A	N/A	N/A	0.17	0.24	0.19	0.27
B×N	0.79*	0.70*	0.72*	0.73*	-0.33	-0.33	-0.34	-0.33	N/A	N/A	N/A	N/A	0.06	0.19	0.05	0.18
G×R	0.81*	0.81*	0.76*	0.83*	-0.17	-0.16	-0.05	-0.04	N/A	N/A	N/A	N/A	0.18	0.23	0.20	0.25
G×N	0.77*	0.79*	0.74*	0.79*	-0.10	-0.08	-0.04	-0.03	N/A	N/A	N/A	N/A	-0.16	-0.12	-0.16	-0.12
R×N	0.84*	0.77*	0.74*	0.81*	-0.37	-0.37	-0.36	-0.36	N/A	N/A	N/A	N/A	0.30	0.39	0.34	0.43
B⁄G	-0.64*	-0.80*	-0.68*	-0.82*	0.33	0.35	0.38*	0.40*	N/A	N/A	N/A	N/A	-0.14	-0.07	-0.13	-0.06
B⁄R	-0.63*	-0.81*	-0.71*	-0.86*	0.18	0.19	0.27	0.28	N/A	N/A	N/A	N/A	-0.76*	-0.75*	-0.77*	-0.75*
B⁄N	-0.53*	-0.64*	-0.67*	-0.76*	0.68*	0.70*	0.65*	0.67*	N/A	N/A	N/A	N/A	-0.46	-0.56*	-0.44	-0.54*
G⁄B	0.71*	0.83*	0.68*	0.82*	-0.41*	-0.43*	-0.38*	-0.40*	N/A	N/A	N/A	N/A	0.13	0.06	0.13	0.06
G⁄R	-0.49*	-0.63*	-0.51*	-0.64*	0.04	0.04	0.07	0.07	N/A	N/A	N/A	N/A	-0.82*	-0.85*	-0.84*	-0.86*
G⁄N	-0.45*	-0.52*	-0.54*	-0.57*	0.69*	0.71*	0.66*	0.68*	N/A	N/A	N/A	N/A	-0.40	-0.54*	-0.39	-0.52*
R⁄B	0.78*	0.90*	0.71*	0.86*	-0.35	-0.36	-0.27	-0.28	N/A	N/A	N/A	N/A	0.78*	0.75*	0.77*	0.75*
R⁄G	0.53*	0.65*	0.51*	0.64*	-0.10	-0.10	-0.07	-0.07	N/A	N/A	N/A	N/A	0.85*	0.86*	0.84*	0.86*
R⁄N	-0.43*	-0.44*	-0.48*	-0.48*	0.68*	0.71*	0.65*	0.67*	N/A	N/A	N/A	N/A	0.29	0.15	0.23	0.09
NIR⁄B	0.76*	0.78*	0.67*	0.76*	-0.61*	-0.63*	-0.65*	-0.67*	N/A	N/A	N/A	N/A	0.42	0.52*	0.44	0.54*
NIR⁄G	0.60*	0.58*	0.54*	0.57*	-0.60*	-0.62*	-0.66*	-0.68*	N/A	N/A	N/A	N/A	0.38	0.50*	0.39	0.52*
NIR⁄R	0.53*	0.49*	0.48*	0.48*	-0.59*	-0.61*	-0.65*	-0.67*	N/A	N/A	N/A	N/A	-0.17	-0.04	-0.23	-0.09
B×G×R	0.76*	0.72*	0.75*	0.78*	-0.12	-0.09	0.04	0.06	N/A	N/A	N/A	N/A	0.05	0.12	0.08	0.14

B×G×N	0.78*	0.70*	0.76*	0.77*	-0.28	-0.27	-0.25	-0.24	N/A	N/A	N/A	N/A	0.00	0.11	-0.01	0.10
B×R×N	0.81*	0.71*	0.75*	0.78*	-0.28	-0.27	-0.24	-0.23	N/A	N/A	N/A	N/A	0.17	0.28	0.21	0.32
G×R×N	0.77*	0.79*	0.74*	0.79*	-0.10	-0.08	-0.04	-0.03	N/A	N/A	N/A	N/A	-0.16	-0.12	-0.16	-0.12
Avg(B;G)	0.69*	0.63*	0.69*	0.63*	0.10	0.13	0.15	0.18	N/A	N/A	N/A	N/A	-0.25	-0.16	-0.26	-0.18
Avg(B;R)	0.73*	0.66*	0.72*	0.66*	0.10	0.14	0.16	0.18	N/A	N/A	N/A	N/A	-0.05	0.04	-0.05	0.04
Avg(B;N)	0.79*	0.70*	0.77*	0.72*	-0.11	-0.09	-0.07	-0.04	N/A	N/A	N/A	N/A	-0.14	-0.02	-0.16	-0.03
Avg(G;R)	0.81*	0.83*	0.76*	0.82*	-0.12	-0.10	-0.05	-0.04	N/A	N/A	N/A	N/A	0.09	0.14	0.10	0.14
Avg(G;N)	0.84*	0.81*	0.77*	0.81*	-0.33	-0.33	-0.31	-0.31	N/A	N/A	N/A	N/A	-0.01	0.07	-0.02	0.07
Avg(R;N)	0.84*	0.81*	0.75*	0.81*	-0.37	-0.37	-0.33	-0.33	N/A	N/A	N/A	N/A	0.34	0.43	0.36	0.45
N-R	0.67*	0.59*	N/A	N/A	-0.56*	-0.59*	N/A	N/A	N/A	N/A	N/A	N/A	-0.34	-0.23	N/A	N/A
Kab1	0.68*	0.82*	N/A	N/A	-0.39*	-0.41*	N/A	N/A	N/A	N/A	N/A	N/A	0.15	0.08	N/A	N/A
NDVI	0.47*	0.48*	N/A	N/A	-0.64*	-0.67*	N/A	N/A	N/A	N/A	N/A	N/A	-0.22	-0.08	N/A	N/A
NRVI	-0.47*	-0.48*	N/A	N/A	0.64*	0.67*	N/A	N/A	N/A	N/A	N/A	N/A	0.22	0.08	0.01	-0.10
OC2	0.65*	0.80*	N/A	N/A	-0.27	-0.28	N/A	N/A	N/A	N/A	N/A	N/A	0.15	0.08	N/A	N/A
SABI	0.61*	0.56*	N/A	N/A	-0.56*	-0.58*	N/A	N/A	N/A	N/A	N/A	N/A	-0.42	-0.29	N/A	N/A
(B-R)/G	-0.67*	-0.83*	-0.80*	-0.90*	0.30	0.31	0.38*	0.40*	N/A	N/A	N/A	N/A	-0.47	-0.41	-0.48	-0.42
(NIR/G)+(NIR/B)	0.70*	0.70*	0.62*	0.69*	-0.61*	-0.64*	-0.67*	-0.69*	N/A	N/A	N/A	N/A	0.40	0.52*	0.42	0.54*
G×(B+G+R)	0.76*	0.74*	0.75*	0.78*	-0.09	-0.06	0.02	0.04	N/A	N/A	N/A	N/A	-0.13	-0.06	-0.13	-0.07
[(1/B)-(1/G)]×N	0.63*	0.72*	N/A	N/A	0.32	0.32	N/A	N/A	N/A	N/A	N/A	N/A	-0.26	-0.39	N/A	N/A
[(1/R)-(1/G)]×N	-0.04	-0.11	-0.03	-0.12	-0.42*	-0.43*	-0.45*	-0.47*	N/A	N/A	N/A	N/A	-0.63*	-0.54*	-0.67*	-0.57*
[(1/R)-(1/B)]×N	-0.56*	-0.67*	-0.62*	-0.72*	-0.39*	-0.40*	-0.42*	-0.44*	N/A	N/A	N/A	N/A	-0.40	-0.28	-0.46	-0.34
[(1/R)-(0.2363×(1/G))]×N	0.51*	0.47*	0.46*	0.45*	-0.58*	-0.60*	-0.63*	-0.66*	N/A	N/A	N/A	N/A	-0.25	-0.13	-0.32	-0.18
(R^-1-B^-1)/N	-0.44*	-0.57*	-0.80*	-0.86*	0.18	0.18	0.38*	0.38*	N/A	N/A	N/A	N/A	-0.44	-0.52*	-0.42	-0.50*
(B/R)×N	0.61*	0.50*	0.55*	0.47*	-0.44*	-0.44*	-0.46*	-0.46*	N/A	N/A	N/A	N/A	-0.26	-0.11	-0.33	-0.17
(G/R)×N	0.78*	0.74*	0.71*	0.73*	-0.52*	-0.53*	-0.59*	-0.59*	N/A	N/A	N/A	N/A	-0.21	-0.09	-0.27	-0.14
(R/B)×N	0.86*	0.82*	0.73*	0.82*	-0.49*	-0.50*	-0.47*	-0.49*	N/A	N/A	N/A	N/A	0.47	0.54*	0.49	0.57*

(R/G)×N	0.80*	0.75*	0.70*	0.76*	-0.47*	-0.48*	-0.48*	-0.49*	N/A	N/A	N/A	N/A	0.47	0.56*	0.50*	0.60*
(R×N)/B	0.86*	0.82*	0.73*	0.82*	-0.49*	-0.50*	-0.47*	-0.49*	N/A	N/A	N/A	N/A	0.47	0.54*	0.49	0.57*
(B/G)×(B/R)	-0.59*	-0.77*	-0.71*	-0.86*	0.18	0.19	0.31	0.33	N/A	N/A	N/A	N/A	-0.59*	-0.56*	-0.62*	-0.58*
(B/G)×(B/N)	-0.52*	-0.66*	-0.70*	-0.81*	0.61*	0.63*	0.60*	0.63*	N/A	N/A	N/A	N/A	-0.43	-0.49	-0.42	-0.48
(B/G)×(R/G)	-0.49*	-0.59*	-0.50*	-0.59*	0.59*	0.63*	0.59*	0.62*	N/A	N/A	N/A	N/A	0.66*	0.71*	0.64*	0.69*
(B/G)×(R/N)	-0.55*	-0.64*	-0.66*	-0.73*	0.74*	0.76*	0.70*	0.73*	N/A	N/A	N/A	N/A	0.20	0.09	0.16	0.06
(B/G)×(NIR/B)	0.60*	0.58*	0.54*	0.57*	-0.60*	-0.62*	-0.66*	-0.68*	N/A	N/A	N/A	N/A	0.38	0.50*	0.39	0.52*
(B/G)×(NIR/G)	0.19	0.10	0.10	0.03	-0.44*	-0.44*	-0.49*	-0.50*	N/A	N/A	N/A	N/A	0.28	0.42	0.29	0.42
(B/G)×(NIR/R)	-0.03	-0.18	-0.11	-0.25	-0.36	-0.37	-0.40*	-0.42*	N/A	N/A	N/A	N/A	-0.19	-0.05	-0.24	-0.10
(B/R)×(B/N)	-0.48*	-0.63*	-0.70*	-0.81*	0.49*	0.51*	0.55*	0.57*	N/A	N/A	N/A	N/A	-0.66*	-0.72*	-0.66*	-0.71*
(B/R)×(G/R)	-0.57*	-0.75*	-0.69*	-0.85*	0.09	0.10	0.22	0.23	N/A	N/A	N/A	N/A	-0.81*	-0.83*	-0.83*	-0.83*
(B/R)×(G/N)	-0.49*	-0.62*	-0.66*	-0.76*	0.58*	0.59*	0.58*	0.60*	N/A	N/A	N/A	N/A	-0.69*	-0.77*	-0.68*	-0.76*
(B/R)×(NIR/R)	-0.30	-0.50*	-0.34	-0.54*	-0.30	-0.30	-0.32	-0.33	N/A	N/A	N/A	N/A	-0.58*	-0.49	-0.63*	-0.53*
(B/N)×(G/N)	-0.41*	-0.51*	-0.63*	-0.70*	0.71*	0.74*	0.66*	0.69*	N/A	N/A	N/A	N/A	-0.45	-0.58*	-0.43	-0.54*
(B/N)×(R/N)	-0.43*	-0.51*	-0.62*	-0.68*	0.74*	0.76*	0.69*	0.71*	N/A	N/A	N/A	N/A	-0.12	-0.26	-0.15	-0.28
(G/B)×(G/R)	0.49*	0.58*	0.50*	0.59*	-0.58*	-0.62*	-0.59*	-0.62*	N/A	N/A	N/A	N/A	-0.61*	-0.68*	-0.64*	-0.69*
(G/B)×(G/N)	-0.04	0.00	-0.10	-0.03	0.54*	0.55*	0.49*	0.50*	N/A	N/A	N/A	N/A	-0.29	-0.43	-0.29	-0.42
(G/B)×(R/B)	0.79*	0.89*	0.71*	0.86*	-0.41*	-0.43*	-0.31	-0.33	N/A	N/A	N/A	N/A	0.64*	0.59*	0.62*	0.58*
(G/B)×(R/N)	0.18	0.31	0.11	0.25	0.44*	0.46*	0.40*	0.42*	N/A	N/A	N/A	N/A	0.30	0.15	0.24	0.10
(G/B)×(NIR/B)	0.83*	0.85*	0.70*	0.81*	-0.58*	-0.61*	-0.60*	-0.63*	N/A	N/A	N/A	N/A	0.40	0.46	0.42	0.48
(G/B)×(NIR/R)	0.74*	0.76*	0.66*	0.73*	-0.65*	-0.68*	-0.70*	-0.73*	N/A	N/A	N/A	N/A	-0.12	-0.02	-0.16	-0.06
(G/R)×(G/N)	-0.44*	-0.54*	-0.55*	-0.61*	0.63*	0.65*	0.61*	0.63*	N/A	N/A	N/A	N/A	-0.65*	-0.75*	-0.65*	-0.75*
(G/R)×(NIR/R)	0.37*	0.29	0.33	0.26	-0.52*	-0.54*	-0.57*	-0.59*	N/A	N/A	N/A	N/A	-0.62*	-0.54*	-0.65*	-0.57*
(G/N)×(R/N)	-0.38*	-0.43*	-0.52*	-0.54*	0.71*	0.74*	0.66*	0.68*	N/A	N/A	N/A	N/A	-0.07	-0.22	-0.12	-0.26
(R/B)×(R/G)	0.78*	0.89*	0.69*	0.85*	-0.32	-0.34	-0.22	-0.23	N/A	N/A	N/A	N/A	0.85*	0.83*	0.83*	0.83*
(R/B(×(R/N)	0.39*	0.57*	0.34	0.54*	0.33	0.34	0.32	0.33	N/A	N/A	N/A	N/A	0.67*	0.56*	0.63*	0.53*

(R/B)×(NIR/B)	0.84*	0.85*	0.70*	0.81*	-0.56*	-0.58*	-0.55*	-0.57*	N/A	N/A	N/A	N/A	0.65*	0.69*	0.66*	0.71*
(R/B)×(NIR/G)	0.77*	0.77*	0.66*	0.76*	-0.57*	-0.59*	-0.58*	-0.60*	N/A	N/A	N/A	N/A	0.67*	0.73*	0.68*	0.76*
(R/G)×(R/N)	-0.30	-0.23	-0.33	-0.26	0.61*	0.64*	0.57*	0.59*	N/A	N/A	N/A	N/A	0.69*	0.59*	0.65*	0.57*
(R/G)×(NIR/G)	0.62*	0.60*	0.55*	0.61*	-0.56*	-0.58*	-0.61*	-0.63*	N/A	N/A	N/A	N/A	0.64*	0.73*	0.65*	0.75*
(NIR/B)×(NIR/G)	0.70*	0.62*	0.63*	0.70*	-0.54*	-0.57*	-0.66*	-0.69*	N/A	N/A	N/A	N/A	0.39	0.50*	0.43	0.54*
(NIR/B)×(NIR/R)	0.69*	0.63*	0.62*	0.68*	-0.55*	-0.58*	-0.69*	-0.71*	N/A	N/A	N/A	N/A	0.18	0.30	0.15	0.28
(NIR/G)×(NIR/R)	0.59*	0.51*	0.52*	0.54*	-0.52*	-0.54*	-0.66*	-0.68*	N/A	N/A	N/A	N/A	0.16	0.29	0.12	0.26

Table F3: TCF Pearson R results: A = Chl-*a* (µg/l), B = Water Colour (TCU), C = TSS (mg/l), D = Turbidity (NTU), 1 = Linear curve, 2 = Exponential Curve, 3 = Logarithmic Curve, 4 = Power curve. *P-value < 0.05

Algorithm	A1	A2	A3	A4	B1	B2	B3	B4	C1	C2	C3	C4	D1	D2	D3	D4
Blue	0.60*	0.55*	0.54*	0.51*	-0.02	0.08	-0.05	0.03	-0.04	-0.05	-0.01	-0.03	-0.05	-0.12	-0.02	-0.08
Green	0.66*	0.68*	0.57*	0.63*	-0.06	0.02	-0.11	-0.05	0.27	0.19	0.26	0.18	0.66*	0.46*	0.52*	0.39
Red	0.69*	0.71*	0.59*	0.66*	0	0.09	-0.01	0.02	0.31	0.26	0.3	0.25	0.68*	0.49*	0.55*	0.42
NIR	0.54*	0.50*	0.46*	0.44*	-0.06	0	-0.12	-0.14	-0.21	-0.24	-0.2	-0.25	-0.1	-0.23	-0.13	-0.25
B×G	0.70*	0.65*	0.57*	0.60*	0	0.1	-0.08	-0.02	0.09	0.06	0.14	0.09	0.54*	0.33	0.35	0.24
B×R	0.72*	0.67*	0.59*	0.63*	0.02	0.12	-0.03	0.03	0.12	0.1	0.16	0.13	0.54*	0.34	0.38	0.26
B×N	0.64*	0.56*	0.52*	0.50*	0	0.09	-0.1	-0.09	-0.16	-0.17	-0.14	-0.19	-0.08	-0.21	-0.09	-0.2
G×R	0.73*	0.69*	0.58*	0.65*	0.01	0.11	-0.06	-0.01	0.29	0.24	0.29	0.22	0.73*	0.48*	0.54*	0.41
G×N	0.68*	0.61*	0.54*	0.56*	-0.06	0.02	-0.11	-0.05	0.27	0.19	0.26	0.18	0.66*	0.46*	0.52*	0.39
R×N	0.71*	0.63*	0.55*	0.58*	0.01	0.11	-0.08	-0.07	-0.05	-0.06	-0.01	-0.07	0.51*	0.29	0.33	0.19
B⁄G	-0.39*	-0.55*	-0.40*	-0.56*	0.21	0.24	0.21	0.22	-0.62*	-0.45	-0.70*	-0.51*	-0.62*	-0.53*	-0.72*	-0.58*
B⁄R	-0.43*	-0.59*	-0.48*	-0.64*	-0.03	0.02	-0.03	-0.01	-0.74*	-0.67*	-0.79*	-0.70*	-0.56*	-0.50*	-0.67*	-0.56*
B⁄N	-0.24*	-0.24*	-0.27*	-0.27*	0.11	0.21	0.14	0.21	0.24	0.31	0.28	0.34	0.1	0.18	0.1	0.18
G⁄B	0.40*	0.56*	0.40*	0.56*	-0.2	-0.2	-0.21	-0.22	0.76*	0.57*	0.70*	0.51*	0.78*	0.60*	0.72*	0.58*
G⁄R	-0.38*	-0.47*	-0.40*	-0.49*	-0.25	-0.21	-0.27	-0.25	-0.1	-0.22	-0.09	-0.22	-0.04	-0.08	-0.04	-0.07
G⁄N	-0.11	-0.03	-0.10	-0.03	0.08	0.18	0.1	0.19	0.66*	0.61*	0.57*	0.57*	0.70*	0.60*	0.66*	0.59*
R⁄B	0.51*	0.66*	0.48*	0.64*	0.02	0.03	0.03	0.01	0.83*	0.73*	0.79*	0.70*	0.76*	0.59*	0.67*	0.56*
R⁄G	0.42*	0.50*	0.40*	0.49*	0.29	0.28	0.27	0.25	0.08	0.22	0.09	0.22	0.04	0.06	0.04	0.07
R⁄N	0.01	0.14	0.03	0.15	0.21	0.29	0.23	0.32*	0.55*	0.55*	0.50*	0.53*	0.75*	0.65*	0.71*	0.65*
NIR⁄B	0.25*	0.26*	0.27*	0.27*	-0.14	-0.18	-0.14	-0.21	-0.3	-0.35	-0.28	-0.34	-0.11	-0.18	-0.1	-0.18
NIR⁄G	0.05	0.01	0.10	0.03	-0.11	-0.18	-0.1	-0.19	-0.50*	-0.54*	-0.57*	-0.57*	-0.59*	-0.57*	-0.66*	-0.59*
NIR⁄R	-0.06	-0.14	-0.03	-0.15	-0.23	-0.33*	-0.23	-0.32*	-0.46	-0.52*	-0.50*	-0.53*	-0.64*	-0.62*	-0.71*	-0.65*
B×G×R	0.74*	0.65*	0.58*	0.63*	0.04	0.13	-0.05	0	0.15	0.12	0.2	0.15	0.68*	0.43	0.44*	0.32

B×G×N	0.70*	0.65*	0.57*	0.60*	0.04	0.13	-0.11	-0.08	-0.08	-0.09	-0.02	-0.08	0.42	0.2	0.24	0.1
B×R×N	0.70*	0.65*	0.57*	0.60*	0.05	0.13	-0.07	-0.05	-0.06	-0.06	-0.01	-0.06	0.42	0.2	0.25	0.12
G×R×N	0.73*	0.63*	0.57*	0.61*	-0.06	0.02	-0.11	-0.05	0.27	0.19	0.26	0.18	0.66*	0.46*	0.52*	0.39
Avg(B;G)	0.65*	0.63*	0.57*	0.59*	-0.04	0.05	-0.08	-0.01	0.12	0.07	0.14	0.09	0.46*	0.28	0.36	0.23
Avg(B;R)	0.66*	0.64*	0.59*	0.61*	-0.01	0.08	-0.03	0.03	0.11	0.08	0.13	0.1	0.39	0.23	0.32	0.2
Avg(B;N)	0.60*	0.55*	0.53*	0.52*	-0.05	0.03	-0.1	-0.06	-0.15	-0.18	-0.14	-0.18	-0.08	-0.19	-0.08	-0.18
Avg(G;R)	0.68*	0.70*	0.58*	0.65*	-0.04	0.05	-0.07	-0.02	0.29	0.22	0.28	0.21	0.68*	0.47*	0.54*	0.41
Avg(G;N)	0.63*	0.61*	0.54*	0.57*	-0.07	0.01	-0.12	-0.11	-0.04	-0.09	-0.01	-0.09	0.48*	0.27	0.36	0.2
Avg(R;N)	0.63*	0.61*	0.53*	0.56*	-0.04	0.03	-0.09	-0.09	-0.07	-0.11	-0.04	-0.11	0.4	0.2	0.3	0.14
N-R	0.26*	0.19	N/A	N/A	-0.12	-0.09	N/A	N/A	-0.43	-0.45	N/A	N/A	-0.80*	-0.70*	N/A	N/A
Kab1	0.37*	0.54*	N/A	N/A	-0.21	-0.24	N/A	N/A	0.71*	0.52*	0.54*	0.37	0.72*	0.59*	N/A	N/A
NDVI	-0.03	-0.15	N/A	N/A	-0.23	-0.32*	N/A	N/A	-0.50*	-0.53*	N/A	N/A	-0.71*	-0.65*	N/A	N/A
NRVI	0.03	0.15	N/A	N/A	0.23	0.32*	N/A	N/A	0.50*	0.53*	N/A	N/A	0.71*	0.65*	N/A	N/A
OC2	0.38*	0.54*	N/A	N/A	-0.21	-0.25	N/A	N/A	0.73*	0.53*	N/A	N/A	0.71*	0.51*	N/A	N/A
SABI	0.02	-0.03	N/A	N/A	-0.19	-0.26	N/A	N/A	-0.46	-0.51*	N/A	N/A	-0.69*	-0.64*	N/A	N/A
(B-R)⁄G	-0.46*	-0.62*	-0.48*	-0.62*	0.07	0.1	0.08	0.07	-0.77*	-0.64*	-0.89*	-0.71*	-0.59*	-0.51*	N/A	N/A
(NIR⁄G)+(NIR⁄B)	0.14	0.12	0.18	0.14	-0.12	-0.18	-0.12	-0.2	-0.41	-0.45	-0.43	-0.46	-0.46*	-0.47*	-0.48*	-0.48*
G×(B+G+R)	0.72*	0.68*	0.58*	0.63*	0	0.1	-0.08	-0.03	0.21	0.16	0.23	0.16	0.69*	0.45*	0.49*	0.35
[(1⁄B)-(1⁄G)]×N	0.23*	0.33*	N/A	N/A	-0.06	0.06	N/A	N/A	0.88*	0.82*	N/A	N/A	0.69*	0.61*	N/A	N/A
[(1⁄R)-(1⁄G)]×N	-0.30*	-0.41*	-0.30*	-0.43*	-0.36*	-0.49*	-0.40*	-0.48*	-0.36	-0.44	-0.34	-0.43	-0.48*	-0.48*	-0.51*	-0.46*
[(1⁄R)-(1⁄B)]×N	-0.30	-0.41	-0.35	-0.49	-0.24	-0.37*	-0.23	-0.35*	-0.58*	-0.63*	-0.77*	-0.72*	-0.66*	-0.61*	N/A	N/A
[(1⁄R)-(0.2363×(1⁄G))]×N	-0.09	-0.17	-0.06	-0.18	-0.25	-0.36*	-0.25	-0.35*	-0.45	-0.51*	-0.48*	-0.52*	-0.64*	-0.62*	-0.71*	-0.65*
(R^-1-B^-1)⁄N	-0.23*	-0.32*	-0.58*	-0.64*	0.04	0.16	0.07	0.06	-0.19	-0.08	-0.28	-0.18	-0.17	-0.1	N/A	N/A
(B⁄R)×N	0.31*	0.22*	0.29*	0.18	-0.12	-0.1	-0.19	-0.21	-0.35	-0.4	-0.38	-0.41	-0.68*	-0.70*	-0.71*	-0.69*
(G⁄R)×N	0.46*	0.42*	0.41*	0.37*	-0.12	-0.09	-0.2	-0.22	-0.23	-0.28	-0.19	-0.26	-0.13	-0.27	-0.14	-0.27
(R⁄B)×N	0.64*	0.62*	0.51*	0.55*	-0.04	0.04	-0.08	-0.1	-0.04	-0.06	-0.01	-0.08	0.59*	0.38	0.42	0.27

(R/G)×N	0.59*	0.55*	0.47*	0.48*	-0.02	0.05	-0.06	-0.08	-0.19	-0.2	-0.2	-0.23	-0.06	-0.16	-0.09	-0.19
(R×N)/B	0.64*	0.62*	0.51*	0.55*	-0.04	0.04	-0.08	-0.1	-0.04	-0.06	-0.01	-0.08	0.59*	0.38	0.42	0.27
(B/G)×(B/R)	-0.40*	-0.56*	-0.46*	-0.63*	0.05	0.12	0.06	0.08	-0.71*	-0.59*	-0.81*	-0.66*	-0.47*	-0.43	-0.71*	-0.58*
(B/G)×(B/N)	-0.28*	-0.33*	-0.36*	-0.42*	0.13	0.23	0.16	0.22	-0.02	0.11	0.03	0.14	-0.33	-0.22	-0.47*	-0.32
(B/G)×(R/G)	-0.11	-0.19	-0.10	-0.20	0.57*	0.54*	0.55*	0.53*	-0.34	-0.16	-0.41	-0.22	-0.56*	-0.47*	-0.67*	-0.53*
(B/G)×(R/N)	-0.17	-0.12	-0.16	-0.13	0.23	0.3	0.25	0.33*	0.2	0.29	0.25	0.33	0.14	0.24	0.15	0.25
(B/G)×(NIR/B)	0.05	0.01	0.10	0.03	-0.11	-0.18	-0.1	-0.19	-0.50*	-0.54*	-0.57*	-0.57*	-0.59*	-0.57*	-0.66*	-0.59*
(B/G)×(NIR/G)	-0.09	-0.15	-0.07	-0.20	-0.04	-0.14	-0.03	-0.14	-0.68*	-0.69*	-0.81*	-0.73*	-0.58*	-0.55*	-0.73*	-0.63*
(B/G)×(NIR/R)	-0.18	-0.27*	-0.19	-0.34*	-0.17	-0.28	-0.16	-0.27	-0.60*	-0.65*	-0.73*	-0.70*	-0.58*	-0.56*	-0.75*	-0.65*
(B/R)×(B/N)	-0.28*	-0.35*	-0.40*	-0.47*	0.06	0.17	0.09	0.15	-0.03	0.08	0.01	0.1	-0.31	-0.22	-0.42	-0.3
(B/R)×(G/R)	-0.39*	-0.53*	-0.48*	-0.62*	-0.1	-0.03	-0.12	-0.09	-0.49*	-0.51*	-0.57*	-0.58*	-0.49*	-0.45*	-0.58*	-0.49*
(B/R)×(G/N)	-0.26*	-0.30*	-0.33*	-0.35*	0.04	0.14	0.06	0.12	0.3	0.33	0.3	0.33	0.07	0.12	0.06	0.11
(B/R)×(NIR/R)	-0.27*	-0.39*	-0.29*	-0.46*	-0.25	-0.35*	-0.26	-0.34*	-0.53*	-0.59*	-0.64*	-0.64*	-0.55*	-0.54*	-0.74*	-0.65*
(B/N)×(G/N)	-0.16	-0.14	-0.19	-0.16	0.06	0.16	0.13	0.21	0.47*	0.47*	0.42	0.46	0.47*	0.46*	0.48*	0.48*
(B/N)×(R/N)	-0.13	-0.08	-0.13	-0.08	0.11	0.19	0.18	0.27	0.41	0.43	0.4	0.45	0.51*	0.50*	0.53*	0.53*
(G/B)×(G/R)	0.08	0.20	0.10	0.20	-0.52*	-0.52*	-0.55*	-0.53*	0.48*	0.29	0.41	0.22	0.74*	0.55*	0.67*	0.53*
(G/B)×(G/N)	0.04	0.19	0.07	0.20	0.02	0.12	0.03	0.14	0.89*	0.73*	0.81*	0.73*	0.80*	0.61*	0.73*	0.63*
(G/B)×(R/B)	0.47*	0.62*	0.46*	0.63*	-0.08	-0.05	-0.06	-0.08	0.88*	0.71*	0.81*	0.66*	0.81*	0.58*	0.71*	0.58*
(G/B)×(R/N)	0.15	0.32*	0.19	0.34*	0.15	0.24	0.16	0.27	0.84*	0.72*	0.73*	0.70*	0.82*	0.63*	0.75*	0.65*
(G/B)×(NIR/B)	0.38*	0.44*	0.36*	0.42*	-0.15	-0.16	-0.16	-0.22	-0.07	-0.15	-0.03	-0.14	0.60*	0.41	0.47*	0.32
(G/B)×(NIR/R)	0.13	0.13	0.16	0.13	-0.24	-0.32*	-0.25	-0.33*	-0.29	-0.36	-0.25	-0.33	-0.16	-0.25	-0.15	-0.25
(G/R)×(G/N)	-0.19	-0.16	-0.20	-0.16	0	0.1	0.01	0.09	0.74*	0.64*	0.63*	0.58*	0.64*	0.53*	0.56*	0.50*
(G/R)×(NIR/R)	-0.19	-0.29*	-0.17	-0.31*	-0.32*	-0.44*	-0.34*	-0.43*	-0.41	-0.48*	-0.44	-0.49*	-0.59*	-0.59*	-0.68*	-0.64*
(G/N)×(R/N)	-0.06	0.05	-0.04	0.06	0.1	0.18	0.16	0.26	0.68*	0.61*	0.54*	0.55*	0.74*	0.61*	0.69*	0.63*
(R/B)×(R/G)	0.54*	0.66*	0.48*	0.62*	0.11	0.13	0.12	0.09	0.64*	0.64*	0.57*	0.58*	0.65*	0.50*	0.58*	0.49*
(R/B(×(R/N)	0.24*	0.41*	0.29*	0.46*	0.27	0.32*	0.26	0.34*	0.77*	0.69*	0.64*	0.64*	0.83*	0.64*	0.74*	0.65*

(R⁄B)×(NIR⁄B)	0.43*	0.50*	0.40*	0.47*	-0.09	-0.07	-0.09	-0.15	-0.03	-0.09	-0.01	-0.1	0.52*	0.35	0.42	0.3
(R⁄B)×(NIR⁄G)	0.33*	0.35*	0.33*	0.35*	-0.06	-0.06	-0.06	-0.12	-0.29	-0.31	-0.3	-0.33	-0.06	-0.11	-0.06	-0.11
(R⁄G)×(R⁄N)	0.14	0.29*	0.17	0.31*	0.36*	0.40*	0.34*	0.43*	0.46	0.49*	0.44	0.49*	0.75*	0.66*	0.68*	0.64*
(R⁄G)×(NIR⁄G)	0.14	0.12	0.20	0.16	0	-0.04	-0.01	-0.09	-0.53*	-0.52*	-0.63*	-0.58*	-0.45*	-0.44*	-0.56*	-0.50*
(NIR⁄B)×(NIR⁄G)	0.08	0.09	0.19	0.16	-0.11	-0.14	-0.13	-0.21	-0.38	-0.44	-0.42	-0.46	-0.43	-0.44*	-0.48*	-0.48*
(NIR⁄B)×(NIR⁄R)	0.04	0.04	0.13	0.08	-0.16	-0.23	-0.18	-0.27	-0.38	-0.45	-0.4	-0.45	-0.51*	-0.52*	-0.53*	-0.53*
(NIR⁄G)×(NIR⁄R)	-0.04	-0.06	0.04	-0.06	-0.15	-0.24	-0.16	-0.26	-0.44	-0.52*	-0.54*	-0.55*	-0.57*	-0.58*	-0.69*	-0.63*

Table F4: TPS Pearson R results: A = Chl-*a* (μg/l), B = Water Colour (TCU), C = TSS (mg/l), D = Turbidity (NTU), 1 = Linear curve, 2 = Exponential Curve, 3 = Logarithmic Curve, 4 = Power curve. *P-value < 0.05

Algorithm	A1	A2	A3	A4	B1	B2	B3	B4	C1	C2	C3	C4	D1	D2	D3	D4
Blue	0.46*	0.46*	0.49*	0.52*	N/A	N/A	N/A	N/A	0.34	0.42*	0.35	0.43*	-0.06	0.00	-0.06	0.00
Green	0.45*	0.47*	0.46*	0.52*	N/A	N/A	N/A	N/A	0.69*	0.76*	0.62*	0.72*	0.18	0.21	0.18	0.21
Red	0.40	0.40	0.43*	0.49*	N/A	N/A	N/A	N/A	0.71*	0.80*	0.65*	0.77*	0.34*	0.39*	0.35*	0.41*
NIR	0.51*	0.50*	0.54*	0.62*	N/A	N/A	N/A	N/A	0.25	0.03	0.18	-0.04	0.49*	0.47*	0.50*	0.48*
B×G	0.43*	0.42*	0.48*	0.53*	N/A	N/A	N/A	N/A	0.58*	0.64*	0.52*	0.61*	0.07	0.10	0.07	0.12
B×R	0.41*	0.37	0.47*	0.52*	N/A	N/A	N/A	N/A	0.61*	0.69*	0.56*	0.66*	0.18	0.23	0.20	0.26
B×N	0.47*	0.42*	0.54*	0.60*	N/A	N/A	N/A	N/A	0.34	0.21	0.27	0.16	0.37*	0.37*	0.41*	0.41*
G×R	0.41*	0.37	0.45*	0.51*	N/A	N/A	N/A	N/A	0.74*	0.78*	0.64*	0.75*	0.28	0.31	0.28	0.33*
G×N	0.45*	0.47*	0.46*	0.52*	N/A	N/A	N/A	N/A	0.69*	0.76*	0.62*	0.72*	0.18	0.21	0.18	0.21
R×N	0.42*	0.35	0.51*	0.58*	N/A	N/A	N/A	N/A	0.67*	0.54*	0.51*	0.46*	0.47*	0.46*	0.48*	0.49*
B⁄G	0.08	-0.02	0.09	0.00	N/A	N/A	N/A	N/A	-0.76*	-0.87*	-0.79*	-0.88*	-0.40*	-0.37*	-0.41*	-0.37*
B⁄R	-0.14	-0.26	-0.11	-0.21	N/A	N/A	N/A	N/A	-0.75*	-0.90*	-0.79*	-0.91*	-0.56*	-0.58*	-0.56*	-0.58*
B⁄N	-0.44*	-0.56*	-0.42*	-0.52*	N/A	N/A	N/A	N/A	0.07	0.41*	0.06	0.40*	-0.49*	-0.45*	-0.52*	-0.48*
G⁄B	-0.10	-0.01	-0.09	0.00	N/A	N/A	N/A	N/A	0.81*	0.89*	0.79*	0.88*	0.40*	0.37*	0.41*	0.37*
G⁄R	-0.25	-0.29	-0.22	-0.25	N/A	N/A	N/A	N/A	-0.54*	-0.66*	-0.55*	-0.67*	-0.45*	-0.52*	-0.43*	-0.50*
G⁄N	-0.43*	-0.50*	-0.42*	-0.48*	N/A	N/A	N/A	N/A	0.31	0.62*	0.36	0.67*	-0.43*	-0.40*	-0.45*	-0.41*
R⁄B	0.08	0.15	0.11	0.21	N/A	N/A	N/A	N/A	0.82*	0.91*	0.79*	0.91*	0.56*	0.57*	0.56*	0.58*
R⁄G	0.20	0.22	0.22	0.25	N/A	N/A	N/A	N/A	0.55*	0.68*	0.55*	0.67*	0.42*	0.47*	0.43*	0.50*
R⁄N	-0.42*	-0.48*	-0.41*	-0.47*	N/A	N/A	N/A	N/A	0.37	0.68*	0.44*	0.73*	-0.36*	-0.29	-0.37*	-0.29
NIR⁄B	0.38	0.46*	0.42*	0.52*	N/A	N/A	N/A	N/A	-0.03	-0.38*	-0.06	-0.40*	0.53*	0.47*	0.52*	0.48*
NIR⁄G	0.40*	0.45*	0.42*	0.48*	N/A	N/A	N/A	N/A	-0.41*	-0.71*	-0.36	-0.67*	0.45*	0.40*	0.45*	0.41*
NIR⁄R	0.40*	0.46*	0.41*	0.47*	N/A	N/A	N/A	N/A	-0.50*	-0.77*	-0.44*	-0.73*	0.36*	0.28	0.37*	0.29
B×G×R	0.40	0.34	0.47*	0.52*	N/A	N/A	N/A	N/A	0.66*	0.70*	0.58*	0.69*	0.17	0.21	0.20	0.25

B×G×N	0.43*	0.36	0.53*	0.59*	N/A	N/A	N/A	N/A	0.58*	0.47*	0.43*	0.40*	0.33*	0.33*	0.37*	0.38*
B×R×N	0.41*	0.32	0.51*	0.57*	N/A	N/A	N/A	N/A	0.64*	0.53*	0.48*	0.46*	0.36*	0.36*	0.41*	0.43*
G×R×N	0.45*	0.47*	0.46*	0.52*	N/A	N/A	N/A	N/A	0.69*	0.76*	0.62*	0.72*	0.18	0.21	0.18	0.21
Avg(B;G)	0.46*	0.47*	0.48*	0.53*	N/A	N/A	N/A	N/A	0.56*	0.64*	0.52*	0.61*	0.07	0.12	0.08	0.12
Avg(B;R)	0.44*	0.44*	0.47*	0.51*	N/A	N/A	N/A	N/A	0.58*	0.66*	0.54*	0.64*	0.15	0.21	0.16	0.22
Avg(B;N)	0.50*	0.50*	0.53*	0.59*	N/A	N/A	N/A	N/A	0.32	0.20	0.29	0.18	0.37*	0.37*	0.39*	0.39*
Avg(G;R)	0.43*	0.44*	0.45*	0.51*	N/A	N/A	N/A	N/A	0.70*	0.78*	0.64*	0.75*	0.27	0.31	0.27	0.31
Avg(G;N)	0.51*	0.51*	0.53*	0.60*	N/A	N/A	N/A	N/A	0.53*	0.44*	0.45*	0.39*	0.44*	0.43*	0.44*	0.44*
Avg(R;N)	0.47*	0.47*	0.51*	0.58*	N/A	N/A	N/A	N/A	0.56*	0.46*	0.47*	0.40*	0.49*	0.49*	0.49*	0.50*
N-R	0.44*	0.42*	N/A	N/A	N/A	N/A	N/A	N/A	-0.33	-0.62*	N/A	N/A	0.39*	0.32	N/A	N/A
Kab1	-0.14	-0.05	-0.13	-0.03	N/A	N/A	N/A	N/A	0.79*	0.88*	0.73*	0.84*	0.41*	0.37*	0.39*	0.35*
NDVI	0.41*	0.47*	N/A	N/A	N/A	N/A	N/A	N/A	-0.43*	-0.73*	N/A	N/A	0.37*	0.29	N/A	N/A
NRVI	-0.41*	-0.47*	N/A	N/A	N/A	N/A	N/A	N/A	0.43*	0.73*	N/A	N/A	-0.37*	-0.29	N/A	N/A
OC2	-0.11	-0.03	-0.07	0.03	N/A	N/A	N/A	N/A	0.82*	0.88*	N/A	N/A	0.39*	0.36*	N/A	N/A
SABI	0.40	0.44*	N/A	N/A	N/A	N/A	N/A	N/A	-0.44*	-0.73*	N/A	N/A	0.38*	0.31	N/A	N/A
(B-R)⁄G	-0.09	-0.18	N/A	N/A	N/A	N/A	N/A	N/A	-0.79*	-0.92*	N/A	N/A	-0.54*	-0.54*	N/A	N/A
(NIR⁄G)+(NIR⁄B)	0.40	0.46*	0.43*	0.51*	N/A	N/A	N/A	N/A	-0.26	-0.58*	-0.23	-0.56*	0.50*	0.44*	0.49*	0.45*
G×(B+G+R)	0.43*	0.41*	0.47*	0.52*	N/A	N/A	N/A	N/A	0.69*	0.74*	0.60*	0.70*	0.17	0.20	0.18	0.22
[(1⁄B)-(1⁄G)]×N	-0.08	0.00	N/A	N/A	N/A	N/A	N/A	N/A	0.85*	0.92*	N/A	N/A	0.35*	0.32	N/A	N/A
[(1⁄R)-(1⁄G)]×N	0.01	0.02	N/A	N/A	N/A	N/A	N/A	N/A	-0.57*	-0.78*	-0.51*	-0.75*	-0.04	-0.14	-0.04	-0.14
[(1⁄R)-(1⁄B)]×N	0.05	0.02	N/A	N/A	N/A	N/A	N/A	N/A	-0.72*	-0.89*	N/A	N/A	-0.29	-0.34*	N/A	N/A
[(1⁄R)-(0.2363×(1⁄G))]×N	0.38	0.44*	0.40	0.45*	N/A	N/A	N/A	N/A	-0.51*	-0.77*	-0.45*	-0.74*	0.33*	0.25	0.34*	0.26
(R^-1-B^-1)⁄N	0.05	0.02	N/A	N/A	N/A	N/A	N/A	N/A	-0.45*	-0.52*	N/A	N/A	-0.46*	-0.48*	N/A	N/A
(B⁄R)×N	0.55*	0.55*	0.57*	0.62*	N/A	N/A	N/A	N/A	-0.30	-0.51*	-0.25	-0.50*	0.32	0.29	0.34*	0.30
(G⁄R)×N	0.58*	0.59*	0.58*	0.67*	N/A	N/A	N/A	N/A	0.04	-0.20	0.02	-0.22	0.43*	0.38*	0.44*	0.39*
(R⁄B)×N	0.39	0.37	0.48*	0.57*	N/A	N/A	N/A	N/A	0.71*	0.53*	0.57*	0.44*	0.56*	0.54*	0.55*	0.54*

(R/G)×N	0.42*	0.39	0.49*	0.56*	N/A	N/A	N/A	N/A	0.44*	0.25	0.33	0.15	0.51*	0.50*	0.52*	0.51*
(R×N)/B	0.39	0.37	0.48*	0.57*	N/A	N/A	N/A	N/A	0.71*	0.53*	0.57*	0.44*	0.56*	0.54*	0.55*	0.54*
(B/G)×(B/R)	-0.07	-0.20	-0.03	-0.13	N/A	N/A	N/A	N/A	-0.76*	-0.91*	-0.81*	-0.92*	-0.52*	-0.52*	-0.54*	-0.53*
(B/G)×(B/N)	-0.37	-0.53*	-0.34	-0.47*	N/A	N/A	N/A	N/A	-0.23	0.03	-0.36	-0.05	-0.50*	-0.46*	-0.55*	-0.50*
(B/G)×(R/G)	0.21	0.17	0.21	0.17	N/A	N/A	N/A	N/A	-0.41*	-0.41*	-0.45*	-0.45*	0.05	0.12	0.03	0.10
(B/G)×(R/N)	-0.40*	-0.53*	-0.40	-0.51*	N/A	N/A	N/A	N/A	0.18	0.49*	0.22	0.54*	-0.44*	-0.37*	-0.46*	-0.38*
(B/G)×(NIR/B)	0.40*	0.45*	0.42*	0.48*	N/A	N/A	N/A	N/A	-0.41*	-0.71*	-0.36	-0.67*	0.45*	0.40*	0.45*	0.41*
(B/G)×(NIR/G)	0.39	0.40	0.37	0.39	N/A	N/A	N/A	N/A	-0.57*	-0.82*	-0.52*	-0.79*	0.33*	0.29	0.33*	0.29
(B/G)×(NIR/R)	0.36	0.37	0.35	0.36	N/A	N/A	N/A	N/A	-0.60*	-0.84*	-0.56*	-0.82*	0.21	0.15	0.21	0.15
(B/R)×(B/N)	-0.39	-0.55*	-0.34	-0.45*	N/A	N/A	N/A	N/A	-0.41*	-0.19	-0.57*	-0.31	-0.50*	-0.49*	-0.57*	-0.54*
(B/R)×(G/R)	-0.23	-0.34	-0.18	-0.25	N/A	N/A	N/A	N/A	-0.68*	-0.83*	-0.74*	-0.87*	-0.55*	-0.60*	-0.54*	-0.58*
(B/R)×(G/N)	-0.44*	-0.56*	-0.38	-0.47*	N/A	N/A	N/A	N/A	-0.08	0.23	-0.16	0.18	-0.49*	-0.48*	-0.54*	-0.52*
(B/R)×(NIR/R)	0.26	0.25	0.26	0.25	N/A	N/A	N/A	N/A	-0.60*	-0.83*	-0.58*	-0.83*	0.03	-0.05	0.04	-0.05
(B/N)×(G/N)	-0.46*	-0.57*	-0.43*	-0.51*	N/A	N/A	N/A	N/A	0.18	0.50*	0.23	0.56*	-0.42*	-0.39*	-0.49*	-0.45*
(B/N)×(R/N)	-0.45*	-0.56*	-0.44*	-0.53*	N/A	N/A	N/A	N/A	0.22	0.54*	0.30	0.62*	-0.41*	-0.36*	-0.47*	-0.41*
(G/B)×(G/R)	-0.20	-0.17	-0.21	-0.17	N/A	N/A	N/A	N/A	0.47*	0.48*	0.45*	0.45*	-0.01	-0.08	-0.03	-0.10
(G/B)×(G/N)	-0.36	-0.38	-0.37	-0.39	N/A	N/A	N/A	N/A	0.43*	0.70*	0.52*	0.79*	-0.32	-0.29	-0.33*	-0.29
(G/B)×(R/B)	-0.01	0.07	0.03	0.13	N/A	N/A	N/A	N/A	0.85*	0.91*	0.81*	0.92*	0.52*	0.52*	0.54*	0.53*
(G/B)×(R/N)	-0.34	-0.34	-0.35	-0.36	N/A	N/A	N/A	N/A	0.48*	0.75*	0.56*	0.82*	-0.21	-0.15	-0.21	-0.15
(G/B)×(NIR/B)	0.29	0.39	0.34	0.47*	N/A	N/A	N/A	N/A	0.51*	0.18	0.36	0.05	0.55*	0.49*	0.55*	0.50*
(G/B)×(NIR/R)	0.38	0.48*	0.40	0.51*	N/A	N/A	N/A	N/A	-0.26	-0.57*	-0.22	-0.54*	0.46*	0.38*	0.46*	0.38*
(G/R)×(G/N)	-0.42*	-0.49*	-0.39	-0.44*	N/A	N/A	N/A	N/A	0.21	0.51*	0.24	0.55*	-0.46*	-0.45*	-0.48*	-0.46*
(G/R)×(NIR/R)	0.27	0.30	0.28	0.32	N/A	N/A	N/A	N/A	-0.53*	-0.78*	-0.48*	-0.75*	0.19	0.10	0.21	0.10
(G/N)×(R/N)	-0.44*	-0.51*	-0.43*	-0.49*	N/A	N/A	N/A	N/A	0.29	0.60*	0.41*	0.71*	-0.38*	-0.34*	-0.42*	-0.36*
(R/B)×(R/G)	0.11	0.15	0.18	0.25	N/A	N/A	N/A	N/A	0.78*	0.88*	0.74*	0.87*	0.51*	0.55*	0.54*	0.58*
(R/B(×(R/N)	-0.26	-0.25	-0.26	-0.25	N/A	N/A	N/A	N/A	0.51*	0.76*	0.58*	0.83*	-0.04	0.05	-0.04	0.05

(R⁄B)×(NIR⁄B)	0.24	0.30	0.34	0.45*	N/A	N/A	N/A	N/A	0.69*	0.41*	0.57*	0.31	0.58*	0.53*	0.57*	0.54*
(R⁄B)×(NIR⁄G)	0.30	0.34	0.38	0.47*	N/A	N/A	N/A	N/A	0.26	-0.08	0.16	-0.18	0.54*	0.51*	0.54*	0.52*
(R⁄G)×(R⁄N)	-0.28	-0.32	-0.28	-0.32	N/A	N/A	N/A	N/A	0.40*	0.69*	0.48*	0.75*	-0.21	-0.10	-0.21	-0.10
(R⁄G)×(NIR⁄G)	0.33	0.36	0.39	0.44*	N/A	N/A	N/A	N/A	-0.26	-0.56*	-0.24	-0.55*	0.48*	0.45*	0.48*	0.46*
(NIR⁄B)×(NIR⁄G)	0.36	0.41*	0.43*	0.51*	N/A	N/A	N/A	N/A	-0.28	-0.59*	-0.23	-0.56*	0.47*	0.42*	0.49*	0.45*
(NIR⁄B)×(NIR⁄R)	0.40*	0.46*	0.44*	0.53*	N/A	N/A	N/A	N/A	-0.39*	-0.68*	-0.30	-0.62*	0.44*	0.38*	0.47*	0.41*
(NIR⁄G)×(NIR⁄R)	0.41*	0.45*	0.43*	0.49*	N/A	N/A	N/A	N/A	-0.51*	-0.76*	-0.41*	-0.71*	0.39*	0.34*	0.42*	0.36*

Table F5: TPD Pearson R results: A = Chl-*a* (µg/l), B = Water Colour (TCU), C = TSS (mg/l), D = Turbidity (NTU), 1 = Linear curve, 2 = Exponential Curve, 3 = Logarithmic Curve, 4 = Power curve. *P-value < 0.05

Algorithm	**A1**	**A2**	**A3**	**A4**	**B1**	**B2**	**B3**	**B4**	**C1**	**C2**	**C3**	**C4**	**D1**	**D2**	**D3**	**D4**
Blue	0.21	0.19	0.26	0.26	0.54	0.47	0.53	0.44	0.46	0.29	0.4	0.25	0.34	0.4	0.36	0.43*
Green	0.57*	0.57*	0.56*	0.62*	0.77*	0.72*	0.79*	0.77*	0.66*	0.48*	0.58*	0.43	0.50*	0.58*	0.56*	0.65*
Red	0.46*	0.48*	0.50*	0.58*	0.84*	0.78*	0.86*	0.86*	0.67*	0.41	0.49*	0.26	0.53*	0.60*	0.60*	0.69*
NIR	0.73*	0.64*	0.71*	0.70*	0.56*	0.60*	0.66*	0.72*	0.05	-0.06	0.07	-0.1	0.25	0.33	0.27	0.36
B×G	0.36*	0.33	0.44*	0.47*	0.66*	0.60*	0.70*	0.64*	0.63*	0.43	0.51*	0.35	0.37	0.43*	0.48*	0.57*
B×R	0.30	0.29	0.42*	0.47*	0.73*	0.65*	0.77*	0.74*	0.68*	0.43	0.48*	0.27	0.39	0.44*	0.53*	0.61*
B×N	0.53*	0.42*	0.57*	0.56*	0.52	0.5	0.67*	0.67*	0.26	0.11	0.24	0.04	0.27	0.33	0.33	0.43
G×R	0.46*	0.44*	0.53*	0.60*	0.78*	0.69*	0.83*	0.83*	0.77*	0.51*	0.54*	0.34	0.44*	0.49*	0.59*	0.68*
G×N	0.74*	0.62*	0.67*	0.70*	0.77*	0.72*	0.79*	0.77*	0.66*	0.48*	0.58*	0.43	0.50*	0.58*	0.56*	0.65*
R×N	0.65*	0.55*	0.63*	0.67*	0.73*	0.67*	0.79*	0.82*	0.47	0.27	0.3	0.09	0.32	0.37	0.45*	0.55*
B⁄G	-0.57*	-0.71*	-0.60*	-0.71*	-0.70*	-0.82*	-0.70*	-0.80*	-0.41	-0.38	-0.44	-0.43	-0.60*	-0.67*	-0.60*	-0.66*
B⁄R	-0.51*	-0.68*	-0.56*	-0.70*	-0.78*	-0.90*	-0.84*	-0.92*	-0.26	-0.05	-0.38	-0.17	-0.61*	-0.68*	-0.64*	-0.70*
B⁄N	-0.45*	-0.46*	-0.51*	-0.51*	-0.44	-0.59*	-0.36	-0.51	0.2	0.34	0.19	0.27	-0.13	-0.18	-0.05	-0.12
G⁄B	0.61*	0.71*	0.60*	0.71*	0.69*	0.78*	0.70*	0.80*	0.46	0.47	0.44	0.43	0.58*	0.64*	0.60*	0.66*
G⁄R	-0.23	-0.34	-0.21	-0.31	-0.88*	-0.95*	-0.90*	-0.94*	-0.17	0.14	-0.21	0.1	-0.54*	-0.60*	-0.54*	-0.59*
G⁄N	-0.22	-0.13	-0.20	-0.10	-0.01	-0.14	0.02	-0.12	0.43	0.53*	0.39	0.47	0.24	0.2	0.26	0.22
R⁄B	0.58*	0.69*	0.56*	0.70*	0.88*	0.91*	0.84*	0.92*	0.50*	0.29	0.38	0.17	0.66*	0.71*	0.64*	0.70*
R⁄G	0.19	0.29	0.21	0.31	0.91*	0.93*	0.90*	0.94*	0.26	-0.05	0.21	-0.1	0.54*	0.59*	0.54*	0.59*
R⁄N	-0.10	0.03	-0.08	0.05	0.63*	0.54	0.60*	0.5	0.71*	0.58*	0.60*	0.52*	0.60*	0.57*	0.58*	0.56*
NIR⁄B	0.56*	0.54*	0.51*	0.51*	0.23	0.37	0.36	0.51	-0.16	-0.17	-0.19	-0.27	-0.03	0.04	0.05	0.12
NIR⁄G	0.17	0.05	0.20	0.10	-0.04	0.1	-0.02	0.12	-0.32	-0.38	-0.39	-0.47	-0.27	-0.23	-0.26	-0.22
NIR⁄R	0.05	-0.09	0.08	-0.05	-0.53	-0.44	-0.60*	-0.5	-0.48	-0.43	-0.60*	-0.52*	-0.55*	-0.55*	-0.58*	-0.56*
B×G×R	0.32	0.29	0.47*	0.52*	0.71*	0.62*	0.78*	0.75*	0.76*	0.51*	0.52*	0.32	0.33	0.38	0.54*	0.63*

B×G×N	0.36*	0.33*	0.44*	0.47*	0.58*	0.54	0.72*	0.72*	0.47	0.29	0.37	0.18	0.27	0.32	0.42	0.51*
B×R×N	0.36*	0.33*	0.44*	0.47*	0.65*	0.58*	0.77*	0.77*	0.54*	0.33	0.35	0.14	0.27	0.31	0.45*	0.54*
G×R×N	0.63*	0.51*	0.61*	0.66*	0.77*	0.72*	0.79*	0.77*	0.66*	0.48*	0.58*	0.43	0.50*	0.58*	0.56*	0.65*
Avg(B;G)	0.43*	0.42*	0.45*	0.49*	0.69*	0.63*	0.70*	0.65*	0.59*	0.41	0.52*	0.37	0.43*	0.50*	0.48*	0.57*
Avg(B;R)	0.36*	0.36*	0.41*	0.45*	0.75*	0.68*	0.76*	0.71*	0.61*	0.38	0.50*	0.29	0.45*	0.51*	0.50*	0.59*
Avg(B;N)	0.54*	0.47*	0.54*	0.53*	0.59*	0.56*	0.64*	0.62*	0.28	0.12	0.26	0.09	0.31	0.38	0.33	0.43
Avg(G;R)	0.52*	0.53*	0.53*	0.60*	0.81*	0.75*	0.83*	0.82*	0.67*	0.45	0.55*	0.35	0.52*	0.59*	0.59*	0.67*
Avg(G;N)	0.69*	0.64*	0.65*	0.68*	0.73*	0.71*	0.76*	0.78*	0.44	0.26	0.37	0.2	0.41	0.49*	0.47*	0.56*
Avg(R;N)	0.63*	0.60*	0.62*	0.66*	0.80*	0.76*	0.81*	0.83*	0.45	0.23	0.33	0.11	0.41	0.49*	0.48*	0.57*
N-R	0.12	0.00	N/A	N/A	-0.80*	-0.69*	N/A	N/A	-0.75*	-0.55*	N/A	N/A	-0.70*	-0.69*	N/A	N/A
Kab1	0.57*	0.69*	0.53*	0.68*	0.66*	0.77*	0.67*	0.80*	0.41	0.41	0.37	0.34	0.57*	0.63*	0.58*	0.64*
NDVI	0.08	-0.05	N/A	N/A	-0.59*	-0.49	N/A	N/A	-0.59*	-0.52*	N/A	N/A	-0.58*	-0.56*	N/A	N/A
NRVI	-0.08	0.05	N/A	N/A	0.59*	0.49	N/A	N/A	0.59*	0.52*	N/A	N/A	0.58*	0.56*	N/A	N/A
OC2	0.60*	0.68*	N/A	N/A	0.66*	0.74*	N/A	N/A	0.48*	0.51*	0.4	0.37	0.56*	0.62*	N/A	N/A
SABI	0.07	-0.06	N/A	N/A	-0.76*	-0.67*	N/A	N/A	-0.55*	-0.43	N/A	N/A	-0.68*	-0.66*	N/A	N/A
(B-R)/G	-0.54*	-0.69*	N/A	N/A	-0.84*	-0.92*	N/A	N/A	-0.4	-0.2	N/A	N/A	-0.64*	-0.70*	-0.61*	-0.65*
(NIR/G)+(NIR/B)	0.44*	0.38*	0.41*	0.36*	0.13	0.28	0.22	0.37	-0.23	-0.26	-0.28	-0.36	-0.15	-0.09	-0.1	-0.04
G×(B+G+R)	0.47*	0.44*	0.52*	0.57*	0.73*	0.66*	0.79*	0.76*	0.72*	0.50*	0.56*	0.39	0.41	0.47*	0.55*	0.63*
[(1/B)-(1/G)]×N	0.63*	0.71*	N/A	N/A	0.47	0.57*	N/A	N/A	0.27	0.36	N/A	N/A	0.53*	0.61*	N/A	N/A
[(1/R)-(1/G)]×N	-0.10	-0.24	N/A	N/A	-0.88*	-0.89*	N/A	N/A	-0.31	-0.03	N/A	N/A	-0.77*	-0.83*	-0.79*	-0.81*
[(1/R)-(1/B)]×N	-0.56*	-0.70*	N/A	N/A	-0.83*	-0.90*	N/A	N/A	-0.35	-0.26	N/A	N/A	-0.75*	-0.84*	-0.69*	-0.71*
[(1/R)-(0.2363×(1/G))]×N	0.03	-0.12	0.06	-0.08	-0.61*	-0.52	-0.68*	-0.59*	-0.52*	-0.43	-0.64*	-0.52*	-0.61*	-0.61*	-0.64*	-0.62*
(R^-1-B^-1)/N	-0.33	-0.54*	N/A	N/A	-0.62*	-0.77*	N/A	N/A	-0.08	0.13	N/A	N/A	-0.50*	-0.57*	-0.60*	-0.67*
(B/R)×N	0.41*	0.23	0.43*	0.27	-0.03	0	0	0	-0.26	-0.29	-0.26	-0.32	0	0.07	-0.12	-0.04
(G/R)×N	0.77*	0.66*	0.74*	0.69*	0.31	0.37	0.42	0.48	-0.05	-0.07	-0.02	-0.09	0.17	0.26	0.15	0.25
(R/B)×N	0.81*	0.75*	0.70*	0.76*	0.82*	0.80*	0.78*	0.85*	0.27	0.13	0.2	0.01	0.36	0.44*	0.43*	0.52*

(R/G)×N	0.64*	0.57*	0.64*	0.66*	0.71*	0.71*	0.76*	0.81*	0.12	-0.03	0.12	-0.1	0.29	0.36	0.34	0.43
(R×N)/B	0.81*	0.75*	0.70*	0.76*	0.82*	0.80*	0.78*	0.85*	0.27	0.13	0.2	0.01	0.36	0.44*	0.43*	0.52*
(B/G)×(B/R)	-0.48*	-0.66*	-0.59*	-0.73*	-0.72*	-0.86*	-0.80*	-0.89*	-0.26	-0.09	-0.42	-0.27	-0.60*	-0.67*	-0.64*	-0.70*
(B/G)×(B/N)	-0.49*	-0.56*	-0.59*	-0.63*	-0.56*	-0.71*	-0.5	-0.64*	0.04	0.2	0.02	0.09	-0.31	-0.36	-0.25	-0.32
(B/G)×(R/G)	-0.44*	-0.50*	-0.45*	-0.50*	0.21	0.12	0.2	0.11	-0.17	-0.47	-0.16	-0.46	-0.19	-0.2	-0.18	-0.2
(B/G)×(R/N)	-0.35	-0.31	-0.40*	-0.36*	0.08	-0.08	0.1	-0.05	0.49*	0.42	0.37	0.29	0.14	0.09	0.19	0.14
(B/G)×(NIR/B)	0.17	0.05	0.20	0.10	-0.04	0.1	-0.02	0.12	-0.32	-0.38	-0.39	-0.47	-0.27	-0.23	-0.26	-0.22
(B/G)×(NIR/G)	-0.27	-0.45*	-0.24	-0.41*	-0.54	-0.47	-0.56*	-0.5	-0.45	-0.54*	-0.54*	-0.61*	-0.51*	-0.51*	-0.54*	-0.53*
(B/G)×(NIR/R)	-0.29	-0.49*	-0.27	-0.45*	-0.83*	-0.85*	-0.83*	-0.81*	-0.58*	-0.56*	-0.69*	-0.62*	-0.73*	-0.77*	-0.75*	-0.76*
(B/R)×(B/N)	-0.48*	-0.59*	-0.61*	-0.68*	-0.61*	-0.76*	-0.65*	-0.77*	-0.01	0.21	-0.05	0.1	-0.37	-0.42	-0.33	-0.4
(B/R)×(G/R)	-0.44*	-0.62*	-0.49*	-0.63*	-0.76*	-0.90*	-0.88*	-0.94*	-0.16	0.09	-0.32	-0.07	-0.58*	-0.65*	-0.62*	-0.69*
(B/R)×(G/N)	-0.47*	-0.53*	-0.55*	-0.59*	-0.60*	-0.75*	-0.60*	-0.73*	0.06	0.28	0.07	0.23	-0.27	-0.32	-0.2	-0.26
(B/R)×(NIR/R)	-0.29	-0.48*	-0.28	-0.45*	-0.87*	-0.95*	-0.90*	-0.90*	-0.53*	-0.37	-0.70*	-0.49*	-0.81*	-0.88*	-0.83*	-0.86*
(B/N)×(G/N)	-0.34	-0.32	-0.40*	-0.35	-0.34	-0.49	-0.21	-0.37	0.31	0.46	0.29	0.37	-0.04	-0.07	0.09	0.04
(B/N)×(R/N)	-0.29	-0.23	-0.34	-0.27	0.01	-0.12	0.07	-0.09	0.54*	0.55*	0.39	0.4	0.15	0.11	0.23	0.18
(G/B)×(G/R)	0.43*	0.48*	0.45*	0.50*	-0.19	-0.09	-0.2	-0.11	0.14	0.45	0.16	0.46	0.18	0.2	0.18	0.2
(G/B)×(G/N)	0.19	0.35	0.24	0.41*	0.56*	0.51	0.56*	0.5	0.62*	0.65*	0.54*	0.61*	0.56*	0.55*	0.54*	0.53*
(G/B)×(R/B)	0.61*	0.71*	0.59*	0.73*	0.84*	0.86*	0.80*	0.89*	0.57*	0.45	0.42	0.27	0.64*	0.70*	0.64*	0.70*
(G/B)×(R/N)	0.20	0.36*	0.27	0.45*	0.80*	0.75*	0.83*	0.81*	0.79*	0.64*	0.69*	0.62*	0.75*	0.74*	0.75*	0.76*
(G/B)×(NIR/B)	0.62*	0.64*	0.59*	0.63*	0.31	0.43	0.5	0.64*	-0.01	0.02	-0.02	-0.09	0.15	0.23	0.25	0.32
(G/B)×(NIR/R)	0.44*	0.41*	0.40*	0.36*	-0.1	0.04	-0.1	0.05	-0.25	-0.16	-0.37	-0.29	-0.24	-0.18	-0.19	-0.14
(G/R)×(G/N)	-0.33	-0.30	-0.30	-0.25	-0.52	-0.65*	-0.48	-0.61*	0.17	0.4	0.21	0.39	-0.05	-0.09	0.02	-0.04
(G/R)×(NIR/R)	-0.05	-0.20	-0.01	-0.14	-0.78*	-0.77*	-0.83*	-0.78*	-0.54*	-0.31	-0.67*	-0.42	-0.76*	-0.79*	-0.79*	-0.80*
(G/N)×(R/N)	-0.17	-0.06	-0.14	-0.01	0.38	0.29	0.35	0.22	0.67*	0.61*	0.50*	0.51*	0.43	0.39	0.42	0.39
(R/B)×(R/G)	0.46*	0.57*	0.49*	0.63*	0.92*	0.90*	0.88*	0.94*	0.50*	0.24	0.32	0.07	0.64*	0.70*	0.62*	0.69*
(R/B(×(R/N)	0.18	0.33	0.28	0.45*	0.86*	0.80*	0.90*	0.90*	0.83*	0.58*	0.70*	0.49*	0.82*	0.81*	0.83*	0.86*

(R/B)×(NIR/B)	0.66*	0.69*	0.61*	0.68*	0.53	0.61*	0.65*	0.77*	0.04	0.01	0.05	-0.1	0.23	0.31	0.33	0.4
(R/B)×(NIR/G)	0.61*	0.61*	0.55*	0.59*	0.52	0.62*	0.60*	0.73*	-0.08	-0.15	-0.07	-0.23	0.1	0.18	0.2	0.26
(R/G)×(R/N)	-0.02	0.11	0.01	0.14	0.82*	0.74*	0.83*	0.78*	0.78*	0.51*	0.67*	0.42	0.79*	0.77*	0.79*	0.80*
(R/G)×(NIR/G)	0.25	0.18	0.30	0.25	0.41	0.53	0.48	0.61*	-0.21	-0.31	-0.21	-0.39	-0.07	-0.01	-0.02	0.04
(NIR/B)×(NIR/G)	0.45*	0.39*	0.40*	0.35	0.06	0.2	0.21	0.37	-0.18	-0.17	-0.29	-0.37	-0.18	-0.13	-0.09	-0.04
(NIR/B)×(NIR/R)	0.39*	0.32	0.34	0.27	-0.09	0.05	-0.07	0.09	-0.21	-0.18	-0.39	-0.4	-0.29	-0.24	-0.23	-0.18
(NIR/G)×(NIR/R)	0.08	-0.07	0.14	0.01	-0.26	-0.13	-0.35	-0.22	-0.29	-0.29	-0.50*	-0.51*	-0.4	-0.38	-0.42	-0.39

Table F6: SHF Pearson R results: A = Chl-*a* (μg/l), B = Water Colour (TCU), C = TSS (mg/l), D = Turbidity (NTU), 1 = Linear curve, 2 = Exponential Curve, 3 = Logarithmic Curve, 4 = Power curve. *P-value < 0.05

Algorithm	**A1**	**A2**	**A3**	**A4**	**B1**	**B2**	**B3**	**B4**	**C1**	**C2**	**C3**	**C4**	**D1**	**D2**	**D3**	**D4**
Blue	0.59*	0.52*	0.57*	0.51*	-0.17	-0.10	-0.17	-0.10	0.11	-0.01	0.09	-0.04	0.18	0.21	0.16	0.20
Green	0.77*	0.74*	0.75*	0.74*	-0.33	-0.22	-0.34*	-0.24	0.67*	0.53*	0.58*	0.46*	0.51*	0.50*	0.44*	0.45*
Red	0.80*	0.76*	0.77*	0.76*	-0.21	-0.05	-0.20	-0.03	0.64*	0.50*	0.56*	0.44*	0.54*	0.56*	0.51*	0.54*
NIR	0.65*	0.56*	0.62*	0.56*	-0.05	0.04	-0.03	0.06	0.34	0.18	0.26	0.11	0.11	0.19	0.10	0.18
B×G	0.73*	0.67*	0.70*	0.67*	-0.27	-0.17	-0.28	-0.19	0.53*	0.39*	0.41*	0.28	0.43*	0.43*	0.35*	0.36*
B×R	0.75*	0.68*	0.72*	0.69*	-0.20	-0.08	-0.19	-0.06	0.52*	0.37	0.41*	0.28	0.43*	0.46*	0.39*	0.42*
B×N	0.65*	0.55*	0.61*	0.55*	-0.11	-0.02	-0.09	0.00	0.31	0.15	0.20	0.06	0.15	0.21	0.13	0.19
G×R	0.78*	0.72*	0.77*	0.76*	-0.26	-0.13	-0.27	-0.13	0.71*	0.55*	0.58*	0.45*	0.57*	0.56*	0.48*	0.50*
G×N	0.77*	0.74*	0.75*	0.74*	-0.33	-0.22	-0.34*	-0.24	0.67*	0.53*	0.58*	0.46*	0.51*	0.50*	0.44*	0.45*
R×N	0.75*	0.65*	0.71*	0.68*	-0.16	-0.03	-0.12	0.01	0.57*	0.40*	0.44*	0.30	0.37*	0.42*	0.34*	0.39*
B⁄G	-0.75*	-0.81*	-0.75*	-0.80*	0.48*	0.36*	0.45*	0.33	-0.78*	-0.73*	-0.81*	-0.74*	-0.61*	-0.59*	-0.64*	-0.61*
B⁄R	-0.78*	-0.84*	-0.79*	-0.83*	0.17	-0.09	0.19	-0.06	-0.77*	-0.71*	-0.81*	-0.73*	-0.75*	-0.79*	-0.77*	-0.79*
B⁄N	-0.55*	-0.51*	-0.57*	-0.51*	-0.18	-0.29	-0.19	-0.30	-0.36	-0.24	-0.40*	-0.27	0.03	-0.09	0.04	-0.09
G⁄B	0.74*	0.77*	0.75*	0.80*	-0.42*	-0.30	-0.45*	-0.33	0.83*	0.75*	0.81*	0.74*	0.65*	0.62*	0.64*	0.61*
G⁄R	-0.38*	-0.38*	-0.38*	-0.38*	-0.48*	-0.73*	-0.49*	-0.73*	-0.10	-0.07	-0.10	-0.06	-0.27	-0.36*	-0.26	-0.36*
G⁄N	0.07	0.18	0.04	0.14	-0.46*	-0.43*	-0.50*	-0.47*	0.55*	0.58*	0.53*	0.56*	0.59*	0.49*	0.56*	0.47*
R⁄B	0.77*	0.79*	0.79*	0.83*	-0.20	0.04	-0.19	0.06	0.85*	0.75*	0.81*	0.73*	0.78*	0.79*	0.77*	0.79*
R⁄G	0.39*	0.38*	0.38*	0.38*	0.50*	0.73*	0.49*	0.73*	0.09	0.05	0.10	0.06	0.26	0.35*	0.26	0.36*
R⁄N	0.25	0.36*	0.22	0.33	-0.29	-0.13	-0.32	-0.15	0.68*	0.70*	0.66*	0.68*	0.79*	0.72*	0.78*	0.72*
NIR⁄B	0.58*	0.51*	0.57*	0.51*	0.19	0.31	0.19	0.30	0.44*	0.30	0.40*	0.27	-0.04	0.08	-0.04	0.09
NIR⁄G	0.00	-0.11	-0.04	-0.14	0.54*	0.51*	0.50*	0.47*	-0.50*	-0.53*	-0.53*	-0.56*	-0.53*	-0.44*	-0.56*	-0.47*
NIR⁄R	-0.18	-0.29	-0.22	-0.33	0.35*	0.19	0.32	0.15	-0.63*	-0.64*	-0.66*	-0.68*	-0.76*	-0.71*	-0.78*	-0.72*
B×G×R	0.75*	0.67*	0.73*	0.72*	-0.24	-0.12	-0.25	-0.13	0.64*	0.48*	0.48*	0.35	0.52*	0.52*	0.42*	0.44*

B×G×N	0.71*	0.61*	0.68*	0.64*	-0.20	-0.10	-0.20	-0.10	0.53*	0.37*	0.37	0.23	0.35*	0.38*	0.27	0.31
B×R×N	0.72*	0.61*	0.69*	0.65*	-0.16	-0.06	-0.14	-0.01	0.53*	0.36	0.36	0.22	0.34*	0.38*	0.30	0.35*
G×R×N	0.77*	0.74*	0.75*	0.74*	-0.33	-0.22	-0.34*	-0.24	0.67*	0.53*	0.58*	0.46*	0.51*	0.50*	0.44*	0.45*
Avg(B;G)	0.72*	0.67*	0.70*	0.67*	-0.27	-0.17	-0.28	-0.19	0.48*	0.34	0.42*	0.29	0.39*	0.40*	0.35*	0.36*
Avg(B;R)	0.72*	0.67*	0.70*	0.67*	-0.20	-0.08	-0.19	-0.07	0.42*	0.28	0.37	0.23	0.37*	0.40*	0.35*	0.38*
Avg(B;N)	0.64*	0.56*	0.61*	0.55*	-0.11	-0.03	-0.10	-0.02	0.24	0.09	0.19	0.05	0.15	0.20	0.14	0.19
Avg(G;R)	0.78*	0.75*	0.76*	0.76*	-0.28	-0.15	-0.28	-0.15	0.66*	0.52*	0.58*	0.46*	0.53*	0.53*	0.48*	0.49*
Avg(G;N)	0.74*	0.68*	0.71*	0.68*	-0.23	-0.11	-0.22	-0.12	0.55*	0.40*	0.47*	0.33	0.38*	0.41*	0.33	0.37*
Avg(R;N)	0.74*	0.67*	0.71*	0.67*	-0.14	0.00	-0.12	0.02	0.51*	0.35	0.43*	0.29	0.35*	0.40*	0.33*	0.39*
N-R	0.08	-0.03	N/A	N/A	0.29	0.18	N/A	N/A	-0.69*	-0.71*	N/A	N/A	-0.76*	-0.67*	N/A	N/A
Kab1	0.74*	0.79*	0.72*	0.80*	-0.45*	-0.33	-0.52*	-0.40*	0.81*	0.75*	0.75*	0.73*	0.64*	0.61*	0.58*	0.57*
NDVI	-0.22	-0.33*	N/A	N/A	0.32	0.15	N/A	N/A	-0.67*	-0.68*	N/A	N/A	-0.78*	-0.72*	N/A	N/A
NRVI	0.22	0.33*	N/A	N/A	-0.32	-0.15	N/A	N/A	0.67*	0.68*	N/A	N/A	0.78*	0.72*	N/A	N/A
OC2	0.72*	0.75*	N/A	N/A	-0.42*	-0.31	N/A	N/A	0.84*	0.74*	N/A	N/A	0.64*	0.60*	N/A	N/A
SABI	-0.11	-0.21	N/A	N/A	0.36*	0.22	N/A	N/A	-0.64*	-0.65*	N/A	N/A	-0.75*	-0.68*	N/A	N/A
(B-R)⁄G	-0.79*	-0.85*	N/A	N/A	0.33	0.12	0.30	0.12	-0.81*	-0.75*	-0.89*	-0.73*	-0.73*	-0.74*	-0.75*	-0.73*
(NIR⁄G)+(NIR⁄B)	0.32	0.22	0.30	0.21	0.47*	0.49*	0.45*	0.47*	-0.14	-0.23	-0.15	-0.24	-0.41*	-0.29	-0.43*	-0.31
G×(B+G+R)	0.76*	0.70*	0.74*	0.73*	-0.28	-0.17	-0.30	-0.20	0.67*	0.52*	0.53*	0.41*	0.52*	0.51*	0.43*	0.44*
[(1⁄B)-(1⁄G)]×N	0.76*	0.81*	N/A	N/A	-0.52*	-0.41*	N/A	N/A	0.81*	0.75*	N/A	N/A	0.62*	0.58*	N/A	N/A
[(1⁄R)-(1⁄G)]×N	-0.40*	-0.46*	-0.39*	-0.45*	-0.21	-0.51*	-0.21	-0.50*	-0.45*	-0.42*	-0.47*	-0.45*	-0.67*	-0.72*	-0.68*	-0.71*
[(1⁄R)-(1⁄B)]×N	-0.73*	-0.80*	N/A	N/A	0.29	0.05	0.27	0.06	-0.81*	-0.75*	-0.91*	-0.75*	-0.80*	-0.80*	-0.82*	-0.79*
[(1⁄R)-(0.2363×(1⁄G))]×N	-0.21	-0.32	-0.25	-0.35*	0.30	0.10	0.27	0.08	-0.64*	-0.65*	-0.67*	-0.68*	-0.79*	-0.75*	-0.80*	-0.75*
(R^-1-B^-1)⁄N	-0.73*	-0.80*	N/A	N/A	0.29	0.05	0.27	0.06	-0.81*	-0.75*	-0.91*	-0.75*	-0.80*	-0.80*	-0.82*	-0.79*
(B⁄R)×N	0.32	0.21	0.24	0.14	-0.27	-0.26	-0.06	-0.06	-0.36	-0.47*	-0.38*	-0.49*	-0.46*	-0.39*	-0.47*	-0.40*
(G⁄R)×N	0.61*	0.52*	0.57*	0.51*	-0.20	-0.16	-0.20	-0.18	0.35	0.19	0.26	0.11	0.06	0.11	0.01	0.05
(R⁄B)×N	0.78*	0.70*	0.74*	0.72*	-0.14	0.02	-0.10	0.07	0.65*	0.49*	0.55*	0.42*	0.44*	0.49*	0.41*	0.47*

(R/G)×N	0.67*	0.58*	0.63*	0.58*	0.07	0.21	0.11	0.26	0.31	0.16	0.25	0.11	0.14	0.24	0.17	0.26
(R×N)/B	0.78*	0.70*	0.74*	0.72*	-0.14	0.02	-0.10	0.07	0.65*	0.49*	0.55*	0.42*	0.44*	0.49*	0.41*	0.47*
(B/G)×(B/R)	-0.78*	-0.86*	-0.79*	-0.83*	0.34*	0.13	0.33	0.14	-0.77*	-0.73*	-0.83*	-0.76*	-0.71*	-0.72*	-0.73*	-0.73*
(B/G)×(B/N)	-0.69*	-0.71*	-0.74*	-0.74*	0.23	0.08	0.24	0.09	-0.66*	-0.58*	-0.75*	-0.64*	-0.45*	-0.50*	-0.49*	-0.54*
(B/G)×(R/G)	-0.53*	-0.59*	-0.53*	-0.59*	0.60*	0.61*	0.56*	0.57*	-0.60*	-0.57*	-0.66*	-0.62*	-0.33	-0.27	-0.38*	-0.32
(B/G)×(R/N)	-0.43*	-0.37*	-0.46*	-0.40*	0.19	0.27	0.18	0.25	-0.31	-0.20	-0.37	-0.26	0.28	0.23	0.26	0.22
(B/G)×(NIR/B)	0.00	-0.11	-0.04	-0.14	0.54*	0.51*	0.50*	0.47*	-0.50*	-0.53*	-0.53*	-0.56*	-0.53*	-0.44*	-0.56*	-0.47*
(B/G)×(NIR/G)	-0.45*	-0.57*	-0.46*	-0.56*	0.58*	0.50*	0.50*	0.43*	-0.66*	-0.66*	-0.73*	-0.71*	-0.57*	-0.51*	-0.63*	-0.56*
(B/G)×(NIR/R)	-0.57*	-0.69*	-0.56*	-0.66*	0.46*	0.31	0.41*	0.26	-0.74*	-0.73*	-0.79*	-0.76*	-0.72*	-0.69*	-0.75*	-0.70*
(B/R)×(B/N)	-0.70*	-0.72*	-0.75*	-0.75*	0.00	-0.24	0.04	-0.20	-0.62*	-0.54*	-0.72*	-0.60*	-0.53*	-0.61*	-0.55*	-0.62*
(B/R)×(G/R)	-0.71*	-0.76*	-0.74*	-0.77*	-0.09	-0.41*	-0.06	-0.37*	-0.62*	-0.56*	-0.70*	-0.62*	-0.68*	-0.75*	-0.71*	-0.77*
(B/R)×(G/N)	-0.56*	-0.54*	-0.59*	-0.55*	-0.36*	-0.58*	-0.37*	-0.57*	-0.30	-0.21	-0.33	-0.22	-0.15	-0.27	-0.12	-0.25
(B/R)×(NIR/R)	-0.64*	-0.75*	-0.61*	-0.70*	0.29	0.05	0.27	0.05	-0.73*	-0.71*	-0.81*	-0.76*	-0.79*	-0.79*	-0.82*	-0.80*
(B/N)×(G/N)	-0.27	-0.19	-0.31	-0.22	-0.39*	-0.42*	-0.43*	-0.46*	0.18	0.27	0.15	0.24	0.45*	0.33	0.42*	0.30
(B/N)×(R/N)	-0.18	-0.08	-0.24	-0.14	-0.26	-0.19	-0.32	-0.26	0.25	0.35	0.22	0.31	0.61*	0.51*	0.59*	0.49*
(G/B)×(G/R)	0.54*	0.58*	0.53*	0.59*	-0.52*	-0.52*	-0.56*	-0.57*	0.71*	0.65*	0.66*	0.62*	0.44*	0.37*	0.38*	0.32
(G/B)×(G/N)	0.45*	0.53*	0.46*	0.56*	-0.42*	-0.35*	-0.50*	-0.43*	0.75*	0.71*	0.73*	0.71*	0.65*	0.57*	0.63*	0.56*
(G/B)×(R/B)	0.74*	0.75*	0.79*	0.83*	-0.31	-0.14	-0.33	-0.14	0.88*	0.76*	0.83*	0.76*	0.74*	0.72*	0.73*	0.73*
(G/B)×(R/N)	0.53*	0.60*	0.56*	0.66*	-0.35*	-0.21	-0.41*	-0.26	0.82*	0.76*	0.79*	0.76*	0.75*	0.69*	0.75*	0.70*
(G/B)×(NIR/B)	0.77*	0.73*	0.74*	0.74*	-0.24	-0.09	-0.24	-0.09	0.81*	0.67*	0.75*	0.64*	0.53*	0.56*	0.49*	0.54*
(G/B)×(NIR/R)	0.47*	0.41*	0.46*	0.40*	-0.17	-0.22	-0.18	-0.25	0.44*	0.32	0.37	0.26	-0.25	-0.20	-0.26	-0.22
(G/R)×(G/N)	-0.08	0.00	-0.11	-0.02	-0.51*	-0.58*	-0.56*	-0.62*	0.38*	0.41*	0.37	0.41*	0.37*	0.26	0.34*	0.23
(G/R)×(NIR/R)	-0.32	-0.41*	-0.34*	-0.43*	0.06	-0.22	0.05	-0.21	-0.59*	-0.58*	-0.62*	-0.61*	-0.79*	-0.79*	-0.80*	-0.80*
(G/N)×(R/N)	0.21	0.31	0.13	0.24	-0.35*	-0.26	-0.43*	-0.33	0.64*	0.66*	0.61*	0.64*	0.71*	0.62*	0.69*	0.61*
(R/B)×(R/G)	0.72*	0.73*	0.74*	0.77*	0.03	0.33	0.06	0.37*	0.77*	0.67*	0.70*	0.62*	0.73*	0.78*	0.71*	0.77*
(R/B(×(R/N)	0.56*	0.61*	0.61*	0.70*	-0.25	-0.05	-0.27	-0.05	0.85*	0.78*	0.81*	0.76*	0.82*	0.78*	0.82*	0.80*

(R/B)×(NIR/B)	0.78*	0.73*	0.75*	0.75*	-0.07	0.15	-0.04	0.20	0.78*	0.64*	0.72*	0.60*	0.56*	0.63*	0.55*	0.62*
(R/B)×(NIR/G)	0.61*	0.55*	0.59*	0.55*	0.38*	0.56*	0.37*	0.57*	0.36	0.24	0.33	0.22	0.09	0.22	0.12	0.25
(R/G)×(R/N)	0.35*	0.44*	0.34*	0.43*	-0.04	0.21	-0.05	0.21	0.65*	0.64*	0.62*	0.61*	0.81*	0.79*	0.80*	0.80*
(R/G)×(NIR/G)	0.13	0.04	0.11	0.02	0.60*	0.65*	0.56*	0.62*	-0.35	-0.39*	-0.37	-0.41*	-0.30	-0.20	-0.34*	-0.23
(NIR/B)×(NIR/G)	0.34*	0.25	0.31	0.22	0.47*	0.49*	0.43*	0.46*	-0.13	-0.21	-0.15	-0.24	-0.39*	-0.27	-0.42*	-0.30
(NIR/B)×(NIR/R)	0.28	0.19	0.24	0.14	0.36*	0.32	0.32	0.26	-0.18	-0.26	-0.22	-0.31	-0.55*	-0.45*	-0.59*	-0.49*
(NIR/G)×(NIR/R)	-0.05	-0.16	-0.13	-0.24	0.50*	0.41*	0.43*	0.33	-0.53*	-0.56*	-0.61*	-0.64*	-0.63*	-0.56*	-0.69*	-0.61*

Table F7: TMF Pearson R results: A = Chl-*a* (µg/l), B = Water Colour (TCU), C = TSS (mg/l), D = Turbidity (NTU), 1 = Linear curve, 2 = Exponential Curve, 3 = Logarithmic Curve, 4 = Power curve. *P-value < 0.05

Algorithm	A1	A2	A3	A4	B1	B2	B3	B4	C1	C2	C3	C4	D1	D2	D3	D4
Blue	0.44*	-0.04	0.36*	-0.09	-0.17	-0.18	-0.18	-0.18	0.17	0.14	0.18	0.11	0.13	0.20	0.18	0.24
Green	0.12	-0.46*	0.08	-0.47*	-0.35	-0.38	-0.39	-0.42	0.27	0.28	0.31	0.30	0.21	0.28	0.29	0.36
Red	0.24	-0.32	0.17	-0.35	-0.34	-0.37	-0.37	-0.40	0.31	0.32	0.36	0.34	0.27	0.33	0.37	0.41
NIR	0.72*	0.44*	0.59*	0.47*	-0.10	-0.22	-0.10	-0.25	0.32	0.28	0.32	0.24	0.28	0.33	0.38	0.43
B×G	0.35	-0.22	0.20	-0.34	-0.23	-0.25	-0.29	-0.31	0.20	0.23	0.26	0.22	0.12	0.19	0.24	0.31
B×R	0.43*	-0.13	0.25	-0.26	-0.22	-0.25	-0.28	-0.29	0.23	0.25	0.30	0.26	0.14	0.21	0.29	0.35
B×N	0.73*	0.32	0.56*	0.31	-0.13	-0.19	-0.15	-0.23	0.23	0.24	0.28	0.21	0.15	0.22	0.32	0.37
G×R	0.25	-0.35	0.12	-0.42*	-0.31	-0.35	-0.38	-0.41	0.24	0.27	0.34	0.32	0.16	0.23	0.33	0.39
G×N	0.12	-0.46*	0.08	-0.47*	-0.35	-0.38	-0.39	-0.42	0.27	0.28	0.31	0.30	0.21	0.28	0.29	0.36
R×N	0.70*	0.25	0.47*	0.13	-0.21	-0.28	-0.24	-0.33	0.26	0.28	0.34	0.29	0.17	0.24	0.38	0.42
B⁄G	0.27	0.70*	0.29	0.73*	0.35	0.41	0.35	0.41	-0.38	-0.47	-0.38	-0.46	-0.64*	-0.70*	-0.64*	-0.69*
B⁄R	0.10	0.50*	0.12	0.53*	0.25	0.29	0.26	0.30	-0.44	-0.49	-0.43	-0.47	-0.60*	-0.61*	-0.60*	-0.61*
B⁄N	-0.45*	-0.68*	-0.52*	-0.67*	-0.12	0.07	-0.12	0.07	-0.32	-0.25	-0.37	-0.30	-0.51*	-0.54*	-0.53*	-0.56*
G⁄B	-0.31	-0.75*	-0.29	-0.73*	-0.35	-0.41	-0.35	-0.41	0.37	0.45	0.38	0.46	0.63*	0.68*	0.64*	0.69*
G⁄R	-0.28	-0.32	-0.28	-0.32	-0.24	-0.30	-0.24	-0.30	-0.44	-0.41	-0.45	-0.41	-0.53*	-0.50*	-0.54*	-0.51*
G⁄N	-0.46*	-0.83*	-0.52*	-0.82*	-0.51	-0.28	-0.54*	-0.31	-0.20	-0.06	-0.23	-0.09	-0.45	-0.47	-0.47	-0.48
R⁄B	-0.14	-0.56*	-0.12	-0.53*	-0.28	-0.31	-0.26	-0.30	0.42	0.46	0.43	0.47	0.60*	0.60*	0.60*	0.61*
R⁄G	0.29	0.33	0.28	0.32	0.23	0.30	0.24	0.30	0.45	0.41	0.45	0.41	0.55*	0.52*	0.54*	0.51*
R⁄N	-0.43*	-0.80*	-0.48*	-0.78*	-0.44	-0.20	-0.49	-0.24	-0.09	0.07	-0.08	0.08	-0.36	-0.40	-0.35	-0.38
NIR⁄B	0.58*	0.62*	0.52*	0.67*	0.11	-0.08	0.12	-0.07	0.40	0.34	0.37	0.30	0.54*	0.56*	0.53*	0.56*
NIR⁄G	0.54*	0.73*	0.52*	0.82*	0.58*	0.35	0.54*	0.31	0.26	0.12	0.23	0.09	0.48	0.49	0.47	0.48
NIR⁄R	0.47*	0.68*	0.48*	0.78*	0.53*	0.28	0.49	0.24	0.07	-0.10	0.08	-0.08	0.33	0.37	0.35	0.38
B×G×R	0.43*	-0.15	0.19	-0.35	-0.23	-0.26	-0.32	-0.34	0.18	0.23	0.30	0.28	0.09	0.16	0.29	0.35

B×G×N	0.69*	0.22	0.43*	0.04	-0.18	-0.22	-0.23	-0.30	0.19	0.23	0.30	0.24	0.09	0.16	0.31	0.37
B×R×N	0.72*	0.24	0.46*	0.08	-0.18	-0.22	-0.23	-0.29	0.20	0.24	0.32	0.26	0.09	0.17	0.33	0.38
G×R×N	0.12	-0.46*	0.08	-0.47*	-0.35	-0.38	-0.39	-0.42	0.27	0.28	0.31	0.30	0.21	0.28	0.29	0.36
Avg(B;G)	0.27	-0.29	0.20	-0.33	-0.25	-0.28	-0.29	-0.31	0.22	0.22	0.25	0.20	0.17	0.24	0.24	0.30
Avg(B;R)	0.35	-0.19	0.26	-0.25	-0.25	-0.27	-0.28	-0.29	0.25	0.24	0.28	0.23	0.20	0.26	0.27	0.33
Avg(B;N)	0.63*	0.24	0.53*	0.19	-0.14	-0.21	-0.15	-0.23	0.26	0.23	0.28	0.20	0.22	0.28	0.30	0.35
Avg(G;R)	0.18	-0.40*	0.12	-0.42*	-0.34	-0.38	-0.38	-0.41	0.29	0.30	0.33	0.32	0.24	0.30	0.33	0.39
Avg(G;N)	0.48*	-0.03	0.34	-0.12	-0.22	-0.30	-0.23	-0.33	0.30	0.29	0.33	0.28	0.25	0.31	0.35	0.40
Avg(R;N)	0.56*	0.09	0.42*	0.01	-0.20	-0.29	-0.21	-0.31	0.32	0.30	0.34	0.29	0.27	0.33	0.38	0.42
N-R	0.57*	0.81*	N/A	N/A	0.28	0.07	0.17	-0.05	0.24	0.11	N/A	N/A	0.26	0.31	N/A	N/A
Kab1	-0.31	-0.74*	-0.26	-0.65*	-0.32	-0.38	-0.30	-0.36	0.37	0.46	0.39	0.48	0.67*	0.72*	0.68*	0.74*
NDVI	0.49*	0.78*	N/A	N/A	0.48	0.23	0.33	0.10	0.08	-0.08	N/A	N/A	0.35	0.38	N/A	N/A
NRVI	-0.49*	-0.78*	N/A	N/A	-0.48	-0.23	N/A	N/A	-0.08	0.08	N/A	N/A	-0.35	-0.38	N/A	N/A
OC2	-0.31	-0.75*	N/A	N/A	-0.35	-0.40	-0.34	-0.40	0.38	0.47	N/A	N/A	0.64*	0.69*	N/A	N/A
SABI	0.50*	0.73*	N/A	N/A	0.48	0.23	0.33	0.09	0.17	0.01	N/A	N/A	0.36	0.40	N/A	N/A
(B-R)⁄G	0.15	0.58*	N/A	N/A	0.27	0.31	N/A	N/A	-0.43	-0.48	-0.39	-0.43	-0.62*	-0.64*	-0.59*	-0.60*
(NIR⁄G)+(NIR⁄B)	0.57*	0.70*	0.53*	0.77*	0.33	0.10	0.31	0.08	0.34	0.24	0.30	0.19	0.51*	0.53*	0.50*	0.52*
G×(B+G+R)	0.26	-0.33	0.13	-0.42*	-0.28	-0.32	-0.36	-0.38	0.22	0.25	0.30	0.28	0.13	0.21	0.29	0.35
[(1⁄B)-(1⁄G)]×N	-0.30	-0.65*	N/A	N/A	-0.42	-0.46	N/A	N/A	0.26	0.41	N/A	N/A	0.35	0.40	N/A	N/A
[(1⁄R)-(1⁄G)]×N	0.08	0.25	0.17	0.36	-0.06	-0.19	0.01	-0.12	-0.48	-0.55*	-0.44	-0.49	-0.47	-0.40	-0.51*	-0.45
[(1⁄R)-(1⁄B)]×N	0.25	0.57*	N/A	N/A	0.36	0.37	N/A	N/A	-0.37	-0.49*	-0.32	-0.43	-0.46	-0.43	-0.47	-0.45
[(1⁄R)-(0.2363×(1⁄G))]×N	0.45*	0.65*	0.47*	0.77*	0.51	0.26	0.47	0.22	0.01	-0.16	0.03	-0.14	0.27	0.32	0.29	0.34
(R^-1-B^-1)⁄N	-0.06	0.24	N/A	N/A	0.37	0.46	N/A	N/A	-0.31	-0.24	-0.37	-0.34	-0.47	-0.51*	-0.46	-0.49*
(B⁄R)×N	0.71*	0.56*	0.60*	0.66*	0.02	-0.07	0.04	-0.07	0.17	0.07	0.16	0.03	0.18	0.25	0.26	0.32
(G⁄R)×N	0.66*	0.39*	0.54*	0.41*	-0.12	-0.25	-0.13	-0.27	0.27	0.23	0.28	0.19	0.23	0.29	0.33	0.39
(R⁄B)×N	0.67*	0.29	0.48*	0.22	-0.23	-0.34	-0.22	-0.36	0.35	0.35	0.38	0.34	0.33	0.38	0.45	0.49

(R/G)×N	0.74*	0.47*	0.59*	0.50*	-0.08	-0.20	-0.07	-0.21	0.35	0.32	0.35	0.28	0.32	0.36	0.42	0.45
(R×N)/B	0.67*	0.29	0.48*	0.22	-0.23	-0.34	-0.22	-0.36	0.35	0.35	0.38	0.34	0.33	0.38	0.45	0.49
(B/G)×(B/R)	0.17	0.59*	0.21	0.66*	0.29	0.34	0.31	0.35	-0.43	-0.49*	-0.42	-0.47	-0.63*	-0.65*	-0.62*	-0.64*
(B/G)×(B/N)	-0.30	-0.27	-0.39*	-0.29	0.03	0.19	0.08	0.23	-0.38	-0.35	-0.40	-0.38	-0.55*	-0.59*	-0.57*	-0.60*
(B/G)×(R/G)	0.32	0.68*	0.35	0.71*	0.44	0.52	0.43	0.51	-0.16	-0.31	-0.14	-0.29	0.05	-0.12	0.04	-0.12
(B/G)×(R/N)	-0.42*	-0.63*	-0.46*	-0.59*	-0.08	0.14	-0.08	0.13	-0.29	-0.20	-0.32	-0.24	-0.49	-0.54*	-0.49	-0.53*
(B/G)×(NIR/B)	0.54*	0.73*	0.52*	0.82*	0.58*	0.35	0.54*	0.31	0.26	0.12	0.23	0.09	0.48	0.49	0.47	0.48
(B/G)×(NIR/G)	0.46*	0.71*	0.48*	0.84*	0.73*	0.58*	0.65*	0.53*	-0.03	-0.21	0.00	-0.18	0.33	0.32	0.33	0.32
(B/G)×(NIR/R)	0.41*	0.67*	0.46*	0.83*	0.66*	0.51	0.58*	0.46	-0.20	-0.37	-0.16	-0.33	0.06	0.07	0.07	0.08
(B/R)×(B/N)	-0.33	-0.34	-0.44*	-0.36	0.00	0.14	0.05	0.19	-0.38	-0.35	-0.42	-0.39	-0.54*	-0.57*	-0.57*	-0.59*
(B/R)×(G/R)	-0.06	0.21	-0.04	0.26	0.16	0.18	0.19	0.21	-0.45	-0.48	-0.45	-0.47	-0.57*	-0.57*	-0.59*	-0.58*
(B/R)×(G/N)	-0.44*	-0.66*	-0.54*	-0.67*	-0.16	0.01	-0.15	0.02	-0.34	-0.26	-0.39	-0.33	-0.51*	-0.53*	-0.55*	-0.56*
(B/R)×(NIR/R)	0.33	0.60*	0.41*	0.78*	0.58*	0.42	0.51	0.38	-0.32	-0.47	-0.30	-0.44	-0.24	-0.20	-0.27	-0.23
(B/N)×(G/N)	-0.40*	-0.75*	-0.53*	-0.77*	-0.26	-0.04	-0.31	-0.09	-0.23	-0.12	-0.32	-0.21	-0.47	-0.50*	-0.51*	-0.52*
(B/N)×(R/N)	-0.39*	-0.75*	-0.51*	-0.75*	-0.23	0.00	-0.29	-0.06	-0.21	-0.09	-0.28	-0.16	-0.46	-0.50*	-0.48	-0.51*
(G/B)×(G/R)	-0.37*	-0.72*	-0.35	-0.71*	-0.42	-0.49	-0.43	-0.51	0.13	0.28	0.14	0.29	-0.03	0.12	-0.04	0.12
(G/B)×(G/N)	-0.44*	-0.85*	-0.48*	-0.84*	-0.56*	-0.46	-0.65*	-0.53*	-0.03	0.14	0.00	0.18	-0.33	-0.32	-0.33	-0.32
(G/B)×(R/B)	-0.24	-0.69*	-0.21	-0.66*	-0.32	-0.36	-0.31	-0.35	0.39	0.44	0.42	0.47	0.60*	0.62*	0.62*	0.64*
(G/B)×(R/N)	-0.41*	-0.82*	-0.46*	-0.83*	-0.50	-0.40	-0.58*	-0.46	0.12	0.29	0.16	0.33	-0.09	-0.10	-0.07	-0.08
(G/B)×(NIR/B)	0.47*	0.30	0.39*	0.29	-0.13	-0.27	-0.08	-0.23	0.42	0.40	0.40	0.38	0.57*	0.59*	0.57*	0.60*
(G/B)×(NIR/R)	0.47*	0.53*	0.46*	0.59*	0.08	-0.13	0.08	-0.13	0.35	0.27	0.32	0.24	0.48	0.52*	0.49	0.53*
(G/R)×(G/N)	-0.46*	-0.80*	-0.53*	-0.80*	-0.53*	-0.34	-0.56*	-0.36	-0.25	-0.13	-0.31	-0.19	-0.47	-0.48	-0.51*	-0.51*
(G/R)×(NIR/R)	0.35	0.55*	0.41*	0.70*	0.45	0.20	0.41	0.15	-0.18	-0.36	-0.16	-0.33	0.05	0.12	0.06	0.13
(G/N)×(R/N)	-0.39*	-0.78*	-0.51*	-0.81*	-0.44	-0.21	-0.52	-0.28	-0.14	0.00	-0.17	-0.02	-0.42	-0.45	-0.42	-0.44
(R/B)×(R/G)	0.01	-0.30	0.04	-0.26	-0.21	-0.23	-0.19	-0.21	0.43	0.45	0.45	0.47	0.59*	0.57*	0.59*	0.58*
(R/B(×(R/N)	-0.36*	-0.75*	-0.41*	-0.78*	-0.44	-0.34	-0.51	-0.38	0.27	0.41	0.30	0.44	0.29	0.26	0.27	0.23

(R⁄B)×(NIR⁄B)	0.54*	0.38*	0.44*	0.36	-0.11	-0.23	-0.05	-0.19	0.43	0.41	0.42	0.39	0.58*	0.59*	0.57*	0.59*
(R⁄B)×(NIR⁄G)	0.61*	0.64*	0.54*	0.67*	0.14	-0.04	0.15	-0.02	0.43	0.37	0.39	0.33	0.57*	0.57*	0.55*	0.56*
(R⁄G)×(R⁄N)	-0.38*	-0.72*	-0.41*	-0.70*	-0.36	-0.11	-0.41	-0.15	0.13	0.30	0.16	0.33	-0.07	-0.14	-0.06	-0.13
(R⁄G)×(NIR⁄G)	0.57*	0.72*	0.53*	0.80*	0.59*	0.38	0.56*	0.36	0.36	0.25	0.31	0.19	0.54*	0.53*	0.51*	0.51*
(NIR⁄B)×(NIR⁄G)	0.58*	0.60*	0.53*	0.77*	0.36	0.13	0.31	0.09	0.39	0.30	0.32	0.21	0.53*	0.54*	0.51*	0.52*
(NIR⁄B)×(NIR⁄R)	0.54*	0.58*	0.51*	0.75*	0.35	0.10	0.29	0.06	0.34	0.23	0.28	0.16	0.48	0.50*	0.48	0.51*
(NIR⁄G)×(NIR⁄R)	0.47*	0.57*	0.51*	0.81*	0.60*	0.35	0.52	0.28	0.19	0.03	0.17	0.02	0.42	0.44	0.42	0.44

Appendix G: Scatterplots of models presented in section 4.4

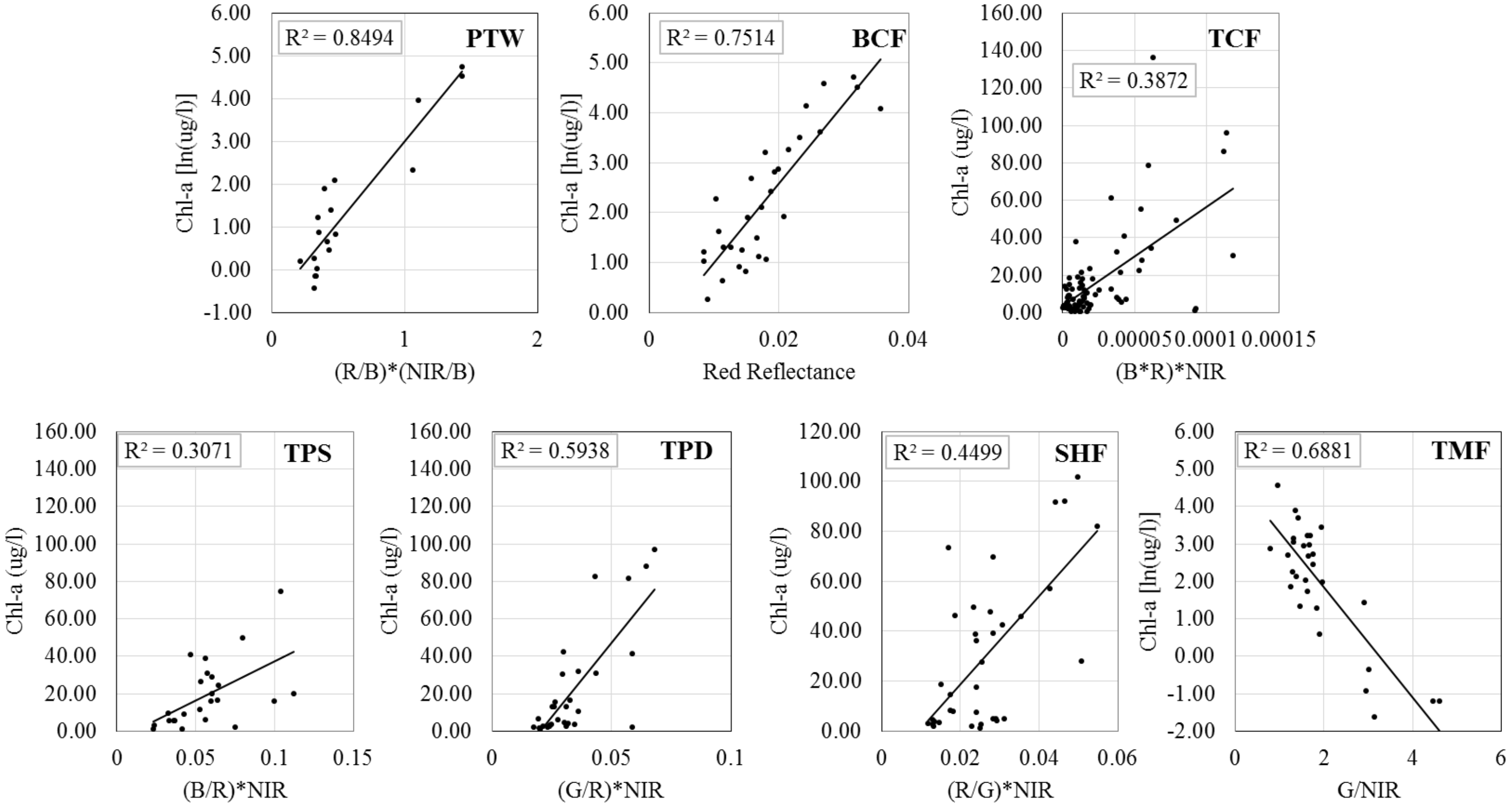

Figure G1: “Optimal” chl-*a* regression plots for all regions. Optimal is defined as algorithms exhibiting the highest R and free of confounding signals

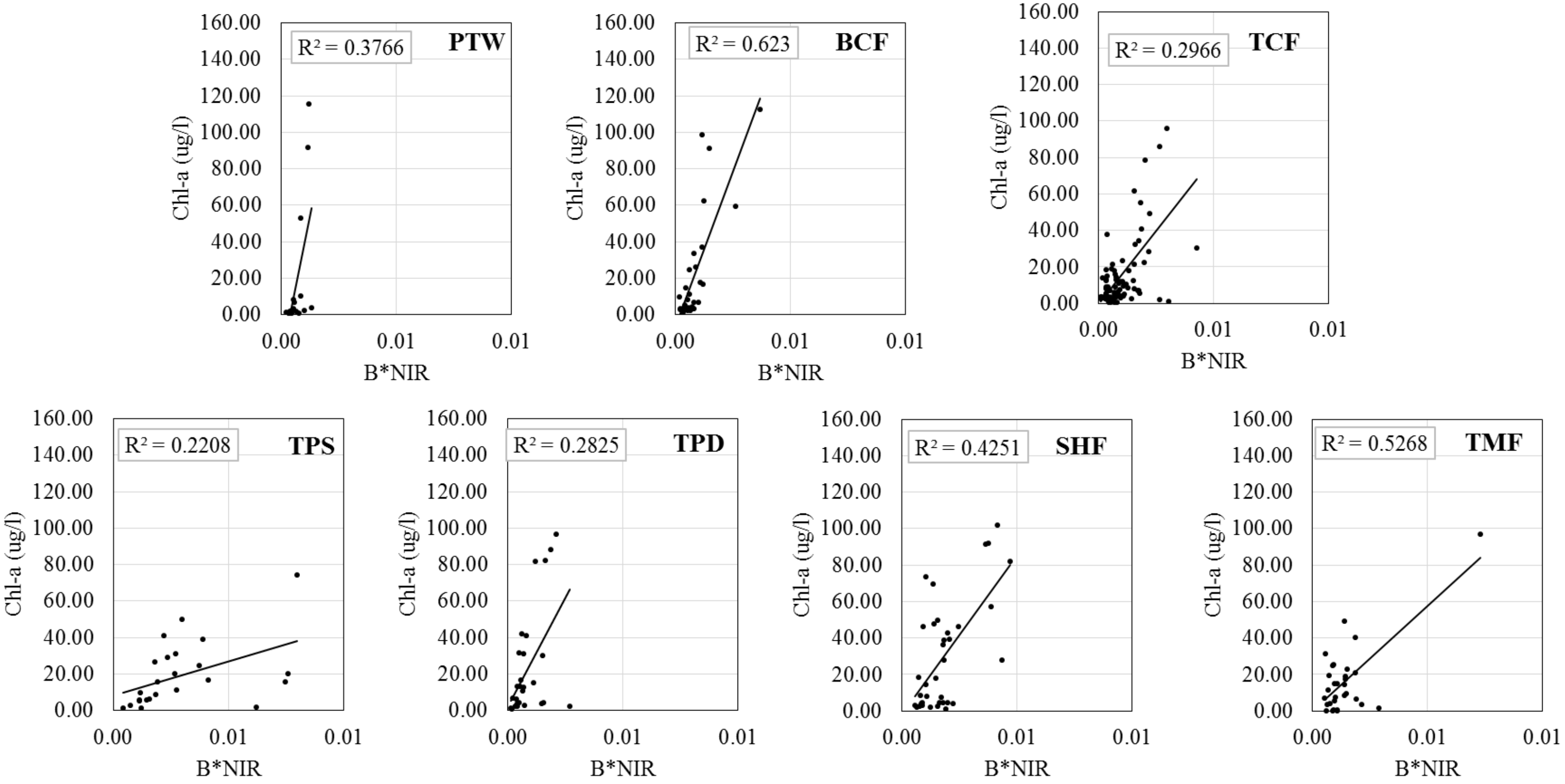

Figure G2: B×NIR chl-*a* regression plots for all regions

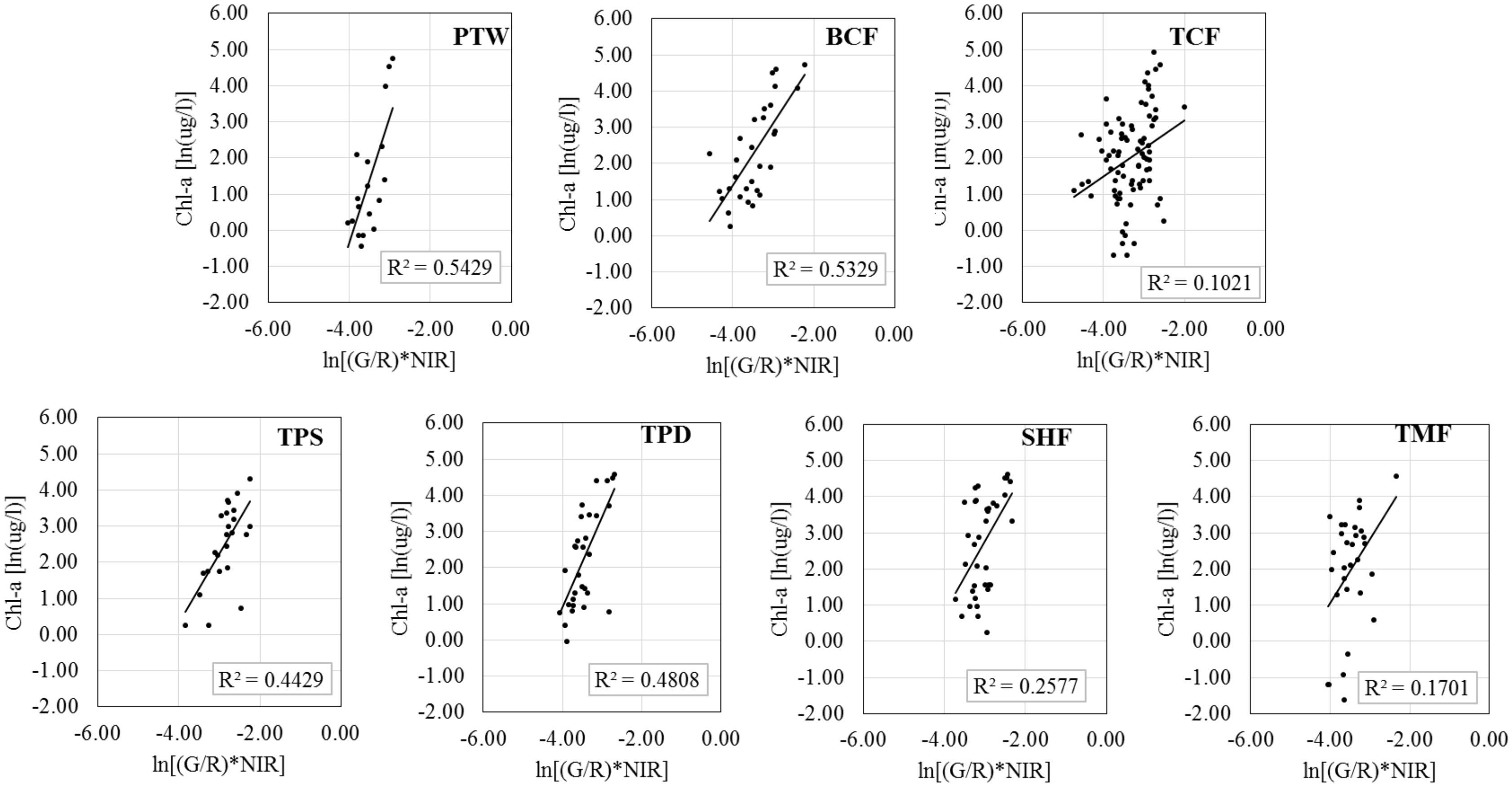

Figure G3: (G⁄R)×NIR chl-*a* regression plots for all regions.

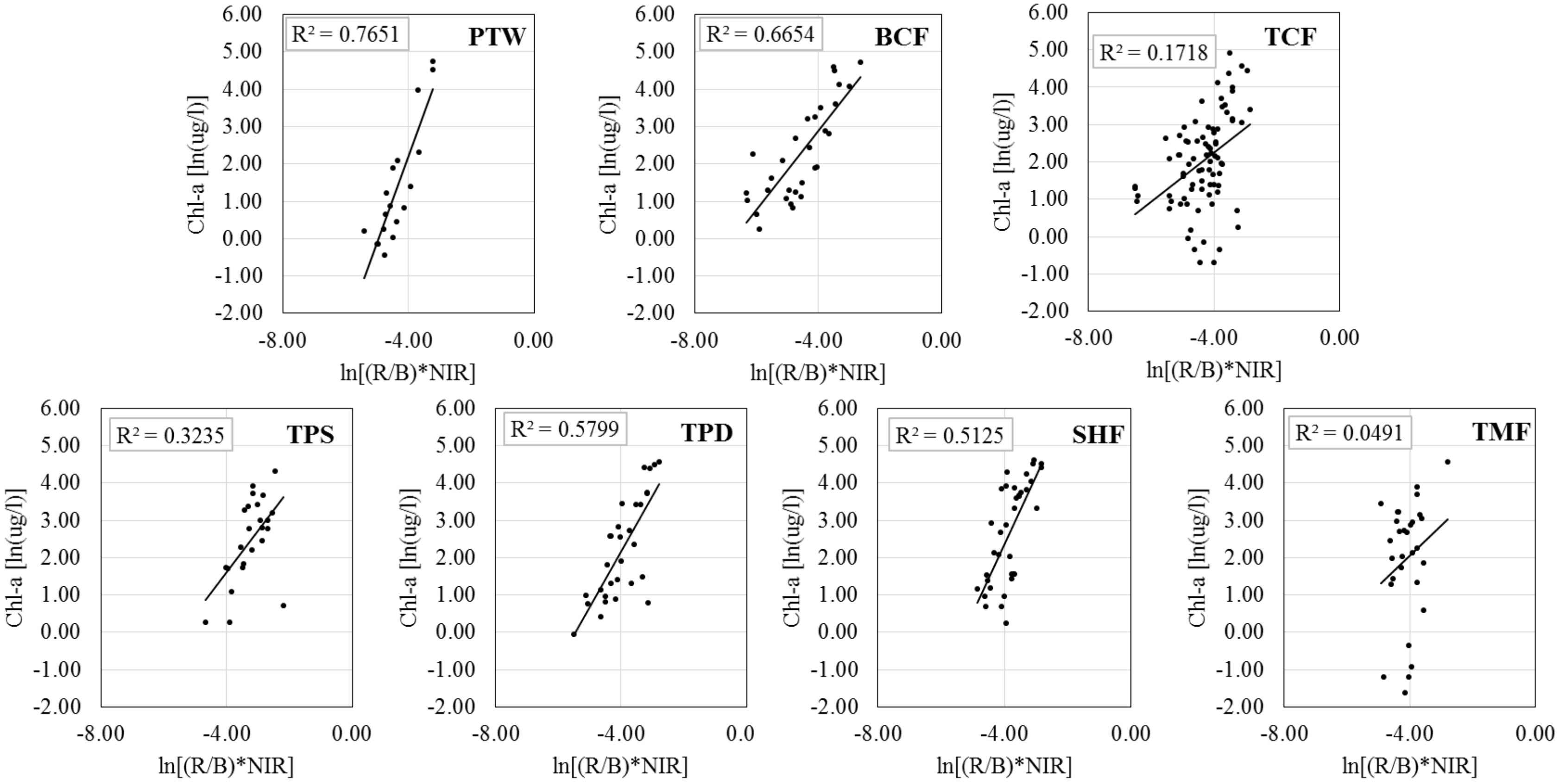

Figure G4: (R⁄B)×NIR chl-*a* regression plots for all regions

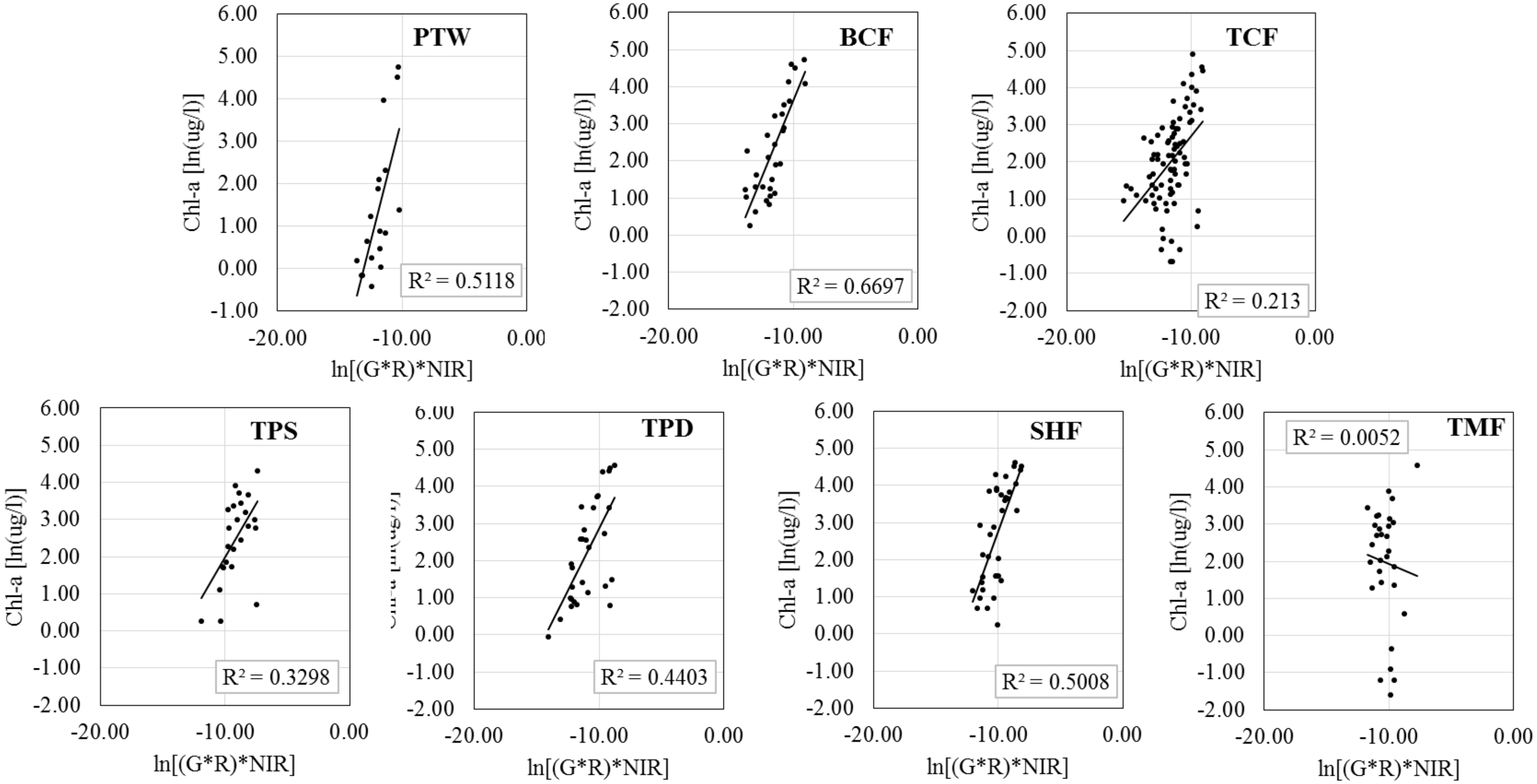

Figure G5: (G×R)×NIR chl-*a* regression plots for all regions

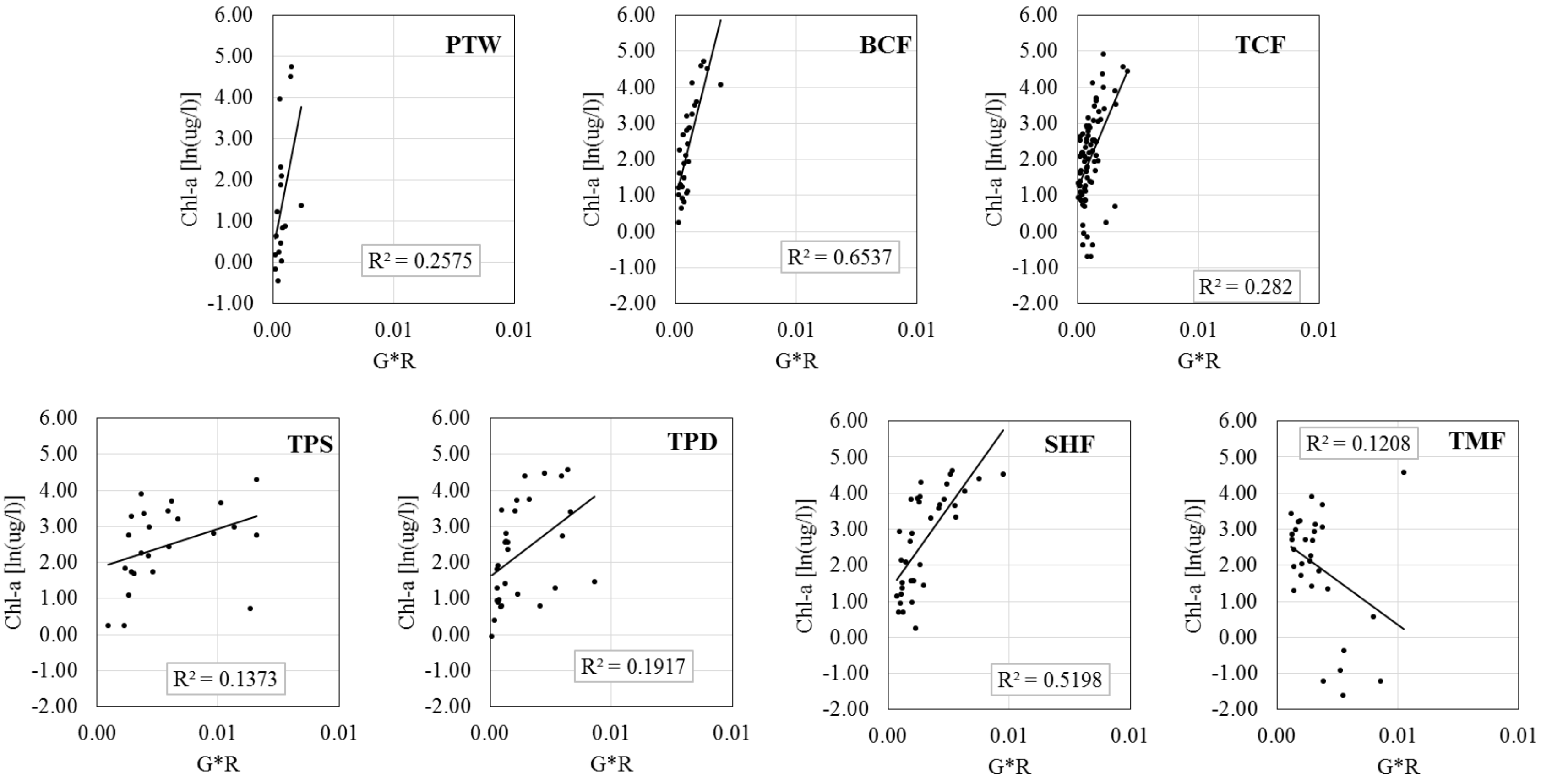

Figure G6: G×R chl-*a* regression plots for all regions

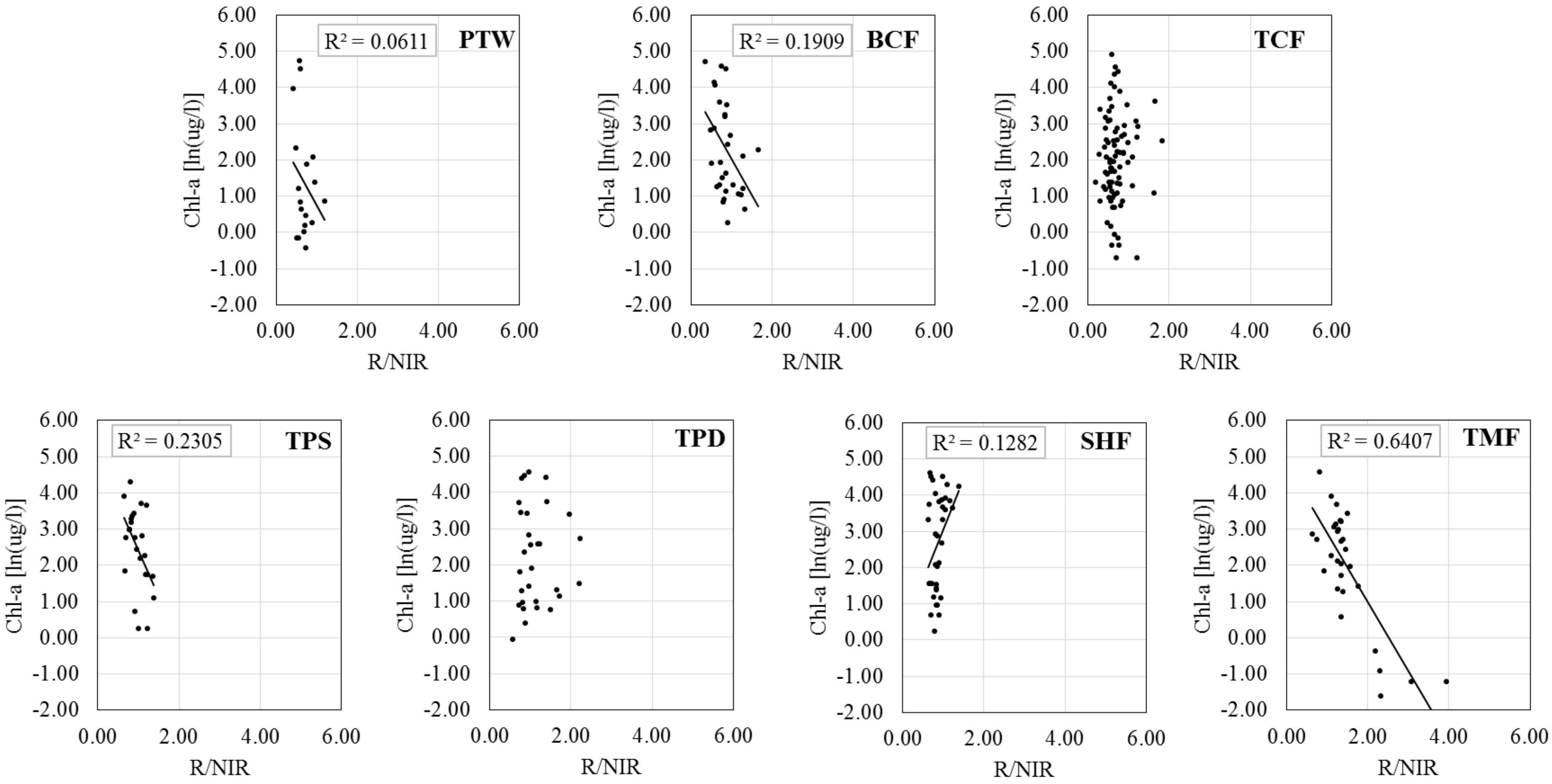

Figure G7: R/NIR chl-*a* regression plots for all regions

Curriculum Vitae

Name:	Michael Arthur Dallosch
Post-secondary Education and Degrees:	Western University London, Ontario, Canada 2015-2016, Master of Environment and Sustainability (MES) University of Waterloo Waterloo, Ontario, Canada 2009-2014, Bachelor of Environmental Studies (BES)
Honours and Awards:	University of Waterloo Arts Entrance Scholarship, 2009 Dean’s Honour list, University of Waterloo, 2014
Related Work Experience	Teaching Assistant Western University 2017/1-2017/12, 2018/1-2018-12 ENVSCI 1021, BIOL/STATS 2244: Environmental Issues, Analysis & Interpretation of Biological Data Graduate Student Research Assistant Western University 2017/5-2017/8, 2018/5-2018/8

Presentations (2018-2019):

Dallosch MA, Creed IF. 2019. Old tools applied at new scales to monitor the frequency and magnitude of algal blooms. Canadian Conference for Fisheries Research/the Society of Canadian Limnologist (CCFR/SCL) 2019, January 3-6, London, ON, Canada. (Oral).

Dallosch MA, Creed IF. 2018. Old tools applied at new scales to monitor the frequency and magnitude of algal blooms in response to climate change. American Geophysical Union Fall Meeting, December 10-14, Washington D.C, USA. (Poster).

Dallosch MA, Creed IF. 2018. Monitoring the frequency and magnitude of algal blooms via spaceborne sensors. 2nd Interdisciplinary Freshwater Algal Blooms Workshop (IFHAB), April 16-18, Toronto, ON. (Oral).